2014

Nanodosimetric particle track simulations in water and DNA media

Marion Ute Bug
University of Wollongong

NANODOSIMETRIC PARTICLE TRACK SIMULATIONS IN WATER AND DNA MEDIA

Marion Ute Bug

A dissertation submitted in fulfilment of
the requirements for the award of the degree

Doctor of Philosophy

from

School of Physics
University of Wollongong
Australia
March 2014

Thesis supervisors:
Dr. Susanna Guatelli and Prof. Dr. Anatoly B. Rosenfeld
Dr. Hans Rabus (PTB, Braunschweig, Germany)

CERTIFICATION

I, Marion Ute Bug, declare that this thesis, submitted in fulfilment of the requirements for the award of Doctor of Philosophy, in the School of Physics, University of Wollongong, is wholly my own work unless otherwise referenced or acknowledged. The document has not been submitted for qualifications at any other academic institution.

Marion Ute Bug
31 March 2014

NANODOSIMETRIC PARTICLE TRACK SIMULATIONS IN WATER AND DNA MEDIA

Marion Ute Bug

A Thesis for Doctor of Philosophy

School of Physics, University of Wollongong, Australia

ABSTRACT

This work provides the first set of electron-impact interaction cross section data of DNA constituents based on experiments. These data permit to investigate the accuracy by which water cross sections can be used to represent DNA media in track structure simulations of electrons with energies between 7 eV and 1 keV. Liquid water or water vapour is conventionally used in track structure simulation codes to estimate radiobiological effects, however, the interaction cross sections of liquid water have not been experimentally verified.

Initially, electron track structure simulations in liquid water with the codes PTra and Geant4 were benchmarked with respective experimental literature data. For this purpose, PTra was augmented with reviewed water cross section data for electrons and protons. The evaluated cross section data for electron impact on the DNA constituents tetrahydrofuran, trimethylphosphate, pyrimidine and purine were implemented in PTra for simulations of monoenergetic electrons in DNA media. The DNA media consisted of a composition of DNA constituents with different water content. Due to substantial differences in the cross section data of water and DNA constituents, a significant enhancement of calculated clustered ionisation and excitation events in DNA media relative to water was observed for electrons with energies below 150 eV. In consequence, the probability to produce biologically relevant ionisation clusters in the vicinity of a 1 MeV proton track is higher for DNA media compared to water.

As a first step towards modelling the transport of ions in DNA medium, simulations of protons (0.1–10 MeV) and alpha particles (0.1–20 MeV) in nitrogen and propane were benchmarked by comparing simulated and measured nanodosimetric quantities.

Acknowledgements

Mein besonderer Dank gilt meinem Chef und Betreuer Hans Rabus für seine Unterstützung und sein unerschöpfliches Wissen.

My greatest appreciation to my professor Anatoly Rosenfeld for his unlimited support. This work is so much better than the Australian traffic!

Ein großes Dankeschön an Elisabetta Gargioni, die mich bereits während meiner Masterarbeit für die Nanodosimetrie begeisterte.

A special thank you to Heidi Nettelbeck for productive discussions and for being such a good boss.

Vielen Dank an meine Kollegen Woon Yong Baek und Gerhard Hilgers, die mir jederzeit für Diskussionen zur Seite standen.

My appreciation goes to Susanna Guatelli for her support on Geant4.

I am grateful to Daniel Bennett for his advice on grammar and stylistics in my thesis.

Heike Nittmann und Simone Shields, die mir oft die Arbeit erleichtert haben.

Meinen Eltern Ute und Axel, die mich bei allen Entscheidungen bedingungslos unterstützen.

Und vor allem, danke Johannes für deinen Beistand und Motivation in den richtigen Momenten!

Table of Contents

List of Abbreviations and Symbols

BEB	Binary encounter Bethe (model)
DDCS	Double differential inelastic cross section
DEA	Dissociative electron attachment
DelCS	Differential elastic scattering cross section
DNA	Deoxyribonucleic acid
G-value	Average number of interactions per 100 eV deposited energy
IAM	Independent atom model
LET	Linear energy transfer
MC	Monte Carlo
NT	Nucleotide
PTra	Track structure simulation code, developed at the PTB
PU	Purine
PY	Pyrimidine
RBE	Relative biological effectiveness
SCOP	Spherical complex optical potential (method)
SDCS	Single differential ionisation cross section
TCS	Total scattering cross section
TelCS	Total elastic scattering cross section
THF	Tetrahydrofuran
TMP	Trimethylphosphate
W-value	Average energy to produce an ion pair

a_0	Bohr radius, ~0.529 Å
B_0	Binding energy of outermost valence-shell electron
B_i	Binding energy of electron in i-th molecular shell
E	Secondary electron energy
E_{Tr}	Transferred energy
F_2	Cumulative probability to produce a cluster of at least size two
M_j	j-th Moment of a cluster size distribution
ν	Cluster size
$P(\nu\|Q)$	Probability distribution of cluster sizes ν arising from radiation quality Q
ϕ	Azimuth scattering angle
Q	Radiation quality, defined by type and energy of a particle
R	Rydberg energy, ~13.606 eV
σ_{el}	Total elastic scattering cross section
$\mathrm{d}\sigma_{\mathrm{el}}/\mathrm{d}\Omega$	Differential elastic scattering cross section
σ_{exc}	Total excitation cross section
$\sigma_{\mathrm{exc},j}$	Partial excitation cross section for j-th excited state
σ_{ion}	Total ionisation cross section
$\sigma_{\mathrm{ion},i}$	Partial ionisation cross section for i-th subshell
$\mathrm{d}\sigma_{\mathrm{ion}}/\mathrm{d}E$	Single differential ionisation cross section
$\mathrm{d}^2\sigma_{\mathrm{ion}}/\mathrm{d}E\mathrm{d}\Omega$	Double differential ionisation cross section
σ_{t}	Total scattering cross section
T	Primary particle energy
θ	Polar scattering angle
$\mathrm{d}\Omega$	Solid angle element of scattering direction
U_i	Average kinetic energy of electron in i-th molecular shell

List of Tables

List of Figures

List of Publications

[Pub1] M. U. Bug, E. Gargioni, S. Guatelli, S. Incerti, H. Rabus, R. Schulte, A. B. Rosenfeld. Effect of a magnetic field on the track structure of low energy electrons: a Monte Carlo study. *Europ. Phys. J. D* **60**: 85–92 (2010).

[Pub2] M. Bug, G. Hilgers, H. Nettelbeck, H. Rabus. Ionisierende Strahlungswechselwirkung mit der DNS: Nanodosimetrie. *PTB-Mitteilungen* **121** (2): 127–135 (2011).

[Pub3] M. U. Bug, W. Y. Baek, H. Rabus. Simulation of ionisation clusters formed in nanometric volumes of the deoxyribose-substitute tetrahydrofuran. *Int. J. Radiat. Biol.* **88**: 137–142 (2012).

[Pub4] P. Lazarakis, M. U. Bug, E. Gargioni, S. Guatelli, S. Incerti, H. Rabus, A. B. Rosenfeld. Effect of a static magnetic field on nanodosimetric quantities in a DNA volume. *Int. J. Radiat. Biol.* **88**: 183–188 (2012).

[Pub5] P. Lazarakis, M. U. Bug, E. Gargioni, S. Guatelli, H. Rabus, A. B. Rosenfeld. Systematic uncertainty of calculated nanodosimetric parameters investigated by comparison of Geant4-DNA and PTB Monte Carlo codes. *Phys. Med. Biol.* **57**: 1231–1250 (2012).

[Pub6] M. U. Bug, H. Rabus, A. B. Rosenfeld. Electron emission from amorphous solid water after proton impact: Benchmarking PTra and Geant4 track structure Monte Carlo simulations. *Rad. Phys. Chem.* **81**: 1804–1812 (2012).

[Pub7] M. U. Bug, E. Surdutovich, H. Rabus, A. B. Rosenfeld, A. V. Solov'yov. Nanoscale characterization of ion tracks: MC simulations versus analytical approach. *Eur. Phys. J. D* **66**: 291 1–6 (2012).

[Pub8] W. Y. Baek, M. Bug, H. Rabus, E. Gargioni, B. Grosswendt. Differential elastic and total electron scattering cross sections of tetrahydrofuran. *Phys. Rev. A* **86**: 032702 1–15 (2012).

[Pub9] W. Y. Baek, A. Arndt, M. U. Bug, H. Rabus, M. Wang. Total electron-scattering cross sections of pyrimidine. *Phys. Rev. A* **88**: 032702 1–8 (2013).

[Pub10] M. U. Bug, E. Gargioni, H. Nettelbeck, W. Y. Baek, G. Hilgers, A. B. Rosenfeld, H. Rabus. Ionization cross section data of nitrogen, methane, and propane for light ions and electrons and their suitability for use in track structure simulations. *Phys. Rev. E* **88**: 043308 1–21 (2013).

[Pub11] G. Hilgers, M. U. Bug, E. Gargioni, H. Rabus. Comparison of measured and Monte-Carlo simulated track structure parameters in nanodosimetric volumes. *Radiat. Prot. Dosim.* doi:10.1093/rpd/nct265 (2013).

[Pub12] M. U. Bug, E. Gargioni, H. Nettelbeck, W. Y. Baek, G. Hilgers, A. B. Rosenfeld, H. Rabus. Proton-impact ionisation cross sections for nanodosimetric track structure simulations. *Radiat. Prot. Dosim.* doi:10.1093/rpd/nct317 (2013).

[Pub13] C. Champion, M. A. Quinto, M. U. Bug, W. Y. Baek, P. F. Weck. Theoretical and experimental quantification of double and singly differential cross sections for electron-induced ionization of isolated tetrahydrofuran molecules. *Eur. Phys. J. D* **68**: 205 1–7 (2014).

[Pub14] M. U. Bug, W. Y. Baek, H. Rabus. An evaluated cross section data set of DNA constituents for electrons of energies between 9 eV and 1 keV. J. Phys. Chem. Ref. Data, submitted (2014).

Chapter 1

Introduction

“You just have to walk slowly enough to stay always in the sun.”

— Antoine de Saint-Exupéry, The Little Prince

The words of the Little Prince were chosen to introduce this thesis as they not only provide an excellent depiction of art and distress in research, but also sustained my motivation during thesis preparation. His words can even be related more specifically to this work, as one has to ‘walk slowly’ to be able to look closely and bring to light the details of the track structure of ionising particles on the nanometric scale.

Ionising radiation is constantly impinging on human bodies. The radiation exposure of the general public originates largely from natural sources, such as cosmic or terrestrial radiation, radon inhalation and ingestion of radionuclides (effective annual dose of 1.5 mSv (65%) in Australia [156] and 2.1 mSv (53%) in Germany [23]). Civilisation sources of ionising radiation lead to an average effective annual dose of 0.8 mSv in Australia and 1.9 mSv in Germany, where nearly the entire dose is due to medical diagnostics. Radiation workers in Australia and Germany receive an additional annual dose of 0.12 mSv and 0.58 mSv, respectively. Furthermore, ionising radiation is applied in radiation treatment, where the difficulty is to control the tumour via a high dose of radiation while protecting the surrounding healthy tissue at the same time.

When traversing a medium, ionising radiation loses energy by inelastic interactions with local molecules, which are left in an excited or ionised state. The deposited energy is subsequently rearranged within the medium and may lead to a rupture of chemical bonds. Radicals may be formed subsequent to an ionisation or fragmentation of a molecule, which can diffuse and attack sensitive structures. The most radiosensitive target in a human cell is assumed to be the DNA present in cell nuclei [74, 145, 147, 164]. The rupture of chemical bonds in the DNA causes its damage, which can be repaired by the cell only to limited extend. Severely damaged DNA may be followed by apoptosis or carcinogenesis, involving complex chemico-biological processes. The apoptosis of cancer cells is the ultimate aim in radiotherapy, while radioprotection regulations aim to prevent carcinogenesis of healthy cells.

Biological effects of radiation are generally dependent on the absorbed dose, a fundamental dosimetric quantity. The absorbed dose is a deterministic quantity, in fact, the sum of the energy deposited in single interactions within macroscopic targets divided by the target mass [102]. The relative biological effectiveness (RBE) of a specific radiation quality[*] is defined as the ratio of absorbed doses by a reference radiation to the applied radiation for the same biological endpoint, such as cell survival. Fluctuations of the imparted energy are, however, present when microscopic sensitive sites are considered, such as DNA segments. Multiple damage of the molecules within DNA

---

[*] Radiation quality Q is defined by the type and energy of a particle.

segments of a few nanometres in length (i.e. complex DNA double-strand breaks) is likely to be unrepairable by the cell, which has the above mentioned radiobiological consequences. The DNA damage originating from interactions within those sites can only be evaluated from the particle track structure. The track structure contains the spatial pattern of interactions of the incident particle and its secondaries with the molecules of the traversed medium. This pattern is characteristic for a specific radiation quality. The importance to consider the particle track structure additionally to the absorbed dose when evaluating the biological effect is illustrated in the following example.

Imagine a specific absorbed dose administered by either photons or ions to a macroscopic volume consisting of an aggregate of several human cells. For photons, the interactions involving an energy deposit are nearly homogeneously distributed across the target volume. This is mainly due to the production of delta electrons with a relatively high energy, on average, and, hence, a large range so that the electron tracks extend over a larger region of the macroscopic volume. Therefore, in the case of photon irradiation, the energy is deposited in a large number of local sensitive DNA sites within the cell nuclei and those sites experience easily repairable damage. However, the LET becomes high in the track ends due to low-energy secondary electrons and a few DNA sites may be severely damaged. For ions, on the other hand, the LET is high across their track, particularly in the regions at the end of the ion trajectory, where the Bragg peak is formed in the depth-dose curve [120]. The LET is also high in the vicinity of the ion trajectory due to the high number of produced low-energy electrons. In this case, the majority of sensitive DNA sites in the macroscopic volume are not traversed but some sites are severely damaged (see figure 1.1). This means that the same absorbed dose leads to a higher number of severely damaged sensitive DNA sites in the case of ions than for photons. Therefore, it is important to characterise the track structure on the DNA scale when dealing with high-LET radiation, such as ions and low-energy secondary electrons. Secondary electrons are, in fact, produced in a large number by any kind of radiation so that highly localised energy deposition events are always considerable.

Parameters related to the particle track structure are used in micro- and nanodosimetry. Microdosimetry has been developed in the middle of the last century by H. Rossi and A. M. Kellerer [112–114, 159]. This technique provides information on the energy deposited within volumes of micrometers in size as well as on frequency distributions of the energy transferred by individual particles. Nanodosimetry derives parameters directly from the particle track structure on the nanometric scale [79, 145, 157, 164]. In both micro- and nanodosimetry, experiments in gaseous volumes, modelling a condensed target of respective microscopic size, are used in conjunction with Monte Carlo

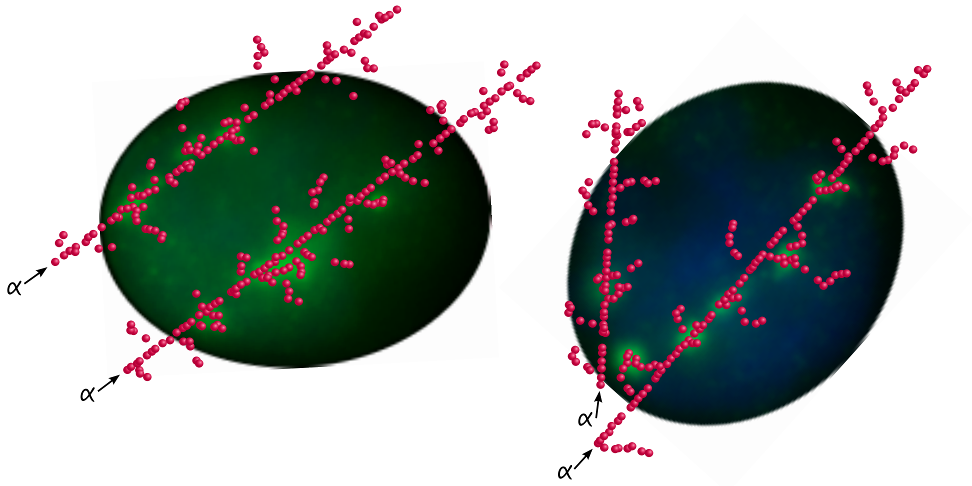

Figure 1.1: Alpha particle tracks traversing human cells with stained nuclei (photos committed by [187]). Pink spheres sketch ionisation interactions by the alpha particles (along straight trajectories) and secondary electrons (in the vicinity of the alpha particle trajectories). An ionisation is leading to a DNA strand break with a specific probability so that double-strand breaks of the DNA result from at least two interactions within sensitive substructures of the cell nucleus. They appear as bright green dots (foci) as fluorescent repair proteins accumulate at the DNA lesion. For a single ion track, the foci are clearly appearing in localised regions close to the ion trajectory, while a large region of the cell nucleus is not affected.

simulations to obtain the desired parameters. For such purpose, detailed Monte Carlo simulations of the particle track structure are essential. Those simulations require the interaction cross sections of the radiation with molecules of the medium of interest. Interaction cross sections describe the probability for a specific interaction, energy transfer and angular scattering. Those data are necessary to solve the particle transport problem numerically via random sampling of derived probability distributions. For DNA medium, a complete set of electron-impact cross sections had only been obtained from theories which are reliable in the high-energy range [45]. Hence, most track structure simulations are performed using liquid water as a model for the DNA. In favour of such an approximation speaks the fact that the biological target, i.e. DNA in cellular environment, contains a large percentage of water molecules. Furthermore, the interaction cross sections of water vapour have been intensively investigated.

Even though both water and DNA consist of covalently bound light atoms, a scaling of the interaction cross sections by the number of electrons in the molecules is applicable only for electrons of energy above several hundreds of electronvolts [9]. Also the ionisation threshold is significantly different, as will be shown later in this work. This means that the physical properties of DNA molecules are not accurately approximated by those of water, so that the question arises if water even is a reasonable model for biological medium.

This thesis investigates the accuracy of using water cross section data to approximate those of the DNA in track structure simulations. Based on electron-impact cross section data for DNA constituents, which were derived from experimental data measured at the PTB, the thesis will address the following questions:

1. How accurate are cross sections of water?
2. How different are the electron-impact cross section data for water and DNA constituents?
3. How sensitive are simulated nanodosimetric parameters to differences in cross section data?

1.1 Outline of this thesis

Basic theoretical background is provided in chapter 2 to illustrate the importance of particle track structure in radiation dosimetry. The structure of the DNA as radiosensitive target and its initial damage by ionising radiation are outlined. The focus is then turned onto physico-chemical properties of the individual DNA constituents used in this work. This topic relates directly to a brief description of essential interaction processes of charged particles with matter and their interaction cross sections. The application of such cross sections in track structure simulations are explained by describing the simulation of radiation transport in detail. Basic ideas of nanodosimetry and the most essential quantities used in this work are then defined based on track structure parameters.

As a first step in this work, track structure simulations using water medium are investigated in chapter 3. This work is essential for the evaluation of a difference between simulations in water and DNA medium for the following reasons. A literature review with focus on cross section models describing the interaction of electrons and protons with vapour, liquid and amorphous water provides a systematic and (probably for the first time and to the best of knowledge) unbiased investigation of the most important cross section models applied in track structure simulations. The track structure code of the PTB (PTra) was then augmented by evaluated data for water vapour and liquid water. Electron and proton transport simulations using either of both media are tested by calculations of W-values and stopping power. A major scientific contribution of this chapter is the benchmark of secondary electron transport using PTra as well as Geant4-DNA for liquid water. The benchmark was performed by comparing simulated secondary electron spectra to measured data from a specifically designed experiment by a group at East Carolina University. This experiment has been modelled by an earlier version of PTra, which has been published [Pub6], and simulations were repeated for the augmented versions comparing results in water vapour and liquid water. Another scientific gain is the comparison of simulated nanodosimetric quantities in the vicinity of a carbon ion trajectory with those obtained from an analytical model, developed by a group at the Frankfurt Institute for Advanced Studies (FIAS). This work was also published [Pub7] and is a step towards an application of nanodosimetry in radiation therapy.

The scientific contribution of chapter 4 is obvious as, for the first time, a comprehensive data set for electron-impact cross sections of DNA constituents was entirely derived from experimental data. Moreover, analytical descriptions were developed for a convenient implementation in simulation codes. The data evaluation is described and discussed in detail for each cross section. The chapter is finalised with a summary, providing the necessary data sources (equations and tables) to reconstruct the cross sections.

The evaluated electron-impact cross section set for DNA constituents was then implemented in PTra. In chapter 5, cross sections of DNA constituents are first compared to those of water medium. The DNA target concept used in this work and subsequently necessary modifications of the simulation procedure are introduced. Parameters obtained from simulations in DNA targets are compared to those in water, such as W-value, stopping power, ionisation cluster size distributions. The influence on simulated parameters by different parametrisations of cross section data for excitation and angular distributions after elastic scattering as well as the water content within the DNA are tested. Finally, a more realistic situation with relation to ion therapy is modelled in both DNA and water media to assess differences of nanodosimetric quantities in the vicinity of a proton trajectory.

Track structure simulations of protons and heavier ions in DNA medium are the logical next step in this work. Such simulations can be benchmarked by simulating the experimental setup of a nanodosimeter. A comparison of measured and simulated nanodosimetric ionisation cluster sizes allows to assess the accuracy of both ion and secondary electron transport. Unfortunately, respective interaction cross section data are not yet available, but measurements in the nanodosimeter were performed for the impact of protons or alpha particles, operating the nanodosimeter with nitrogen or propane. Both media are constituents of tissue-equivalent gas and particularly for propane, similar physical properties as for DNA constituents are expected as those mainly consist of hydrogen and carbon atoms. Therefore, the study in chapter 6 is a first step towards a simulation of ions in DNA medium. Here, track structure simulations of protons and alpha particles in nitrogen and propane are benchmarked versus quantities measured in the nanodosimeter. This involved an extensive review on relevant ionisation and charge transfer cross section data. The work provided in this part of the thesis was published [Pub10,Pub12].

Final conclusions and an outlook for future work are provided in chapter 7.

Chapter 2

Importance of particle track structure – theoretical background

2.1 The biological target

2.1.1 DNA – structure and damage

Deoxyribonucleic acid (DNA) is an essential component of living cells. Its functions are the storage and transfer of the genetic information to the next cell generation as well as providing the information for a direct synthesis of proteins. In these processes, a key role is played by the DNA structure. In this section, the DNA structure is examined, followed by a description of structural modifications arising from ionising radiation.

The basic DNA structure is a double-stranded helix, consisting of two antiparallel polynucleotide strands [190]. Alternating deoxyribose and phosphate groups form a backbone structure to which one of four nucleobases attaches to the deoxyribose molecule. This group, consisting of three molecules, is defined as a nucleotide. The nucleobases of both strands are hydrogen bonded and have a basic structure of either pyrimidine (cytosine and thymine) or purine (adenine and guanine). Specifically, adenine is always linked to guanine and thymine to cytosine, hence the antiparallel order. The genetic information is encoded in the sequence of the nucleobases.

The repeating nucleotide chains of the DNA can adopt three different conformations, A-DNA, B-DNA and Z-DNA, which differ in their structure. In a living cell, the DNA is usually present in B-form, where it has a diameter of 2.3 nm and a distance for a full helix turn of 3.4 nm with 10 base pairs per convolution. The right-handed twisting of the DNA strands into the helical structure results in alternating major and minor grooves. The A-form of the DNA contains 11.6 base pairs per convolution and a diameter of 2.6 nm. In the cell, the DNA chains are wrapped around histone proteins, which have the task to restrict the DNA into the volume of the cell nucleus. The arrangement of the DNA around eight histone proteins is the lowest order of packing and called a nucleosome. Further packing leads finally to the formation of chromosomes.

Water molecules are also present within the cell nucleus and can be considered as an integral part of the DNA structure, where they hydrate the major and minor grooves and link to polar atoms at the edges of base pairs [29, 46, 60, 115]. The water molecules are arranged in a complex pattern (e.g. water hexagons hydrated by up to four solvation shells) [29, 46]. Chaplin [29] pointed out in a review article, that the hydration is dependent on the sequence of nucleobases and therefore important for the recognition of the DNA sequence by proteins. Furthermore, the level of hydration determines the conformation of the DNA (A- or B-form) [46, 60, 115]. For example, dry DNA (A-form) contains, on average, 2.5 water molecules per base pair [163]. Higher levels of hydration lead to an organisation in B-form, which is reversible with dehydration. Franklin and Gosling [60] investigated the influence of hydration level on DNA conformation by X-ray crystallography and found that the B-form is always present when more than eight water molecules are present per nucleotide. Egli et al. [46] used the same technique with improved resolution and counted, on average, 12.5 water molecules per nucleotide in the first hydration shell organised within the DNA B-form. Additional 8.3 water molecules were observed in the second and third hydration shells, leading to a total of about 20 water molecules per nucleotide. Recently, Khesbak et al. [115] observed structural changes in B-DNA due to variations in water content by Fourier transform infrared spectroscopy. These authors found that solvation-dependent substate transitions, which are essential for the readout mechanisms of the DNA, can only occur if the number of water molecules per nucleotide is larger than 12.

The main focus of this work lies on initial effects of ionising radiation on DNA molecules. Ionising radiation is able to produce a broad spectrum of DNA damage [20, 72]. Generally, direct energy depositions at DNA molecules lead to their ionisation or excitation which may result in a rupture of chemical bonds and the generation of DNA lesions [72]. This is referred to as direct damage, while indirect damage to the DNA arises from secondary species (water radicals, radicals of other biomolecules surrounding the DNA, hydrated electrons), which are produced in the vicinity of the DNA molecules and may diffuse towards sensitive structures. It is well known that spatially concentrated ionisations increase the biological effectiveness even if a small number of DNA segments are affected [72]. Generally, the damage to a target volume of nanometric dimensions most likely results from a single primary ionising particle [20].

DNA damage is classified into three major types [72]: single-strand break (SSB), i.e. a damage of a backbone molecule; double-strand break (DSB), which is defined as two SSB on opposite strands within a DNA segment of 10 base pairs; and base damage (BD). The occurrence of additional lesions is known as complex or clustered damage [20, 72]. While simple DNA lesions are usually repaired error-free by the cell, complex damage has a potential to initiate carcinogenesis or cell death [72].

2.1.2 DNA constituents – structure and properties

The DNA damage by ionising radiation can be evaluated from the damage to constituents of the DNA. This has the advantage that interactions with different DNA constituents can easily be analysed to distinguish strand breaks from base damages. This section introduces the molecules which are commonly used as models for DNA constituents, with particular attention to the molecules relevant for this work.

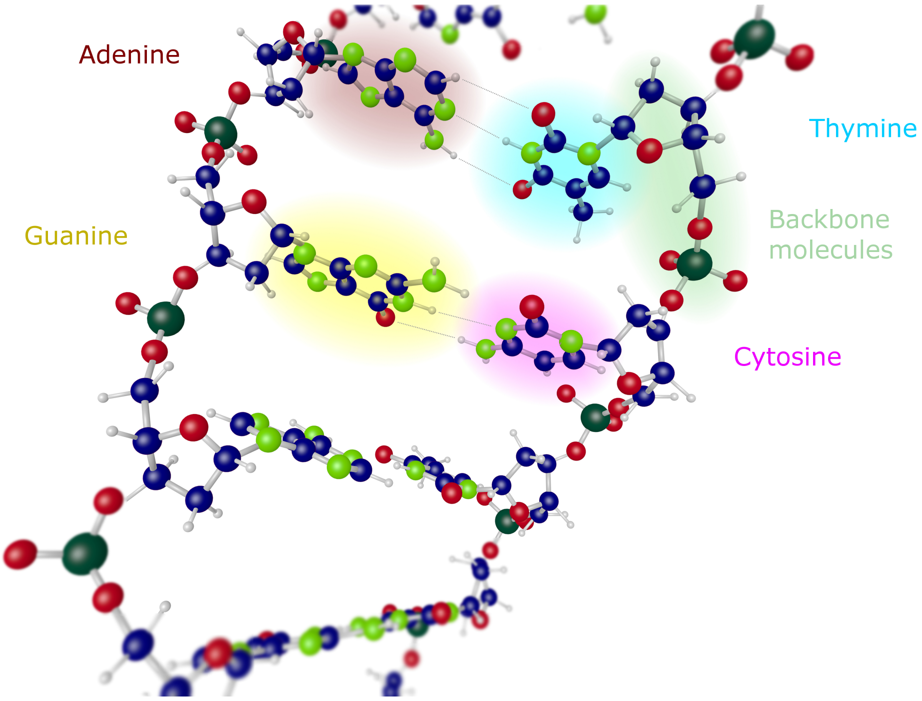

Figure 2.1: Chemical structure of a DNA segment containing the four nucleobases adenine, guanine, thymine and cytosine. Different atoms are colour coded spheres: C — blue, O — red, N — green, P — large dark green, H — small grey. Hydrogen bonds between the nucleobases are indicated by dashed lines.

The chemical structure of a DNA segment is schematically shown in figure 2.1. When bound in the DNA, the deoxyribose molecule (figure 2.2) is esterified at its C4-atom to the phosphoric acid (figure 2.3). The phosphate group of the preceding nucleotide is attached to the C3-atom of the deoxyribose. Both connections lead to the loss of two hydroxyl groups from the deoxyribose and two hydrogen atoms of the phosphoric acid. Particularly for this reason, the molecular structure of the DNA backbone can also be represented by alternating tetrahydrofuran (THF) and trimethylphosphate (TMP) molecules (figures 2.4 and 2.5). THF is a precursor of the deoxyribose; in combination with THF, TMP provides a representation of the trimethyl ester of the phosphoric acid at the C4-atom of THF.

There is an alternative model for the sugar-phosphate group in the DNA. Instead of using THF and TMP, the combination of phosphoric acid (H_3PO_4) and α-tetrahydrofurfuryl alcohol ($C_5H_{10}O_2$) may also be a good model [137]. On the other hand, isolated deoxyribose molecules, or more accurately 2-deoxy-D-ribose, would not be a good model for the sugar moiety in the condensed DNA due to three additional OH-groups in the isolated molecule, which have a significant impact on cross section data at low electron energies [1].

Pyrimidine (PY) and purine (PU) are precursors of the nucleobases (figures 2.6 and 2.7). The nucleobase cytosine is a PY ring with an oxygen atom linked to its C2-atom and a shift of the hydrogen atom at C2 in PY to N1 in cytosine. A NH_2-group replaces the hydrogen atom at C4. In thymine, oxygen atoms are linked to the C2 and C4 positions of the PY ring, while the hydrogen atoms are shifted from those positions in PY to N1 and N3 in thymine. The hydrogen atom at C5 is substituted by a CH_3-group. In the nucleobases adenine and guanine, the hydrogen atom at position C6 in PU is shifted to N1 and a NH_2-group and an oxygen atom are attached to C6, respectively. In guanine, a NH_2-group replaces the hydrogen atom at the C2-atom. The nucleobases are linked to the C1-atom of the deoxyribose (or THF) at N1 (PY nucleobases) and N9 (PU nucleobases). Those nitrogen sites are deprotonated by the respective molecules. The two strands of the DNA are connected by two hydrogen bonds between the complementary bases adenine and thymine. Similarly, guanine and cytosine are connected via three hydrogen bonds.

Further characteristics of the described DNA constituents are listed in figures 2.2–2.7 and described in the following, i.e. molecular formula, chemical structure, point group, electric dipole moment, static dipole polarisability and the ionisation potential.

The point group provides information about the geometrical symmetry properties of the molecule in its electronic ground state. In this work, the point group is required as an input parameter for the calculation of the electron density distribution by means of the quantumchemical code GAMESS [75]. This calculation is, for example, achieved by Hartree Fock or density functional methods and provides the parameters used in section 2.2.6. In that section, the calculation with GAMESS is described in more detail.

The permanent dipole moment is required to estimate the influence of rotational transitions on measured electron scattering cross sections, which becomes significant if the dipole moment is large (see section 2.2). Experimental data are only available for THF and PY (values given below), but data calculated by various theories are available for some molecules in the Computational Chemistry Comparison and Benchmark DataBase (CCCBDB) at NIST [141]. In this data base, density functional calculations (BLYP) using the 6-31G(2df,p) basis set provided the closest value to the experimental dipole moment of THF. For PY, however, one of the best agreements with the experimental data give the Hartree Fock (HF) calculations with the 6-311G** basis set (2.368 D). The BLYP calculations underestimate the large dipole moment of PY, while the HF calculations give larger values for THF (about 1.9 D). Therefore, both values are shown below for the other molecules, where available. In summary, the dipole moment of the nucleobases are larger than those of backbone molecules and PU has the largest value. Dipole moments for the DNA nucleobases adenine, thymine, cytosine and guanine are 3.0, 4.1, 7.0, 7.2, 4.1 and 3.0 D, respectively [107]. These data are experimental except the value for guanine.

The dipole polarisability describes the distortion of the molecular charge distribution by the presence of an electric field. In general, a large dipole polarisability reduces the probability for an ionisation of the molecule by passing ions. In contrast, for passing electrons the dipole polarisability enhances the probability for ionisation and also increases the probability for large scattering angles of an elastically scattered electron. For some molecules, experimental values are available from measurements of the refractive index [15], otherwise data were taken from the CCCBDB of NIST [141]. Among the molecules of interest, TMP and PU have the largest dipole polarisabilities, followed by THF and PY for which the dipole polarisability is similar. Dipole polarisabilities for the DNA nucleobases are larger than those of the respective precursors. Experimental values are 69.5, 75.8, 88.4 and 91.8 a_0^2 for cytosine, thymine, adenine and guanine, respectively.

The vertical ionisation potential is the energy required for the most probable transition from the ground state of the molecule to the continuum. The value of the vertical ionisation potential has a considerable influence on the ionisation cross sections in this work. Experimental data were found for THF, PY and TMP in the literature [92, 141, 178]. The other data were obtained using Koopmans' theorem [119] and the results of Hartree Fock calculations with the G6-31(2df,p) basis sets (HF), given in the CCCBDB of NIST [141]. In Koopmans' theorem it is assumed that the energy levels of a molecule do not change during the ionisation, with the consequence that the vertical ionisation potential is equal to the negative binding energy of the highest occupied molecular orbital. It should be noted that the HF values of the first ionisation potential are about 1.1 eV and 0.4 eV larger than the experimental values for THF and PY, respectively. The experimental values of ionisation potentials will be used in section 4.4.2.

Name: 2-Deoxyribose, DR
Molec.formula: $C_5H_{10}O_4$
Structure: five-membered, heterocyclic, aromatic, organic; dominantly six-membered in gaseous form [136]
Point group: C_1

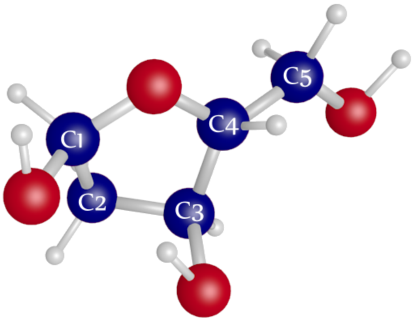

Figure 2.2: 2-Deoxyribose

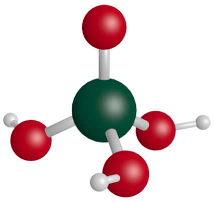

Name: Phosphoric acid
Molec.formula: H_3PO_4
Structure: tetrahedrical, inorganic acid
Point group: C_3
Dipole moment: 0.1 D (BLYP), 0.376 D (HF) [141]
Dip.polaris.: 33.1 a_0^3 (BLYP), 25.02 a_0^3 (HF) [141]
Ionis.pot.: 12.7 eV (HF) [141]

Figure 2.3: Phosphoric acid

Name: Tetrahydrofuran, THF
Molec.formula: C_4H_8O
Structure: five-membered, heterocyclic, aromatic, organic
Point group: predominantly C_2 [141]
Dipole moment: 1.63 D (experiment) [141]
Dip.polaris.: 53.78 a_0^3 (experimental) [15]
Ionis.pot.: 9.74 eV (experimental) [141]
Specifics: precursor of the DR.

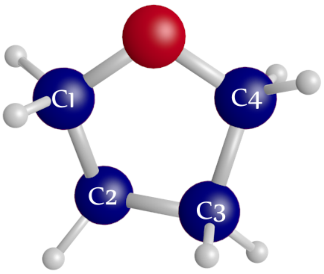

Figure 2.4: Tetrahydrofuran

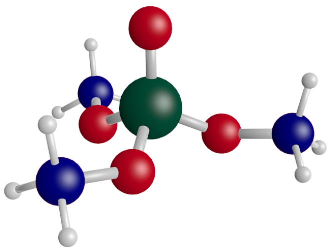

Name:	Trimethylphosphate, TMP
Molec.formula:	$(CH_3)_3PO_4$
Structure:	tetrahedrical, inorganic
Point group:	C_3 [88, 178]
Dipole moment:	0.64-1.01 D [69]
Dip.polaris.:	74.70 a_0^3 (experimental) [15]
Ionis.pot.:	10.81 eV (experimental) [178]

Figure 2.5: Trimethylphosphate

Name:	Pyrimidine, PY
Molec.formula:	$C_4H_4N_2$
Structure:	six-membered, heterocyclic, aromatic, organic with nitrogen atoms at positions 1 and 3.
Point group:	C_{2v} [141]
Dipole moment:	2.33 D (experiment) [12]
Dip.polaris.:	57.97 a_0^3 (experimental) [15]
Ionis.pot.:	9.73 eV (experimental) [92]
Specifics:	precursor of nucleobases thymine, cytosine and uracil.

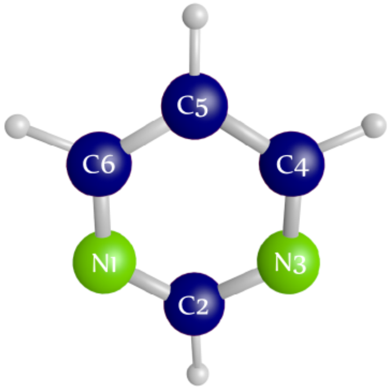

Figure 2.6: Pyrimidine

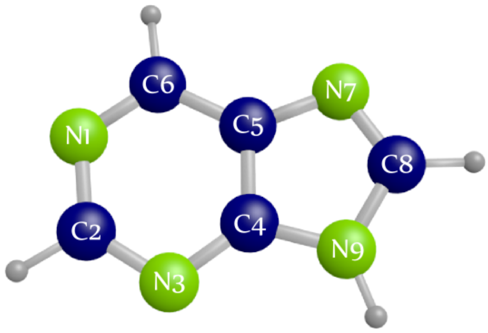

Name:	Purine, PU
Molec.formula:	$C_5H_4N_4$
Structure:	heterobicyclic, aromatic, organic
Point group:	C_s [141]
Dipole moment:	3.67 D (HF and BLYP) [141]
Dip.polaris.:	73.92 a_0^3 (BLYP), 66.44 a_0^3 (HF) [141]
Ionis.pot.:	9.092 eV (HF) [141]
Specifics:	precursor of nucleobases adenine and guanine.

Figure 2.7: Purine

2.2 Interactions of charged particles with matter

In this section, general interaction pathways of the particles of interest in this work and the de Broglie wavelength are introduced. In the subsections, a separation between fast and slow projectiles (above and below energies[†] of about 500 eV for electrons and 1 MeV/u for ions, respectively) was made on the basis of dominant interaction mechanisms involved in the collision. An overview of the most important interaction pathways of electrons and light ions in the energy range below several MeV is provided in table 2.1. Some of the subsequent dissociation pathways of the molecule are also listed.

Table 2.1: List of electromagnetic interactions of electrons (e^-) or positive ions (A^{x+}, $x > 0$) with target molecules (B). Subsequent dissociation paths into molecular fragments (b) are included as well as an incomplete list of radical species formed. In the case of ionisation, electron capture and electron loss processes, more than one electron can be ejected or transferred. Several interactions can occur simultaneously (e.g. ionisation and electron loss by an ion or neutral projectile $A^{0/x+}$).

Electromagnetic interactions:		
Ionisation	$\mathrm{A}^{x+} + \mathrm{B} \rightarrow \mathrm{A}^{x+} + \mathrm{B}^{+} + \mathrm{e}^{-}$;	$\mathrm{e}^{-} + \mathrm{B} \rightarrow 2\ \mathrm{e}^{-} + \mathrm{B}^{+}$
Excitation	$\mathrm{A}^{x+} + \mathrm{B} \rightarrow \mathrm{A}^{x+} + \mathrm{B}^{*}$;	$\mathrm{e}^{-} + \mathrm{B} \rightarrow \mathrm{e}^{-} + \mathrm{B}^{*}$
Elastic scattering	$\mathrm{A}^{x+} + \mathrm{B} \rightarrow \mathrm{A}^{x+} + \mathrm{B}$;	$\mathrm{e}^{-} + \mathrm{B} \rightarrow \mathrm{e}^{-} + \mathrm{B}$
Electron capture	$\mathrm{A}^{x+} + \mathrm{B} \rightarrow \mathrm{A}^{(x-1)+} + \mathrm{B}^{+}$	
Electron loss	$\mathrm{A}^{0/x+} + \mathrm{B} \rightarrow \mathrm{A}^{(x+1)+} + \mathrm{B} + \mathrm{e}^{-}$	
Transient molecular anion		$\mathrm{e}^{-} + \mathrm{B} \rightarrow \mathrm{B}^{-*}$
Dissociation paths:		
Ionic dissociation		$\mathrm{B}^{+} - > \mathrm{b}_1 + \mathrm{b}_2^{+}$
Neutral dissociation		$\mathrm{B}^{*} - > \mathrm{b}_1 + \mathrm{b}_2$
Dissociative electron attachment		$\mathrm{e}^{-} + \mathrm{B} - > \mathrm{B}^{-} - > \mathrm{b}_1 + \mathrm{b}_2^{-}$
Radical species:		
e^{-}_{aq}, b_{*}, $\mathrm{b}^{+}{}_{*}$ [188]		

It is important to consider electrons of energies lower than 500 eV which are produced as secondary particles in high number and their inelastic mean free path length is in the order of 1–2 nanometers [51, 163]. Therefore, these electrons contribute largely to the (lateral) energy deposition by any kind of radiation (charged particles as well as photons) and, subsequently, to DNA damage. The majority of secondary electrons is in the energy range below 1 keV. Electrons in this energy range interact with molecules via electromagnetic interactions, where they lose energy in inelastic collisions and change their direction of motion in the case of inelastic or elastic scattering from the target potential. During an inelastic collision, one or several electrons of the target molecules

---

[†] Throughout this thesis, the energy of a particle is always referring to its kinetic energy.

are excited to a higher bound or continuum state. The latter results in an ionisation of the target. The single ionisation potential of an atom or molecule is given by the binding energy of an electron present in the outermost valence shell. Due to the indistinguishability of incident and ejected electrons, the slower electron is conventionally defined as the secondary electron with an energy $E \leq (T - B_i)/2$, where T is the energy of the incident electron and B_i is the binding energy of the i-th target orbital. Resonant electron-impact processes can occur for electron energies below several electronvolts and may significantly contribute to DNA damage [17]. For example, transient molecular anions can be formed by the attachment of the electron into a resonant state of the molecule [17]. The electron can then either autodetach and may leave behind a vibrationally excited molecule, or it may lead to a dissociation of the molecule.

Interactions of light ions (protons and helium particles) of energies between 100 keV and 20 MeV were also investigated in this work, due to their importance in nanodosimetric measurements [86]. Light ions in this energy range also interact with the medium via electromagnetic processes, namely ionisation, excitation and charge-transfer. Elastic collisions can be neglected in this energy range, as these are of low probability and have very small scattering angles [126]. Ions with higher energies are not of primary importance for nanodosimetric applications due to their large total mean free path length relative to the dimensions of a DNA segment. Furthermore, the formation of anions by charge-transfer interactions is neglected due to the low cross section for those processes in the considered energy range [158].

Before the interaction processes are described in more detail, we recall the de Broglie wavelength, which is necessary to follow the arguments below. For particles of momentum p and velocity v, the de Broglie wavelength is given by

$$\lambda_{\mathrm{DB}} = \frac{h}{p} = \frac{h}{mv}, \tag{2.1}$$

where h is the Planck constant and m the particle mass. For an electron of 10 eV, which has the same velocity as a proton of about 20 keV, the de Broglie wavelength is $\lambda_{\mathrm{DB}} = 0.39$ nm. This value is larger than the diameter of a water molecule. A 30 eV electron has a de Broglie wavelength of 0.22 nm, which is approximately the diameter of a carbon atom. An electron of 150 eV (proton of 300 keV) has $\lambda_{\mathrm{DB}} = 0.1$ nm, which is approximately the minimum bond length between carbon atoms [191].

2.2.1 Fast projectiles

For fast projectiles, meaning that their velocity is much greater than the average velocity of valence electrons in the medium (electrons and light ions with energies above 500 eV and 1 MeV/u, respectively), the distortion of the target electron distribution by the passing projectile is small. This is due to the short interaction time (compared to the orbital time period of the target electrons) and, hence, the sudden transfer of momentum from the incoming fast projectile to the target electrons. As a consequence, the electric charge distribution of the target can be assumed to be spatially static during the scattering process (static-field approximation) and mostly small momenta are transferred to the target. Furthermore, the interaction between the projectile and the target can be treated within the framework of the first Born approximation, which is a first order perturbation theory. Within this theory, the initial and final states of the incident particle can be represented by plane waves [10, 95].

For elastic collisions, the interaction can be described as a scattering of the projectile by a central static potential $V(r)$. This potential is obtained by integrating over the electron density distribution of the target molecule [101, 127]. As long as the de Broglie wavelength of the projectile is much smaller than the distance between the target atoms [101] (see equation 2.1), the interaction can be assumed to occur with a single atom, known as the independent atom model (IAM), so that only the potential of a single atom is required to describe the scattering process.

The dominant interaction process of fast projectiles is the direct ionisation of the target. The response of the target to inelastic collisions of fast projectiles can be described via the generalised oscillator strength [57]. Within the first Born approximation, the interaction is assumed to have dipole character so that the generalised oscillator strength can be approximated by the optical oscillator strength. This quantity characterises the transition probabilities within the molecule in the limit of zero momentum transfer and is proportional to the absorption cross section of photons.

2.2.2 Slow projectiles

As the energy of the projectile decreases, electronic, vibrational and rotational excitation as well as charge-transfer and elastic processes become increasingly important in comparison to ionisation processes. At electron energies of several electron volts, either elastic collisions, rotational excitations or vibrational excitations are the dominant process. Rotational excitation depends on the dipole moment of the molecule and is dominant if the dipole moment is large. Often, the contribution of rotational excitations is included in the elastic scattering process to be able to compare with experimental data, where rotational excitations cannot be resolved. In the interactions of slow projectiles often a significant momentum is transferred between the low-energy projectile and the target, leading to a change of the projectile's direction of motion. For electrons, both energy and magnitude of momentum of the projectile are conserved in the case of elastic collisions while inelastic events lead to a change in the magnitudes of momentum and energy.

An appropriate model for the target potential describing the elastic scattering of electrons with energies above about 100 eV by atoms is the spherical complex optical potential (SCOP) model. In this model, the scattering potential is approximated by the optical potential $V_{\mathrm{opt}}(r)$ by [57, 101]

$$V_{\mathrm{opt}}(r) = V_{\mathrm{st}}(r) + V_{\mathrm{exch}}(r) + V_{\mathrm{pol}}(r) - iV_{\mathrm{abs}}(r), \tag{2.2}$$

where r is the distance from the centre of mass of the molecule or atom (the latter is assumed in the independent atom model mentioned in section 2.2.1). This potential contains the short-range potential $V_{\mathrm{st}}(r)$, which is assumed to be spherically symmetric and static within the collision time.

As electrons are indistinguishable particles, a possible interchange between the incident and target electrons during the collision has to be considered. These exchange interactions are taken into account by the exchange potential $V_{\mathrm{exch}}(r)$. This process is particularly important when the velocities of both electrons are similar [48].

The correlation-polarisation potential $V_{\mathrm{pol}}(r)$ describes the dynamical interference of the incoming particle wave with the electron distribution of the molecule. The polarisation effect leads to a change in scattering probabilities [54, 57, 101, 168]. While projectile ions exert an attractive force onto the target electron distribution, projectile electrons constitute a repulsive force. In both cases, the induced dipole moment of the target acts on the projectile by forming a polarisation potential, which depends on the polarisability of the target [57]. The screening of the target potential evoked by passing ions subsequently decreases the ionisation probability of an electron with decreasing projectile energy [54]. In contrast, passing electrons lead to an antiscreening effect, increasing the ionisation probability with decreasing projectile energy.

An additional imaginary potential $V_{\mathrm{abs}}(r)$ accounts for the absorption into inelastic channels, the relative contribution of which increases with increasing projectile energy [101].

In the case of molecular targets, the multi-center potential can be converted to yield a similar form as the atomic scattering potential given above by referring to the center of mass of the molecule and taking into account intramolecular coherent scattering of the incident electron wave on different atoms [48, 101]. This is particularly important for electrons of energy below a few tens of electron volts as their wavelength spans across several target atoms (see equation 2.1). A detailed description of the scattering process of electrons by polyatomic molecules can, for example, be found in the work of Gianturco and Jain [70].

Inelastic collisions of electrons with energies below about 500 eV involve higher-order perturbation effects. The consequence related to the secondary electron spectra after ionisation processes, which are particularly relevant for this work, are outlined in the following section.

For incident ions of energy below about 1 MeV/u charge-transfer processes play an important role. The probability for an ionisation of the target by electron-capture to a bound state of the projectile increases with decreasing ion energy and reaches a maximum when the projectile has a velocity similar to that of the target electrons [168]. The probability for ionisation by ions of lower charge states are significantly lower than for bare projectiles, which arises from the screening of the projectile potential by its captured electrons [126, 168]. Electrons can, in turn, be lost from the projectile, leaving one or more free electrons behind. A charge equilibrium of an incident ion beam is reached after a few interactions. In this case, the probability for a specific charge state of a projectile is described by the equilibrium condition that the rate of projectiles gaining a specific charge state is equal to that losing this charge state. More details of charge transfer processes will be provided in section 6.2.

2.2.3 Secondary electron spectra after ionisation

Secondary electrons of *low energy* (in the order up to several electron volts) are produced in soft or distant inelastic collisions, characterised by small momentum transfers. In this case, incident particles are subsequently scattered into small angles, while low energy secondary electrons have a high probability to be scattered within the potential of the ionised target due to their large wavelength. The resulting scattering angle of the electron is therefore nearly isotropic [168]. The production of low energy secondary electrons has a high probability for fast projectiles because a large part of the scattering process of high energy projectiles occurs with large impact parameters, in other words, as distant collisions with only a small amount of momentum transferred (see section 2.2.1).

Secondary electrons of *intermediate energies* (in the order of several tens of electron volts) produced by projectile ions may experience two-centre effects if their velocity is similar to the velocity of the leaving projectile ion (centres are target and projectile). In this case, the ejected electron has a probability of being temporarily captured into a projectile continuum state [168]. This process leads to an enhancement of the electron emission in the forward direction [162, 168].

A distinct feature in angular distributions of secondary electrons is the binary peak, which arises from *'high' energy* electrons produced in hard or close collisions. Such scattering events can be approximated by classical theories, describing a large momentum transfer of a projectile of initial energy T and mass M with a free electron initially at rest (rest mass m_0) [162]. This case is valid if the energy T and the energy of the emitted secondary electron E are much larger than the binding energy of the emitted secondary electron and small with respect to the energy at rest. The angular distribution of non-relativistic fast secondary electrons of energy E shows the binary peak at a scattering angle

$$\cos\,\theta_B = 0.5\sqrt{\frac{E}{T}\frac{M}{m}}(1+\frac{m}{M}). \tag{2.3}$$

For projectile ions, $M \gg m$ such that equation 2.3 reduces to

$$\cos\,\theta_B = 0.5\sqrt{\frac{E}{T}\frac{M}{m}}. \tag{2.4}$$

As this expression has to be smaller than unity, the energy E is restricted to

$$E \leq 4T\frac{m}{M}. \tag{2.5}$$

For primary electrons with $M = m$, equation 2.3 becomes

$$\cos\,\theta_B = \sqrt{\frac{E}{T}}. \tag{2.6}$$

Corresponding scattering angles of secondary and primary electrons of relativistic energies, θ_s and θ_p, respectively, are frequently provided in the literature [26, 81, 185]:

$$\sin^2\theta_\mathrm{s} = \frac{1-E/T}{1+E/\left(2m_0c^2\right)}. \tag{2.7}$$

$$\sin^2\theta_\mathrm{p} = \frac{E/T}{1+T\left(1-E/T\right)/\left(2m_0c^2\right)}. \tag{2.8}$$

In the case of electron impact, the distinction between the scattered primary electron and the secondary electron is based on the convention that secondary electrons are those fulfilling

$$E \leq \frac{T-B_0}{2}, \tag{2.9}$$

where B_0 is the binding energy of the outermost target orbital.

2.2.4 Interaction cross sections

A total interaction cross section is defined as the ratio of the number of particles scattered per unit time and scatterer to the flux of incident particles. Hence, the cross section has the dimension of an area and depends on the type of scatterer (i.e. the electron density distribution) as well as on the radiation quality of the incident particles. If the flux of scattered particles $\dot{N}_{\mathrm{sc}}$ is a consequence of a uniform incident particle beam with a flux $\dot{N}_0$ penetrating a (thin) target of thickness Δx, consisting of n_ρ scattering centers per unit volume, the total scattering cross section is given by [18]

$$\sigma_{\mathrm{t}} = \frac{\dot{N}_{\mathrm{sc}}}{\dot{N}_0 n_\rho \Delta x}. \tag{2.10}$$

The definition in equation 2.10 is only valid for uniformly distributed scattering centres in the target which are far enough apart to allow each interaction to take place with a single scattering center.

Differential cross sections characterise the scattering process with respect to a specific property of the scattered particle. The differential elastic scattering cross section, for example, describes the ratio of the number of particles $d\dot{N}_{\mathrm{el}}$ elastically scattered per unit time and scatterer into the solid angle $\mathrm{d}\Omega$, centred about a direction $\Omega = (\theta, \phi)$ with respect to the incidence axis of the beam, to the number of incident particles per unit time $\dot{N}_0$. It is given by

$$\frac{\mathrm{d}\sigma}{\mathrm{d}\Omega}(\theta, \phi) = \frac{\mathrm{d}\dot{N}_{\mathrm{el}}}{\dot{N}_0 n_\rho \Delta x \mathrm{d}\Omega}. \tag{2.11}$$

Figure 2.8 is a simplified sketch of an incident particle beam scattered into the solid angle $\mathrm{d}\Omega$ by a single central field. From equation 2.11 it becomes evident that the probability of the particle being scattered by the single scatterer into the solid angle $\mathrm{d}\Omega$ is essentially described by the effective area of the central field observed by the incident particles. The total elastic scattering cross section σ_{el} is obtained by integrating the differential cross section over the full solid angle, where the differential solid angle is given by $\mathrm{d}\Omega = 2\pi \sin\theta \, \mathrm{d}\theta$.

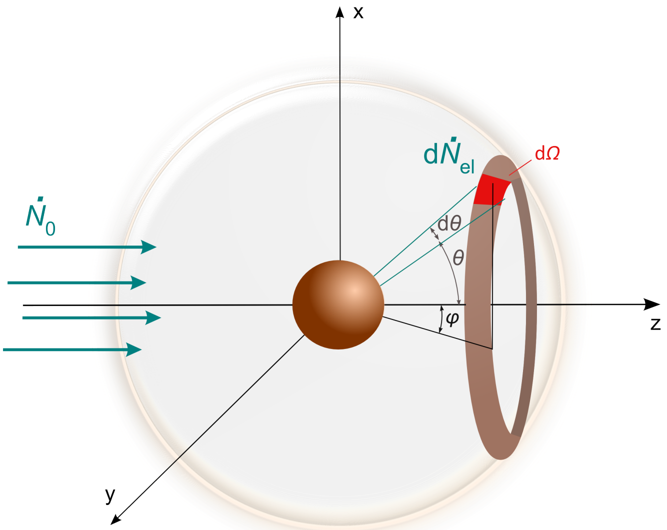

Figure 2.8: Classical description of the elastic scattering of charged particles by a central field. A number $d\dot{N}_{\mathrm{el}}$ of the incident particles with flux $\dot{N}_0$ is scattered per unit time about the direction (θ, ϕ) into the solid angle segment $\mathrm{d}\Omega$.

Properties of the inelastic scattering process are, for example, described by double-differential ionisation cross section $\mathrm{d}^2\sigma_{\mathrm{ion}}/\mathrm{d}E\mathrm{d}\Omega$. This cross section is defined as the ratio of the flux of secondary electrons $\mathrm{d}^2\dot{N}_{\mathrm{e}}$, emitted with an energy in the interval $\mathrm{d}E$ around energy E into the solid angle $\mathrm{d}\Omega$, to the incident particle flux $\dot{N}_0$. The integration of the double-differential cross section over the full solid angle leads to the single-differential ionisation cross section $\mathrm{d}\sigma_{\mathrm{ion}}/\mathrm{d}E$. Further integration over all secondary electron energies E provides the total ionisation cross section σ_{ion}.

2.2.5 Analytic cross sections and consistency requirements

Analytic formulae for interaction cross sections are available for fast charged particles.

a) Elastic scattering cross section

The elastic scattering cross section was determined by Rutherford for the interaction of a charged fast particle of energy T and rest mass m_0 with a much heavier atomic nucleus of charge Z. A parameter was introduced by Moliere [81, 185] to account for the screening of the nuclear charge by orbiting electrons. The screened Rutherford formulae for the differential and total elastic scattering cross sections are given by

$$\frac{d\sigma_{\mathrm{el}}}{d\Omega}(T) = r_{\mathrm{e}}^2 \, \frac{Z(Z+1)}{(1 - cos\ \theta + 2\eta)^2} \, \frac{1-\beta^2}{\beta^4}, \tag{2.12a}$$

$$\sigma_{\mathrm{el}}(T) = \pi r_{\mathrm{e}}^2 \, \frac{Z(Z+1)}{\eta(\eta+1)} \, \frac{1-\beta^2}{\beta^4}, \tag{2.12b}$$

where r_e is the classical electron radius, Z the charge of a target atom and $\beta^2 = v^2/c^2 = 2\tau$ is the reduced particle velocity and $\tau = T/m_0c^2$. The screening parameter η is given by

$$\eta = \eta_c \ 1.7{\cdot}10^{-5} \ Z^{2/3} \, \frac{1}{\tau(\tau+2)}. \tag{2.13}$$

Parameter $\eta_c = 1.13 + 3.76(Z/137)^2/\beta^2$ was determined by Moliere and is only a good approximation in the higher energy range (above several tens of keV) [81, 185]. For lower energies, η_c has been obtained from fitting equation 2.12b to various experimental data (see e.g. [81]).

b) Inelastic scattering cross section

An analytical formula is also known for inelastic cross sections. As mentioned in section 2.2.1, the cross sections for an ionisation of the i-th subshell induced by fast projectiles are derived using the Bethe-Born approximation:

$$\sigma_i = \frac{4\pi a_0^2 R}{T} M_i^2 \ln\left(4c_{\mathrm{E}}T/R\right), \tag{2.14}$$

where R is the Rydberg energy, $M_i^2 = \int\limits_0^{(T-B_0)/2} \left(\frac{R}{E}\frac{\mathrm{d}f}{\mathrm{d}E}\right) \mathrm{d}E$ is the i-th matrix element for the respective transition, $\mathrm{d}f/\mathrm{d}E$ is the differential optical dipole oscillator strength and c_E is a constant [64, 95]. Equation 2.14 is applied in this work to test the consistency of the ionisation cross section at high energies by arranging the data in a Fano plot [55]. Here, a straight line with slope M_i^2 should occur when $\sigma_i T/(4\pi a_0^2 R)$ is plotted versus $\ln(T/R)$. The intercept with the vertical axis provides the value of c_E [95].

Bethe [10] showed that the ionisation cross section of a bare nucleus moving with velocity v is proportional to the number of valence electrons Z_{targ} of the target molecule and to the square of the projectile charge Z_{proj}, such that

$$\sigma_\mathrm{ion} \propto \frac{Z_\mathrm{targ} Z_\mathrm{proj}^2}{\beta^2} \ln(\beta^2), \tag{2.15}$$

where $\beta = v/c$. This relation is independent of the mass and sign of charge of the projectile, which was demonstrated by Hooper et al. [90] to be valid for electrons with energies above about 300 eV and for protons with energies greater than about 550 keV. This relation is an advantage if the optical oscillator strength of a molecule is unknown because it allows for the scaling of the ionisation cross section data by Z_targ and/or Z_proj^2.

As stated above, higher order effects become dominant as the particle energy decreases, which are not accounted for in the first Born approximation. To give an example, higher order effects lead to 30–40% reduction of the ionisation cross section for the interaction of electrons with water molecules below 100 eV [48].

Independent of the projectile energy, inelastic collisions involving large energy transfer (hard collisions) can be treated to a good approximation by classical theories, leading to analytical expressions, such as the Thomson cross section [129]. It describes the energy transfer $E_\mathrm{Tr} = E + B$ of an incident electron of energy T and mass M to a free electron initially at rest when B is the binding energy of the target electron and E is its kinetic energy post interaction. The Thomson cross section is given under the condition that $E \gg B$ by

$$\frac{\mathrm{d}\sigma_\mathrm{ion}^\mathrm{Thomson}}{\mathrm{d}E_\mathrm{Tr}}(T) = 4\pi a_0^2 \frac{Z_p^2 R^2}{T E_\mathrm{Tr}^2} \frac{M}{m_e}, \tag{2.16}$$

where Z_p the projectile charge and m_e is the electron mass. Hence, the Thomson cross section for electron impact is the pendant to the Rutherford cross section for proton impact [100]. The Rutherford cross section, on the other hand, has been used as a valuable tool for the consistency analysis of single differential ionisation cross sections of protons [162]. In fact, by normalising a given single differential ionisation cross section to the Rutherford cross section, the Platzman plot of quantity $Y(E_\mathrm{Tr})$ is constructed, where

$$Y(E_{\mathrm{Tr}}) = \frac{\mathrm{d}\sigma_{\mathrm{ion}}}{\mathrm{d}E_{\mathrm{Tr}}} \frac{T}{4\pi a_0^2} \left(\frac{E_{\mathrm{Tr}}}{R}\right)^2 \tag{2.17}$$

By plotting this quantity against R/E_{Tr}, the area under the curve becomes equal to $\sigma_{\mathrm{ion}} 4\pi a_0^2/T$. A benefit of the Platzman plot is that the normalisation of the actual single differential cross section to the Rutherford cross section directly provides the number of target electrons, participating in the collision, for $R/E_{\mathrm{Tr}} \to 0$. This is, because the Rutherford cross section is for a single electron. Furthermore, the shape of the Platzman plot should be similar to that of the continuum dipole oscillator strength. Hence, if this quantity is known, single differential cross sections can by extrapolated to $E = 0$. Platzman plots for consistency analysis will be applied for electron impact in section 4.4.3, where the single differential ionisation cross sections were normalized to the Thomson cross section.

The Thomson cross section was extended by Mott [129] by taking into account the exchange effect for projectile electrons with a bound target electron. The Mott cross section for the energy transfer E_{Tr} of projectile electrons is given by

$$\begin{aligned}\frac{\mathrm{d}\sigma_{\mathrm{ion}_{\mathrm{Mott}}}}{\mathrm{d}E_{\mathrm{Tr}}}(T) =& 4\pi a_0^2 \frac{R^2}{T} \big(\frac{1}{E_{\mathrm{Tr}}^2} + \frac{1}{(T - E_{\mathrm{Tr}})^2} \\ & - \frac{1}{E_{\mathrm{Tr}}\,(T - E_{\mathrm{Tr}})} \cos\left(\sqrt{\frac{2R}{T}} \ln\left[\frac{E_{\mathrm{Tr}}}{T - E_{\mathrm{Tr}}}\right]\right) \big).\end{aligned} \tag{2.18}$$

The Mott cross section in the limit of high energies T and large energy transfers E_{Tr} is provided by the ICRU [100].

Other analytical models have also been developed, which are mostly semi-empirical. Reviews of classical and semiclassical approximations for ionisation cross sections were published by Kim [116] and Younger and Märk [197]. Of these models, the Binary Encounter Bethe (BEB) model is the most general approach and is free of adjustable parameters. Furthermore, it can be extended to relativistic energies. The following section explores the BEB model in more detail.

2.2.6 Binary-encounter Bethe model

The BEB model [116] describes the electron-impact ionisation cross section without requiring empirical parameters. It combines the binary-encounter theory with the Bethe-Born approximation, which are expected to be realistic models for collisions with high momentum transfer (preferentially occurring for low energy electrons) and very low momentum transfer (mostly for high incidence electron energies), respectively. In the binary-encounter theory, a velocity distribution is assigned to the bound target electrons, enabling a more accurate description of hard collisions. A relativistic version of the BEB model is provided in [117]; for most of the energy range considered in this work the non-relativistic formula is adequate. The total ionisation cross section is then

$$\sigma_{\text{ion}}(T) = \sum_i \frac{S_i}{t + (u+1)/n_{\text{BEB}}} \left[0.5 \cdot Q \left(1 - \frac{1}{t^2}\right) \ln t + (2 - Q) \left(1 - \frac{1}{t} - \frac{\ln t}{t+1}\right) \right] . \tag{2.19}$$

The single-differential ionisation cross section is given by

$$\frac{\mathrm{d}\sigma_{\text{ion}}}{\mathrm{d}E} = \sum_i \left(\frac{S_i}{B_i(t + (u+1)/n_{\text{BEB}})} \sum_{n=1}^{3} F_n \left[f_n(w) + f_n(t-w) \right] \right) , \tag{2.20}$$

where

$$F_1 = -\frac{F_2}{t+1}, \qquad F_2 = 2 - Q, \qquad F_3 = Q \ln t \tag{2.21}$$

$$f_n(w) = (w+1)^{-n}, \qquad f_n(t-w) = (t-w)^{-n} \tag{2.22}$$

with $t = T/B_i$, $u = U_i/B_i$, $w = E/B_i$ and $S_i = 4\pi a_0^2 N_i (R/B_i)^2$. In all equations, R is the Rydberg constant, a_0 is the Bohr radius, i is an index for the subshells, B_i and U_i are the binding and kinetic energies of electrons occupying the i-th subshell of the molecule and N_i is the number of electrons in this subshell [93]. The factor Q can be set to unity according to Kim and Rudd when the oscillator strength distribution for the molecule of interest in unknown [116]. Later, the factor n_{BEB} was introduced in the BEB model [103] and is set to unity in most cases. It is empirical and equals the principal quantum number of the highest populated atomic orbital, if the molecular orbital is dominated by atomic orbitals with $n_{\text{BEB}} \geq 3$ (Mulliken population is >0.5) [103]. The Mulliken population provides the probability for the presence of an electron in a specific atomic orbital.

The binding and kinetic energies B_i and U_i as well as the Mulliken population distribution can be computed by dedicated quantumchemistry codes, such as GAMESS [75]. The determination of these parameters will be further described in section 4.4.2.

2.2.7 Condensed phase effects

In the previous sections, the interaction processes were described for individual atoms or molecules. However, living cells consist of condensed phase media, where the neighbouring molecules distort the local electron density distribution [101, 163]. This results in several changes to the scattering process and the interaction cross sections.

In condensed matter, the nuclear Coulomb fields of single scattering centres are screened by the electrons of the neighbouring molecules. The resultant electron density distribution causes a shift of the oscillator strengths to higher energies [49, 53, 96, 147] so that the probability for electronic excitation is reduced. In addition, the distributions for discrete transition probabilities are broadened in the liquid phase, so that the characteristic excitation peaks visible in gas disappear [11, 53, 195]. According to Winter et al. [195], the peak broadening is due to the mutual influence of the neighbouring molecules, depending on their orientation and functionality of hydrogen bonds. Furthermore, molecules present at a surface of liquid water or water ice are oriented and therefore form a surface potential [195].

The screening of the nuclear coulomb field also leads to a decrease in the ionisation potentials of the subshells in the condensed phase relative to the gas phase by 1–2 eV [47, 195] (these authors provide a comprehensive summary of the ionisation mechanism in water). Moreover, the polarisation of the molecular electron density distribution by a passing projectile is weaker compared to the gas phase, as was pointed out by Inokuti [96] and Liljequist [127]. This means for incident electrons, that the probability for forward scattering in elastic collisions is lower in the liquid phase, and therefore the total elastic scattering cross section may be reduced, as was suggested by Champion [28]. The weaker polarisation effect results also in a lower probability of ionisation by low energy incident electrons in the liquid phase [195].

Coherent scattering effects are enhanced in the condensed phase relative to the gas phase. This is due to the wavelength of an incident low energy electron being large compared not only to intra-molecular but also to inter-molecular dimensions (see equation 2.1). The resulting coherent interference effects may, therefore, span across a large number of molecules. This affects primarily the elastic scattering cross section, which is dominant in the low energy region [101, 127]. However, a reduction of the ionisation cross section in the low energy range is also indicated from theory [40, 53, 96]. This reduction is due to a multiple scattering of emitted secondary electrons within the multi-centre target potential. Affected are particularly electrons with energies below 100 eV, due to their comparatively large wavelength. As low energy secondary electrons are likely to be emitted into small angles, the differences in the single differential cross sections for water in liquid and vapour phases might lead to a negligible effect on the track structure [127].

2.3 Track structure Monte Carlo simulations

An analytical description of the transport of charged particles in a medium is generally very complex and in most cases unfeasible to solve. Monte Carlo simulations are *per se* well suited to numerically solve the transport problem as the interactions of charged particles in a medium are of stochastic nature (i.e. interaction cross sections describe the probability for a specific interaction; see section 2.2.4). For example, the Monte Carlo approach is used in dosimetry to calculate the absorbed dose distribution within a volume. A comparison of Monte Carlo codes applied in radiation dosimetry was provided by Nikjoo [147], which is briefly summarised in this section. Subsequently, the principle of radiation transport applied in the Monte Carlo code used in this work is introduced.

Monte Carlo codes for radiation transport can be separated in two main groups: so-called condensed history simulations and track structure simulations. Condensed history simulations are useful if the target size is macroscopic. Such simulations combine many single interactions in one step to allow a fast transport calculation of adequate accuracy. Many of these codes use the stopping power[‡] to determine the energy loss of the incident particles in the medium and generally multiple scattering theories are applied for electron transport. A listing of condensed-history codes together with treated particle types, energy ranges and target media can be found in [147].

For microscopic target volumes such as the DNA, track structure Monte Carlo codes are better suited. Such codes transport a particle interaction-by-interaction and, therefore, provide detailed histories of the particle's track[§]. The modelling of individual interactions is enabled by the exclusive use of interaction cross sections instead of multiple scattering theories and macroscopic quantities, such as the stopping power. The downside of such detailed simulations is that they are time-consuming and therefore limited to microscopic spatial dimensions. Track structure codes have been developed since the 1960s and can be classified in three groups based on the time scale [147]. The first group of codes provide the physical track structure, occurring in the first 10^{-15}s [152] (examples are Geant4-DNA [94] or the code PTra [79] used in this work). The subsequent transport of chemical products, produced in the physical stage, is additionally handled in codes such as PARTRAC [61] and KURBUC [184]. Biokinetic processes, such as DNA damage repair, are additionally treated after the chemical stage, for example, in the code PARTRAC [61]. For a comprehensive list of codes, please refer to [147].

[‡] The stopping power is the energy deposited per unit path length.

[§] A particle track contains the information on successive positions and types of interactions of a single incident particle and its secondaries with a medium.

Track structure codes utilise DNA models of different complexity. The complexity ranges from a simplified linear DNA segment, which is modelled in the form of a cylinder filled with water [80] or water vapour [146] to segmented targets of water [202]. Highly structured DNA targets have also been developed, where the radiation transport calculations are, however, performed using interaction cross sections of water [9, 61, 144]. Simulations codes using interaction cross sections of DNA constituents also exist for electron transport simulations [45]. However, the cross section data applied in this code were calculated from theoretical models that are accurate for projectiles of high energy (electrons above 1 keV).

Simulation procedure of PTra.

In the following, an overview is provided on the simulation procedure adopted in the code PTra, which was used in this work. The flow diagram in figure 2.9 sketches the electron transport in PTra, but the code is also suited for the transport of light ions. Generally, single interactions are sampled from an interaction cross section data set. For this purpose, each interaction cross section is transferred into a cumulative probability distribution. Those distributions are then used for random sampling of the required parameters. Each incident particle and its secondaries produced in ionisation processes are individually followed until they either leave a specified ‘world volume’, containing the geometry of the modelled experimental setup, or until their energy falls below a specified threshold. The latter case applies particularly to electrons, which are then assumed to be absorbed at their position.

Starting with the first incident particle, its path length Δx to the next point of interaction is determined by random sampling from a probability distribution based on the reduction of the particle flux according to the Lambert-Beer law, i.e. using a random number R, uniformly distributed in the range [0,1] Δx is calculated by

$$\Delta x = -\lambda(T)\,\ln(R). \tag{2.23}$$

The mean free path length $\lambda(T) = 1/(\sigma_\mathrm{t}(T)n_\rho)$ is a function of particle energy T and is determined from the total scattering cross section σ_t using the number density n_ρ of the traversed matter. Using the path length Δx and taking into account the direction cosines of the particle, the subsequent interaction position is determined.

Next, the type of interaction is determined from the integral cross sections for all possible interaction types of the particle relative to σ_t. If the particle was 'chosen' to ionise a molecule of the medium, the i-th molecular subshell from which an electron is ejected is determined by random sampling of the partial ionisation cross sections $\sigma_{\mathrm{ion},i}$. Using the cumulative probability distribution based on the single differential ionisation cross section $\mathrm{d}\sigma_\mathrm{ion}/\mathrm{d}E$, the energy E of the ejected (secondary) electron is randomly sampled. The energy of the incident particle is subsequently reduced by the sum of energy B_i expended to release a molecular electron from the i-th subshell and the energy E transferred to the secondary electron, keeping conservation of energy, such that

$$\Delta E = B_i + E. \tag{2.24}$$

The secondary electron is emitted into a solid angle $\mathrm{d}\Omega$, centred about a direction $\Omega = (\theta, \phi)$. The determination of the polar scattering angle θ based on the double differential ionisation cross section $\mathrm{d}\sigma^2_\mathrm{ion}/(\mathrm{d}E\mathrm{d}\Omega)$. As the orientation of the target molecules in the scattering process is rotationally symmetric, the azimuthal scattering angle ϕ is randomly sampled between 0 and 2π.
If an ionisation occurs in an inner orbital, the molecular ion is left in an excited state after the scattering process. This state predominantly decays non-radiative via the production of one or two Auger electrons, which are usually assumed to be isotropically emitted.

In the case of target excitation, the j-th excitation level is randomly sampled from the partial excitation cross sections $\sigma_{\mathrm{exc},j}$. The energy of the incident particle is subsequently reduced by the respective excitation energy. For most target molecules, no data on the angular distribution of scattering after discrete excitation exist, while the few literature data show that the angular distribution is strongly peaked in forward direction [109]. Hence, the electron is always assumed to be scattered in 0° in the simulations. This assumption is usually applied in simulations, for example by [26].

If the particle is instead elastically scattered, the very small energy loss to the target molecule (on the order of meV) is neglected. The polar angle of scattering θ is determined from a cumulative probability distribution based on the differential elastic scattering cross section $\mathrm{d}\sigma_\mathrm{el}/\mathrm{d}\Omega$. Again, the azimuthal scattering angle ϕ is randomly sampled between 0 and 2π. Due to the energy range of light ions used in PTra simulations (above 100 keV), elastic scattering is neglected and only applied to electrons [126].

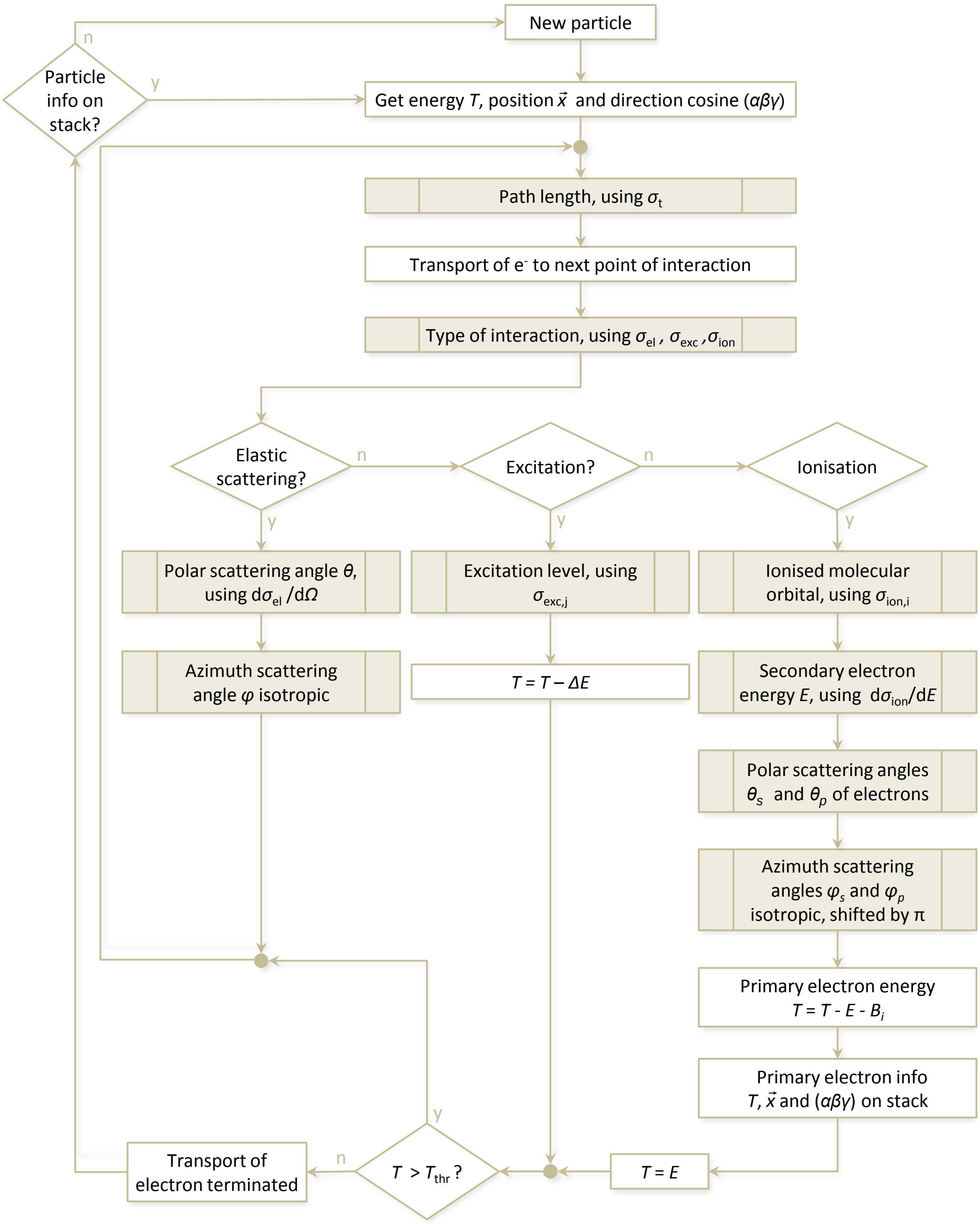

Figure 2.9: Flow diagram illustrating the electron transport in the Monte Carlo code PTra. Shaded boxes indicate random sampling procedures. T and E are the energies of primary and secondary electrons, the respective scattering angles are indicated by indices 'p' and 's' and T_{thr} is a threshold energy. The particle position and direction cosines are $\vec{x}$ and $\alpha, \beta\gamma$, respectively. Refer to cross section symbols σ in the list of abbreviations.

As discussed in section 2.2, charge transfer interactions apply for ions of energy below 1 MeV/u. The implementation of these processes is discussed in detail in section 6.2. Vibrational excitation and electron-attachment processes for electrons of energy below 100 eV are implemented in PTra for water medium and further described in section 3.4.1.

The above summary of the simulation procedure shows that the accuracy of track structure simulations is essentially dependent on the validity of the interaction cross sections. In addition to uncertainties in the interaction cross section data, the following assumptions are generally applied. The target molecules are

- randomly oriented (therefore the scattering process has cylindrical symmetry),
- homogeneously distributed within the volume without any spatially defined scattering centres,
- always neutral before the collision,
- independent, which means that intermolecular interactions are neglected (gas phase approximation).

It is also interesting to notice the physical inconsistency in the assumption of a localised energy deposition by low-energy electrons [127, 152]. For electrons of energy below 100 eV, the de Broglie wavelength is greater than the molecular dimensions (see equation 2.1) and therefore coherent scattering from multiple target centres occurs during the interaction. In addition, the uncertainty principle in quantum mechanical considerations is contrary to the assumption that an electron with a specific momentum has a well defined trajectory in the simulations [179].

2.4 Basics of nanodosimetry

In microscopic dimensions of the target structure (e.g. DNA segments), the concept of the absorbed dose is not applicable and the dosimetry has to be based on a detailed particle track description for the following two reasons: first, molecular changes in the target do not depend on the mean energy lost by the passing projectile (as determined from the stopping power) but on the energy deposited or even the number of interactions in the target [97]. A difference between those two quantities arises for microscopic volumes due to the energy transported beyond the target volume by secondary electrons of high energy. High energy means that the residual range of those electrons is much larger than the dimensions of the target volume. In this case, the secondary electron equilibrium, which is a condition for the determination of the absorbed dose is no longer established. The second reason is that the amount of energy deposited has to be accurately determined. For macroscopic targets, the number of ionisations is related to the energy deposited by the W-value. The W-value is the mean energy required for the production of an ion pair and provides a good approximation of the energy deposited per ionisation if the number of ionisations is large. However, this is generally not the case in microscopic volumes. In these volumes, the energy deposited has to be described by a specific probability density distribution, i.e. the partial ionisation cross section of a subshell [97].

Nanodosimetry is linking parameters of the particle track structure to radiation damage produced within nanometric volumes. In the literature, there are two major approaches. Some authors [145, 146] relate the energy deposited within a nanometric volume to initial[¶] DNA damage. Other authors propose an estimate of the DNA strand break yield from the mean number of inelastic events per unit absorbed dose [7]. The main advantage of these approaches is that also excitations, which can lead to neutral dissociations of the DNA molecules, are taken into account. However, energy depositions are not directly measurable. Instead, measurements are always based on the collection of charges produced by ionisations of the target medium, which are transformed to values of energy deposition by the W-value. As stated above, this approach is not applicable to microscopic dimensions.

To overcome this limitation, other researchers [37, 79, 157, 164] have developed a nanodosimetry concept based on experimental work and track structure Monte Carlo simulations. On the experimental side, nanodosimeters enable the measurement of track structure parameters (described in the following paragraph), within a low-density gas volume. The experiments allow, in fact, a validation of the Monte Carlo simulation

---

[¶] ‘initial’ means the damage to the DNA before chemical and biological mechanisms set in.

programs [Pub10], which can then be adjusted for simulations in condensed target materials [37, 80, 157]. This is the approach applied here.

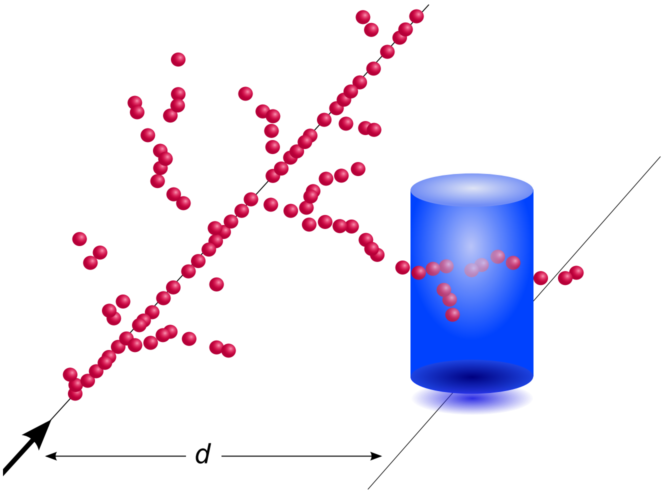

Figure 2.10: Illustration of an ion track passing a target volume in distance d. In nanodosimetry, a target volume is usually approximated by a cylinder filled with liquid water. Ionisations by the ion and its secondaries are represented by the spheres.

The most important nanodosimetric quantity is the ionisation cluster size, which is defined by the number of ionisations induced by individual particle tracks in a specified nanometric volume [79]. A typical target volume is a cylinder with the dimensions of a DNA segment 10 base pairs in length, i.e. of 3.4 nm height and 2.3 nm diameter. Usually, it is assumed that the cylinder is filled and surrounded by water. In figure 2.10 an ion track is illustrated, where an ionisation cluster is formed within a sensitive target volume located in the vicinity of the ion trajectory. Ionisations occur at random positions along a particle track, with subsequent ionisations spatially separated, on average, by the ionisation mean free path. Therefore, the ionisation cluster size ν is a stochastic quantity and characterised by a probability distribution. Since the ionisation mean free path is a function of the radiation quality Q, the probability distribution of ionisation cluster size $P(\nu|Q)$ is a characteristic of the track structure of a specific radiation quality Q. Further quantities describing the track structure for a given radiation quality can be derived from the statistical momenta of $P(\nu|Q)$ by

$$M_k = \sum_{i=0}^{\infty} \nu^k P(\nu|Q). \tag{2.25}$$

Nanodosimetric quantities based on the ionisation cluster size distribution $P(\nu|Q)$ could be related to results from biological experiments [65, 66, 80, 143]. This leads to the assumption that the probability to produce an ionisation in a target molecule is

proportional to the probability for its dissociation, although other dissociation channels such as electronic excitation followed by neutral dissociation and dissociative electron attachment (see table 2.1) are neglected. These findings indicate that the nanodosimetric approach based on the ionisation cluster size distribution is appropriate to estimate biological effects.
In this work, the cumulative probability

$$F_2 = \sum_{i=2}^{\infty} P(\nu|Q). \tag{2.26}$$

is used as a parameter, describing the complexity of clustering. The biological rationale behind this parameter is that at least two ionisations of the DNA strands are required to form a double-strand break.

Ionisation cluster size distributions are frequently used in nanodosimetry, but in this work excitation clusters are also taken into account as those have a probability to cause subsequent fragmentation of a molecule, leading to DNA damage. The number of excitations per incident particle are counted, considering only electronic excitations and, for water vapour, neutral dissociative excitation states. Vibrational excitations are not included, as these can be expected to be less likely to cause a fragmentation of the molecule.
Even though the probabilities of fragmentation are different when initiated by direct ionisation or excitation and also depend on the excitation state, clusters of inelastic collisions are additionally considered in the results. For those, clusters from ionisations and excitations were scored.

Chapter 3

Benchmarking track structure codes for electrons in water

3.1 Introduction

Water is one of the most abundant molecules in the universe and the dominant component in living cells. Therefore, water is generally used in track structure simulations as a model medium for biological matter. For such simulations, interaction cross section data are essential input parameters and their accuracy determines the validity of simulation results (see section 2.3). Due to the differences in physical properties of water in different phases (see also section 2.2.7), a significant influence of phase effects on the track structure can be expected and were already indicated in the literature from comparisons of simulated parameters as performed, for example, by [11, 152, 155, 183].

At this point, we are facing an obstacle: interaction cross sections of water have been measured frequently for the vapour phase, but such measurements cannot be performed for liquid water (for most cross section data) as single scattering conditions cannot be fulfilled. Theories are used to obtain the data for liquid water, however, these show large discrepancies due to different parameterisations (as will be discussed below). Generally, the cross section data implemented in track structure codes for water are a mixture of both phases; this was pointed out in the review of Nikjoo [147] and is also the case for the codes PTra and Geant4-DNA [94] used in this work.

The present situation on simulations using water medium is complicated by large differences in cross section sets available not only for liquid water but also for water vapour. In fact, different Monte Carlo codes also use different sets of cross section data for the same medium, which can lead to substantial deviations in the simulated quantities. For example, in the course of this thesis, nanodosimetric quantities were calculated by means of PTra and Geant4-DNA [Pub1, Pub5]. Significantly discrepant ionisation cluster size distributions and derived predictions for the probabilities of DNA strand breaks were observed and attributed to the differences in cross section sets for liquid water used in both codes. The work related to this thesis started with the investigation of ionisation cluster size distributions produced by electron impact [Pub1] and was continued in collaboration with Peter Lazarakis from CMRP for protons and alpha particles [Pub5].

The objective of this chapter is to benchmark track structure simulation codes for electrons in liquid water and water vapour, using the codes PTra and Geant4-DNA.

To achieve this, section 3.2 summarises a literature search on interaction cross sections of water for electron and proton impact. As excellent reviews on experimental water vapour data already exist, the focus here was on data for the liquid phase and cross section models for the vapour phases. This review does not claim to be exhaustive but provides an overview of the most frequently used models in simulation codes. Finally, the cross section data selected for implementation in the code PTra to perform simulations in water are discussed.

In section 3.3, calculated W-values and nanodosimetric quantities, obtained with the new versions of PTra, are compared for water in the vapour and liquid phase.

Section 3.4 discusses the benchmark of electron transport simulations with PTra and Geant4-DNA for water by a specifically designed experiment [180]. A publication on this topic, using the earlier version of PTra as well as Geant4-DNA, is included in section 3.4.1. In section 3.4.2, the simulations are repeated with the new versions of PTra.

Section 3.5 shows work towards an application of nanodosimetry parameters in radiation therapy. The objective of this published study was to investigate the feasibility of an analytical model [166] to calculate track structure parameters. Such a model is advantageous with respect to track structure simulations for an application in radiation therapy, due to the fast and efficient calculation of parameters. The publication was a collaboration with the developers of the analytical model, where the simulations and the discussion of the results were part of my work.

The chapter is summarised in section 3.6.

3.2 Literature review on interaction cross sections

3.2.1 Electron cross section data

3.2.1.1 Ionisation

a) Water vapour.

Reviews on electron-impact cross sections of water vapour were published by many authors, the most recent comprehensive review was by Itikawa and Mason [106]. These authors recommend data for each cross section type. Their recommendations for the ionisation cross section are based on the measurements of Straub et al. [170] for electrons of energies between 13.5 eV and 100 eV with an uncertainty of 6% (figure 3.1). Generally, experimental data for energies below 1 keV differ by 25% up to a factor of two (see NIST database [142]).

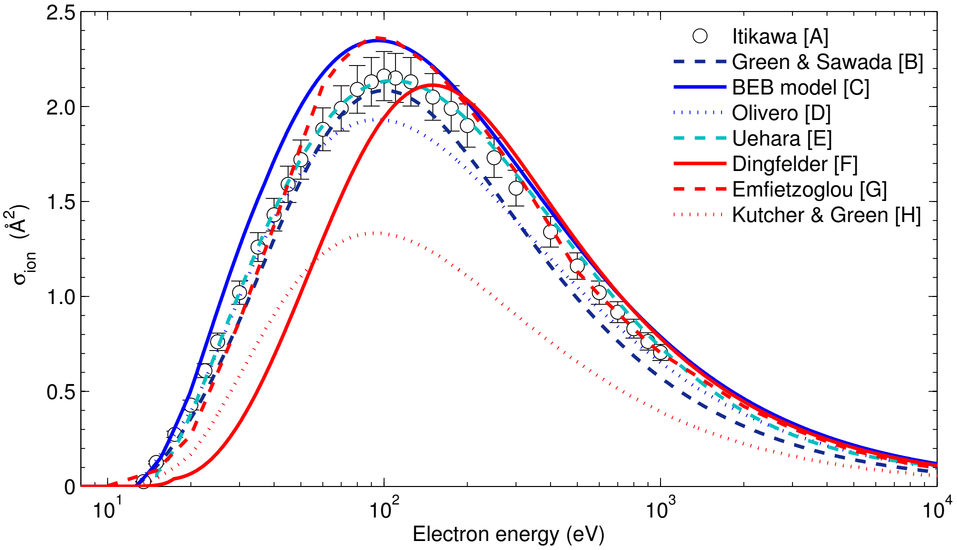

Figure 3.1: Ionisation cross sections σ_{ion} for the interaction of electrons with gaseous (blue, A–E [77, 93, 106, 148, 186]) and liquid water (red, F–H [39, 48, 121]). Measured data for the vapour phase, recommended by Itikawa and Mason, are shown (symbols) as well as proposed models (lines).

An assessment of experimental data and several models for water vapour cross sections used in Monte Carlo track structure codes was performed by Uehara et al. [186]. They obtained an empirical function by fitting evaluated experimental data, which is also in excellent agreement with the data recommended by Itikawa and Mason (figure 3.1). However, the ionisation potential of 15 eV, assumed in their model of Uehara, is higher than the experimental value of 12.62 eV [142].

The cross section data of Champion [26], calculated from *ab-initio* methods, also support the recommended experimental data within the experimental uncertainties and assume a more realistic ionisation potential of 12.60 eV (not shown).

The BEB model, parameterised by Hwang et al. [93] provides excellent agreement with the recommended experimental data at energies above 200 eV. At lower energies, the model data are up to 60% larger than the experimental values. However, the BEB model is still within the scatter of the data given in the NIST database [142]. Hwang et al. also calculated a binding energy of 12.61 eV for the outermost orbital of water vapour, which is in agreement with the experimental value. An advantage of the BEB model is that ionisation cross sections for the molecular subshells can be determined (see section 2.2.6).

Green and Sawada [77] developed a semi-empirical model for the ionisation cross section. The model function was fitted to experimental data of water vapour, assuming an ionisation potential of 12.60 eV. In fact, Green and Sawada based their model function in form of a Lorentzian on measured differential cross sections for an electron energy of 500 eV [149]. Despite those restricted conditions, a good agreement is obtained with the recommended experimental total ionisation cross section, where the model reproduces the maximum cross section between 50 and 150 eV and underestimates the measured data by less than 20% which is well within the overall experimental uncertainties.

Olivero et al. [148] fitted the formula developed by Green and Sawada [77] to experimental partial ionisation cross sections, assuming an ionisation potential of 12.62 eV. Compared to the previous parameterisation [77], their total ionisation cross section is about 7% lower in the region of the maximum, but up to 40% higher for energies above and below the maximum. Hence, the model data of Olivero et al. are in better agreement with the recommended experimental data of Itikawa and Mason [106] than those of Green and Sawada in the energy ranges below 70 eV and above 800 eV, but have the lowest values in the region of the maximum.

b) Liquid water.

As stated in the introduction, a measurement of the cross sections of liquid water is not feasible, because single interactions cannot be resolved. However, it was experimentally shown that the ionisation potential of water in the liquid phase is by about 2 eV to 4 eV lower than for the vapour [155]. Also, the oscillator strengths are shifted to higher energies [85, 195] (see section 2.2.7). Existing data for liquid water have been mostly derived from theory using the dielectric formalism, which describes the response of the material upon a sudden transfer of energy and momentum and is based on the energy loss function [39, 147]. The energy loss function is generally determined from experimental optical spectra [83–85, 189] in the dipole limit where the momentum transfer is zero. Dispersion algorithms have then been used for an extrapolation to finite momentum transfers. Emfietzoglou et al. [48, 50] published extensive investigations on the influence on inelastic cross sections by the different optical data sets, various dispersion algorithms as well as different approaches for using Born corrections, which account for perturbation and exchange effects. In summary, these studies showed variations up to 25% for energies above 50 eV, increasing to 40% at 10 eV for the different optical data sets. Different dispersion algorithms lead to variations up to 30% above 100 eV and even larger differences of a factor of three for energies below. Born corrections lead to a reduction of 30–40% at 100 eV.

Kutcher and Green [121] probably developed the first set of ionisation cross sections for liquid water using the optical absorption spectrum for the energy loss function [85] to calculate the oscillator strength distribution. As shown in figure 3.1, their ionisation cross section data are more than a factor of two lower than those of water vapour.

Dingfelder et al. [39] determined inelastic cross sections of liquid water using the dielectric response algorithm. Their ionisation cross sections are by up to 10% larger than the recommended experimental data of water vapour for energies above 200 eV; below this energy, their data are up to a factor of two lower. As will be seen later, this reduction is due to the differences in single differential ionisation cross sections.

In the recent years, Emfietzoglou et al. proposed several inelastic cross sections while continuously elaborating their approach [48, 49, 52]. Here, their most recent model [48, 50] is used for the comparison because it considers measured data from inelastic X-ray scattering spectroscopy, offering an optical spectrum of liquid water across a larger energy range together with data on non-zero momentum transfers [189]. The latter data enable the first experimental validation of dispersion algorithms. In their publication, Emfietzoglou et al. [48] provide inelastic cross section data and the ionisation efficiency (i.e. the energy-dependent probability that an inelastic process is an ionisation). Therefore, the ionisation efficiency given for the 'extended-Drude dispersion using Hayashi's data' [48] was used in this thesis to calculate the ionisation and excitation cross sections from the inelastic cross sections. Their data are very similar to those of water vapour, as seen in figure 3.1, and suggest that phase effects may not affect the total ionisation cross section in this energy range. For energies below 50 eV they are as much as 20% lower than the recommended experimental data [106], increasing to a maximum value at about 100 eV, which coincides with the predictions of the BEB model (15% higher than the experimental data). For energies above 200 eV the data of Emfietzoglou et al. continue to agree well with the recommended cross section data within the experimental uncertainties.

The ionisation potential has a large influence on the ionisation cross section, particularly for incident electrons of low energy. The value calculated by Kutcher and Green [121] is equal to the ionisation potential of water vapour at 12.61 eV. On the other hand, the values calculated by Dingfelder [39] and Emfietzoglou [50] are at 10.79 eV and 10.00 eV, respectively. A vertical ionisation potential of 11.16 eV has been determined for liquid water by photoelectron spectroscopy [195]. According to a statement of these authors, the latter measurements were more accurate than the first existing and often cited measurements of the vertical ionisation potential of 10.92 eV by Faubel et al. [56].

c) Single differential cross sections (SDCS).

SDCS for water vapour have been determined from measured double-differential data by Opal et al. (500 eV, 30–150°) [149] and Bolorizadeh and Rudd (50–2000 eV, 15–150°) [14] as well as from *ab-initio* theory by Champion [26]. All three data sets are in good agreement (see discussion in [26]). As shown in figure 3.2, the predictions by the BEB model [93] are also in very good agreement with the experimental data for secondary electron energies below 200 eV. For energies above, the measured values of Bolorizadeh are up to a factor of two larger. However, for an implementation in simulation codes this deviation is not significant because in this energy range, the SDCS are more than two orders of magnitude lower than their maximum values.

The changes in screening and polarisation effects in the liquid phase lead to a suppression of the emission of low-energy electrons [40, 53] (as described in section 2.2.7). Figure 3.2 compares the SDCS determined by the BEB model and the formula of Kutcher and Green [121] for the vapour and liquid phases of water, respectively. The reduction of the SDCS at low energies is up to an order of magnitude, leading to the low values of the total ionisation cross section observed in figure 3.1. However, both data sets are in good agreement for electrons of incident energies above several hundreds of electron volts and for secondary electron energies above 50 eV. There is again disagreement for large energy transfers, where the BEB model predicts the typical rise of the SDCS which is due to electron exchange interactions, while the data of Kutcher are continuously decreasing with increasing secondary electron energy.

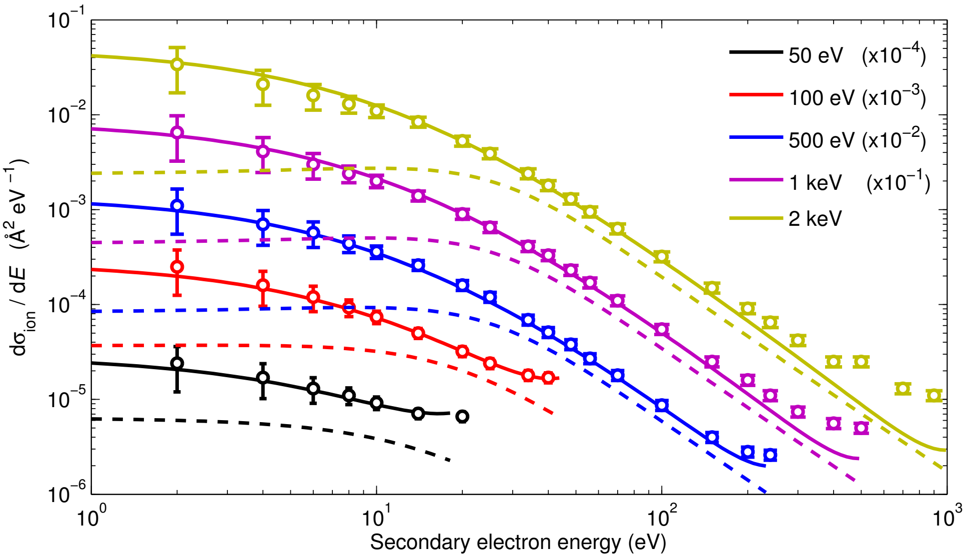

Figure 3.2: SDCS $d\sigma_{\rm ion}/dE$ for the interaction of electrons with gaseous (symbols and solid lines) and liquid water (dashed lines), measured [14] (symbols) as well as calculated data from the BEB model [93] (solid) and the model of Kutcher and Green [121] (dashed).

3.2.1.2 Excitation

a) Water vapour.

Only relative cross sections have been measured for discrete electronic excitations, therefore, Itikawa and Mason [106] did not recommend a cross section set. A few measurements exist for vibrational excitation cross sections, which become dominant for electrons with energies below about 10 eV. For a better handling in the simulation code, the recommended cross sections for the vibrational bending and stretching modes of water vapour were summed and fitted by the empirical model function

$$\log_{10}(\sigma_{\rm vibr.exc.}) = -1.86x^3 + 3.189x^2 - 1.505x - 0.09466 \qquad (3.1)$$

in units Å^2 and with $x = \log_{10}(T)$ and T is the incident electron energy in eV (see figure 3.3).

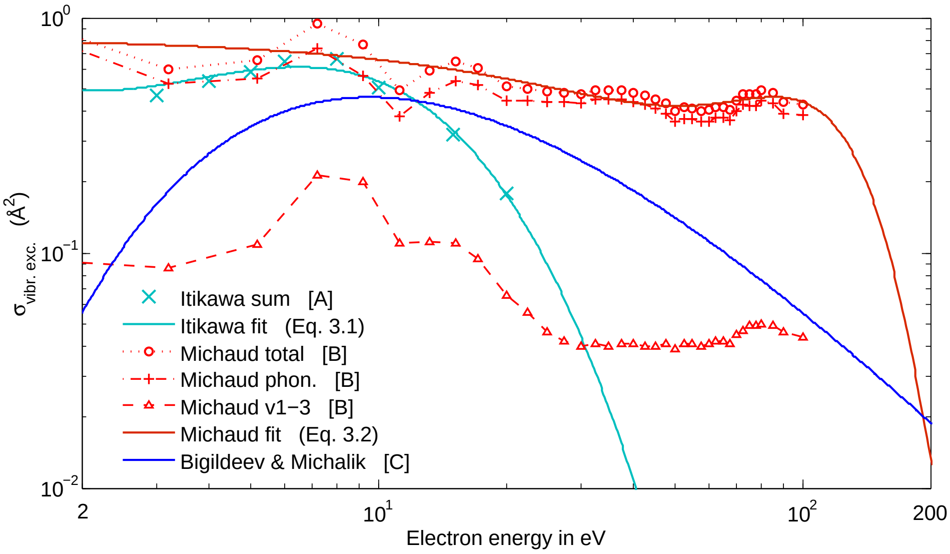

Figure 3.3: Vibrational excitation cross sections $\sigma_{\mathrm{vibr.exc.}}$ for the interaction of electrons with gaseous (A [106]), amorphous solid (B [132]) and liquid (C [11]) water. Lines for the experimental data (symbols) are guides to the eye. The model functions of data for gaseous and amorphous solid water (Eq. 3.1 and 3.2 on page 52, respectively) are also shown.

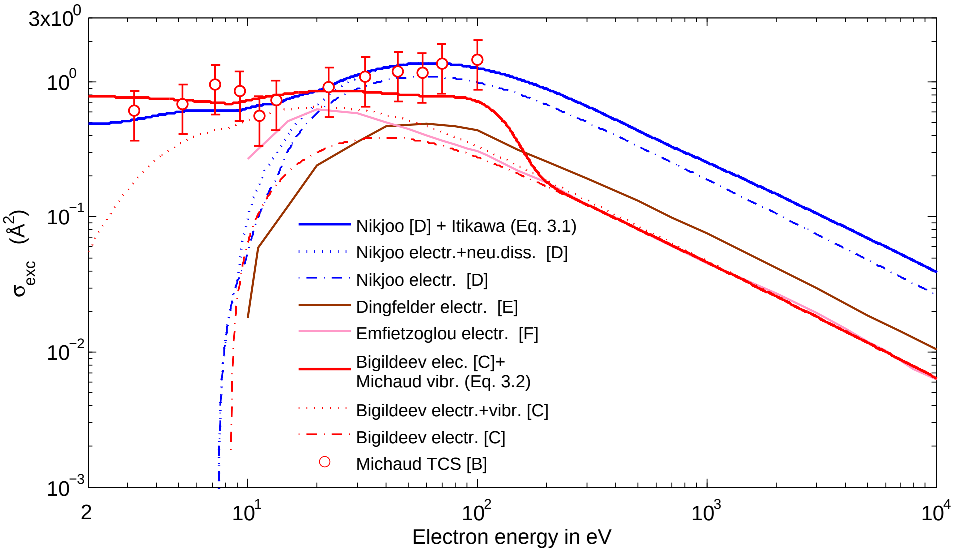

Figure 3.4: Total excitation cross sections σ_{exc} for the interaction of electrons with water vapour (D [147] and eq. 3.1), amorphous solid (B [132] and eq. 3.2 and liquid water (C–E, F [11, 39, 48]). In some cases, electronic and vibrational excitations are shown separately.

Semi-empirical models for excitation cross sections of water vapour were developed by several groups. The first data set, containing 26 different excitation states, was published by Olivero et al. [148], who fitted the analytical model of Green and Stolarski [78] to experimental data. Zaider et al. [198] repeated the fit of this model to the latest available data at that time. A different model was used by Paretzke (shown in [147]) to fit experimental data. Excitation cross sections obtained by the models of Olivero et al. [148], Zaider et al. [198] and Paretzke [147] were evaluated by Uehara et al. [186], who found relatively large discrepancies in magnitude between the data sets. For example, at the maximum cross section occurring at about 60 eV, the total excitation cross section of Paretzke is 20% and 40% larger than the data of Olivero et al. and Zaider et al., respectively. In Paretzke's data, the cross section for the diffuse bands (this state has the highest contribution to the total excitation cross section) is about 50% larger compared to the two other data sets. The semi-empirical model of Green and Stolarski was also used by Emfietzoglou et al. [53], who adopted the parameters of Olivero et al. for some partial excitation cross sections and also fitted the model to experimental data. The total excitation cross section of Emfietzoglou et al. is up to 10% larger than the data of Olivero et al. All four data sets are applied in different Monte Carlo track structure codes [26, 53, 186]. Those codes generally consider only the largest partial excitation cross sections, which are five discrete levels: the discrete excitation to the diffuse bands and Rydberg states A+B and C+D as well as the dissociative continua A^1B_1 and B^1A_1. Often also the most significant dissociative excitation states are considered (at least the three largest contributors) and also the vibrational states as, for example in the code of Champion [26]. In figure 3.4 the total excitation cross section data given by Nikjoo et al. [147] are shown, which were based on the model developed by Paretzke. For comparison, the sum of the five discrete levels without the contribution of the three dissociative excitation states are given.

b) Liquid water.

For liquid water, the same situation as for ionisation cross section data leads to the existing data being based on the dielectric response theory. The first data set was published by Kutcher and Green [121], who calculated discrete excitation cross sections based on experimental optical data [85]. Their calculated data were then fitted by the analytic formula of Green and Stolarski [78]. This formula was used previously for water vapour by Olivero et al. [148] and Zaider et al. [198]. Kutcher and Green considered the five discrete levels and added plasmon excitations, which have however not been proven to exist in liquid water [123].

The data of Kutcher and Green were compiled by Bigildeev and Michalik [11] to obtain the branching ratios for the discrete levels. Bigildeev and Michalik then performed an independent determination of a total excitation cross section for discrete excitations. Their rationale was to determine a cross section for liquid water, which is only accounting for experimentally established data. Hence, the total cross section for excitation to discrete states was obtained using the Born approximation and data from optical reflectance measurements [85]. In addition, Bigildeev and Michalik determined the cross sections for the three major vibrational states. As seen in figure 3.4, their total excitation cross sections have the same energy dependence as those of water vapour (data of Paretzke/Nikjoo are shown). However, they are by a factor of 5 lower in the energy range between 200 eV and 10 keV. Even if only the sum of the cross sections for the five discrete states is compared, the data of Bigildeev and Michalik are by a factor of 4 lower than those of Nikjoo et al. [147] at energies above 100 eV. This is not surprising and arises from the shift of the oscillator strength distribution towards larger energies in the liquid phase, as described in section 2.2.7.

Emfietzoglou et al. [48] calculated total excitation cross sections for the discrete states using the dielectric response theory as described in section 3.2.1.1. These data are in good agreement with the sum of the cross sections for discrete and vibrational excitations of Bigildeev and Michalik [11] within 20% for energies above 20 eV. Even the maximum occurs at the same energy of 25 eV. For lower energies, however, the data deviate by more than a factor of two.

The total excitation cross section of Dingfelder et al. [39] is up to a factor of 1.5 higher than the data of Bigildeev and Michalik [11] and Emfietzoglou et al. [48] at energies above 45 eV. Their maximum is shifted to 60 eV, which is a similar energy as the maximum cross sections of water vapour. At 10 eV, the values of Dingfelder et al. are by a factor of 10 lower than those of Emfietzoglou et al., but are in much better agreement (factor of two) with the sum of the discrete cross sections of Bigildeev and Michalik. These data are also shown in figure 3.4.

Vibrational cross sections for the liquid phase were, so far, only considered by Bigildeev and Michalik [11]. Such data have been measured for amorphous ice by Michaud et al. [132] for the impact of electrons with energies up to 100 eV. Amorphous ice has similar physical properties as liquid water. In the work of Michaud et al., the same bending and stretching modes that are present in the vapour phase were observed but were stiffer due to the directional hydrogen bonding. This lead to a lower cross section for the ice (figure 3.3). However, additional channels for lattice and liberational phonon modes open and contribute largely to vibrational excitations. Consequently, the vibrational cross sections of amorphous ice have about the same magnitude as those recommended by Itikawa and Mason [106] for water vapour in the energy range between 2 eV and 10 eV. However, the data points at the two highest energies in the vapour phase suggest a steep decrease of the vibrational cross section with increasing energy, while the data for ice are only slightly decreasing. To compare total excitation cross sections, including the vibrational excitation data of Michaud et al. for liquid water, their vibrational excitation cross section was fitted as function of the electron energy by the superposition of two Gaussian functions. The resulting model function is

$$\sigma_{\text{vibr.exc.}} = 6.131 \times 10^{-3}\ \text{Å}^2\ \mathrm{e}^{-\left(\frac{T+2733}{483.3}\right)^2} - 0.3672\ \text{Å}^2\ \mathrm{e}^{-\left(\frac{T-95.45}{52.71}\right)^2}, \tag{3.2}$$

where T is the electron energy in eV. Unfortunately, the total cross section given in the publication of Michaud et al. and shown in figure 3.4 contains contributions from ionisations. With this in mind, the same magnitude of those data compared to the total excitation cross section of Nikjoo et al. [147] supports the observation that excitation cross sections are lower in the liquid phase.

3.2.1.3 Elastic scattering

a) Water vapour.

Several data sets for total elastic scattering cross sections were determined for water vapour. Itikawa and Mason [106] found good agreement between the recommended data of an earlier review [22] to a new set of experimental data, obtained by integrating differential cross sections measured between 10° and 180° [30]. Due to the finite angular and energy resolutions in the experiments, measured elastic cross sections always contain forward scattered electrons (below 20°) following rotational excitations. For the water molecule, those inelastic contributions are considerable for incident electrons below 300 eV [106] due to the strong electric dipole moment of 1.85 D [142]. The recommended values of Itikawa and Mason for electron energies between 1 eV and 100 eV are based on two data sets, i.e. the data set of Cho et al. [30] for energies above 50 eV and those calculated by Gorfinkiel et al. [76] for energies below 6 eV. The values interpolated by Itikawa and Mason [106] are shown in figure 3.5 with the uncertainties given by Cho et al. [30]. As recommended data are only provided until 100 eV, the total elastic scattering cross section data of Katase et al. [111] (100–1000 eV) are also shown, which were based on their measured differential cross sections. The data of Katase et al. agree within the experimental uncertainties with the recommended data set.

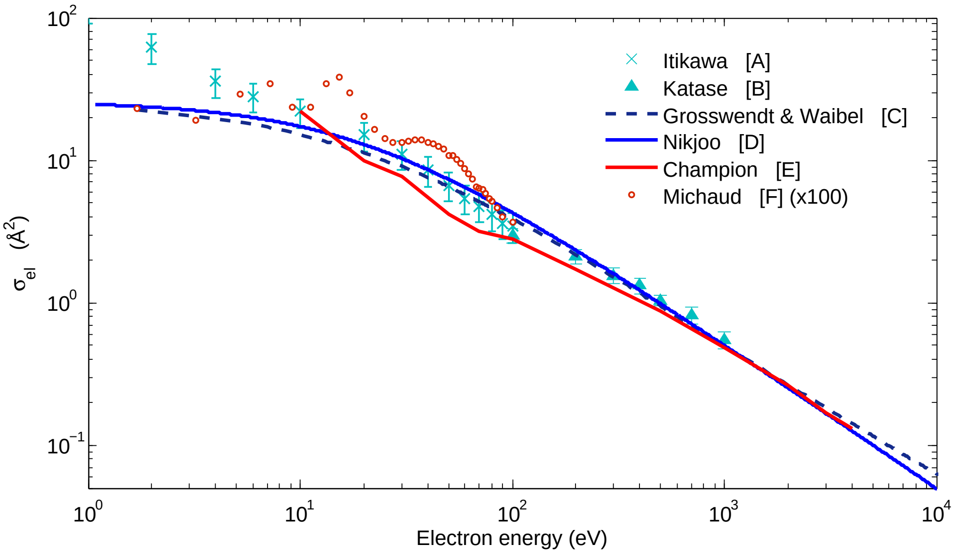

Figure 3.5: Total elastic scattering cross sections σ_{el} for electrons with gaseous (experimental data of A, B [106, 111] and models of C, D [81, 147]), liquid (E [26]) and amorphous solid water (F [132]).

Champion [26] calculated differential elastic scattering cross sections in an *ab-initio* approach (not shown). His integrated data are in good agreement with the experimental data of Katase et al. [111] and within the experimental uncertainties of those of Cho et al. [30] at energies above 20 eV.

Grosswendt and Waibel [81] used the screened Rutherford formula (see section 2.2.5), where a screening parameter was obtained by least-square fitting to experimental data of hydrogen and oxygen. The cross section of water was then calculated by the additivity rule. Their model data underestimate the recommended experimental values of Itikawa and Mason at energies below 50 eV by up to a factor of 2.5 and overestimate at higher energies up to 13% at 100 eV (figure 3.5). Between 200 and 1000 eV, the model data describe those of Katase et al. [111] well within the experimental uncertainties. At about 1 keV, the model is intersecting with the theoretical data of Champion [26] but continues with a lower slope at higher energies. Unfortunately, experimental data are not available for electrons with energies above 1 keV, so that the model data at those energies cannot be validated.

Nikjoo et al. [147] used the same approach as Grosswendt and Waibel [81] but assumed an effective charge for the water molecule, instead of adding the cross sections for individual atoms. They obtained a constant screening parameter for electrons with energies below 50 keV by least-square fitting to experimental data for water vapour of several groups. Below 40 eV, their data underestimate the measured values by up to a factor of 2.5 but are by 12% higher than the model data of Grosswendt and

Waibel [81] (figure 3.5). At 100 eV, the data of Nikjoo et al. are 23% higher than the experimental values recommended by Itikawa and Mason [106]. Above 800 eV, Nikjoo's model predictions are in good agreement with the theoretical data of Champion [26] but are 26% higher than the values of Grosswendt and Waibel at 10 keV.

b) Liquid water.

Only the calculated elastic scattering data of Champion et al. [28] were found in the literature (see figure 3.5). In the energy range between 10 eV and 10 keV, these data are by as much as 15% lower that the values obtained for water vapour by the same author [26] but both data sets coincide at energies above 10 keV. The decrease of the elastic scattering cross section in liquid water relative to the vapour is expected due to the lower polarisation effect.

Experimental data were obtained for amorphous ice by Michaud et al. [132]. As shown in figure 3.5, these elastic cross sections have a similar general energy dependence as the vapour data (disregarding the structures), but are two orders of magnitude smaller. We are conform with the statement of Liljequist et al. [127], who conclude from these findings that electron elastic scattering in condensed material are presently not well understood.

c) Differential elastic scattering cross sections.

For water vapour, Brenner and Zaider [21] fitted a semi-empirical function to experimental differential elastic scattering cross section data of several groups. Model function and data were shown to be in good agreement for electron energies up to 100 eV [21]. The data calculated from *ab-initio* theories by Champion et al. [26, 28] for water vapour are also in good agreement with several experimental data sets. From their calculations of liquid water cross sections, these authors observed a suppression of electron emission in forward direction in the liquid phase. This is in accordance with theory, where the weaker polarisation effect leads to a lower probability for elastic scattering of an incident electron by the nuclear potential of the target.

3.2.1.4 Dissociative electron attachment

An anion state is obtained when a low energy electron is captured in an empty orbital of the molecule for a time period longer than the scattering time. In the gas phase, such a state was shown to be repulsive and likely leads to dissociative electron attachment [132]. For water vapour, the measured cross sections for production of H^-, O^- and OH^- anions, recommended by Itikawa and Mason [106] agree well with the model predictions of Olivero et al. [148] for the sum of anion states for H^-, O^- (figure 3.6). Unfortunately, only a few data points were measured by Michaud et al. [132] in amorphous ice. Nonetheless, a similar magnitude of the total dissociative electron attachment cross section can be identified.

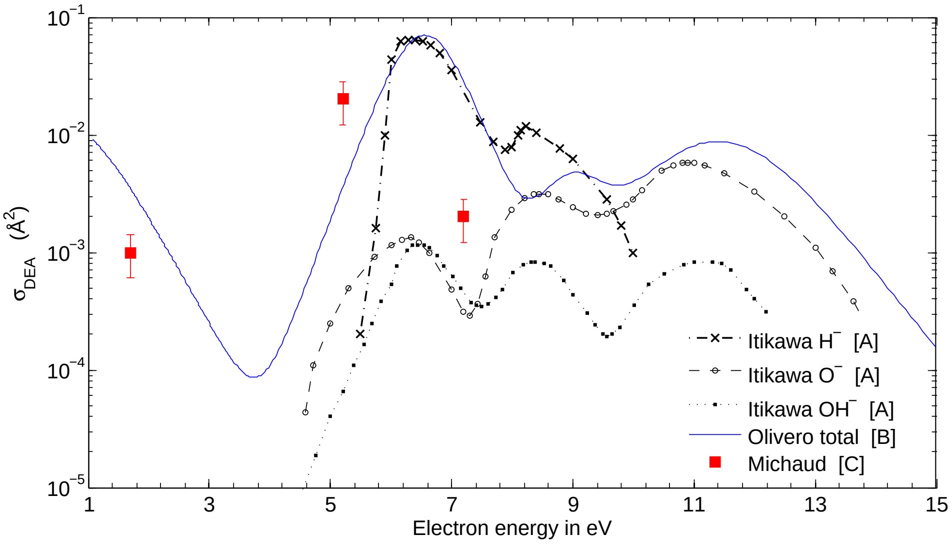

Figure 3.6: Dissociative electron attachment cross sections σ_{DEA} of gaseous (A, B [106, 148]) and amorphous solid water (C [132]).

3.2.1.5 Total scattering

Itikawa and Mason [106] reported total scattering cross sections measured by several groups but only in restricted energy ranges. Above 30 eV, those data are in good agreement but significantly deviate for lower energies (by 40% at 10 eV). As pointed out by Itikawa and Mason, those differences are due to the strong dipole moment of the water molecule, leading to enhanced forward-peaked scattering after rotational excitations. These cannot be discriminated in the linear transmission experiments used by all authors and lead to an underestimation of the total scattering cross section. Itikawa and Mason provide recommended values for electrons with energies between 1 eV and 1 keV. For energies below 10 eV, those recommendations are based on the data of Kimura et al. (1–400 eV) [118]. This group corrected their measurements by the contribution of forward scattered electrons which interacted by rotational excitation. Their data agree well with the elastic scattering cross section calculated by Gorfinkiel et al. [76], including rotational excitations. Above 10 eV, the data of Kimura et al. are consistent with experimental values of other authors where the data of Zecca et al. [200] cover the largest energy range up to 1 keV; hence, their data have been recommended.

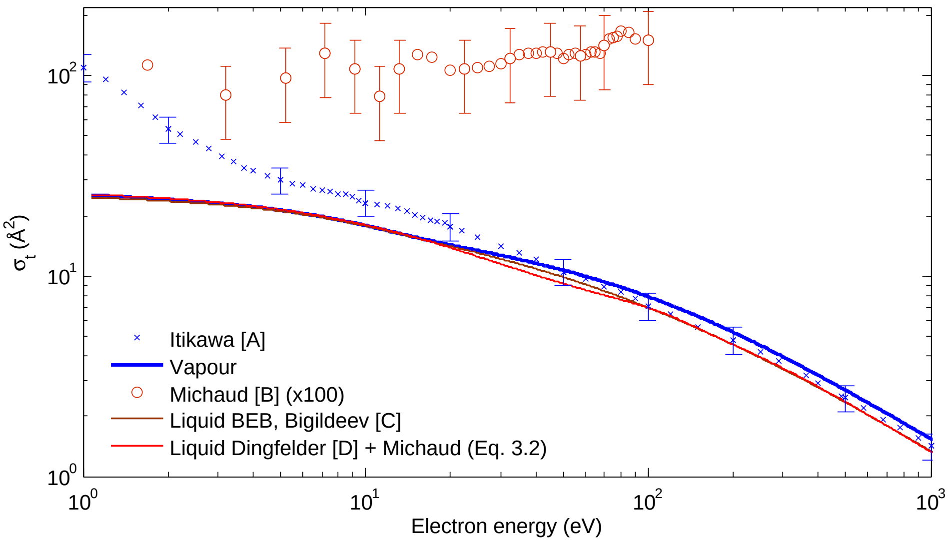

Figure 3.7: Total scattering cross sections σ_{t} for electrons with gaseous (A [106]), amorphous (B [132]) and liquid water (C,D [11, 39]) from experimental data (symbols) and the sum of total cross sections using different models (lines). Errorbars are shown for selected data points.

Total scattering cross sections, recommended by Itikawa and Mason [106] are shown in figure 3.7 together with the TCS of amorphous water, measured by Michaud et al. [132] and the sum of total cross sections for the different scattering processes using different models. The TCS of liquid water were determined using either the BEB model [93] or Dingfelder's [39] ionisation cross section together with discrete excitation cross sections of Bigildeev and Michalik [11] and vibrational excitation data of Michaud et al. [132]. Alternatively, the BEB model for ionisation was combined with the total excitation cross section (including also vibration) from Bigildeev and Michalik [11]. Deviations between the model data for liquid water lead to a variation in the TCS of less than 9% in the energy region 20–100 eV. On the other hand, the TCS of water vapour and liquid water deviate at all energies higher than 20 eV. For example at 1 keV, the TCS model data for water vapour are 17% larger than the data for liquid water. Generally however, all calculated TCS data agree with the recommended TCS for water vapour within the experimental uncertainties at electron energies above 25 eV. At 10 eV, the model data are 30% lower with increasing deviation towards lower energies, as rotational excitations are not included in the modelled data. In summary, the sum of ionisation, elastic scattering and excitation cross section data for water vapour are in good agreement with the experimental data of the TCS within the experimental uncertainties, while the calculated TCS of liquid water are similar to those of water vapour.

3.2.2 Proton cross section data

a) Ionisation.

Comprehensive reviews of proton-impact ionisation cross sections of water vapour are available in the ICRU report 55 [100] as well as in [161, 162]. *Ab-initio* calculations of double-differential ionisation cross sections (DDCS) have also been reported by several authors, for example by Fainstein et al. [54].

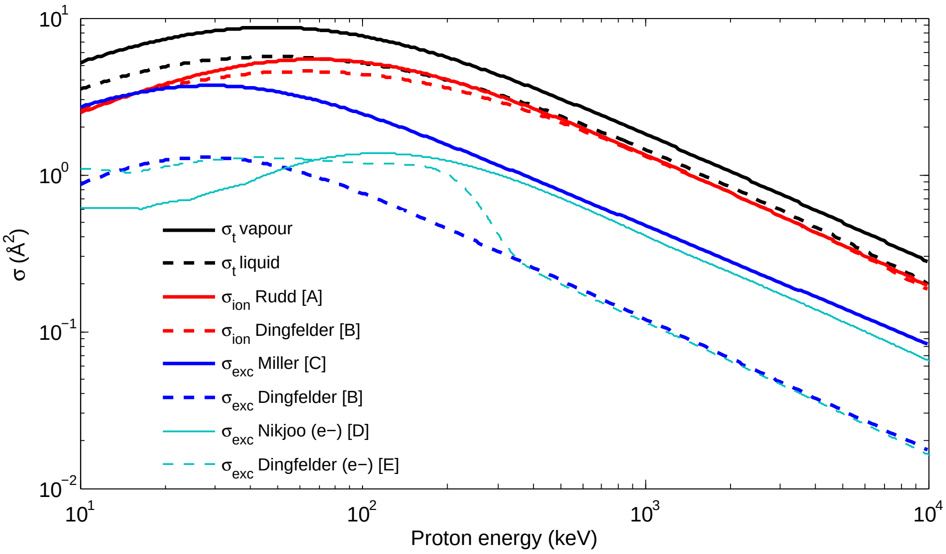

Figure 3.8: Total cross sections for ionisation σ_{ion} and excitation σ_{exc} (A [162], B [40], C [133]) and total scattering cross sections σ_{t} for protons in water vapour (solid lines) and liquid water (dashed lines). Excitation cross sections for electrons of same velocity as protons are also shown for comparison (D [147], E [39]).

Total ionisation cross section for water vapour were measured by Rudd et al. [161]. They also developed semi-empirical models for total and single differential ionisation cross sections (SDCS) on the basis of an extensive evaluation of experimental data for different molecules [162]. In case of the SDCS, the comparison was with those obtained from DDCS measured by Toburen and Wilson (0.3–1.5 MeV) [181]. Their models, also recommended by the ICRU [100], are shown in figures 3.8 and 3.9.

Another semi-empirical model for the proton-impact ionisation cross sections of water vapour was developed by Emfietzoglou et al. [53] (not shown). Their SDCS agree well with experimental data within the experimental uncertainties for protons of energy between 300 keV and 1.5 MeV.

Zaider et al. [198] used also a semi-empirical model, which was fitted to experimental DDCS data and analytically integrated (not shown). Their SDCS are in reasonable agreement with experimental data for secondary electron energies above 20 eV. Below, their model predicts a plateau value while the experimental data show maxima at about 10 eV. Therefore, their total ionisation cross section is by 10–40% lower than the predictions of the Rudd model [162] in the energy range between 300 keV and 2 MeV.

The theoretical model of Hansen et al. (HKS model), which was revised and corrected by Bernal et al. [8], is free of adjustable parameters but also does not well describe the SDCS for secondary electron energies below 20 eV. The data of the HKS model increase even further towards lower energies with respect to experimental data (see [8]). Consequently, the total ionisation cross section determined from the HKS model has a different energy dependence when compared to the data of the other authors. In fact, these data decrease with a larger slope for increasing proton energies [63].

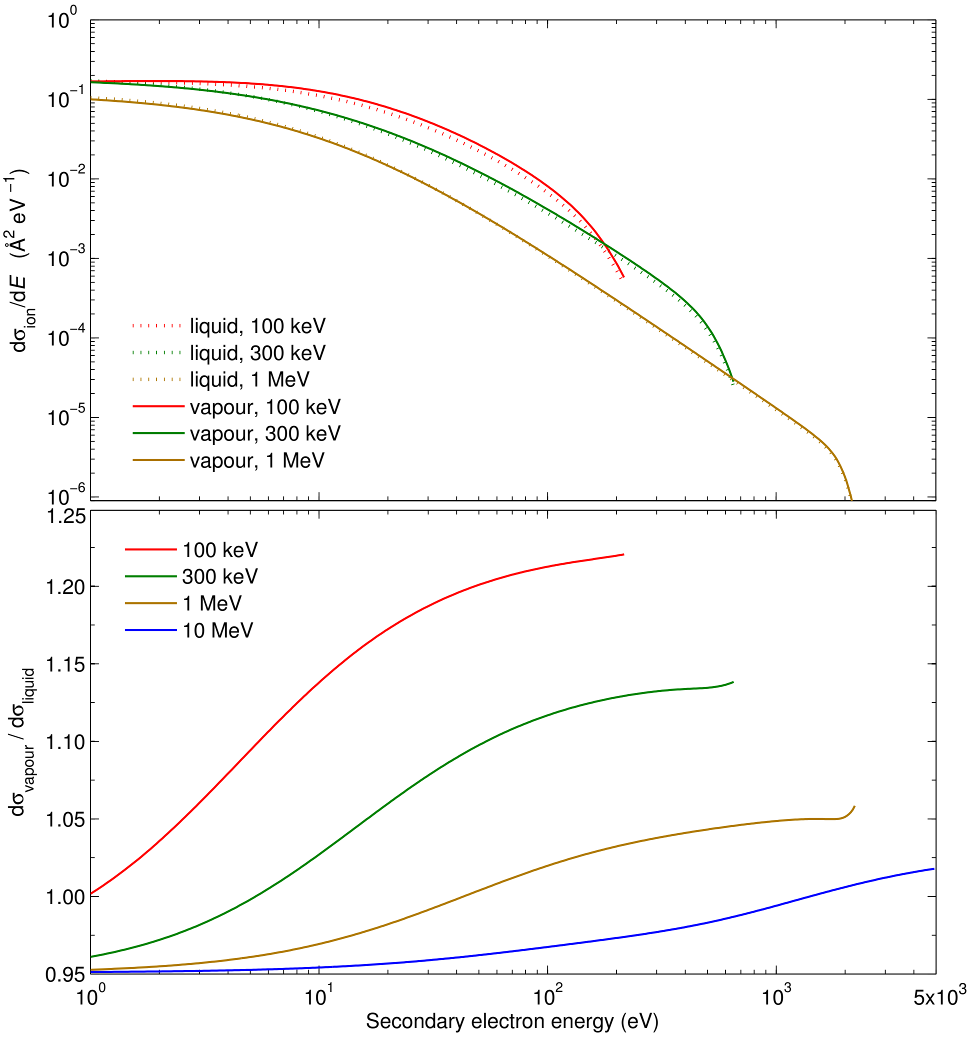

Figure 3.9: SDCS for proton impact on water vapour [162] and liquid water [40] (top) and ratio of SDCS (bottom).

For liquid water, Dingfelder et al. [40] used the Rudd model [162] to calculate the SDCS and modified the parameters to obtain the ICRU stopping cross section for the liquid phase [99]. They point out that the Rudd model for water vapour does not yield the respective ICRU stopping cross section. The total ionisation cross sections for liquid water agree within 4% with the water vapour data for proton energies larger than 500 keV (figure 3.8. Both data sets reach a maximum value at the same energy of about 80 keV, where the liquid water data are 17% lower but become higher than the vapour cross sections for energies below about 20 keV.

Dingfelder et al. [40] compared also the SDCS for liquid water with those of Rudd et al. [162] for water vapour and to experimental data of Toburen and Wilson [181]. Figure 3.9 shows the SDCS for secondary electron production, i.e. the total SDCS was obtained from the sum of SDCS for the individual subshells without any normalisation factors. This information is required in simulation codes to determine the secondary electron energy. In fact, the probability for ejection of an electron by protons of low energy is up to 23% larger for water vapour. This is due to the larger polarisation effect of low energy protons for water vapour [127]. With increasing proton energy, the ratio of the SDCS for the vapour and liquid phases approaches unity (figure 3.9 right). Generally for protons of higher energies, the SDCS are larger for water vapour only if the secondary electron energy is high. For low energy electrons, the probability of ejection is up to 5% larger in the liquid phase. Generally however, the calculated SDCS for both phases is within the uncertainties of the experimental values (between 20% and a factor of two [181]).

b) Excitation.

A semi-empirical model for partial excitation cross sections was developed by Miller and Green [133]. These data were based on the scaling of electron cross sections at high energies according to the Born approximation and corrections were applied for lower proton energies. This was necessary due to the lack of experimental data for proton impact. Miller and Green considered 28 different excitation states. The sum of the data for discrete states, which contribute by 50–60% to the total excitation cross section, is shown in figure 3.8 (page 58). In agreement with the Bethe-Born theory, the total excitation cross section is similar for protons and electrons of same velocity for proton energies above 500 keV. Miller and Green consider their data as reasonably accurate in the high energy range while they may be uncertain by a factor of two or more in the maximum region. The electron data were obtained by the model of Paretzke (as described by Nikjoo [147]), which yields the largest electron-impact cross section of the investigated models (see figure 3.4). Hence, the model of Miller and Green may overestimate (rather than underestimate) the total excitation cross section for protons.

Another set of total proton excitation cross sections was determined by Zaider et al. [198] by a similar approach (not shown). Those data are estimated from the graphs in their paper to be about 15–20% lower than the values of Miller and Green.

Dingfelder et al. [40] obtained proton-impact excitation cross sections for liquid water by a similar approach as Miller and Green [133]. The authors scaled electron data [39] by the velocity and adjusted the proton cross section at low energies. Therefore, their scaled excitation cross sections for electrons deviate by less than 10% from those of protons with energies above 100 keV.

The deviation between total excitation cross sections of water in the vapour and liquid phases increases with increasing energy. In fact, the water cross sections are between a factor of 3 to 5 lower than the vapour data but both show a maximum at about 30 keV. The magnitude of deviation is in accordance with the deviation between electron-impact excitation cross sections for the water vapour and liquid water and can be attributed to the shift of the oscillator strength distribution to higher energies.

c) Total scattering cross sections.

Total scattering cross sections for protons shown in figure 3.8 were obtained for water vapour by the sum of the ionisation cross section of Rudd et al. [161] and the excitation cross section of Miller and Green [133]. For liquid water, the total ionisation cross section obtained from a new parameterisation of Rudd's SDCS model [162] by Dingfelder et al. [40] was added to the excitation cross section of the same author. The vapour data are by 30% larger than those for liquid water for protons in the energy range between 300 keV and 10 MeV. For lower energies, the data deviate as much as 50%.

Please note, that charge transfer processes become important for protons with energies below 100 keV and the angular deflection of protons due to elastic scattering is significant only below 1 keV [40]. As in this work protons with energies above 100 keV are of interest, the equilibrium fraction of neutral hydrogen is below 20% (this value was measured by [3] for protons traversing hydrogen and oxygen gas). Hence, neither charge transfer nor elastic scattering processes are taken into account for proton impact.

3.2.3 Cross section data implemented in PTra

A previous version of PTra [79] existed for particle transport in liquid water. In the course of this work, a new version was developed with the option of a transport in either water vapour or liquid water. The models implemented in a previous and the augmented versions of PTra are listed in tables 3.1 and 3.2 for electron and proton impact, respectively. The data are also shown in figures 3.10 and 3.8. In the following, the choice of the models is discussed.

3.2.3.1 Electron-impact cross sections

a) Previous PTra version.

In the previous version of PTra, the total ionisation cross section was determined according to Dingfelder et al. [39]. In fact, the following model function was obtained by fitting to those data and was implemented in PTra [82],

$$\sigma_{\mathrm{ion}}(T < 17.35\ \mathrm{eV}) = 2.1262 \times 10^{-3}\ \pi a_0^2\,(T/R)^{12.6143} \tag{3.3a}$$

$$\sigma_{\mathrm{ion}}(T \geq 17.35\ \mathrm{eV}) = 4\pi a_0^2 R^2 \left(1 - \mathrm{e}^{-0.1573(t-1)}\right) \frac{1.744 \times 10^{-2}}{t + 9.7081} \left(\ln t + 3.3836 + \frac{-14.9523}{t} + \frac{15.1212}{t^2}\right) \tag{3.3b}$$

with $t = T/9.5$ eV, the Rydberg constant R and Bohr radius a_0.

Partial ionisation cross sections for different ionic fragmentation products were calculated from the semi-empirical model of Kutcher and Green [121] and the parameterisation of the SDCS of the same authors (using the model of Green and Sawada [77]) was implemented. The angular distribution after ionisation was obtained from the analytical model of Berger [81]. Excitation cross sections for five discrete and three vibrational states were calculated by the semi-empirical model of Bigildeev and Michalik [11]. The code had been augmented by substituting the vibrational excitation cross sections of Bigildeev and Michalik by the measured cross section data of Michaud et al. [132] for vibrational excitations and dissociative electron attachment (see details in [Pub6]). The model of Grosswendt and Waibel [81] was used to calculate the total elastic scattering cross section. The angular distribution of elastically scattered electrons with energies above 200 eV was determined by the same model, while for energies below, the model of Brenner and Zaider [21] was applied. The same experimental data as used for their fit model have also been directly applied in Monte Carlo simulations [147] to determine angular distributions of elastically scattered electrons with energies below 1 keV.

Table 3.1: Electron-impact cross section data in current and previous versions of PTra.

	vapour	liquid	liquid (previous) [79]
σ_{ion}	BEB model [93]	a) BEB model [93] b) Dingfelder [39]	Dingfelder [39]
$\sigma_{\mathrm{ion},j}$	BEB model [93]	BEB model [93]	Kutcher & Green [121]
$\mathrm{d}\sigma_{\mathrm{ion}}/\mathrm{d}E$	BEB model [93]	a) Kutcher & Green [121]	Kutcher & Green [121]
	BEB model [93]	b) BEB model [93]	Kutcher & Green [121]
$\sigma_{\mathrm{exc,discrete}}$	Paretzke/Nikjoo [147]	Bigildeev & Michalik [11]	Bigildeev & Michalik [11]
$\sigma_{\mathrm{exc,vibr.}}$	Itikawa & Mason [106]	Michaud [132] & Dingfelder [41]	a) Bigildeev & Michalik [11] b) Michaud [132] & Dingfelder [41]
σ_{el}	Nikjoo [147]	Nikjoo [147]	Grosswendt & Waibel [81]
$\mathrm{d}\sigma_{\mathrm{el}}/\mathrm{d}\Omega$	— — — — — — $T \leq 200$ eV Brenner & Zaider [21] — — — — — — —		
	— — — — — — $T > 200$ eV Grosswendt & Waibel [81] — — — — — —		
σ_{DEA}	Olivero [148]	Olivero [148]	Michaud [132] & Dingfelder [41]

b) Present PTra version.

The present version of PTra utilises the the BEB model [93] to calculate total and differential ionisation cross sections of water vapour. Despite the worse agreement with the recommended experimental data [106], this model was preferred to the model published by Uehara et al. [186] for several reasons. The model of Uehara et al. has an ionisation threshold of 15 eV, which is significantly higher than the ionisation potential of the water molecule of about 12.61 eV and therefore disregards ionisations by electrons below this energy. Furthermore, the overestimation by the BEB model of the experimental total ionisation cross section by up to 60% at energies below 50 eV leads to only a negligible difference (not more than 3%) of the ionisation cross section relative to the total scattering cross section. In fact, this ratio is the significant quantity in the simulation. Finally, the BEB model can also be used to determine the ionisation cross sections for the subshells separately.

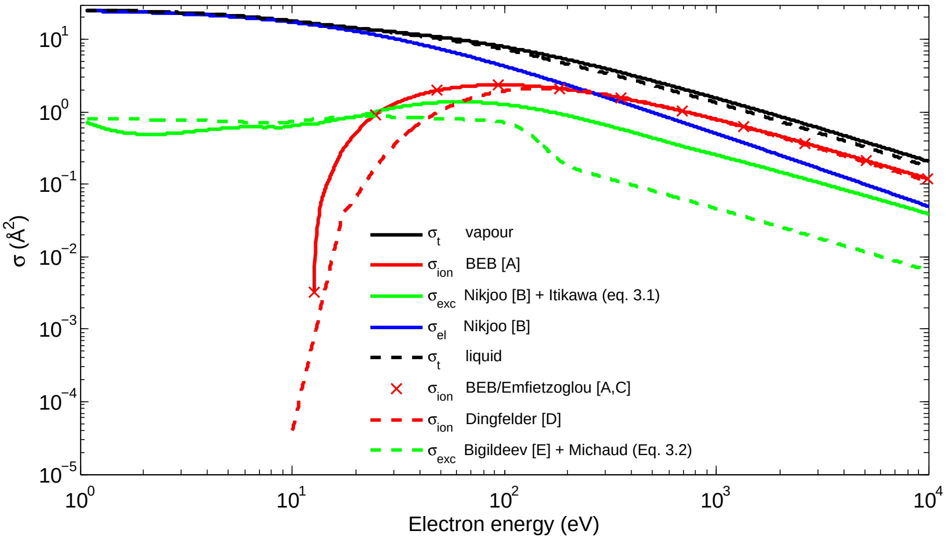

Figure 3.10: Total electron-impact cross sections implemented in PTra for water vapour (solid lines, A [93], B [147]) and liquid water (dashed lines and symbols, C [48], D [39], E [11]).

The comparison of ionisation cross section data in the liquid and vapour phases of water reveals that, despite the lower ionisation threshold of liquid water, the cross sections are of similar magnitude as those for water vapour (except the data set of Kutcher and Green). In fact, the most recently published data of Emfietzoglou et al. [48, 50] has no greater deviation from the recommended experimental data [106] than the predictions of the different models for water vapour. There is, however, a considerable discrepancy between the mass stopping power, where the data calculated by Emfietzoglou et al. are up to 30% lower at energies below 1 keV than other calculated or measured data [48]. On the other hand, the mass stopping power of Dingfelder et al. [39] is in much better agreement with the ICRU data [39, 48] , while their ionisation cross section data are by a factor of two lower than those of Emfietzoglou et al. for energies below 200 eV. Therefore, PTra for liquid water contains the option of using either the BEB model [93], which yields an ionisation cross section similar to the one of Emfietzoglou et al., or the Dingfelder model given in equation 3.3b (page 62). For simplicity, ionisation cross sections for the subshells are calculated by the BEB model for both approaches. This is reasonable because only small differences have been found for ionisation cross sections of individual subshells of both water phases [39].

In PTra, the SDCS for water vapour are also obtained by the BEB model due to its excellent agreement with experimental data. For liquid water, two different data sets can be chosen to investigate the influence of the SDCS on simulation results. These are the model of Kutcher and Green [121] due to its large reduction of the production of low energy electrons and the BEB model with water vapour data. Scattering angles of the primary and secondary electrons after ionisation are determined analytically as described by Grosswendt and Waibel [81].

The excitation cross sections for water vapour are calculated by the model of Paretzke, using the parameters listed in [147] for discrete levels and dissociative excitation states. The model of Paretzke yields the highest total excitation cross section of the investigated models [148, 186, 198] (see figure 3.4). This model was chosen as it leads to the greatest difference between the total inelastic cross sections for the liquid and vapour phases (the ionisation cross sections for electrons of energy above 200 eV were observed to be similar, while the excitation cross sections for the vapour phase are higher than in the liquid). Vibrational excitation cross sections are included using the model function in equation 3.1 (page 48). Branching ratios and energy levels for those states were taken from Olivero et al. [148], following the approach of Champion [26]. For liquid water, vibrational excitation cross sections of Michaud et al. [132] are included as described by Dingfelder et al. [41]. As their data are only given for energies up to 100 eV, a sudden drop by a factor of two occurs in the total excitation cross section at 100 eV. The impact of this drop on simulation results is negligible because the elastic scattering cross section is nearly an order of magnitude larger at this energy and the energy loss by vibrational excitations is low. The discrete excitation levels are calculated from the model of Bigildeev and Michalik [11]. The sum of their data and the vibrational cross sections of Michaud et al. is in good agreement with the total inelastic cross section of Michaud et al. up to an energy of about 30 eV, where ionisations become dominant. The discrete excitation data of Bigildeev and Michalik were preferred to those of Emfietzoglou et al. [48] because the latter would yield larger values for the total excitation cross section, i.e. when added to the vibrational data of Michaud et al. Furthermore, partial excitation cross sections for the discrete levels are readily available via the model of Bigildeev and Michalik. The inclusion of the model of Dingfelder et al. [39] was also considered because its total excitation cross sections at energies above 60 eV are by a factor of 1.5 larger. However, this model was not used as no significant change in the track structure is expected. This is due to the excitation cross section being an order of magnitude smaller than the ionisation cross section, which is dominant in this energy range.

For elastic scattering, the model published by Nikjoo et al. [147] is implemented in PTra, due to the good agreement of their data with those of Katase et al. [111], Champion [26] and the screened Rutherford model at higher energies. The same model is used for cross sections of gaseous and liquid water due to the lack of data supporting the low values measured for amorphous ice [132]. The angular deflection after elastic scattering is determined according to the model of Brenner and Zaider [21] for energies above 200 eV, due to the good representation of experimental data. For energies below 200 eV, the approach as described by Grosswendt and Waibel [81] or Nikjoo et al. [147] is used, sampling the differential cross sections of oxygen and hydrogen atoms separately.

The model published by Olivero et al. [148] for dissociative electron attachment cross sections of water vapour is also used for the liquid phase because the available measured data for gaseous and liquid water appear to be in accordance (see figure 3.6).

The total cross section data of the different processes for electron impact, implemented in the present version of PTra for water vapour and liquid water, are shown in figure 3.10. Total scattering cross sections were calculated from the sum of total cross sections of the different processes.

3.2.3.2 Proton-impact cross sections

a) Previous PTra version.

In the previous version of PTra the total ionisation cross section of liquid water was obtained by a model function, which was fitted to the ratio of the ionisation cross sections of Rudd et al. [161] and Dingfelder et al. [40]. This model function was then multiplied with the cross sections calculated by Rudd's model. Partial cross sections for ionisation of the subshells and SDCS were calculated by the HKS model [8, 63]. Excitation cross sections were calculated as suggested by Dingfelder et al. [40].

Table 3.2: Proton-impact cross section data in present and previous versions of PTra.

	vapour	liquid	liquid (previous) [79]
σ_{ion}	Rudd [161]	Model to Dingfelder [40]	Correction to Dingfelder [40]
$\sigma_{\mathrm{ion},j}$	Rudd [161]	Dingfelder [40]	HKS [8, 63]
$\mathrm{d}\sigma_{\mathrm{ion}}/\mathrm{d}E$	Rudd [162]	Dingfelder [40]	HKS [8, 63]
σ_{exc}	Miller & Green [133]	Dingfelder [40]	Dingfelder [40]

b) Present PTra version.

The present version of PTra uses the semi-empirical models of Rudd et al. [161, 162] for the SDCS and total ionisation cross section of water vapour, due to their good agreement with experimental data. For liquid water, the parameterisation of their SDCS by Dingfelder et al. [40] is applied. Those data were integrated and fitted by superpositioned Gaussian functions to enable a convenient implementation of the total ionisation cross section for protons of energy T (in keV), such that

$$\sigma_{\text{ion}}(T) = 2.237\ \text{Å}^2\ e^{-\left(\frac{x-4.204}{1.884}\right)^2} + 2.334\ \text{Å}^2\ e^{-\left(\frac{x-3.93}{3.303}\right)^2} \tag{3.4}$$

with $x = \ln(T)$. This model function improves the agreement with Dingfelder's data with respect to the model used in the previous version of PTra. The ionisation cross sections for the subshells of liquid water are also obtained from the Rudd model [161] for water vapour and an integration of the SDCS parameterised by Dingfelder et al. [40] for each subshell of liquid water.

Excitation cross sections for water vapour are determined by the model of Miller and Green [133]. Those for liquid water are calculated as in the previous version from the parameterisation of this model by Dingfelder et al. [40], who considered the five major (discrete) excitation levels.

The set of total cross sections for proton impact on water vapour and liquid water used in PTra is shown in figure 3.8. Total scattering cross sections were calculated from the sum of total cross sections for ionisation and excitation processes.

3.3 Track structure simulations in water and water vapour

Simulations of electrons and protons were performed in water vapour and liquid water, using the cross sections as specified in section 3.2.3. An accurate simulation of the particle transport was verified by comparing calculated W-values (mean energy required to produce an ion pair) to experimental data. This quantity is frequently used in dosimetry so that experimental data are available. Also the yields of ionisations and excitations per 100 eV deposited energy (G-values) are compared to literature data. Finally, nanodosimetric parameters are calculated for both phases of water.

To abbreviate the discussion, the following acronyms are used for the different parameterisations of total ionisation cross sections σ_{ion} and single differential ionisation cross sections $\mathrm{d}\sigma_{\mathrm{ion}}/\mathrm{d}E$ of liquid water:

- SigIon1: σ_{ion} BEB model [93] and $\mathrm{d}\sigma_{\mathrm{ion}}/\mathrm{d}E$ BEB model [116]
- SigIon2: σ_{ion} Dingfelder et al. [39] and $\mathrm{d}\sigma_{\mathrm{ion}}/\mathrm{d}E$ BEB model [116]
- SigIon3: σ_{ion} Dingfelder et al. [39] and $\mathrm{d}\sigma_{\mathrm{ion}}/\mathrm{d}E$ Kutcher and Green [121]; this version uses the cross section data implemented in the prevous version of PTra [79].

3.3.1 W-values

W-values are calculated by counting the total number of ionisations produced by the complete slowing down of an incident particle. Therefore, this quantity is sensitive with regard to ionisation and excitation cross sections as well as to secondary electron spectra. The W-value approaches an asymptotic value towards high energies, as the number of inelastic events is large enough to average out the fluctuations in energy lost in single inelastic events. Also, the energy loss is dominated by distant interactions of projectiles with outer-valence-shell electrons. As the complete slowing down of the projectiles is contained in the W-value, the asymptotic value is well suited to indicate if the cross section data across the entire energy range of the primary and secondary particles is realistic.

Simulated W-values for electrons in water vapour are in reasonable agreement with experimental data [33] (figure 3.11). The asymptotic W-value, given in the literature between 29.15 and 29.9 eV [98] (with less than 2% uncertainty) is slightly underestimated by 28.6 eV for 10 keV electrons. To investigate the influence of different excitation cross sections on the W-value, simulations were repeated, considering only electronic excitation processes; the exclusion of neutral dissociation and vibrational excitation processes reduces the W-values by 2 eV.

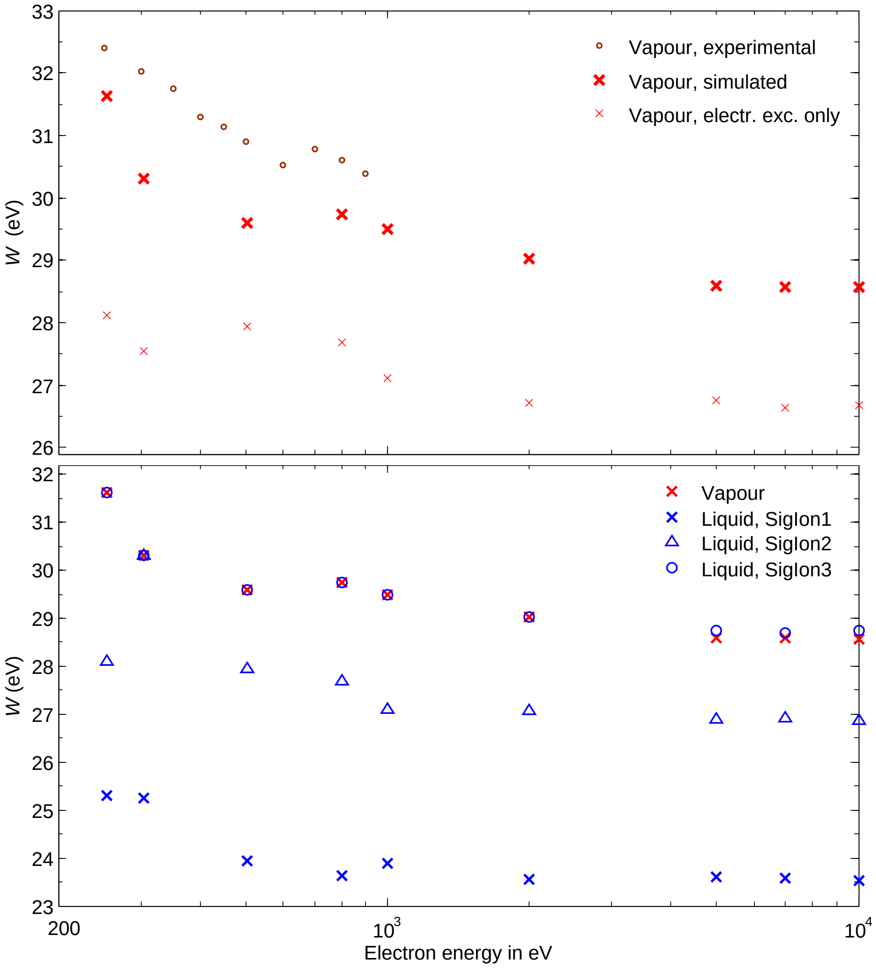

Figure 3.11: W-values of electrons in water vapour (top) and liquid water (bottom).

In the liquid phase, the calculated W-value at 10 keV of 23.5 eV may be compared to a W-value, estimated from measurements of the initial yield of hydrated electrons per 100 eV deposited energy after the traversal of 20 MeV electrons [108, 172]. The W-values calculated from those yields are between 19.6 eV and 22.7 eV (including experimental uncertainties). However, the energy deposition by excitations is not taken into account and would lead to higher results for the W-values. In this case, the values estimated from the experiments are in reasonable agreement with the asymptotic W-value of 23.5 eV, calculated for liquid water using PTra. This W-value is obtained when using the BEB model for the ionisation cross sections (SigIon1). In this case, the same ionisation cross sections are used as for water vapour so that essentially the excitation cross sections are different from those used in the vapour phase. Figure 3.11 also shows W-values obtained in liquid water using the combinations of cross section data in SigIon2 and SigIon3. Due to the reduced total ionisation cross section for low-energy electrons, a smaller number of ionisations is produced. Hence, with SigIon2 the calculated W-values are about 3 eV higher than the BEB model calculations with SigIon1. With SigIon3, the W-values are very similar to those calculated for water vapour. These results suggest that the use of the BEB model (SigIon1) for total and differential ionisation cross sections is best suited to describe the electron transport in liquid water.

Experimental data for W-values of water vapour for protons with energies above 100 keV are not available in the literature. An asymptotic W-value for water vapour of 30.5 eV has been estimated from data of other gases [122]. Theoretical W-values of 29.5 eV and 25.5 eV have been obtained from cross section data of vapour and liquid water, respectively [5]. The calculated W-values using PTra at proton energies of 10 MeV of 29.1 eV and 23.5 eV for vapour and liquid water, respectively, are in reasonably good agreement with the literature data listed above.

3.3.2 G-values

In addition to W-values, the realistic performance of a simulation can be investigated by calculating the yields of ionisations and excitations per 100 eV deposited energy (G-values). In table 3.3, literature data obtained in the high-energy limit are listed [11, 110, 153, 155] and compared to G-values obtained for water vapour and liquid water in PTra. The simulations in liquid water were performed using the three different descriptions for the ionisation cross sections. The ionisation yields are in excellent agreement with the literature data for water vapour and when SigIon1 is used. The Dingfelder model [39] for the total ionisation cross section leads to a slightly lower ionisation yield, particularly when used in combination with the SDCS of Kutcher and Green [121] in SigIon3. The G-value for ionisation in water vapour is always lower than in liquid water, which correlates with the higher W-value in the vapour phase, since the number of ionisations per 100 eV energy deposited strongly depends on the ratio of excitation and ionisation cross sections. The observed increase of the G-value for ionisation in liquid water is due to the shift of oscillator strength distributions to higher energies (reducing the excitation cross section), while the ionisation threshold is lower.

G-values for excitation (without vibrational excitations) show greater variation when obtained by different authors and models. The values obtained in this work agree well with those given in the literature. Except the values of Paretzke [153], the G-values for excitation are lower in the liquid phase than in the vapour. This is in agreement with the increase of G-values for ionisation for the reasons given above. Comparing the different models for ionisation cross sections of liquid water the opposite trend as for the ionisation G-value can be observed. In fact, the use of the BEB model (SigIon1) leads to the lowest G-value for excitation and SigIon3 results in the highest value.

Table 3.3: Yield of ionisations G(ion) and excitations G(exc) produced per 100 eV deposited energy by fast electrons in water. Literature data are listed in the order of citation [11, 110, 153, 155].

	vapour		liquid			
	literature [11, 110, 153, 155]	this work	literature [11, 110, 153, 155]	this work: SigIon1	SigIon2	SigIon3
G(ion)	3.5, 3.4, 3.3, 3.5	3.6	4.4, 6.0, 3.9, 4.8	4.5	4.0	3.8
G(exc)	3.5, 3.8, 3.0, 3.7	3.0	2.8, 1.4, 3.3, 3.1	1.7	2.5	3.1

In nanodosimetry, the absolute yields of inelastic interactions are of interest as these allow an estimation of DNA damage. G-values are average values taken over the complete slowing down spectrum and very sensitive to the ratio of ionisation and excitation cross sections. Therefore, individual yields of interactions by single particles of specific energy within a particular target volume cannot be derived from those values. Such individual ionisation and excitation yields are compared in the following section.

3.3.3 Nanodosimetric cluster size distributions

In this section, cluster size distributions of ionisations and excitations by incident electrons are shown for water vapour and liquid water. Cluster size distributions were introduced in section 2.4. In the simulations, electrons were transported until their energy fell below 7 eV.

Mean ionisation cluster sizes in water obtained as a function of incident electron energy are shown in figure 3.12 (top). For energies above 250 eV, the mean ionisation cluster size is nearly independent of the water phase and the applied cross section models. A maximum is present at an energy of 150–200 eV, which is characteristic for a target volume of this size as the formation of the ionisation cluster size depends on both the ionisation mean free path and the particle range. The mean ionisation cluster size of liquid water is generally larger than for water vapour when SigIon1 is used for the ionisation cross sections. The observed deviations are 6% in the region of the maximum. The use of SigIon2 significantly reduces the mean ionisation cluster size at all energies, i.e. 6% above 250 eV and 10–20% in the region of the maximum. SigIon3 leads to the same results as SigIon2 at energies below 200 eV but increases the mean ionisation cluster sizes at higher energies to yield results similar to those of water vapour. The observed enhancement at high energies when using SigIon3 instead of SigIon2 is due to the reduced probability to produce secondary electrons with low energies in SigIon3. This reduction has a larger effect on single differential cross sections for electrons of higher energies as seen in figure 3.2. To investigate the observed deviations in the maximum and high-energy regions in more detail, probability distributions for ionisation cluster sizes are shown in figure 3.12 (top) for electrons of energies 200 eV and 1 keV. From those it is obvious that the mean ionisation cluster size obtained with different cross section models changes due to deviations in probabilities to produce large ionisation clusters above 4 for 200 eV and above 3 for 1 keV.

Calculations of ionisation cluster sizes in water produced by electrons have been published in the course of this work [Pub1, Pub5]. At that time, the previous version of PTra has been used, which yielded similar results as SigIon3 due to similar cross section data used in the code. Ionisation cluster size distributions and their first moments have been compared to those obtained by means of the Geant4-DNA Monte Carlo system. The deviations between the simulated data have been attributed to the differences in interaction cross section data, which is supported in the present study. In fact, Geant4-DNA uses the ionisation cross section data of Emfietzoglou et al. [48, 94] which are similar to the BEB model data (see section 3.2.1.1). As expected, the results obtained using SigIon1 are in good agreement with the Geant4-DNA data (shown in [Pub1] and [Pub5]).

The mean excitation cluster size is sensitive to the different models for ionisation, since the excitation cross section significantly changes with electron energy. Figures 3.12 and 3.13 (middle) show the mean excitation cluster size and respective probability distributions for the different parameterisations (considering only electronic excitations and, for water vapour, neutral dissociative states). The results for electronic excitations are about a factor of two larger for water vapour than for liquid water, due to the larger cross section. Hence, the formation of large excitation cluster sizes has a higher probability in water vapour. Neutral dissociative processes further increase the excitation cluster size in the vapour phase.

The comparison of excitation cluster sizes obtained by the different parameter sets of ionisation cross sections shows that SigIon2 and SigIon3 produce larger excitation cluster sizes than SigIon1. In the energy range below 100 eV, this is due to the larger ratio of total ionisation to excitation cross sections (the latter are the same in all results shown). The maximum is reached at 150 eV and coincides with the maximum of the mean ionisation cluster size. This coincidence arises from the constant ratio between ionisation and excitation cross sections as function of electron energy above 100 eV.

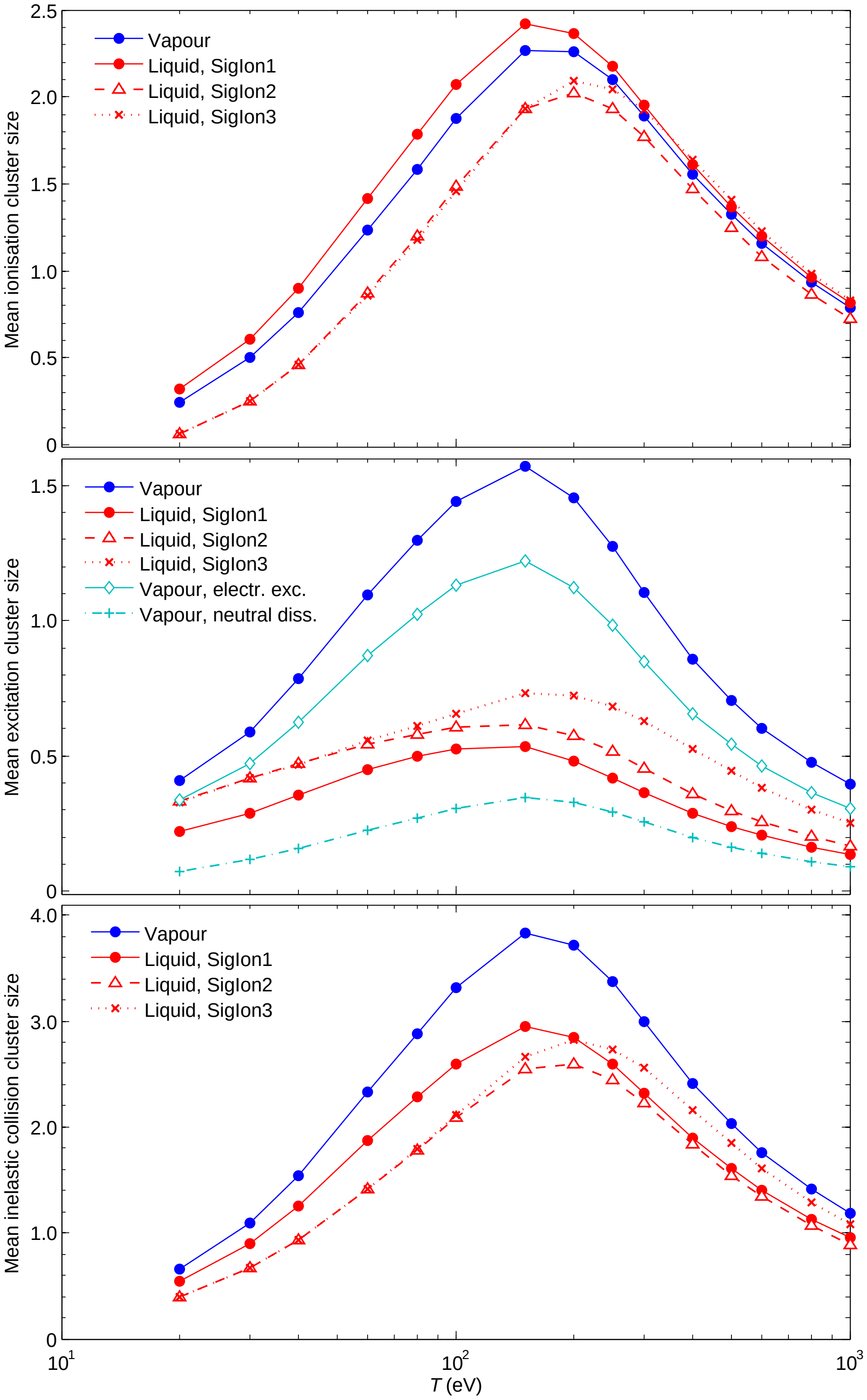

Figure 3.12: Influence of different cross section data on the mean cluster size M_1 for ionisation, excitation and all inelastic collisions in gaseous and liquid water.

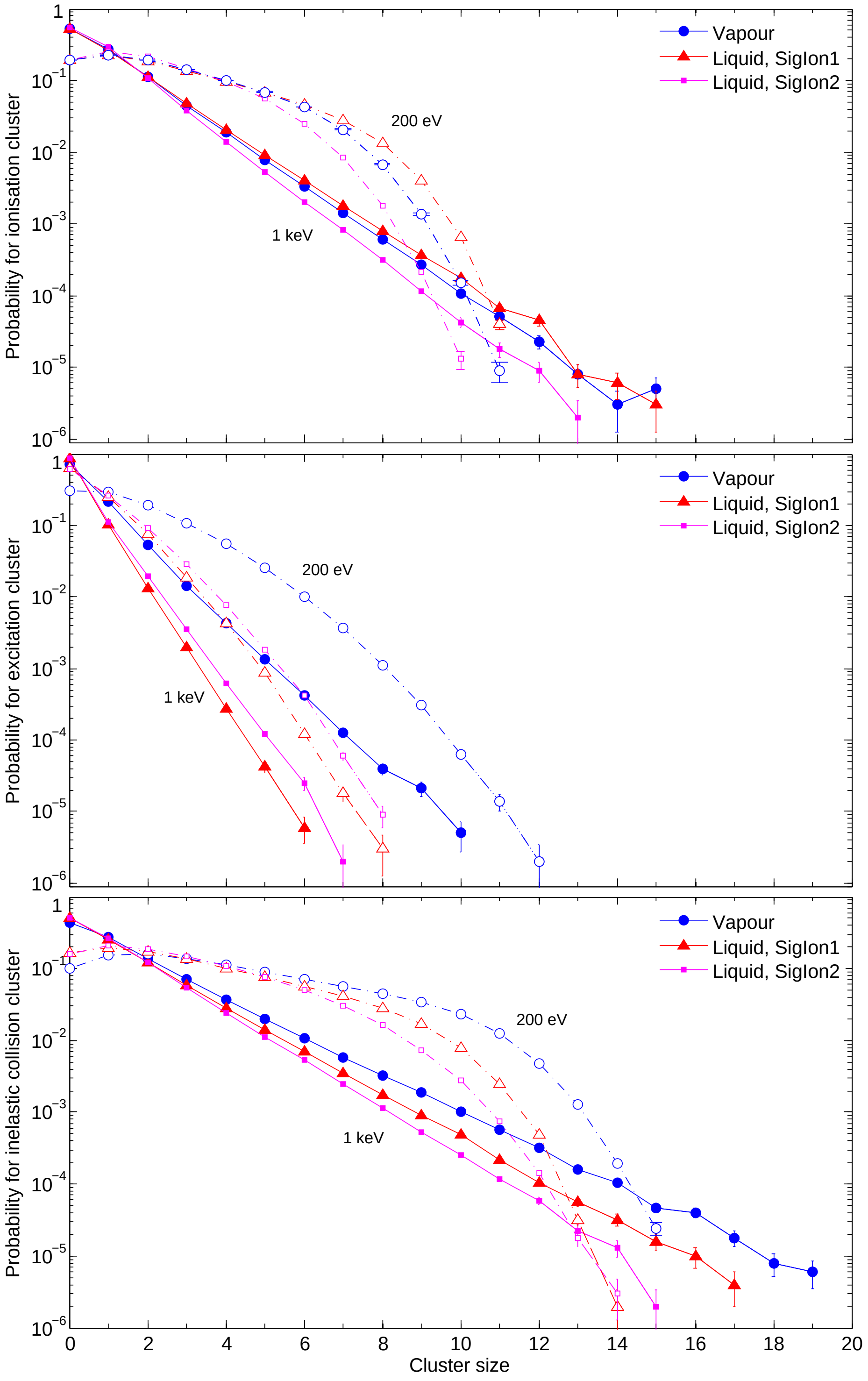

Figure 3.13: Influence of different cross section data on the probability distributions of cluster sizes for ionisation, excitation and all inelastic collisions in gaseous and liquid water for 200 eV (broken lines) and 1 keV (solid lines) electrons.

At energies above 100 eV, results from SigIon2 approach those of SigIon1, as more secondary electrons of energy above 100 eV are produced, for which the ionisation cross sections are similar. On the other hand, the excitation cluster sizes of SigIon3 are nearly a factor of two larger in this energy range. This can only be due to the different parameterisations of the SDCS where less electrons of low energy are produced in the liquid phase.

The lower parts of figures 3.12 and 3.13 are concerned with the cluster sizes produced by all inelastic collisions, i.e. scoring clusters from ionisations and excitations. Due to the much higher excitation cross section in water vapour, the probability to produce large clusters of inelastic collisions is highest, leading to the largest mean values. The mean values calculated with the set of ionisation cross sections SigIon1 (yielding the highest mean ionisation cluster sizes), are 14–24% lower, showing the largest deviations in the region of the maximum. From figure 3.13 this reduction in the region about 200 eV can be attributed to the strong decrease of large cluster sizes for inelastic collisions, which are due to the lower probability to produce cluster of excitation events. The mean inelastic collision cluster size from SigIon2 is 20–23% lower than from SigIon1 due to the reduction of ionisation cluster sizes.

The most important findings of this study on ionisation and excitation cluster sizes calculated using different interaction cross section data of vapour and liquid water are the following.

- The greatest deviations are observed between calculations using SigIon1 and SigIon3.
- Ionisation cluster size distributions and mean values calculated by Geant4-DNA and the revised versions of PTra are in excellent agreement for the electron energy range 20–1000 eV when using the same ionisation cross section data.
- The two findings above support that the differences in ionisation cluster size distributions discussed by Lazarakis et al. [Pub5], provide an estimate of the sensitivity of such quantities on different cross section models.
- Excitation cluster size distributions are influenced by ionisation cross sections, where also the SDCS are found to have a significant impact.

Unfortunately, experimental data are not available to compare the simulated ionisation and excitation cluster sizes. However, an experiment has been developed [180] to benchmark secondary electron transport in track structure simulations. This benchmark is discussed in the following section.

3.4 Benchmark: Secondary electron emission from amorphous solid water

In the following publication, the secondary electron transport in the previous version of PTra and in Geant4-DNA were successfully benchmarked by simulating an experiment, which had been specifically designed for this purpose by Toburen et al. [180]. The simulations, described in section 3.4.1, were repeated with the new versions of PTra, using the different combinations of ionisation cross section data of liquid water. Results obtained from those simulations are presented in section 3.4.2.

3.4.1 Benchmarking PTra and Geant4 track structure Monte Carlo simulations

Abstract. Track structure Monte Carlo simulations of ionising radiation in water are often used to estimate radiation damage to DNA. For this purpose, an accurate simulation of the transport of densely ionising low-energy secondary electrons is particularly important, but is impaired by a high uncertainty of the required physical interaction cross section data of liquid water. A possible tool for the verification of the secondary electron transport in a track structure simulation has been suggested by Toburen et al. (2010), who have measured the angle-dependent energy spectra of electrons, emitted from a thin layer of amorphous solid water (ASW) upon a passage of 6 MeV protons. In this work, simulations were performed for the setup of their experiment, using the PTB Track structure code (PTra) and Geant4-DNA. To enable electron transport below the ionisation threshold, additional excitation and dissociative attachment anion states were included in PTra and activated in Geant4. Additionally, a surface potential was considered in both simulations, such that the escape probability for an electron is dependent on its energy and impact angle at the ASW/vacuum interface. For vanishing surface potential, the simulated spectra are in good agreement with the measured spectra for energies above 50 eV. Below, the simulations overestimate the yield of electrons by a factor up to 4 (PTra) or 7 (Geant4-DNA), which is still a better agreement than obtained in previous simulations of this experimental situation. The agreement of the simulations with experimental data was significantly improved by using a step-like increase of the potential energy at the ASW surface.

This work was initiated and performed by myself in consultation with Larry Toburen. In the following, the article is presented, which is reprinted from

M. U. Bug, H. Rabus, A. B. Rosenfeld, Electron emission from amorphous solid water after proton impact: Benchmarking PTra and Geant4 track structure Monte Carlo simulations, Vol. 81, Pages No. 1804-1812, Copyright (2012), with permission from Elsevier ([Pub6]).

Bug, M. U., Rabus, H. & Rozenfeld, A. (2012). Electron emission from amorphous solid water after proton impact: Benchmarking PTra and Geant4 track structure Monte Carlo simulations. Radiation Physics and Chemistry, 81 (12), 1804-1812.

3.4.2 Benchmarking the new version of PTra

The simulations described in the above publication were repeated, using the cross section data listed in tables 3.1 and 3.2 for electrons and protons, respectively. For liquid water, the different electron-impact ionisation cross sections are compared (as in section 3.3). Figure 3.14a shows the electron emission spectra obtained after integration over the emission angles for water vapour and liquid water. For electron energies above 6 eV, the spectra calculated in water vapour are very similar to those in liquid water, using the BEB model [93] (SigIon1) for the ionisation cross sections of electrons. Below this energy, the number of emitted electrons is up to 50% lower in the vapour phase. The structures in electron emission spectra below 8 eV are due to dissociative electron attachment processes. Both emission spectra are in good agreement with experimental data at energies above 20 eV. Compared to the spectra obtained using the BEB model, those calculated using the Dingfelder model [39] for the total ionisation cross section for electrons (and either model for the SDCS; SigIon2 or SigIon3) lead to higher yields of electrons with energies between 10–100 eV. This is due to the lower ionisation cross section for electron energies below 100 eV. The spectrum obtained using the Dingfelder model is similar to the published data, as the same electron-impact ionisation cross section was applied, and only slightly more increasing towards lower energies due to the different SDCS model for proton impact.

More realistic simulations considered a surface potential, which was applied as described in section 3.4.1. The best agreement with the experimental data was obtained when using a surface potential of 3 eV (figure 3.14b). In this case, the spectra obtained when using the cross section set SigIon1 are in excellent agreement with the measured data, except in the energy region 5–10 eV. As stated before, this deviation might be due to the neglected autoionisation in the simulations. The electron emission spectra calculated using SigIon2 are 35% larger than the experimental data in the energy region 5–100 eV. This agreement is worse than obtained with the previous version of PTra (SigIon3), suggesting that the combination of total and differential ionisation cross sections for protons and electrons plays an important role.

A comparison of measured and simulated angular-dependent electron emission spectra is shown in figure 3.15. The calculations were performed using SigIon1 and a surface potential of 3 eV. At most angles, good agreement of both data within the indicated statistical uncertainties of the simulation results is observed. Exceptions are 45° and 60°, where the simulated electron yield is significantly lower. Particularly at backward angles, the measured electron spectra are better reproduced at high electron energies than previously published.

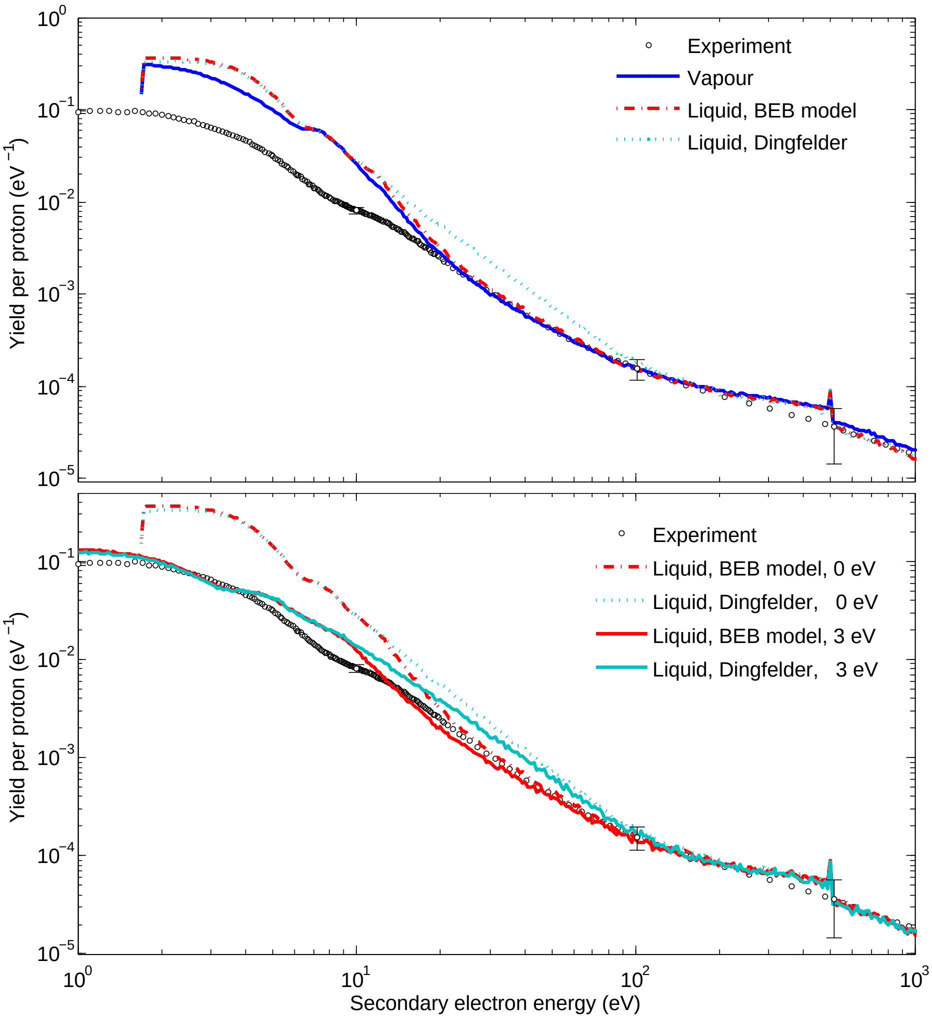

Figure 3.14: Single differential yield of secondary electrons as a function of their energy. (Top) Simulations in water vapour and liquid water with different sets of ionisation cross section data. (Bottom) Simulations in liquid water using a surface potential of 3 eV.

To summarise the findings, the agreement is inferior to our published work when Dingfelder's model is used for both electron and proton cross sections and independent of the SDCS for electron impact. The results from the latter simulations can be improved when using the HKS model for the SDCS of proton impact, which was the case in the previous PTra code presented in the publication. However,the combination of electron cross sections using the ionisation cross sections obtained by the BEB model for electrons and Dingfelder's model for proton impact leads to excellent agreement with the experimental data.

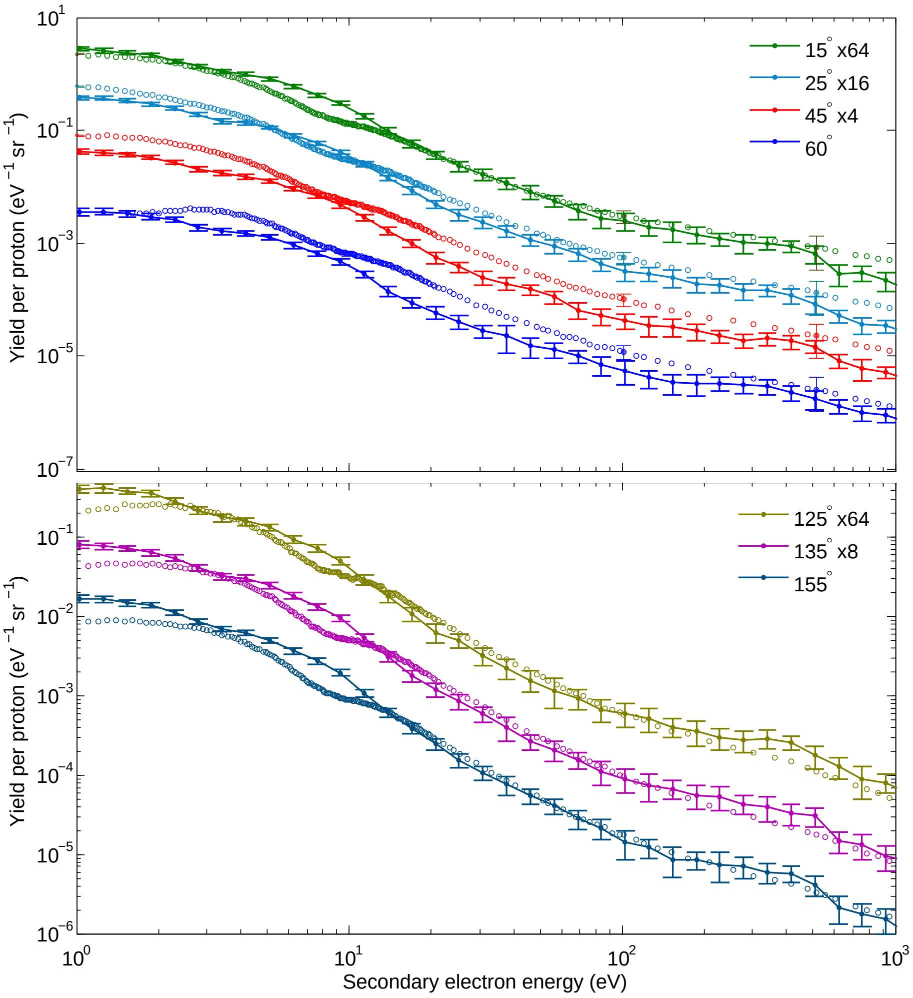

Figure 3.15: Secondary electron spectra obtained from the experiment and simulations for selected forward (top) and backward (bottom) scattering angles.

After publishing the results (section 3.4.1), we became aware of the work of Elles et al. [47]. The authors discuss the surface potential of liquid water relative to the vacuum, which is given in the literature with values of either −1.2 eV or between −0.12 and 0.0 eV. These values are much higher than the −3 eV which had to be applied in this work to obtain the optimum agreement of simulated and measured [180] electron emission spectra. An increase of the absolute value for the surface potential may be attributed to the absence of solvent stabilisation due to the lack of molecular mobility in amorphous ice or to a charging effect arising from ionised molecules. The charging effect should increase with increasing radiation time until a charge flow equilibrium is achieved and may be worthwhile to investigate experimentally. On the other hand, more accurate cross section data for electrons and protons for liquid water are invaluable to improve the accuracy of track structure simulations.

3.5 Nanoscale characterisation of ion tracks: MC simulations versus analytical approach

Abstract. The goal of this work was to investigate the agreement of physical parameters related to the particle track structure on the nanometer scale, obtained by means of a detailed track structure simulation (PTra) as well as by a rapid analytical approach. Parameters describing the tracks of secondary electrons produced by 0.3 MeV/u C^{6+}-ions were of particular interest as those particles are densely ionizing. For this purpose, the target volume in form of a nanometric water cylinder was positioned at different radial distances from the ion trajectory and track structure parameters were determined as function of the radial distance. While the fluence of electrons through the target surface and the mean ionisation cluster size obtained by both approaches were in good agreement, the probabilities of specific cluster sizes (one, two and three) turned out to be rather different in the two approaches.

The publication was prepared in collaboration with the developers of the analytical model. My contribution consisted of the simulations and the discussion of the results. The article M. U. Bug, E. Surdutovich, H. Rabus, A. B. Rosenfeld, A. V. Solov'yov. *Eur. Phys. J. D* **66**: 291 1-6 (2012) [Pub7] is reprinted with kind permission of The European Physical Journal (EPJ).

Bug, M. U., Surdutovich, E., Rabus, H., Rozenfeld, A. & Solov''Yov, A. V. (2012). Nanoscale characterization of ion tracks: MC simulations versus analytical approach. The European Physical Journal D, 66 (11), 291-296.

3.6 Conclusions

Literature data on interaction cross section data for electrons and protons with water vapour and liquid water were reviewed with particular interest in the most frequently used cross section models used in simulation codes. Significant discrepancies in cross section data determined by different authors are present and may be used to estimate the uncertainties of those data. The most important findings are summarised. For electron-impact on water vapour, deviations in experimental data for the ionisation cross section amount to 15% in the region of the maximum and deviate as much as a factor of two for lower electron energies. All model functions are well within those values. Calculated total ionisation cross sections for electron-impact on liquid water agree well among each other at energies above 200 eV but deviate by a factor of two for energies below. The data obtained from the model yielding the larger ionisation cross section values for liquid water are similar to those of the vapour phase. Excitation cross sections, on the other hand, are as much as a factor of five larger for the vapour phase than for the liquid. Different model data agree within 50%. Models for proton-impact interaction cross section data are generally in good agreement with experimental data. Regarding differential cross section data, forward scattering is suppressed in the liquid phase, leading to a reduction in the SDCS for low-energy secondary electrons.

Interaction cross section sets were selected for both the vapour and liquid phase and implemented in the code PTra (see tables 3.1 and 3.2) to substitute the previous version. Due to the large discrepancies in ionisation cross section data for electrons in liquid water, three different options were implemented in PTra to investigate the sensitivity of simulated parameters on ionisation cross section data.

Calculated W-values for electrons and protons are in excellent agreement with experimental data for water vapour and for liquid water. For the latter, the application of the total and differential ionisation cross section models (BEB models), producing similar values to those of water vapour, leads to better agreement with the experimental W-value than the other two options. Calculated G-values for electrons of 10 keV energy agree well with literature data, particularly when the BEB models are used for liquid water. Nanodosimetric cluster size distributions for ionisation and excitation (counting electronic and neutral dissociative interactions) were calculated for electron-impact on cylindrical volumes in size of one convolution of the DNA. Significant deviations are again observed for the use of the different ionisation cross sections. Those deviations provide an estimate of the sensitivity of nanodosimetric quantities of the different cross section models as was already pointed out in our published work [Pub5].

The secondary electron transport in liquid water with the codes PTra and Geant4-DNA was benchmarked by simulating an experiment, which has been specifically developed for this purpose [180]. This work was published for the previous version of PTra [Pub6]. The simulation of this experiment was repeated with the present version of PTra, where the best agreement was obtained when the using the combination of the BEB models and those of Dingfelder for electron and proton ionisation cross sections, respectively. An important finding of this work is that the combination of cross section data is crucial, as the previous version of PTra used a very different set of proton and electron cross section data but also led to excellent agreement with the experimental electron emission spectrum. Such a good agreement could not be obtained by the other combinations of cross section models in this work.

The code PTra was then used to investigate the feasibility of an analytical model [166] to calculate track structure parameters. Such a model would be advantageous for use in applied dosimetry as it provides a fast and efficient calculation of the desired parameters. This study was published in [Pub7]. In its current status, the analytical model reproduces the fluence of secondary electrons through the surface of the nanometric target volume in the vicinity of a carbon ion trajectory as well as the mean ionisation cluster size. However, improvement is necessary to calculate more complex quantities such as ionisation cluster size distributions, for which the energy spectrum of electrons is important to consider. On the other hand, simulations of carbon ions in water were performed with crude approximations of charge-transfer interactions. Hence, PTra will also be augmented, for example by the comprehensive set of carbon ion cross section data developed by Liamsuwan et al. [125].

Chapter 4

Interaction cross sections of DNA molecules for electrons

4.1 Introduction

The aim of this part of the work was to obtain analytic parameterisations for a consistent set of electron-impact cross section data of DNA constituents that could be conveniently implemented in simulation codes. Of interest were the cross section data for the interaction of electrons with energies above the ionisation threshold with the DNA constituents tetrahydrofuran (THF), trimethylphosphate (TMP), pyrimidine (PY) and purine (PU). Those data were based on the experimental work of Woon Yong Baek at the PTB [Pub8, Pub9]. In those measurements, the total scattering cross sections (TCS) as well as the differential elastic (DelCS) and double-differential inelastic scattering cross sections (DDCS) were determined on an absolute scale in two different experimental setups. The measurements were not part of this work and will, therefore, only be briefly introduced in sections 4.3.1 and 4.4.1.1.

In this chapter, each type of interaction cross section is comprehensively described, which involves data fitting, extrapolation and integration procedures. The consistency of the data was carefully investigated. The following section provides an overview of the the uncertainty analysis applied in this work, which is aligned with the Guide to the Expression of Uncertainty in Measurement (GUM) [24].

4.2 Data analysis techniques

4.2.1 Fitting procedure

Least-squares fitting was applied to retrieve the optimum parameters ($\vec{a}$) for a model function to the observation values. This goal is generally achieved by minimizing the weighted sum of squares of the residuals

$$\sum_{i=1}^{N} w_i r_i^2 = \sum_{i=1}^{N} w_i \left(y_i - f(x_i;\vec{a})\right)^2 = \min, \tag{4.1}$$

where the function $f(x_i;\vec{a})$ is the model function to be fitted to the data y_i for a total number of N observations, x_i and w_i are the weighting factors assigned to the observations. The weighting factors are proportional to the reciprocal of the squared data uncertainties $1/u_i^2$. For numerical stability, the factors w_i were reduced by their mean value. Hence for the i-th observation, the weighting factors are

$$w_i = \frac{1}{u^2(y_i)} \Bigg/ \left(\frac{1}{N} \sum_{j=1}^{N} \frac{1}{u^2(y_j)} \right) \quad \equiv \quad \frac{\bar{u}^2(\vec{y})}{u^2(y_i)} \ . \tag{4.2}$$

For linear dependence of the model function on the n-element parameter vector $\vec{a}$, which is the case for polynomial functions, $f(x_i;\vec{a})$ can be expressed by

$$\sum_{j=1}^{n} \frac{\partial f(x_i;\vec{a})}{\partial a_j} a_j. \tag{4.3}$$

Using this expression, equation 4.1 can be rewritten as

$$\sum_{i=1}^{N} w_i \left(y_i - \sum_{j=1}^{n} G_{ij} a_j \right)^2 = \min, \tag{4.4}$$

where the G-matrix is a Jacobian matrix with respect to the parameters $\vec{a}$

$$G_{ij} = \frac{\partial f(x_i;\vec{a})}{\partial a_j}. \tag{4.5}$$

For linear model functions, the minimum of the squared residuals is obtained when the gradient of equation 4.4 is zero. Partial derivation after a_j leads to the Euler-Lagrange equations ($j = 1..n$)

$$\sum_{i=1}^{N} w_i G_{ij} y_i = \sum_{i=1}^{N} \sum_{l=1}^{n} w_i G_{ij} G_{il} a_l \tag{4.6}$$

which can be rewritten as

$$G^T W\vec{y} = G^T WG\vec{a}. \tag{4.7}$$

The diagonal matrix W contains the weighing factors w_i on its main diagonal, such that

$$W_{ij} = \delta_{ij} w_i. \tag{4.8}$$

$G^T WG$ is a symmetrical matrix containing the following elements in the case of polynomial functions

$$(G^T WG)_{kk'} = \sum_{i=1}^{N} w_i x_i^{k+k'} \tag{4.9}$$

with $k, k' = 0..n$ where n is the polynomial degree. Consequently, the linear least-squares fitting procedure leads to the following system of linear equations for the parameters $\vec{a}$

$$\vec{a} = \left(G^T WG\right)^{-1} G^T W\vec{y}. \tag{4.10}$$

For non-linear dependence of the model function on parameters $\vec{a}$, iterative techniques have to be used. In the k-th iteration step, the optimisation problem can be linearised by the Taylor series expansion of the function

$$f(x_i;\vec{a}) \approx f^{(k)}(x_i;\vec{a}) + \sum_{j=1}^{n} \frac{\partial f^{(k)}(x_i;\vec{a})}{\partial a_j}(a_j - a_j^{(k)}). \tag{4.11}$$

Applying again a weighted fitting procedure, equation 4.1 becomes

$$\sum_{i=1}^{N} w_i \left(r_i^{(k)} - \sum_{j=1}^{n} G_{ij} \Delta a_j^{(k)} \right)^2 = \min. \tag{4.12}$$

In non-linear least-squares fitting, the minimum of the squared residuals is also obtained when the gradient of equation 4.12 is zero, which finally leads to the following system of equations:

$$\Delta\vec{a}^{(k)} = \left(G^T WG\right)^{-1} G^T W\vec{r}^{(k)}. \tag{4.13}$$

The iteration process is aborted when the variation of the values calculated by the non-linear and the linearised model function falls below a specified threshold. In a (k+1)-th iteration step, parameters $\vec{a} = \vec{a}^{(k)} + \Delta\vec{a}^{(k)}$ finally enter in the model function.

4.2.2 Covariance matrix of the parameters

To calculate the uncertainty of the fit, the covariance matrix of the parameters $\vec{a}$ in the model function has to be taken into account. A covariance matrix C generally describes the correlation between the elements of a random vector $\vec{A}$ and contains the variances of each element on the main diagonal. The covariance for the random variables A_i and A_j in vector $\vec{A}$ is given by

$$C(A_i, A_j) = \langle \left(A_i - \bar{A}_i\right) \left(A_j - \bar{A}_j\right) \rangle. \tag{4.14}$$

When $\vec{A}$ represents the vector of random variables $U(\vec{a})$ which provides the distribution of possible values of the model function parameters $\vec{a}$, the covariance matrix is given by the tensor product

$$C(\vec{a}) = \langle U(\vec{a}) \otimes U(\vec{a})^T \rangle. \tag{4.15}$$

To evaluate the correlation between the parameters, the elements of the covariance matrix may be normalised to the product of the standard deviations of both parameters via

$$C'_{ij} = \frac{C_{ij}}{\sqrt{C_{ii}}\sqrt{C_{jj}}} \tag{4.16}$$

The quantity C'_{ij} describes the relation between two statistical variables and can have any value between -1 and 1. A factor of 1 or -1 shows a strong positive or negative correlation, respectively, a factor of 0 means that the variables are uncorrelated.

The uncertainties of parameters $\vec{a}$ have two contributions, namely, the uncertainties of the data points $u(\vec{y})$ and those related to the imperfect description of the observations by the model function. *The contribution of the data point uncertainties* can be evaluated by applying uncertainty propagation according to the GUM [24]. Using equation 4.10, this contribution is given by

$$U_{\text{data}}(\vec{a}) = \left(G^T W G\right)^{-1} G^T W u(\vec{y}). \tag{4.17}$$

Equation 4.17 applies to linear as well as non-linear dependence of the model function on parameters $\vec{a}$ because $u(\vec{r}) = u(\vec{y})$ and hence $U_{\text{data}}(\Delta\vec{a}) = U_{\text{data}}(\vec{a})$.

Using equation 4.17 and equation 4.15, the covariance matrix of the parameter uncertainties is

$$C_{\text{data}}(\vec{a}) = \langle (G^T W G)^{-1} G^T W u(\vec{y}) \otimes \left[(G^T W G)^{-1} G^T W u(\vec{y})\right]^T \rangle. \tag{4.18}$$

As $\left[(G^TWG)^{-1}\right]^T = \left[(G^TWG)^T\right]^{-1}$ and (G^TWG) is a symmetrical matrix where $(G^TWG)^T = (G^TWG)$, it follows that

$$C_{\text{data}}(\vec{a}) = \langle (G^TWG)^{-1}G^TWu(\vec{y}) \otimes u(\vec{y})^TW^TG(G^TWG)^{-1}\rangle \tag{4.19}$$

As W is a diagonal matrix, $W^T = W$ and

$$C_{\text{data}}(\vec{a}) = (G^TWG)^{-1}G^TW\langle u(\vec{y}) \otimes u(\vec{y})^T\rangle WG(G^TWG)^{-1}\ . \tag{4.20}$$

If the uncertainties $u(\vec{y})$ of the observations are correlated, the covariance matrix $\langle u(\vec{y}) \otimes u(\vec{y})^T\rangle$ in equation 4.20 has to be taken into account. This is, for example, the case for the experimental data as systematic contributions to the uncertainties for different data point have the same origin. Using equations 4.2 and 4.16, it is

$$\langle u(\vec{y}) \otimes u(\vec{y})^T\rangle = W^{-1/2}\ C'(u(\vec{y}))\ W^{-1/2}\ \bar{u}^2(\vec{y}). \tag{4.21}$$

In the data analysis, complete correlation is assumed by choosing the correlation matrix $C'(u(\vec{y}))$ as a square matrix of ones. The mean squared uncertainty value $\bar{u}^2(\vec{y})$ was defined in equation 4.2.

The uncertainties arising from an imperfect description of the observations by the model function were evaluated by the reduced chi-square value, which is given by

$$\chi^2_{\text{red}} = \sum_{i=1}^{N}\left(w_i\,(y_i - f(x_i;\vec{a}))^2\right)\cdot\frac{1}{N-n} \tag{4.22}$$

The division by N - n takes into account the degrees of freedom. If the deviations of the data points from the model curve were caused by statistics, χ^2_{red} would be a random variable with a χ^2 probability distribution and an expectation value of $\bar{u}^2(\vec{y})$, due to the normalisation of the weighting factors in equation 4.2. Hence, equation 4.21 was applied, substituting $\bar{u}^2(\vec{y})$ by χ^2_{red}. These uncertainties are uncorrelated so that $C'(u_{model}(\vec{y}))$ is the identity matrix. Tying in with equation 4.20, the contribution of the uncertainties of the model function is described by the covariance matrix $C_{\text{model}}(\vec{a})$

$$\begin{aligned} C_{\text{model}}(\vec{a}) &= (G^TWG)^{-1}G^TW^{1/2}W^{1/2}G(G^TWG)^{-1}\chi^2_{\text{red}} && \text{(4.23a)}\\ &= (G^TWG)^{-1}\chi^2_{\text{red}}\ . && \text{(4.23b)}\end{aligned}$$

The covariance matrix $C(\vec{a})$ of the parameters used in the model function is the sum of equations 4.20 and 4.23b, such that

$$C(\vec{a}) = (G^T W G)^{-1} G^T W \ \langle u(\vec{y}) \otimes u(\vec{y})^T \ \rangle W G (G^T W G)^{-1} + (G^T W G)^{-1} \chi^2_{\text{red}} \ . \quad (4.24)$$

In this way, the contributions of both uncertainties, those of the data points and those of the description of the data points by the model function, are taken into account and uncertainty propagation is fulfilled. In the following, this matrix $C(\vec{a})$ is used to determine the covariance matrix $C(\vec{y}_{\text{fit}})$ of the data calculated by the model function.

4.2.3 Uncertainty of the model function values

The covariance matrix of the data obtained by the model function is given by

$$C_{\text{data}}(\vec{y}_{\text{fit}}) = G \ C_{\text{data}}(\vec{a}) \ G^T, \quad (4.25a)$$

$$C_{\text{model}}(\vec{y}_{\text{fit}}) = G \ C_{\text{model}}(\vec{a}) \ G^T, \quad (4.25b)$$

$$C(\vec{y}_{\text{fit}}) = C_{\text{data}}(\vec{y}_{\text{fit}}) + C_{\text{model}}(\vec{y}_{\text{fit}}). \quad (4.25c)$$

The main diagonal contains the variances of each data point, such that the uncertainties $u(\vec{y}_{\text{fit}})$ are given by

$$u(\vec{y}_{\text{fit}})_i = \sqrt{C(\vec{y}_{\text{fit}})_{i,i}}. \quad (4.26)$$

The determination of the uncertainties related to the model function values by equation 4.26 was applied throughout the data analysis in the following sections.

4.3 Total scattering cross sections

4.3.1 Experimental data of THF and PY

The total scattering cross section (TCS) σ_t for THF and PY were measured by colleagues at the PTB for electrons with impact energies ranging from 5 eV to 1 keV [Pub8, Pub9]. The measurement was performed in a linear transmission experiment in which the reduction of the initial electron count rate was determined after the beam traversed a specified volume of the target gas.

In brief, a beam of monoenergetic electrons is directed towards a target containing the scatterers in the gas phase. The number of molecules in the interaction region is adjusted by the gas pressure such that single scattering conditions are fulfilled. Unscattered electrons leave the gas volume through an aperture and are discriminated in an hemispherical energy analyser against those, which were inelastically scattered in forward direction. The count rate resulting from unscattered electrons is determined by means of a channel electron multiplier that has finite angular and energy resolutions (solid angle of $7{\cdot}10^{-3}$ sr; FWHM of relative energy resolution is 0.25%).

Due to these finite resolutions, a discrimination of scattered electrons which interacted via rotational excitations is not feasible because they lose energy in the order of a few meV and are preferentially scattered in the forward direction [Pub9]. Therefore, such electrons contribute to the measured count rate in the detector. Rotational excitations are, however, dominant for the interaction of electrons of energies below about 20 eV with molecules possessing a large dipole moment. For such molecules, the total scattering cross section would be underestimated in the experiment. This is the case for both THF and PY, but the dipole moment of PY is larger (see section 2.1.2). This issue was comprehensively discussed by Baek et al. [Pub9], where the contribution of the cross section for rotational excitation to the total scattering cross section of PY was calculated from theory.

4.3.1.1 Comparison to literature data

a) Tetrahydrofuran.

Several electron scattering cross section data of THF can be found in the literature. TCS were measured using also the linear transmission technique by Fuss et al. [62] (50–5 keV), Możejko et al. [138] (1–370 eV) and Zecca et al. [201] (2–21 eV). Allan [2] determined the TCS at 6 eV and 10 eV, based on measured elastic and vibrational excitation cross sections as function of electron energy (0.1–20 eV) and scattering angle (15–180°). The measured THF data from the PTB [Pub8] agree within combined experimental uncertainties with those of Allan, Fuss et al. and Możejko et al. but do not show the shoulder around 30–50 eV, present in the data of Możejko et al. Only the deviation of the data point of Fuss et al. at 50 eV from those of the PTB by 19% exceeds the experimental uncertainties. The values of Zecca et al. [201] are qualitatively similar but systematically lower due to a an inferior angular resolution (as already stated by Fuss et al. [62] and Do et al. [42]).

TCS of the deoxyribose analogue α-tetrahydrofurfuryl alcohol ($C_5H_{10}O_2$) have also been measured [137]. As stated in section 2.1.2, this molecule in combination with phosphoric acid may be an alternative model for the sugar-phosphate group in the DNA. Due to its larger size, the TCS of α-tetrahydrofurfuryl alcohol is about 30% larger compared to the TCS of THF but shows a similar energy dependence. More details on the comparison of both molecules are given by Możejko et al. [137].

b) Pyrimidine.

The total scattering cross sections of PY, measured at the PTB [Pub9], are the only experimental data we are aware of. They were published together with calculations of Baek et al., using the SCOP model for molecules. The theoretical data, obtained without considering rotational excitations, agree well with the experimental TCS with deviations of less than 15% for energies down to 20 eV. Zecca et al. [199] also calculated TCS of PY using the IAM-SCAR method. The theoretical data of Baek et al. deviate by up to 40% from those of Zecca et al. being generally higher. The data of Zecca et al., obtained without accounting for rotational excitations, are within the experimental uncertainties for energies above 200 eV. For energies below 200 eV, the experimental data are significantly larger (up to 50% at 30 eV). Theoretical data of both authors, including rotational excitations provide evidence that this process becomes increasingly important when the electron energy decreases below 1 keV.

4.3.2 Model functions

In this work, the total scattering cross sections for electrons of energy T (in eV) were interpolated by the superposition of Gaussian functions (figure 4.1)

$$\sigma_{\mathrm{t}} = \sum_{i=1}^{i_{\max}} a_i e^{-\left(\frac{x-b_i}{c_i}\right)^2} \tag{4.27}$$

with $x = \log_{10} T$ and using the parameters specified in table 4.1. For THF and PY [Pub8, Pub9], the model function was fitted to the experimental data. The respective uncertainties were calculated as described in section 4.2.3, using equation 4.24 together with equation 4.21 to determine the covariance matrix of the function parameters. The parameterisations of the model functions for PU and TMP are described in section 4.3.3.

Table 4.1: Parameters used in equation 4.27 to fit the total scattering cross sections of THF, PY, PU and TMP.

	a_1(Å^2)	b_1	c_1	a_2(Å^2)	b_2	c_2	a_3(Å^2)	b_3	c_3
THF	9.206	0.856	0.184	49.04	0.911	1.517			
PY	9.854	1.008	0.204	40.45	1.164	1.406	38.890	–0.0378	1.023
PU	10.33	0.980	0.130	68.42	1.012	1.446			
TMP	2.894	0.750	0.105	85.45	0.790	1.575	8.767	1.626	0.575

The first consistency requirement for total cross sections is that the sum of total cross section data for ionisation, elastic scattering and excitation equals the TCS. To fulfil this requirement, the model function for the TCS of PY (figure 4.1) was not an optimum fit to the experimental data, rather, the experimental data were substituted in the energy region 25–800 eV by the theoretical data, calculated by the spherical complex optical potential model (SCOP) method [Pub9] (see figure 4.1). In the stated energy region, the SCOP data without the contribution of rotational excitations are up to 8% larger than the experimental data, which results in more consistent values of the excitation cross section.

A second consistency requirement arises from the similarity of physical properties of THF and PY and therefore the TCS of both molecules should be similar for electrons of intermediate and high energies. In fact, the SCOP data for PY agree with the experimental TCS of THF in the energy range above 25 eV. At lower energies, the underestimation of the experimental TCS of PY with respect to THF is likely due to the finite energy and angular resolutions of the linear transmission device. As discussed previously, this leads to an underestimation of the TCS when the dipole

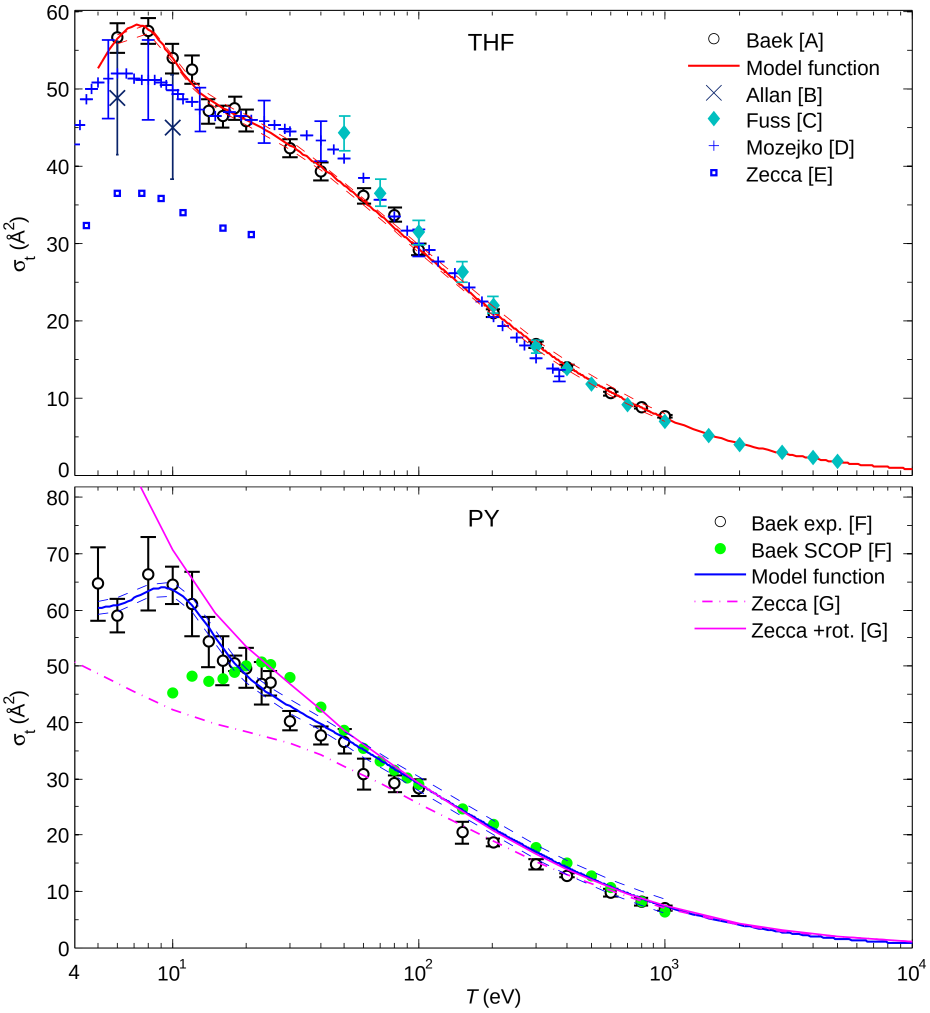

Figure 4.1: Measured and interpolation models for total scattering cross sections σ_t of THF and PY as a function of electron energy T, including experimental data of several groups (A [Pub8], B [2], C [62], D [140], E [201], F [Pub9], G [199]). Thin lines indicate the uncertainties of the model functions.

moment is large. Due to the larger dipole moment of PY, this underestimation is more significant than for THF. The justification for using the theoretical SCOP data without the contribution of rotational excitations for PY, instead of the data accounting for those processes, is that there are significantly different predictions of the magnitude of rotational excitation cross sections when theoretical data of different authors are compared [Pub9]. Additionally, no experimental data exist to support the theoretical calculations. Therefore, the TCS of both THF and PY obtained in this work neglect rotational excitations in consistency with the finite angular and energy resolution in the experiments and insufficient knowledge of the contribution of rotational excitations.

4.3.3 TCS of PU and TMP

TCS for the other DNA constituents of interest in this work, TMP and PU, have not yet been measured nor were they calculated by *ab-initio* theories. They can, however, be estimated by a semiempirical approach, where the TCS of a polyatomic molecule is obtained from the sum of the TCS of smaller molecular groups. The applicability of this additivity procedure has been shown for THF and PY by Baek et al. [Pub8, Pub9]. Also, Domaracka et al. [44] showed the validity of this approach for polyatomic molecules containing nitrogen or cyclic-ether molecules $(CH_2)_nO$, $n = 2$–4, for electron energies down to 8 eV or 20 eV, respectively. They state that this approach is applicable for molecules of similar dipole polarisability. In fact, Szmytkowski [173] showed by an analysis of experimental TCS of various targets a proportionality between the TCS and the dipole polarisability of the molecules.

a) Purine.

The TCS of purine $C_5H_4N_4$ were calculated from the following sum

$$\sigma_{\mathrm{C_5H_4N_4}} = \sigma_{\mathrm{C_4H_4N_2}} + \sigma_{\mathrm{N_2}} + \sigma_{\mathrm{CH_4}} - 2\ \sigma_{\mathrm{H_2}}. \tag{4.28}$$

The TCS of pyrimidine $C_4H_4N_2$ are taken from equation 4.27. Those of molecular nitrogen N_2 were taken from the review of Itikawa [104], while the data of methane CH_4 have been measured by Sueoka and Mori [171]. The TCS of hydrogen H_2 were taken from the review of Yoon et al. [196]. All data are shown in figure 4.2 as well as the model function fitted to the calculated TCS of PU with parameters given in table 4.1 (page 108). Again, the model function is not an optimum fit to the semi-empirical values for PU but slightly overestimates the TCS in the energy region 50–100 eV. However, it should be noted that the model function provides consistency with the excitation cross section, which will be discussed in section 4.6.

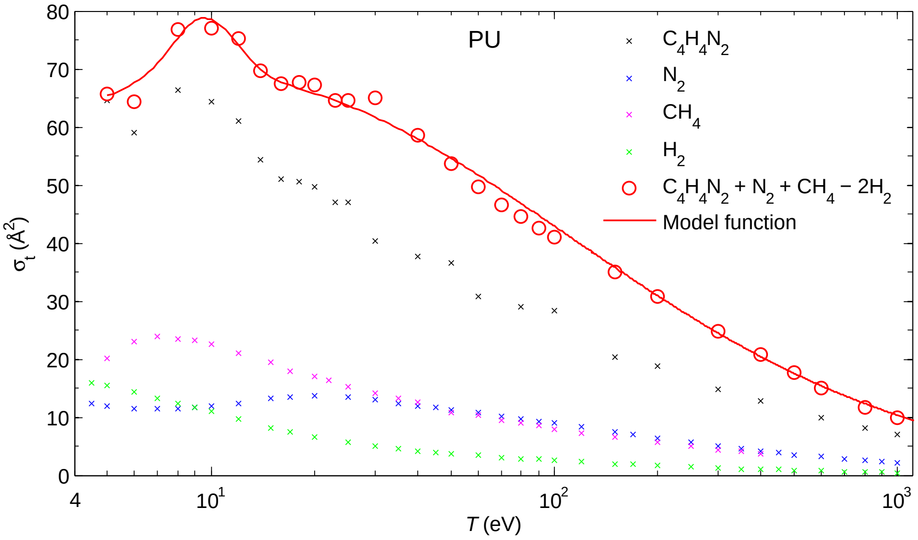

Figure 4.2: Total scattering cross sections σ_t of PU as a function of electron energy T. PU data were obtained from the model function for PY $C_4H_4N_2$ and experimental data for nitrogen N_2, methane CH_4 and hydrogen H_2.

b) Trimethylphosphate.

TCS of TMP $(CH_3)_3PO_4$ were obtained from the sum of the TCS of submolecular structures as given by

$$\sigma_{(\mathrm{CH_3})_3\mathrm{PO_4}} = \sigma_{(\mathrm{CH_3})_3\mathrm{P}} + 2\ \sigma_{\mathrm{O_2}}. \tag{4.29a}$$

$$\sigma_{(\mathrm{CH_3})_3\mathrm{PO_4}} = \sigma_{\mathrm{PH_3}} + \sigma_{\mathrm{C_3H_6}} + 2\ \sigma_{\mathrm{O_2}}. \tag{4.29b}$$

The TCS of trimethylphosphine $(CH_3)_3P$ have been measured by Domaracka et al. [43] for electrons in the energy range 0.4–400 eV using the linear transmission technique. The sum of those data and oxygen molecules [105] is shown in figure 4.3. Alternatively, the TCS of TMP can be obtained by equation 4.29b, using the experimental data of oxygen O_2 [105], propene C_3H_6 [174] and phosphine PH_3 [4, 175]. Propene consists of the same atoms as cyclopropane but the molecules have a open-chain and circular molecular structure, respectively, leading to different dipole moments and polarisabilities. The conformer with the larger dipole moment (0.366 D) and polarisability (42.2 a_0^3) [174] was selected because these values are closer to those expected for TMP (see section 2.1.2). Nonetheless, the sum of TCS calculated from equation 4.29b is up to 20% larger than from equation 4.29a in the energy region below 25 eV and shows a peak at 10 eV. This peak does not appear in the data of trimethylphosphine [43], which has nearly the same dipole moment and polarisabilities as TMP (1.2 D and 54.0–67.5 a_0^3 [43]). As also the molecular geometries of TMP and trimethylphosphine are similar, the TCS of TMP were calculated from equation 4.29a. As those data are provided only up to 400 eV, the TCS of THF were scaled by the ratio of the number of valence electrons to those of TMP at energies above 1 keV (the data of THF are in agreement with those of PY). In this way, consistency was obtained for the high-energy behaviour of the data. The model function given in equation 4.27 was fitted to those data yielding the parameters provided in table 4.1 (page 108).

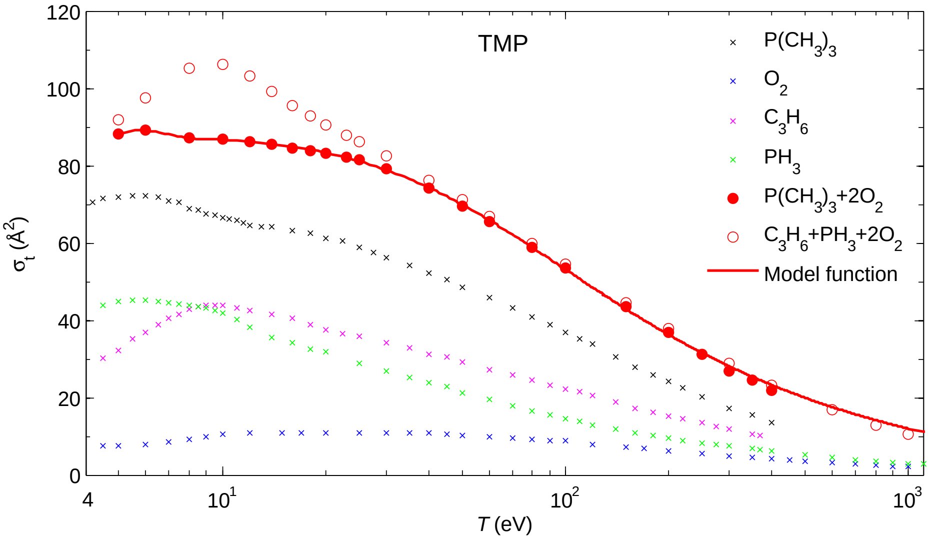

Figure 4.3: Total scattering cross sections σ_t of TMP as a function of electron energy T and experimental data for trimethylphosphine $(CH_3)P$, oxygen O_2, propene C_3H_6 and phosphine PH_3.

4.4 Ionisation cross sections

4.4.1 Double differential ionisation cross sections

4.4.1.1 Experimental data

Double differential inelastic cross sections (DDCS) were determined at the PTB using a crossed-beam arrangement. The experiment is described in detail by Baek et al. [Pub8]. In brief, a well-collimated beam of mono-energetic electrons with low beam currents between 1 pA and 1 nA is perpendicularly crossing the molecular beam. The density of the molecular beam is chosen low enough to fulfil single scattering conditions. The number of electrons ΔN of energy within a specified energy window $(E,\ E+\Delta E)$ scattered per time interval into the solid angle segment $\Delta\Omega$ is measured. The detector system was placed in angles θ relative to the direction of the incident particle (i.e. $\theta = 15, 20, 25, 35, 45, 60, 75, 90, 105, 120, 135°$) and the energies E, selected in the hemispherical energy analyser, were altered between 2.7 eV and the primary electron energy T. Due to the random orientation of the molecules in the gas beam, measured data provide cross sections averaged over the azimuthal scattering angle ϕ. The absolute DDCS can be obtained from the experimental data by

$$\frac{\mathrm{d}^2\sigma}{\mathrm{d}E\mathrm{d}\Omega} = \sigma_{\mathrm{t}}\frac{e}{\eta\ \Delta I}\frac{\Delta N}{\Delta E\Delta\Omega}, \tag{4.30}$$

using the total scattering cross section σ_{t}, the electron charge e, the detection efficiency η and the reduction of the initial electron current ΔI, which is also measured after the passage of the molecular beam. While the DDCS of THF and PY were determined on the absolute scale, those of TMP had to be measured by the relative flow technique as described in [135]. This was necessary, because total scattering cross sections of TMP could not yet be measured due to the low vapour pressure of the gas.

Angular-dependent electron spectra measured for 1 keV electrons in THF, PY and TMP are shown in figure 4.4. The elastic peak is not included and will be separately discussed. Generally, the spectra consist of two parts; according to convention, the spectrum below an energy of $(T-B_0)/2^*$ arises from the emission of secondary electrons with energy E, while for energies above an energy loss spectrum of the primary particles is recorded. K-edges and the respective Auger-electron emission peaks for carbon, nitrogen and oxygen are distinct features in the measured spectra, which have to be separated from the measured spectra to obtain the DDCS. This separation process is described in section 4.4.1.2 and the Auger peaks are separately discussed in section 4.4.5.

---

[*] Reminder: T is the initial electron energy before the interaction and B_0 the binding energy of the outermost shell of the target molecule

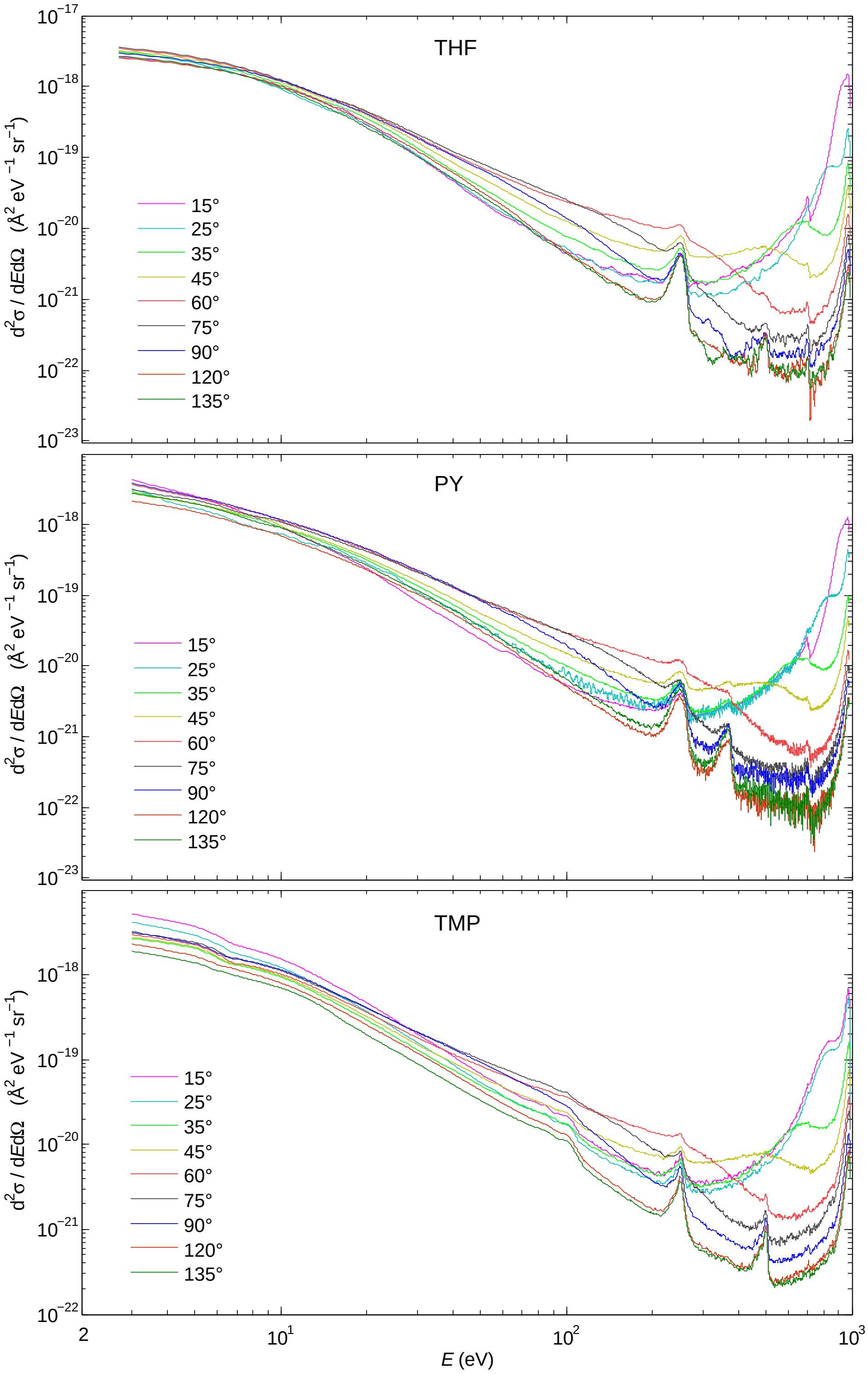

Figure 4.4: Experimental DDCS of THF, PY and TMP as a function of detected electron energy E for an initial electron energy of 1 keV shown for selected emission angles (not corrected for Auger electron emission).

The DDCS spectra of secondary electrons generally decrease with increasing secondary electron energy E. At energies below about 10 eV, the DDCS plateau and become nearly isotropic. Electrons of such low energy are produced in soft collisions with outer valence electrons in the molecule and mostly lead to small angle scattering of the incident electron. This can be seen in the spectra, where the DDCS of incident electrons which lost only a few tens of eV (the maximum is around 975 eV) is largest in forward direction. Low energy secondary electrons produced in these collisions are repelled by the outgoing primary electron and, therefore, are scattered into an angle close to 90°. In figure 4.4, the DDCS of secondary electrons with energies between 20 eV and 200 eV (arising from scattered primary electrons contributing to the peak between 800 eV and 975 eV) is, in fact, highest for emission angles between 60° and 90°. Kinematic calculations, using equations 2.8 and 2.7, reveal that incident electrons transferring almost the maximum amount of momentum have a high probability to be scattered into an angle close to 45°. This is also the case for the respective secondary electrons. Therefore, both electrons contribute to the count rate at the same angle, leading to a 'flat' spectrum and large DDCS at 45° compared to the other emission angles.

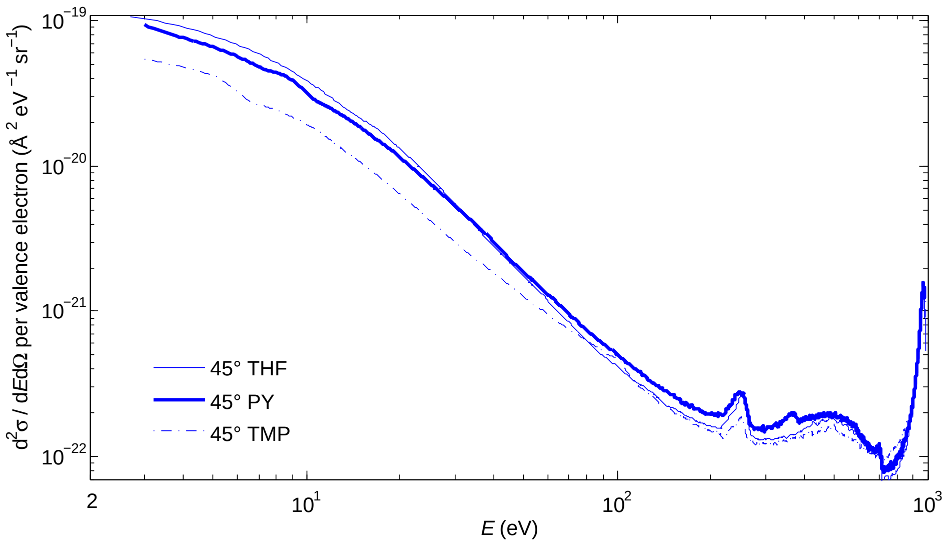

Figure 4.5: Experimental DDCS of THF, PY and TMP at 45° emission angle for an initial electron energy of 1 keV (not corrected for Auger electron emission). The data were divided by the number of valence shell electrons.

In figure 4.5, measured secondary electron spectra of THF, PY and TMP were divided by the number of valence shell electrons to enable quantitative comparison of the data. The spectra are shown for incident electrons of 1 keV and a emission angle of 45° but the differences between the three molecules are typical. In fact, the most noticeable difference is the lower emission of low-energy secondary electrons from TMP, which is a factor of two lower at $E = 3$ eV than for THF or PY in the presented case. On the other hand, the spectra of THF and PY agree within the experimental uncertainties.

4.4.1.2 Spline function

As a first step in the evaluation of the DDCS in this work, spline functions were fitted to the experimentally obtained DDCS as function of secondary electron energy for each emission angle and incident electron energy. The main purpose of this procedure was to interpolate the DDCS in the region of the Auger peak, which has to be separately taken into account in the data evaluation (see section 4.4.5). This was achieved using linear least-squares fitting and the Gaussian elimination procedure to solve equation 4.7. Previously written PTB software was transferred into MATLAB and extended by an uncertainty analysis of the spline function. The spline function could be chosen with piecewise polynomial functions of variable degree and a flexible number of intervals and border energies. The secondary energy range of the spline fit was in accordance with the convention that scattered electrons of energy E below $(T - B_0)/2$ are secondary electrons produced in the ionisation interaction and those of higher energy are the scattered incident electrons. To ensure a smooth connection of the polynomial functions, the constraint that the spline is twice continuously differentiable at the interval borders was included by Lagrange multipliers in equation 4.7.

The spline function was fitted to the logarithm of the experimental DDCS. For the experimental DDCS of THF, PY and TMP two or three intervals were chosen and polynomials between second and fifth order were applied. The weighting factors in the regions of the Auger peak were set to zero, such that the contribution of Auger electrons to the measured count rate was eliminated. Using the obtained parameter vector $\vec{a}$, the spline function as well as its first and second derivative were determined via the Horner scheme [91]. The first and second derivative of the fitted data are useful to evaluate the quality of the fit. The uncertainties of the spline functions were determined from equation 4.26, using the covariance matrix given in equation 4.24 and assuming that the uncertainties of the experimental data are completely correlated.

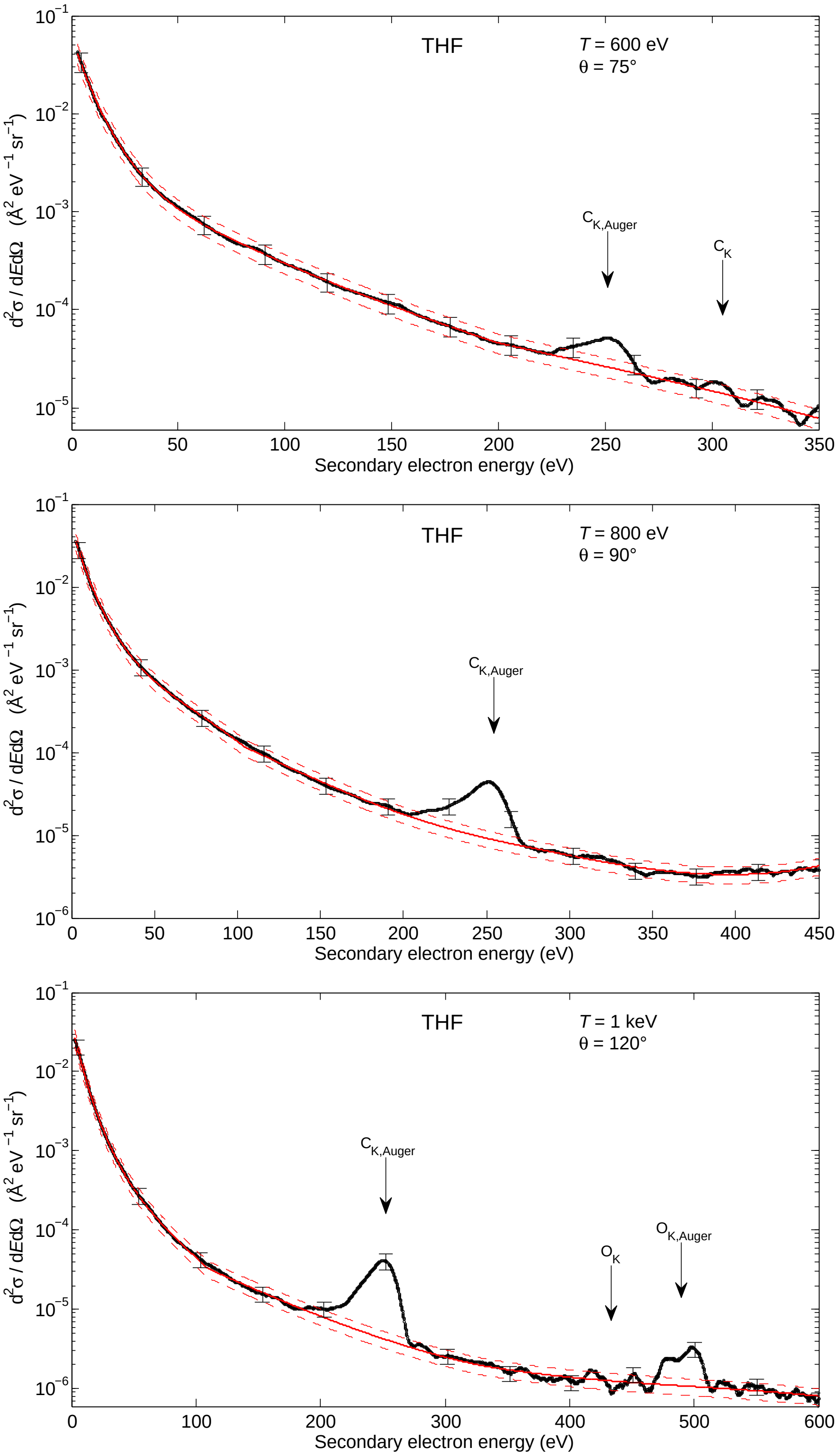

Figure 4.6: Spline fit (red) to experimental DDCS (black) of THF for incident electrons of several energies and emission angles. Dashed red lines show the uncertainties of the spline function. Uncertainties of the experimental data are shown for selected data points.

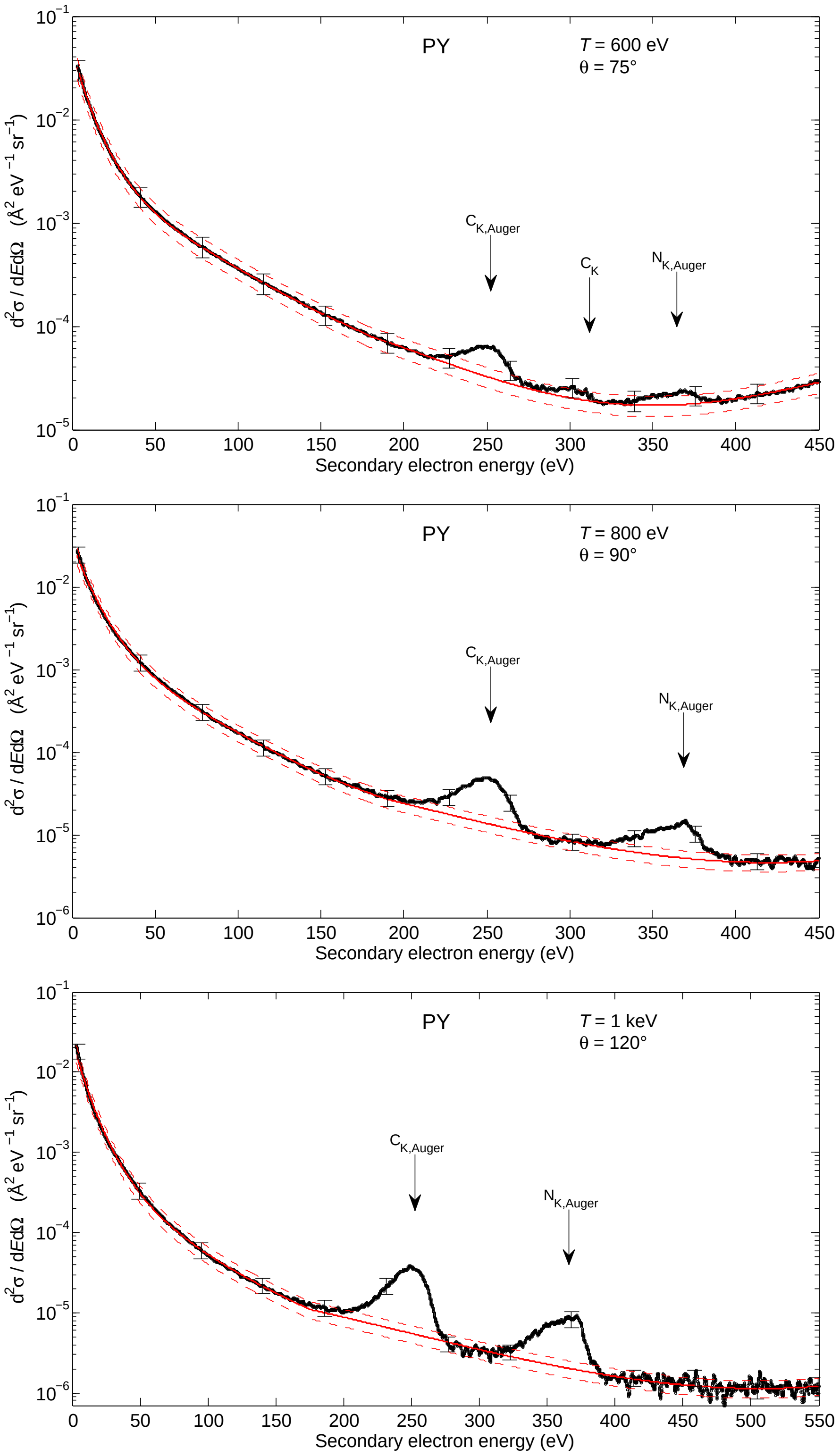

Figure 4.7: Spline fit (red) to experimental DDCS (black) of PY for incident electrons of several energies and emission angles. See caption of figure 4.6.

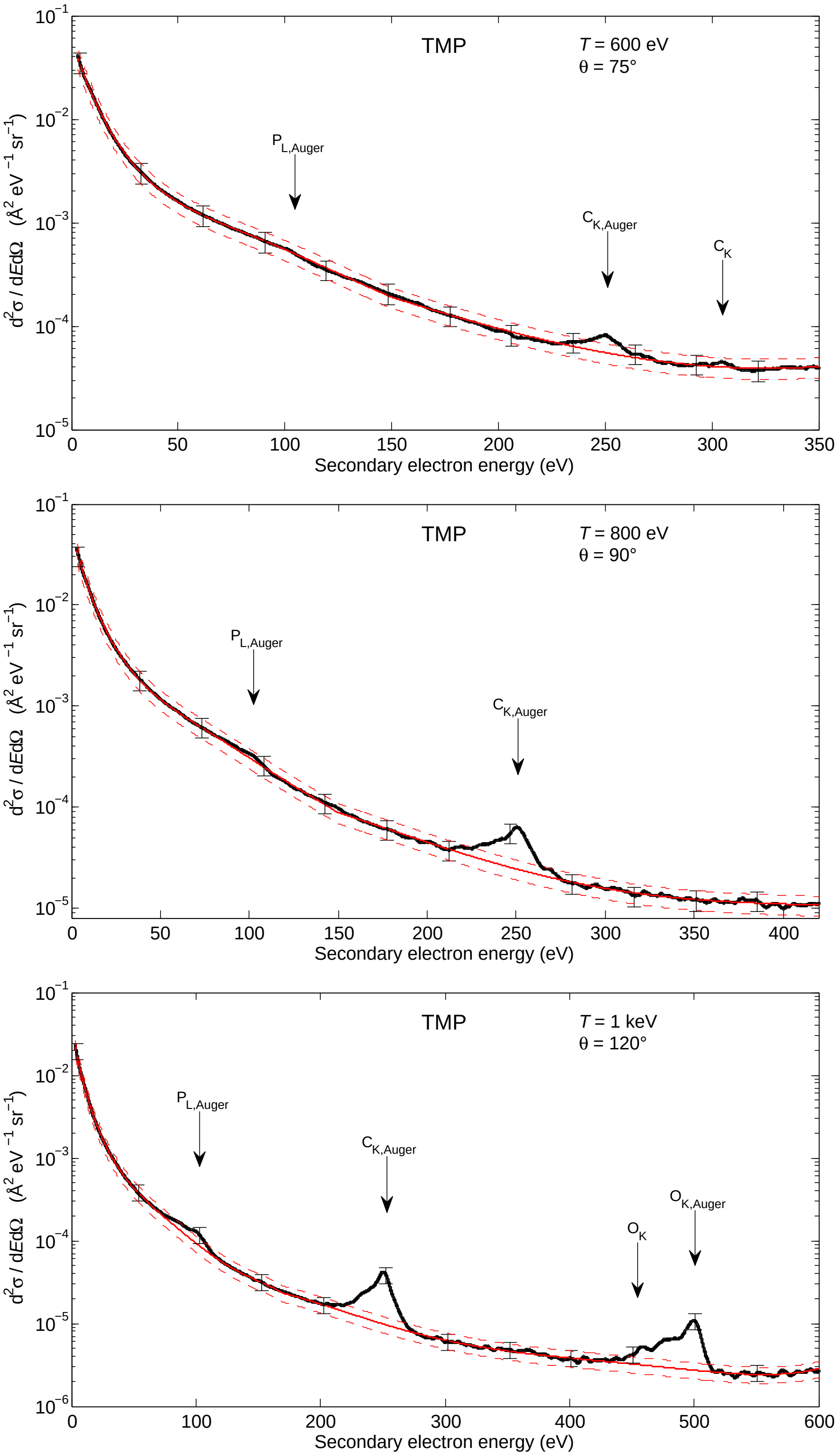

Figure 4.8: Spline fit (red) to experimental DDCS (black) of TMP for incident electrons of several energies and emission angles. See caption of figure 4.6.

Figures 4.6, 4.7 and 4.8 show spline functions fitted to the experimental spectra of THF, PY and TMP, respectively, for several incident energies and emission angles. The interpolation of the Auger peak regions was carried out for incident electron energies above 600 eV. The graphs of THF and TMP exhibit the carbon Auger peak between 190 and 285 eV. For incident electrons of 600 eV, the carbon K-edge is visible at about 300 eV. In the DDCS of PY, the Auger peak arising from ionisation of the nitrogen K-shell appears between 300 and 400 eV. The nitrogen K-edge is guessable in the spectra of 800 eV electrons where it appears at around 380 eV. In the case of incident electrons of 1 keV on THF or TMP, the oxygen K-edge is visible at about 450 eV, directly followed by the oxygen Auger peak between 470 and 520 eV. In the spectra of TMP, Auger electrons from the phosphor L-shells produce the peak between 70 and 120 eV. Cross sections for direct ionisation were successfully obtained from the interpolation by the spline functions, which truncates the Auger peaks of the measured DDCS in the respective energy regions. K-shell ionisation and Auger electron emission will be discussed in section 4.4.5.

4.4.1.3 Model function

An analytical description for the DDCS as function of the emission angle is required for an extrapolation of the measured data to 0° and 180°. This is achieved by fitting the data from the previous spline function as function of the polar emission angle θ for each secondary electron energy E. To evaluate an optimum function, the following model functions were compared: superposition of Legendre polynomials up to fifth degree using

$$\frac{\mathrm{d}^2\sigma}{\mathrm{d}E\mathrm{d}\Omega} = \sum_{i=0}^{5} p_i P_i(\cos\theta) \tag{4.31}$$

where p_i are the fitting parameters and P_i the Legendre polynomials of i-th degree. Alternatively, a formula developed by Rudd [160] was applied, given by

$$\frac{\mathrm{d}^2\sigma}{\mathrm{d}E\mathrm{d}\Omega} = a\left[\frac{1}{1+\left(\frac{\cos\theta-b}{c}\right)^2} + \frac{d}{1+\left(\frac{\cos\theta+1}{e}\right)^2}\right] \tag{4.32}$$

with parameters a, b, c, d, e. The motivation for using this model was given by Rudd [160], who observed that the binary encounter peak can be described by a Lorentzian function; a second Lorentzian function accounts for a backscatter peak. On the other hand, Legendre polynomials constitute a term in the quantum mechanical description of the scattering amplitude. For the fitting procedures it was almost always necessary to estimate the value at 180°. At this angle it was assumed that the value is the same as at 135°, which may lead to an underestimation of the ionisation cross section data. Experimental data measured at angles below 25° were omitted in the fitting procedure as these are likely to be overestimated in the experiment (see Bolorizadeh and Rudd [14]). This trend can be observed for some cases in figure 4.9, particularly for large energies of the incident electrons. For TMP, some data points of the experimental data are not shown as the respective measurements will be separately published. Equation 4.26 and the covariance matrix determined by equation 4.24 were used to calculate the uncertainties of the model function values, assuming complete correlation of the experimental uncertainties.

The model functions are also shown in figure 4.9. The results reveal that the Rudd model is suited to fit the DDCS for incident electrons above an energy of 200 eV. On the other hand, for lower incident electron energies, the superposition of Legendre polynomials up to fifth degree better reproduce the DDCS[†].

The DDCS of THF and PY are similar to each other within combined experimental uncertainties for the entire ranges of energies and emission angles. For incident electron energies below 200 eV, the DDCS of THF is slightly larger than the DDCS of PY. An approximate agreement, particularly for low momentum transfer, is expected as both molecules consist of the same number of valence electrons and have similar molecular geometries. The DDCS of TMP show the same angular dependence as those of THF or PY but are larger due to the higher number of electrons in this molecule.

Results obtained from the kinematic model given in equations 2.8 and 2.7 for the scattering angles of primary and secondary electrons are also shown in the figures. Grosswendt and Waibel [81] state that this model is applicable for oxygen or nitrogen as long as the energy of incident electrons is above 200 eV and secondary electron energies are above 50 eV. As seen in figure 4.9, emission angles for secondary electrons determined from the kinematic model provide approximately the mean emission angle determined from the experimental data for all DDCS independent of the energies of both electrons. Furthermore, it is observed that the secondary electron emission for THF, PY and TMP is nearly isotropic for secondary electron energies below about 15 eV, but the magnitude of the DDCS varies by more than 20% for higher energies. Grosswendt and Waibel [81] found an isotropic emission of secondary electrons of energies below 50 eV for smaller molecules.

[†] Please address any requests for the data to marion.bug@ptb.de

Purine. Due to the lack of data for the DDCS of PU and the similarity of the molecular structures of PY and PU, it was decided to use the angular dependence of PY. Hence, the absolute values of the DDCS of PU were obtained by scaling the DDCS of PY by the ratio of the total scattering cross sections for PU to those of PY.

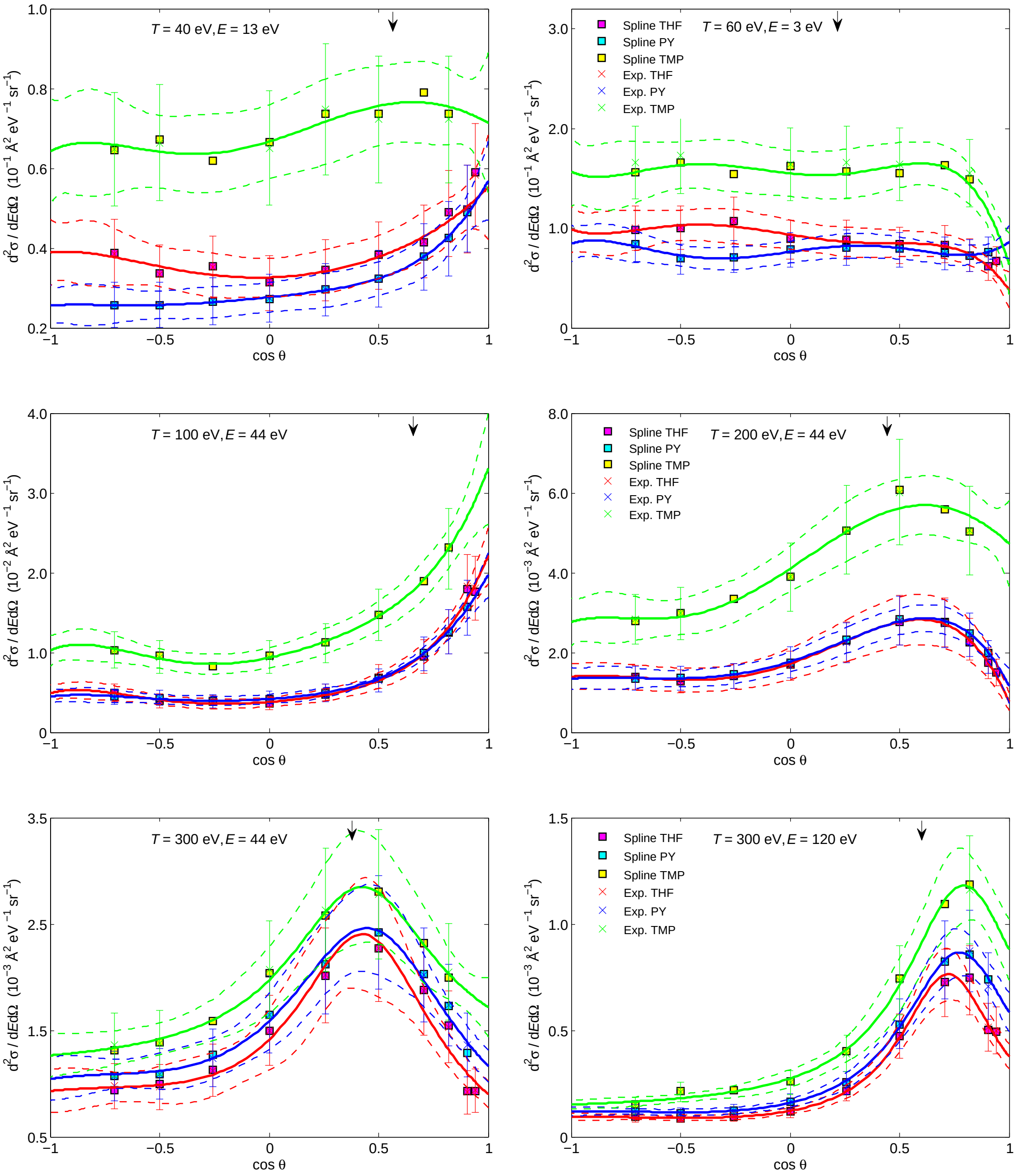

Figure 4.9: DDCS of THF, PY and TMP for incident electrons of energy T and secondary electrons of energy E. Experimental data are shown as well as those obtained from the spline fit and the model functions (solid lines). Dashed lines are the uncertainties of the model functions. The arrow indicates the emission angle obtained from the Berger model in equation 2.7.

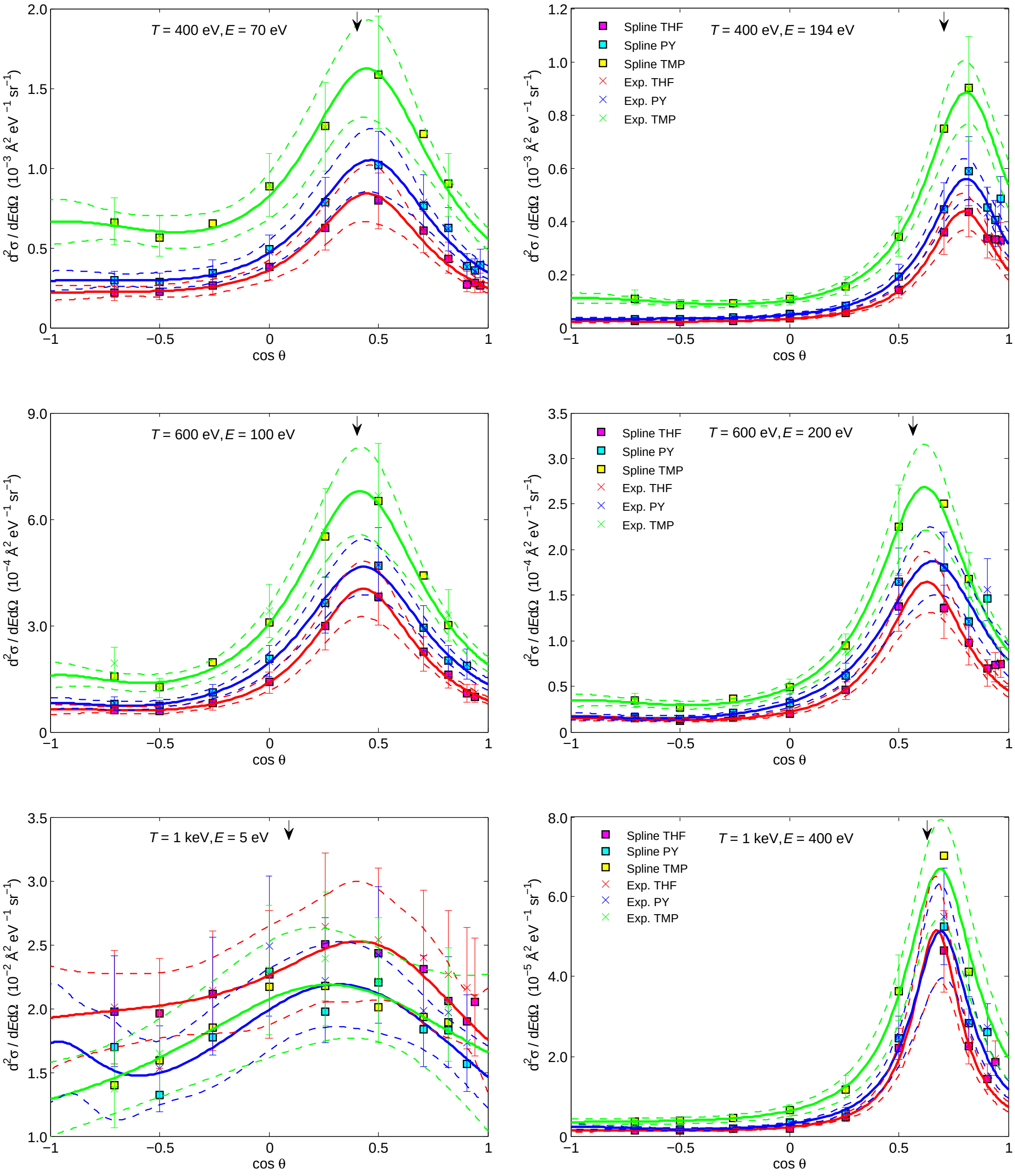

Figure 4.9: Continued...

4.4.2 Parameters for the BEB model

The BEB model, introduced in section 2.2.6, was used in the evaluation of the ionisation cross sections. This model requires input parameters, i.e. binding and mean kinetic energies B_i and U_i for individual orbitals i as well as the empirical factor n_{BEB} from a Mulliken population analysis (see [103] and page 30). The determination of these parameters for THF, TMP, PY and PU was performed by means of the quantum chemistry system GAMESS [75].

GAMESS [75] is an *ab-initio* quantum chemistry system. In this work, the restricted Hartree-Fock (RHF) method, also called self-consistent field method, was applied to optimise the molecular wave functions. Such calculations require the input of a basis set, which contains wave functions for a finite number of atomic orbitals within the molecule. Those atomic orbitals are approximated by linear combinations of Gaussian functions. This technique was applied in this work by using the Pople split-valence triple zeta basis set 6-311G. GAMESS further requires the specification of the molecular point group (listed for THF, TMP, PY and PU in section 2.1.2). Also, an initial guess of the position of atoms in the molecule is needed, which were taken from the Computational Chemistry Comparison and Benchmark Data Base (CCCBDB) [141].

The binding and kinetic energies B_i and U_i obtained by means of GAMESS for THF, TMP, PY and PU are listed in table 4.2. However, orbital energies calculated by the RHF method are often higher than the ground state energies [18]. Therefore, we followed the example of other authors and substituted the binding energies of the outermost valence electrons by the experimental value of the ionisation threshold. In the case of TMP, the binding energies of the four outermost electrons were adjusted due to the C_3 symmetry of the molecule.

The calculated binding energies of THF are significantly larger (in their absolute values) than those given by Champion [27], who applied RHF/3-21G calculations and yielded a good agreement with experimental ionisation potentials. Differences with our calculations are 1.49 eV for the lowest binding energy and about 72 eV for the innermost K-shells. However, despite the superior prediction of the ionisation potential, the binding energies of Champion for inner orbitals are too low as will be discussed in section 4.4.5. Therefore, it is assumed that the values presented in table 4.2 are overall more realistic than those of Champion.

Table 4.2: Absolute binding energies B_i and kinetic energies U_i of orbital electrons in THF, TMP, PY and PU.

	THF		TMP		PY		PU	
i	B_i (eV)	U_i (eV)	B_i (eV)	U_i (eV)	B_i (eV)	U_i (eV)	B_i (eV)	U_i (eV)
1	557.94	792.08	2178.05	2884.91	423.44	600.34	424.98	600.10
2	306.17	434.60	559.41	792.92	423.44	600.26	423.64	600.28
3	306.17	434.55	559.40	792.92	307.52	434.52	423.43	600.33
4	305.08	434.55	559.40	792.92	307.09	434.53	423.31	600.29
5	305.07	434.50	557.34	793.18	307.09	434.56	308.17	434.53
6	36.97	64.50	306.92	435.01	305.92	434.53	308.14	434.49
7	28.97	41.98	306.92	435.01	36.57	49.14	307.64	434.53
8	27.21	40.28	306.92	435.00	33.02	56.54	307.19	434.54
9	22.25	41.00	209.59	431.58	29.75	46.27	306.53	434.48
10	22.14	37.51	152.44	401.58	24.64	45.73	38.22	48.15
11	18.69	28.34	152.42	401.50	24.55	45.85	36.26	50.28
12	18.19	32.70	152.42	401.50	20.52	29.17	33.67	55.49
13	16.28	27.08	39.64	68.08	19.37	45.44	32.44	57.92
14	15.97	37.84	37.67	72.85	17.98	34.88	29.34	49.57
15	15.11	42.95	37.67	72.85	16.53	37.22	25.41	45.45
16	13.60	38.10	35.23	76.82	16.27	40.42	24.35	48.62
17	13.57	35.51	27.43	46.58	15.96	29.49	23.52	44.56
18	12.99	30.83	26.20	44.06	12.58	50.73	21.70	40.36
19	12.31	53.44	26.20	44.06	11.54	36.60	20.09	40.14
20	9.74[*]	55.63	21.40	56.86	10.96	51.35	19.11	46.88
21			19.37	47.92	9.73[†]	31.00	17.90	43.80
22			19.37	47.92			17.88	30.70
23			18.44	44.65			17.18	42.92
24			17.85	36.99			16.56	39.21
25			17.85	36.99			15.05	33.83
26			17.13	36.25			13.44	52.33
27			17.09	42.62			12.92	36.81
28			17.09	42.62			12.22	52.04
29			15.90	50.66			10.97	52.39
30			14.33	49.71			10.57	42.28
31			14.33	49.71			9.58	35.13
32			13.59	56.69				
33			13.32	53.35				
34			13.32	53.35				
35			12.90	61.39				
36			10.81[‡]	60.91				
37			10.81[‡]	60.91				

---

[*] Experimental value [141]

[†] Experimental value [92]

[‡] Experimental value [178]

Table 4.3: Mulliken populations in atomic orbitals with principal quantum numbers n for each molecular orbital of THF, TMP, PY and PU.

	THF		TMP		PY		PU	
n i	3	4	3	4	3	4	3	4
1	0.00	0.00	0.01	0.00	0.00	0.00	0.00	0.00
2	0.00	0.00	0.00	0.00	0.00	0.00	0.00	0.00
3	0.00	0.00	0.00	0.00	0.00	0.00	0.00	0.00
4	0.00	0.00	0.00	0.00	0.00	0.00	0.00	0.00
5	0.00	0.00	0.00	0.00	0.00	0.00	0.00	0.00
6	0.54	0.43	0.00	0.00	0.00	0.00	0.00	0.00
7	0.49	0.39	0.00	0.00	0.61	0.30	0.00	0.00
8	0.48	0.36	0.00	0.00	0.62	0.34	0.00	0.00
9	0.42	0.30	–0.03	0.54	0.61	0.18	0.00	0.00
10	0.41	0.30	–0.14	0.02	0.57	0.22	0.61	0.36
11	0.39	0.26	–0.14	0.02	0.58	0.15	0.62	0.34
12	0.44	0.25	–0.14	0.02	0.41	0.21	0.61	0.34
13	0.36	0.18	0.42	0.45	0.63	0.09	0.60	0.32
14	0.41	0.23	0.50	0.49	0.41	0.05	0.65	0.27
15	0.44	0.20	0.50	0.49	0.47	0.14	0.59	0.22
16	0.47	0.19	0.45	0.50	0.44	0.15	0.62	0.21
17	0.48	0.14	0.40	0.31	0.44	0.37	0.52	0.25
18	0.35	0.11	0.40	0.35	0.46	0.26	0.52	0.19
19	0.51	0.26	0.40	0.35	0.43	0.41	0.51	0.17
20	0.38	0.22	0.37	0.26	0.46	0.27	0.59	0.15
21			0.37	0.31	0.45	0.22	0.46	0.39
22			0.37	0.31			0.54	0.15
23			0.37	0.30			0.49	0.14
24			0.38	0.27			0.47	0.14
25			0.38	0.27			0.44	0.40
26			0.38	0.22			0.46	0.32
27			0.41	0.25			0.45	0.39
28			0.41	0.25			0.48	0.30
29			0.35	0.24			0.48	0.29
30			0.35	0.25			0.43	0.40
31			0.35	0.25			0.47	0.36
32			0.40	0.26				
33			0.37	0.27				
34			0.37	0.27				
35			0.39	0.32				
36			0.40	0.35				
37			0.40	0.35				

GAMESS was also used to obtain the parameter n_{BEB} in the BEB model from a Mulliken population analysis of atomic orbitals [103]. The Mulliken population per electron in a atomic orbitals with principal quantum number 3 and 4 is given in table 4.3 for each molecular orbital. As stated in section 2.2.6, it was suggested by Irikura et al. [103] to apply the correction factor n_{BEB} in the BEB model to molecular orbitals, if the population in an atomic orbital with principal quantum numbers larger than 2 is greater than 0.5. In this case, n_{BEB} should be equal to the principal quantum number of the respective atomic orbital and used to reduce the orbital energies in the BEB model. In the following sections 4.4.3 and 4.4.4, the effect of n_{BEB} on the BEB cross sections of the molecules investigated in this work is quantified and an optimal value is determined semi-empirically.

4.4.3 Single differential ionisation cross sections

The single differential ionisation cross section (SDCS) $\mathrm{d}\sigma_{\mathrm{ion}}/\mathrm{d}E$ was determined by integrating the DDCS over the polar and azimuth emission angles θ and ϕ by

$$\frac{\mathrm{d}\sigma_{\mathrm{ion}}}{\mathrm{d}E}(T) = \int_0^{\pi}\int_0^{2\pi} \sin\theta \frac{\mathrm{d}^2\sigma}{\mathrm{d}E\mathrm{d}\Omega}\mathrm{d}\theta\mathrm{d}\phi \ . \tag{4.33}$$

This integration was performed for the DDCS fitted by the Rudd model for energies between 300 eV and 1 keV and the Legendre polynomials for the lower energies. The influence of the SDCS by the extrapolation of the DDCS was not more than 5% when compared to an integration only over the angular range of the experiment (between 15° and 135°).

Uncertainty propagation was applied using the integrated values of the G-matrices, subject to

$$G_{\mathrm{SDCS}} = 2\pi \int_0^{\pi} \sin\theta \ G_{\mathrm{DDCS}} \ \mathrm{d}\theta \tag{4.34}$$

to determine the squared uncertainties $u^2_{\mathrm{data}}(\vec{Y})$ and $u^2_{\mathrm{model}}(\vec{Y})$ of the SDCS data $\vec{Y}$ by equations 4.25a and b. The covariance matrix of the SDCS data was obtained, taking into account the correlation of $u_{\mathrm{data}}(\vec{Y})$ which arise from systematic contributions to the uncertainties of the experimental data. Hence, the following procedure was applied

$$C_{data}(\vec{Y})_{i,j} = u_{\mathrm{data}}(Y_i) \ u_{\mathrm{data}}(Y_j) \ + \ \delta_{ij}u^2_{\mathrm{model}}(Y_i) \tag{4.35}$$

For a convenient implementation in the simulation code and to obtain a reasonable extrapolation of the SDCS to 0 eV secondary electron energy, an appropriate model function is required. For large energy transfers, the Thomson and Mott cross sections [100] provide estimations of the SDCS (see section 2.2.5) and will be discussed in section 4.4.3.2. On the other hand, the BEB model (see section 2.2.6) inherently extrapolates the SDCS to low secondary electron energies, as it was developed to fulfil the conditions of the dipole limit. The suitability of this model for the SDCS of THF and PY is discussed in the following.

4.4.3.1 BEB model

The BEB model, used with the parameters given in table 4.2 and a factor $n_{\mathrm{BEB}} = 1$, is found to generally underestimate the SDCS at low secondary electron energies. As seen in figure 4.10, the integrated experimental are between 8% and 41% larger at 3 eV for PY and between 31% and 67% at 2.7 eV for THF data at incident electron energies between 30 eV and 1 keV. The SDCS at 20 eV for THF are between 33% and 76% larger than the BEB model data. For TMP, the BEB model data are 40–50% lower at $E = 3$ eV than the integrated experimental values for incident electron energies 40–200 eV. At higher impact energies, better agreement is observed. Furthermore, the slope of the BEB model predictions as function of secondary electron energy is lower than the slope of the experimental data. Hence, the BEB model underestimates the experimental data at energies E below 25 eV and overestimates the SDCS at intermediate secondary electron energies by up to 45% for THF and 20% for PY. At the highest secondary electron energies, the BEB model data are mostly similar to the experimental SDCS of THF and PY. The description of the SDCS of TMP is worse at energies 40–200 eV with deviations of up to 50%. At higher incident electron energies, the BEB model overestimates the experimental data at energies E above several eV by up to 50%.

A slightly better agreement for low incident energies (below 200 eV) could be obtained when using the BEB cross section with the factors $n_{\mathrm{BEB}} = 3$ if the Mulliken population in a molecular orbital (given in table 4.3) exceeds a specified value. As will be discussed in section 4.4.4, the best agreement with the total ionisation cross sections obtained from the integrated experimental data was obtained for populations larger than 0.4, 0.47 and 0.34 for THF, PY and TMP respectively. The impact of the applied correction on the SDCS increases with decreasing energy and provides a slightly better agreement with the data from experiments. However, as the dependence of the SDCS on E is not significantly affected, the BEB model is still an unsatisfactory representation of the experimental data.

4.4.3.2 Thomson and Mott cross sections

As stated previously and in section 2.2.5, the Thomson and Mott cross sections [100] are useful to examine the behaviour of the SDCS for large energy transfers $E_{\mathrm{Tr}} = E + B$ where $E \gg B$. It is obvious from figure 4.10 that both models agree reasonably well with the data derived from the experiment for secondary electron energies E above several tens of electron volts. A different shape is present for the Thomson cross section, which does not account for exchange effects of the interacting electrons and, hence, continuously decreases with increasing energy E, while the other data form a plateau of the SDCS at large E. Comparing the Thomson and Mott SDCS, the plateau in the Mott data is accompanied by a steeper slope at energies above 10 eV, originating from the interference between direct ionisation and exchange interactions. The deviation between both SDCS amounts to up to 35% in the energy ranges $T > 80$ eV and $E > 50$ eV. In this energy range, the experimental data agree in magnitude with the Thomson SDCS, while the shape is similar to the predictions of the Mott cross sections.

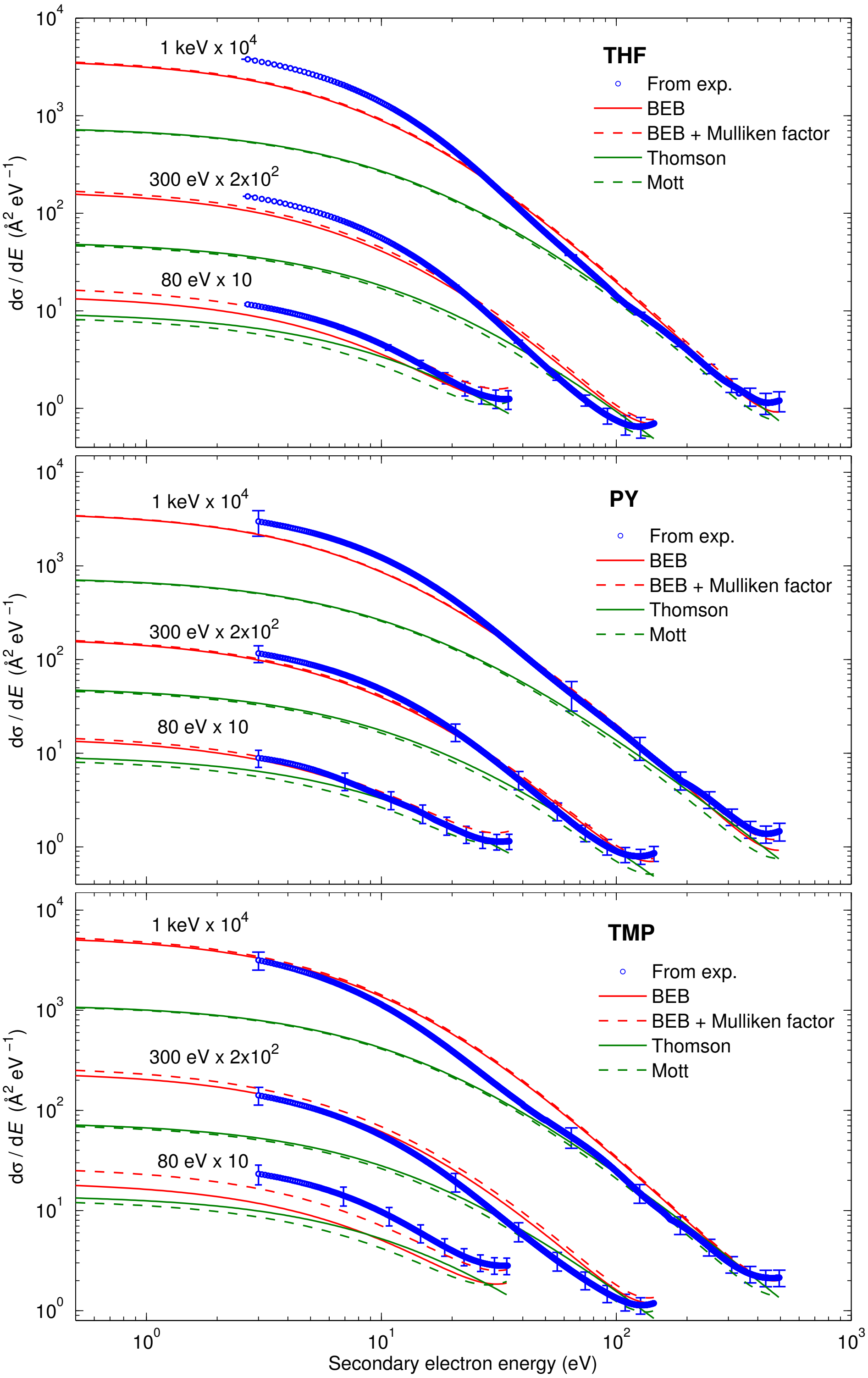

Figure 4.10: SDCS of THF, PY and TMP for primary electrons of selected energies obtained from the experimental data, the Thomson and Mott models as well as the BEB model with and without using the correction factor n_{BEB}. Uncertainties of data derived from the experiment are shown for selected data points to keep readability.

4.4.3.3 SDCS model function

The models discussed in section 4.4.3.1 do not provide an optimal description of the experimental SDCS data. To improve the agreement with the experimental data and to be able to extrapolate to low secondary electron energies, a fit of the BEB model to the data obtained by equation 4.33 was applied. In this case, equations 2.20 and 2.21 become

$$\frac{\mathrm{d}\sigma_{\mathrm{ion}}}{\mathrm{d}E}(T) = \frac{S'}{B'(t'+u'+1)} \sum_{n=1}^{3} F_n \left[f_n(w') + f_n(t'-w') \right] , \tag{4.36}$$

where

$$F_1 = -\frac{F_2}{t'+1}, \qquad F_2 = 2-1, \qquad F_3 = Q'\mathrm{ln}t', \tag{4.37a}$$

$$f_n(w) = (w+1)^{-n}, \qquad f_n(t-w) = (t-w)^{-n}, \tag{4.37b}$$

$$t' = T/B', \qquad u' = U'/B', \qquad w' = E/B' \tag{4.37c}$$

with fitting parameters S' (in units of Å^2), B' and U' (in units of eV) and Q'. Please note that due to the energy range of the available experimental data, this model function is applicable only for energies T in the range between 25 eV and 1 keV. For lower primary electron energies, a constant dependence of the SDCS on the secondary electron energy can be assumed as is obvious from the experimental data.

The parameters of equation 4.36 were also fitted as a function of the incident electron energies T (in eV). This was to achieve an interpolation of the SDCS with respect to T as well as a convenient handling of the data for the implementation of the model in the simulation code. The following model functions were used

$$Q' = q \tag{4.38a}$$

$$B' = \sum_{j=1}^{2} ba_j \mathrm{e}^{-bb_j \ \log_{10} T} \tag{4.38b}$$

$$S'/B' = \sum_{j=0}^{s_{\max}} s_j \ (\log_{10} T)^j \tag{4.38c}$$

$$U' = \sum_{j=0}^{u_{\max}} u_j T^j \tag{4.38d}$$

The optimum fit parameters are given in table 4.4. The parameters were fitted consecutively in the order above. This means that after the model function of one parameter was obtained, equation 4.36 was re-fitted to the SDCS data using only the remaining parameters. In this way, a good agreement with the SDCS data could be maintained.

Table 4.4: Parameters for equations 4.38a–4.38d.

				THF			
q	200	ba_1	2.245×10^{1}	s_0	-1.069×10^{-2}	u_0	-1.463×10^{1}
		bb_1	1.368×10^{-1}	s_1	1.921×10^{-2}	u_1	-3.618×10^{-1}
		ba_2	-4.398×10^{2}	s_2	-1.686×10^{-3}	u_2	2.236×10^{-4}
		bb_2	2.871×10^{0}			u_3	-2.278×10^{-7}
				PY			
q	200	ba_1	1.772×10^{1}	s_0	4.012×10^{-3}	u_0	-4.548×10^{0}
		bb_1	6.047×10^{-3}	s_1	1.170×10^{-2}	u_1	-3.054×10^{-1}
		ba_2	-1.088×10^{2}	s_2	-1.395×10^{-3}	u_2	3.872×10^{-4}
		bb_2	2.199×10^{0}			u_3	-2.258×10^{-7}
				TMP			
q	200	ba_1	5.896×10^{1}	s_0	-8.507×10^{-2}	u_0	-1.006×10^{1}
		bb_1	4.216×10^{-1}	s_1	1.329×10^{-1}	u_1	-9.881×10^{-1}
		ba_2	-2.044×10^{2}	s_2	-6.452×10^{-2}	u_2	2.183×10^{-4}
		bb_2	1.575×10^{0}	s_3	1.028×10^{-2}		

The covariance matrix of the SDCS model function in equation 4.36 was determined by

$$C(\vec{Y}_{\text{fit}}) = C_{\text{data}}(\vec{Y}_{\text{fit}}) + C_{\text{model}}(\vec{Y}_{\text{fit}}) + C_{\text{para}}(\vec{Y}_{\text{fit}}). \tag{4.39}$$

Using G_{SDCS} (equation 4.34), it is

$$C_{\text{data}}(\vec{Y}_{\text{fit}}) = G_{\text{SDCS}}\ C_{\text{data}}(\vec{a}_{\text{SDCS}})\ G^{T}_{\text{SDCS}}, \tag{4.40a}$$

$$C_{\text{model}}(\vec{Y}_{\text{fit}}) = G_{\text{SDCS}}\ C_{\text{model}}(\vec{a}_{\text{SDCS}})\ G^{T}_{\text{SDCS}}, \tag{4.40b}$$

$$C_{\text{para}}(\vec{Y}_{\text{fit}}) = G_{\text{SDCS}}\ C_{\text{para}}(\vec{a}_{\text{SDCS}})\ G^{T}_{\text{SDCS}}. \tag{4.40c}$$

Uncertainty propagation was taken into account in $C_{\text{data}}(\vec{a}_{\text{SDCS}})$, using the covariance matrix of the experimental SDCS $C_{\text{data}}(\vec{Y})$ (equation 4.35) in equation 4.20.

The covariance matrix $C_{\text{model}}(\vec{a}_{\text{SDCS}})$ accounts for the imperfect description of the experimental SDCS by the model function and is obtained by the reduced chi-square value in accordance with equation 4.23b.

The matrix $C_{\text{para}}(\vec{a}_{\text{SDCS}})$ accounts for the imperfect description of the SDCS model function parameters by equations 4.38a–d as function of energy T. The uncertainties of those parameters are uncorrelated and, hence, the chi-square value and constant weighting factors were used to obtain the squared uncertainty of each parameter and energy T, in accordance with equations 4.23b and 4.25b. Matrix $C_{\text{para}}(\vec{a}_{\text{SDCS}})$ contains those values for a specific energy T on its diagonal.

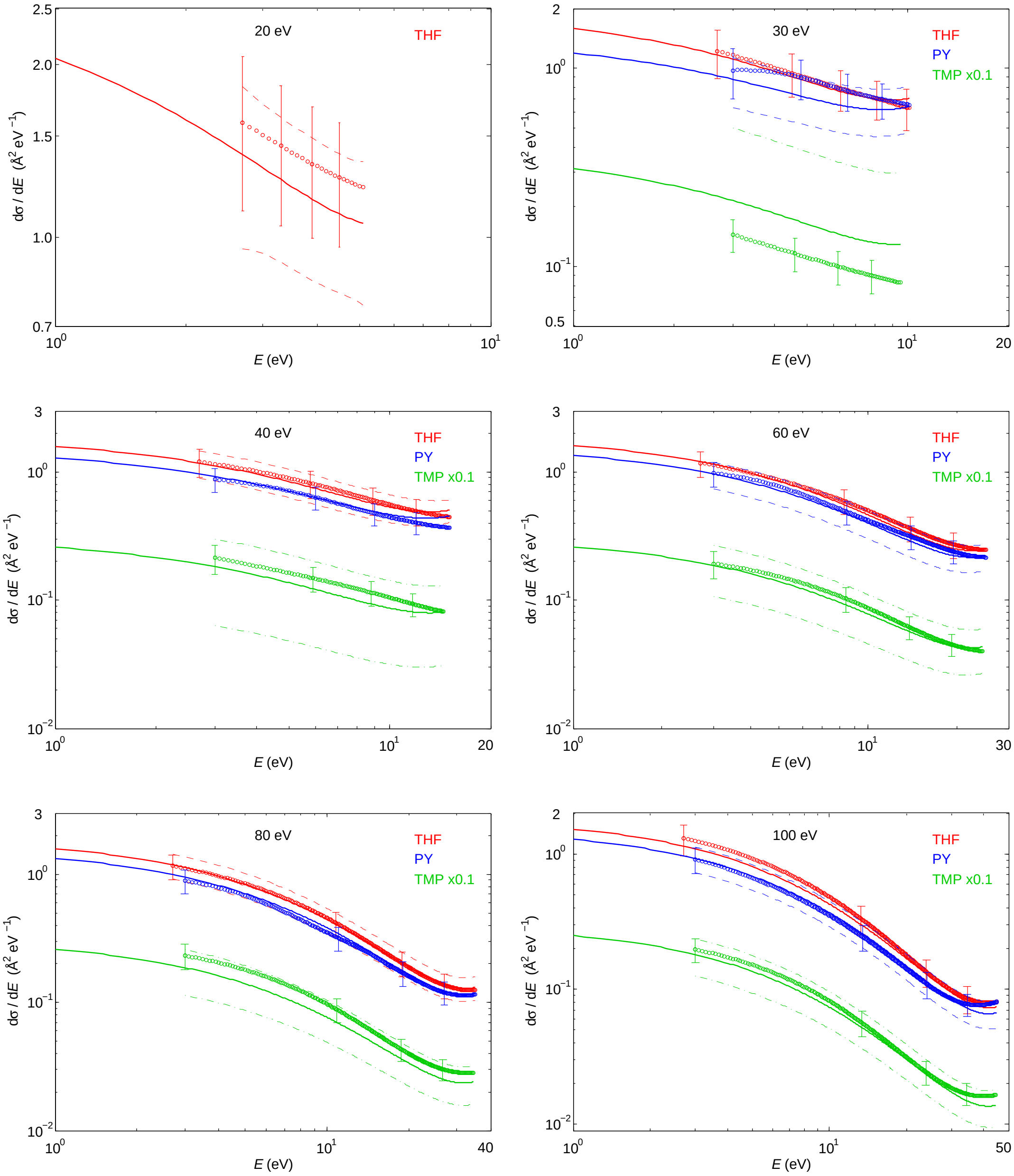

Figure 4.11: SDCS of THF, PY and TMP for different primary electron energies, obtained from the experimental data by equation 4.33 (symbols) and the model function (lines). Uncertainties of the experimental data are shown for selected data points, while those of the model function are indicated by broken lines (For better readability, either the uncertainties of THF or PY are shown).

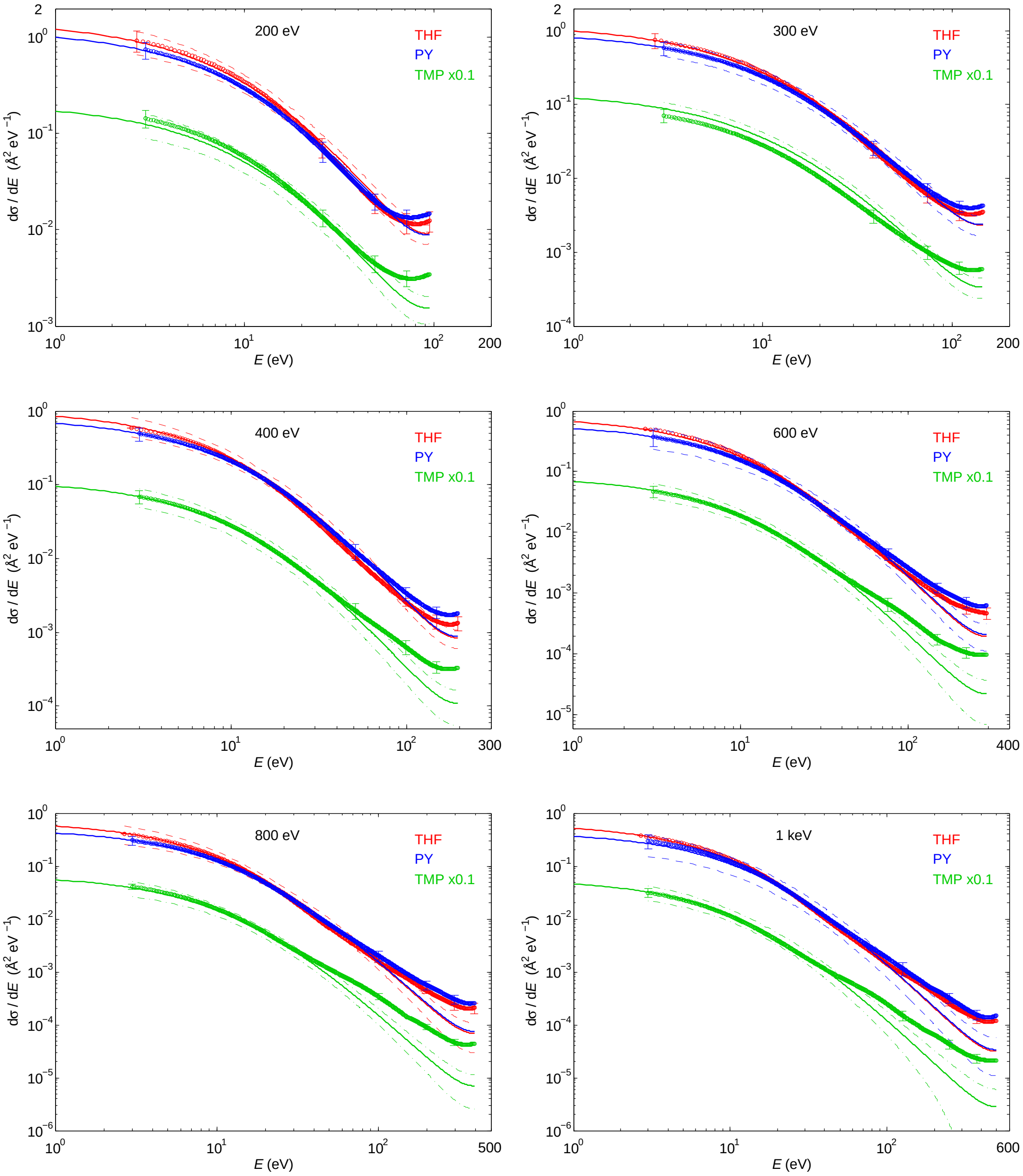

Figure 4.11: Continued.

.

The model functions of the SDCS are compared to the experimental data in figure 4.11. The uncertainties of experimental data are generally in the order of 25%.
For 20 eV impact energy, the experimental SDCS data of THF are about 16% larger than the model data for all secondary electron energies, which is well within the experimental uncertainties and arises from the fit of the model function parameters.
At 30 eV impact energy, the model data of THF are in excellent agreement with experimental data, while those of PY are up to 12% lower, which is well within experimental uncertainties. For TMP, the model function data overestimate the experimental data by a factor of 1.5, which leads to large uncertainties of the model function values.
For incident electrons of energies between 40 eV and 1 keV, the SDCS are in good agreement within the experimental uncertainties for secondary electron energies E below about 50 eV. Only at an energy T of 300 eV, the model function values are up to 27% larger than experimental data. Due to the choice of the BEB model for the fit, the model function underestimates the experimental data at energies E above 50 eV. The magnitude of deviations increases with increasing incident electron energy T and are a factor of two at 200 eV and a factor of five at 1 keV. However, in the energy regions of the observed deviations the SDCS is two to three orders of magnitude smaller than for low secondary electron energies. In fact, the highest cross section is always present for secondary electron energies below 10 eV, where the model functions agree in most cases within 10% with the data derived from experiments for THF, PY and TMP.

When comparing the SDCS of THF and PY, it is observed that the data of THF are generally larger than those of PY at low energies E and lower at high energies E. However, deviations are always within the experimental uncertainties, which is in accordance with the observed deviations of the DDCS. Comparing the experimental SDCS data of THF, PY and TMP, normalised to the number of electrons (not shown), all SDCS agree within the uncertainties at energies T below 200 eV. At higher energies T, the agreement persists for energies E above several tens of eV, while the TMP data are up to 70% lower at an energy E of 3 eV. Such deviations are unexpected, as the production of low-energy electrons is well described within the first Born approximation and the respective cross sections should approximately scale by the number of electrons in the target molecule. The observed deviations may arise from the different measurement technique applied for TMP, namely the relative flow technique [6]. In this, nitrogen data were used to put the measured values to the absolute scale.

a) Purine.

Regarding the data for PU, the decision was made in section 4.4.1.3 that the relative energy and angle dependence of the DDCS of PU is the same as for PY, with their magnitude scaled by the ratio of the respective TCS (given in equation 4.27).

4.4.3.4 Platzman plot

The Platzman plot is a powerful tool to examine the consistency of the SDCS. In figure 4.12, the quantity $Y(E_{\mathrm{Tr}})$ given in equation 2.17 is plotted for selected incident electron energies. The energy transfer E_{Tr} was determined by summing the secondary electron energy E and the binding energy of the outermost valence electron (9.74 eV for THF, 9.73 eV for PY and 10.81 eV for TMP, provided in table 4.2). Due to the choice of x-axis in the Platzman plot, deviations between the experimental data and the different models appear enhanced. Hence, the superior agreement of the fitted model function with the experimental data compared to the conventional BEB model is clearly observed. For $R/E_{\mathrm{Tr}} \to 0$, the value $Y(E_{\mathrm{Tr}})$ approaches the number of electrons in the target molecule (40, 42 and 74 for THF, PY and TMP, respectively). For the PY and TMP data of incident electron energies above 60 eV, this number is overestimated, indicating an overestimation of either the experimental DDCS or the DDCS model functions at those energies. For all data, the initial drop of the SDCS for increasing R/E_{Tr} followed by the minimum related to the electron exchange effect occurs in agreement with the predictions of the Mott cross section.

Generally, the Platzman plot supports the suitability of the model function given in equation 4.36 for the SDCS. These model functions can be directly implemented in Monte Carlo codes. They are also used in the following to calculate the total ionisation cross section.

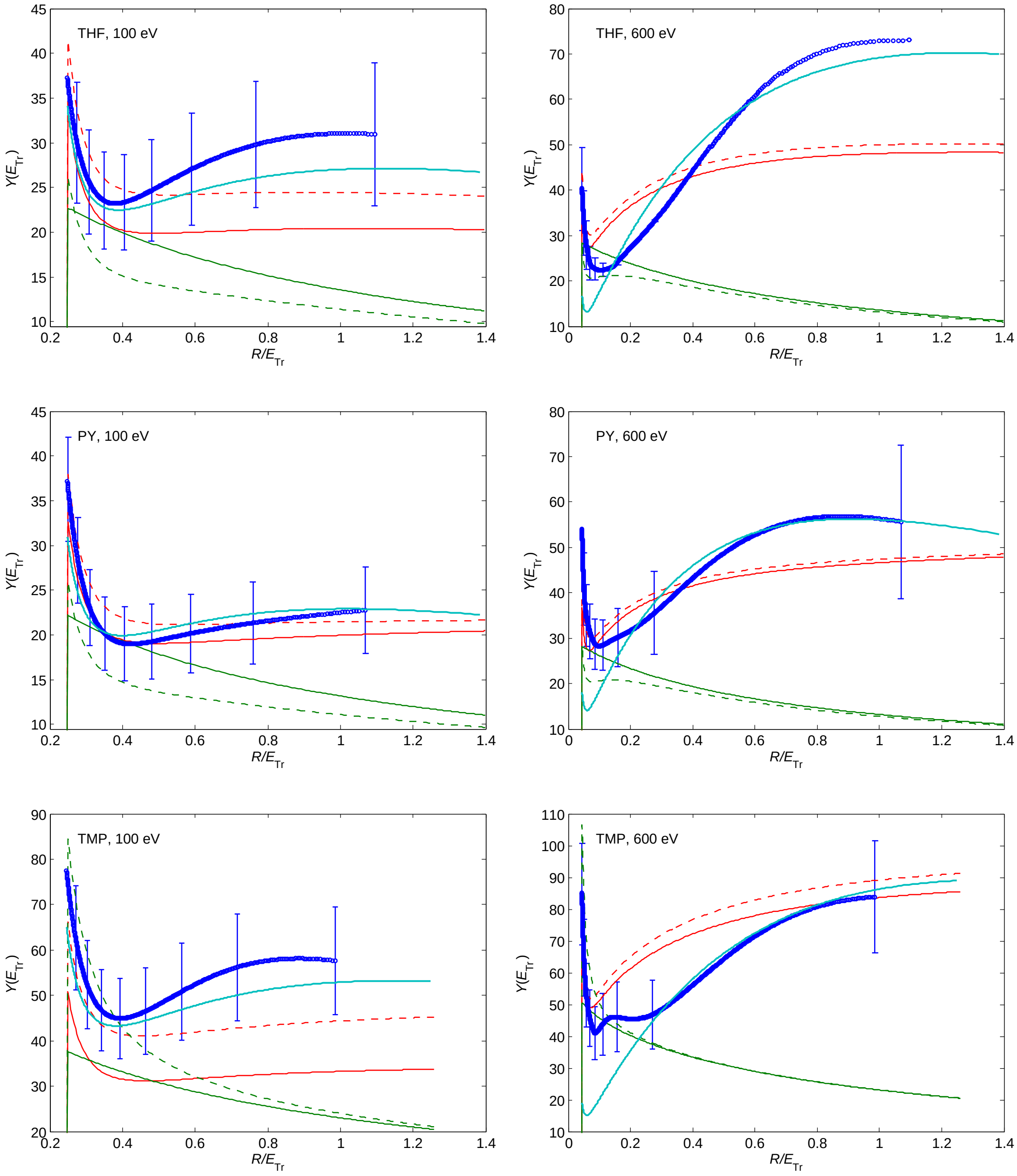

Figure 4.12: Platzman plot for THF, PY and TMP for primary electrons of selected energies obtained from the experimental data (blue symbols), the Thomson (solid green line) and Mott (dashed green line) models as well as the BEB model with and without using the correction factor n_{BEB} (solid and dashed red lines, respectively). The model function is represented by the light blue lines.

4.4.4 Total and partial ionisation cross sections

The total ionisation cross section σ_{ion} was obtained by integrating the SDCS by

$$\sigma_{\text{ion}}(T) = \int\limits_{E_{\min}}^{(T-B_0)/2} \frac{\mathrm{d}\sigma}{\mathrm{d}E}\mathrm{d}E, \tag{4.41}$$

where B_0 is the energy of an outermost valence electron. The SDCS were previously obtained from the model functions provided in equation 4.36.

The uncertainties of the integrated ionisation cross section data $\vec{Z}$ were calculated similarly to the procedure described for the uncertainties of the SDCS data. The G-matrices of the SDCS (G_{SDCS}) were integrated over the secondary electron energies to yield G_{Z}. Those were used to determine the squared uncertainties $u^2_{\text{data}}(\vec{Z})$ and $u^2_{\text{model}}(\vec{Z})$ by equations 4.25a and b. Additional uncertainties arise from the fit of the model functions in equations 4.38a–d to the SDCS parameters $\vec{a}_{SDCS}$ as function of energy T. The covariance $C_{para}(\vec{Z})$ of the parameters $\vec{p}$ for those model functions are described in $C(\vec{p})$ (naturally, correlations are only present for parameters belonging to the same model function). It is then,

$$C_{para}(\vec{Z}) = G_Z\ C(\vec{p})\ G_Z^T \tag{4.42}$$

with $G_Z = \partial\vec{Z}/\partial\vec{p}$ calculated by

$$(G_Z)_{ni} \ = \ \frac{\partial Z_i}{\partial p_n} \ = \sum_m \frac{\partial Z_i}{\partial a_{SDCS,m}} \frac{\partial a_{SDCS,m}}{\partial p_n}. \tag{4.43}$$

The covariance matrix of the total ionisation cross section $\vec{Z}$ is then obtained by

$$C_{data}(\vec{Z})_{i,j} = u_{\text{data}}(Z_i)\ u_{\text{data}}(Z_j) \ + \ \delta_{ij} u^2_{\text{model}}(Z_i) + C_{para}(\vec{Z})_{ij}. \tag{4.44}$$

A delicate issue is the extrapolation of the SDCS towards zero electron energy. The minimum secondary electron energies $E_{\min}$ in the experiment were 2.7 eV for THF data and 3.0 eV for PY and TMP data. Due to the much larger values of the SDCS for low energies E, the extrapolation of the SDCS increases the total ionisation cross section. A comparison of data integrated with both lower energy limits, $E_{\min}$ used in the experiments and $E_{\min} = 0$ eV, is shown in figures 4.13. In fact, the total ionisation cross section for electrons of energies T above 40 eV is larger than the integral starting at the experimental $E_{\min}$ by 20–40%. At 20 eV and 30 eV, the deviation is up to a factor of 2.5. This means that the extrapolation of the SDCS has to be carefully estimated.

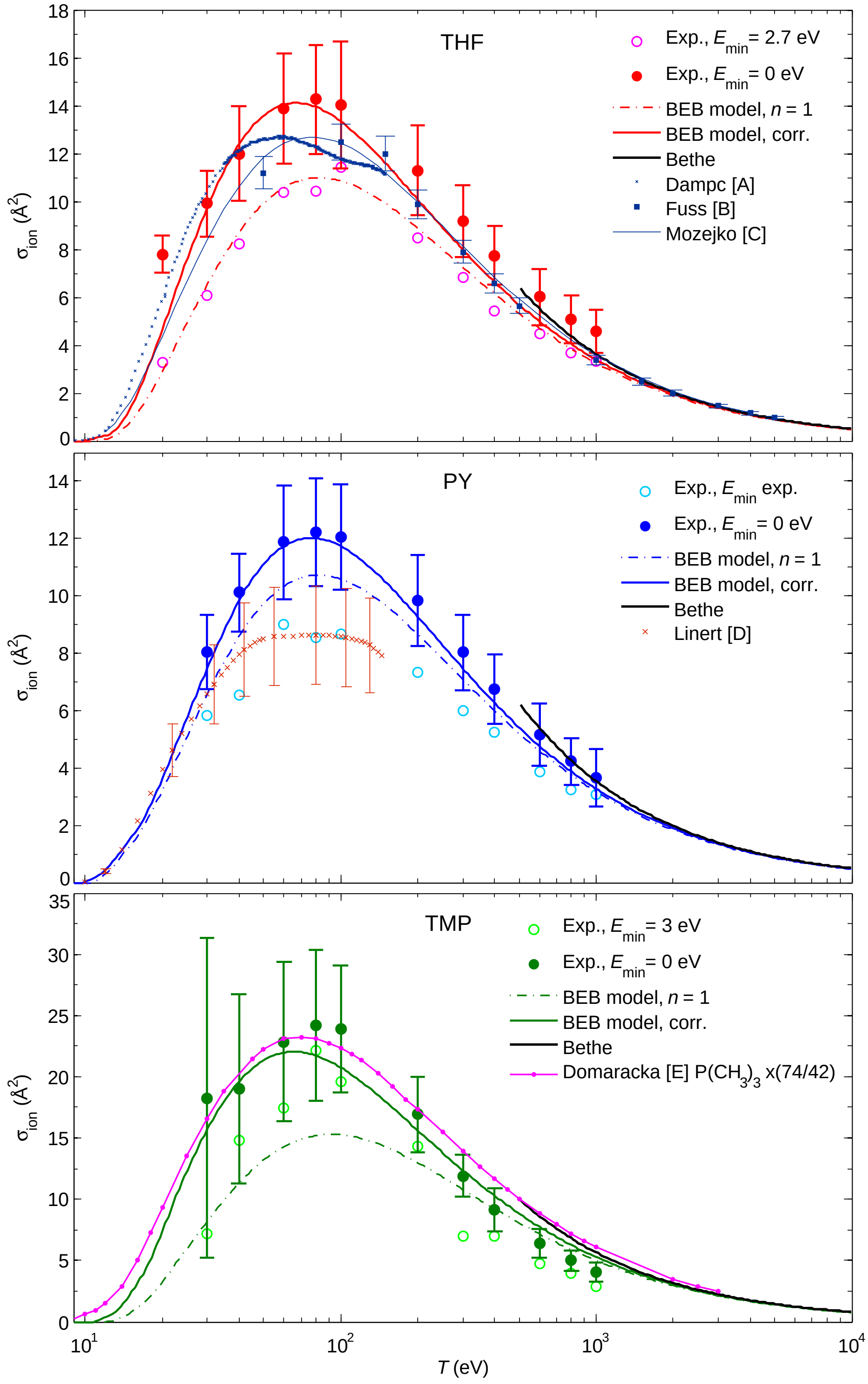

Figure 4.13: Total ionisation cross sections of THF, PY and TMP obtained by integrating the measured DDCS data and calculated from the BEB model and the Bethe approximation. These are compared with literature data (A [36], B [62], C [140], D [128], E [43]).

4.4.4.1 BEB model function

In this work, the BEB model given in equation 2.19 was used to determine the total ionisation cross section. This model was chosen because it enables the calculation of partial ionisation cross sections for each molecular orbital. This is important for the determination of the energy loss of the incident electron by an ionisation interaction in track structure calculations.

The original version of the BEB model (without factor n_{BEB}, see section 2.2.6) using parameters from table 4.2 dramatically underestimates the integrated experimental data at energies below about 300 eV, when an extrapolation to zero secondary electron energy is applied. This is in accordance with the underestimation of the SDCS for the production of low energy secondary electrons observed in section 4.4.3.1.

It is worthwhile to notice that the total ionisation cross section significantly changes when applying the experimental value for the ionisation potential instead of the calculated value (see section 4.2). This not only results in a lower threshold for ionisation processes but also increases the total ionisation cross section at low electron energies. The increase was 8–10% at 20 eV and factors of 22, 7 and 11 at the calculated ionisation thresholds for THF (10.94 eV), PY (10.56 eV) and TMP (12.02 eV), respectively.

Table 4.5: Factors n_{BEB} applied to the BEB model for the calculation of the total ionisation cross sections of THF, PY, PU and TMP listed for each molecular orbital.

	THF	PY	PU	TMP
1	1	1	1	1
2	1	1	1	1
3	1	1	1	1
4	1	1	1	1
5	1	1	1	1
6	3	1	1	1
7	3	3	1	1
8	3	3	1	1
9	3	3	1	3
10	3	3	3	1
11	1	3	3	1
12	3	1	3	1
13	1	3	3	3
14	3	1	3	3
15	3	3	3	3
16	3	1	3	1
17	3	1	3	1
18	1	1	3	1
19	3	1	3	1
20	1	1	3	1
21		1	1	3
22			3	3
23			3	3
24			1	3
25			1	3
26			1	3
27			1	3
28			3	3
29			3	3
30			1	3
31			1	3
32				3
33				3
34				3
35				3
36				3
37				3

To improve the description of the integrated experimental data (from zero electron volts), a correction factor $n_{\text{BEB}} = 3$ was applied for molecular orbitals where the Mulliken population exceeded a specified threshold (see section 4.4.3). This factor was used because the contributions from atomic orbitals with principal quantum numbers of three were always dominant with respect to those of larger principal quantum numbers. The best agreement with the data derived from the experiment is obtained for Mulliken populations larger than 0.40 for THF, 0.47 for PY and 0.34 for TMP. The factors n_{BEB} are listed in table 4.5 for each molecular orbital.

For PY, the corrected BEB model agrees well within the experimental uncertainties with data measured at the PTB (figure 4.13). The maximum in the cross section data is well reproduced, while the model is up to 13% lower than the integrated experimental data for energies above 100 eV, which is within the data uncertainties.

For THF (figure 4.13), integrated experimental data agree with the BEB model within the uncertainties except the data points at 20 eV and 1 keV. Excellent agreement is observed in the region of the maximum, while for energies above 100 eV relative deviations increase with increasing energy to 27% at 1 keV. The data point at 20 eV is a factor of 1.8 larger than the model data, despite the underestimation of the experimental SDCS by the SDCS model function. The Mulliken population threshold for calculating the BEB model data of THF may even be chosen to be somewhat larger. However, a threshold of 0.5 would decrease the cross section data in the maximum region by 20%.

For TMP the situation is less satisfying (figure 4.13). For energies up to 400 eV, the model function describes the integrated experimental data within the uncertainties. However we point out that the data point at 30 eV is 16% larger than the model data and has a very large uncertainty, which is both due to the overestimation of the SDCS data by the SDCS model function. On the other hand, the data points at energies 80, 100 and 200 eV are 10% larger, despite the lower SDCS model data compared to the experimental SDCS values. The deviations of the SDCS model data essentially arising from the fit of the SDCS model function parameters. Nonetheless, the resulting larger uncertainties of the total cross section data are acceptable, as the absolute values are more realistic. At energies 600–1000 eV, the model function of the total ionisation cross section is underestimated by as much as 25%. This deviation is not due to the underestimation of the SDCS at high energies E by the SDCS model function, as this affects the total cross section by less than 6%. As stated before, the observed deviations in the total and differential TMP data may arise from the data analysis of the data measured by the relative flow technique and put to the absolute scale by using nitrogen data [6].

4.4.4.2 Bethe approximation

In the high energy range, the cross section data are compared to the Bethe approximation given in equation 2.14. The relativistic version of the Bethe cross section was given by Kim et al. [117] as

$$\sigma_{\mathrm{Bethe}} = \frac{4\pi a_0^2\alpha^2}{\beta_t^2}\sum_{i=1}^{i_{\max}} M_{\mathrm{i}}^2\left[\ln\left(\frac{\beta_t^2}{1-\beta_t^2}\right)-\beta_t^2+C_{Ri}\right], \tag{4.45}$$

where $\beta_t^2 = 1 - 1/\left(1+T/mc^2\right)^2$, $M_{\mathrm{i}}^2 = N_i R/2B_i$, N_i is the number of electrons in the i-th orbital $C_{Ri} = \ln(R/B_i) + 2M_{\mathrm{i}}^2(1-\ln\,\alpha)$ and α is the fine structure constant. Due to the absence of data for differential oscillator strenghts, required for equation 2.14, the above formula was used. Ionisation cross sections obtained by equation 4.45 are also shown in figures 4.13 to reproduce the BEB cross section data at energies above 1 keV.

4.4.4.3 Comparison to literature data

a) Tetrahydrofuran.

In the literature, measurements of ionic fragments were carried out for THF by several groups [36, 62]. Ionisation cross section data were also calculated by Możejko and Sanche [140] using the BEB model and by Champion [27] applying *ab-initio* theories within the first Born approximation. Those data are shown in figure 4.13.

Fuss et al. [62] determined the ionisation cross section from measuring ionic fragments of THF produced by the impact of electrons of energies between 50 eV and 5 keV using time-of-flight spectrometry. Their data are supported by the calculated values of Możejko and Sanche [140] (12 eV–4 keV). Dampc et al. [36] applied the mass spectrometry technique for electron impact up to an energy of 150 eV to determine relative cross section data. In figure 4.13, these data were normalised at their maximum to the maximum value of Możejko and Sanche [140] as their data had been previously compared in that way [36]. In comparison to the data of Fuss et al. and Możejko and Sanche, the data of Dampc et al. increase faster with increasing energy from the ionisation threshold to the energy of the maximum. Moreover, the maximum is shifted from about 85 eV to 60 eV. For energies between 60 eV and 150 eV, the data of Dampc et al. show a different behaviour than those of other authors due to a dip at 100 eV. At 150 eV, their data appear to continue to be in agreement with those of other authors. The *ab-initio* calculations of Champion [27] (not shown) are in good agreement with the data of Dampc et al. at energies below 100 eV (when the experimental data are normalised to the maximum of the values determined by Champion). However, the theoretical data of Champion are up to about 60% lower than ionisation cross sections of other authors at energies above 100 eV.

The BEB model data for the total ionisation cross sections in this work (using factor n_{BEB}), also agree well with the experimental data of Fuss et al. [62] for energies above 100 eV. At 50 eV, the data of Fuss et al. and Możejko and Sanche [140] are about 20% lower. The larger cross section values at energies 30–100 eV are supported by the data of Dampc et al. [36] and Champion [27], where the maximum appears also at a similar energy of 58.5 eV. In fact, the absolute maximum value in the data of Champion is only 5% lower than the BEB model data in our work.

b) Pyrimidine.

Ionisation cross sections of PY were published by Linert et al. [128]. This group measured ionic fragments of PY by mass spectrometry and additionally determined the absolute total ionisation cross section with a total ion collection technique. Their data support our experimental data and, hence, the BEB model function at energies up to 25 eV. Both data form a maximum at 80 eV, but the maximum in the data of Linert et al. is 42% lower in magnitude.

It is interesting to compare the PY data also to ionisation cross sections of the pyrimidine nucleobases cytosine and thymine. Shafranyosh et al. [165] determined total ionisation cross sections of cytosine from measuring the absolute yield of positive ions by a mass spectrometry technique. The energy dependence of their data is similar to the cross sections measured by Linert et al. within the experimental uncertainties, being about 11% lower in the maximum region.

Total ionisation cross sections for cytosine and thymine have been calculated by several groups. Bernhardt and Paretzke [9] used the Deutsch-Märk formalism as well as the BEB model with orbital electron energies obtained from RHF calculations with two different basis sets. Both basis sets lead to similar values of the total ionisation cross sections at lower energies [9]. However, the deviation between the models increases with increasing energies, reaching 30% higher values for the BEB model at 1 keV (see [9]). Możejko and Sanche [139] also used the BEB formalism to determine total ionisation cross sections of the nucleobases. The absolute ionisation cross sections for cytosine are the lowest among the four nucleobases. However, the data are similar or slightly larger than those of thymine when they are divided by the number of electrons in the respective molecule. Figure 4.14 shows that those normalised cross sections agree within 16% in the region of the maximum and 12% at 1 keV. In the region of the maximum, the PY model function is best reproduced by the data of Możejko and

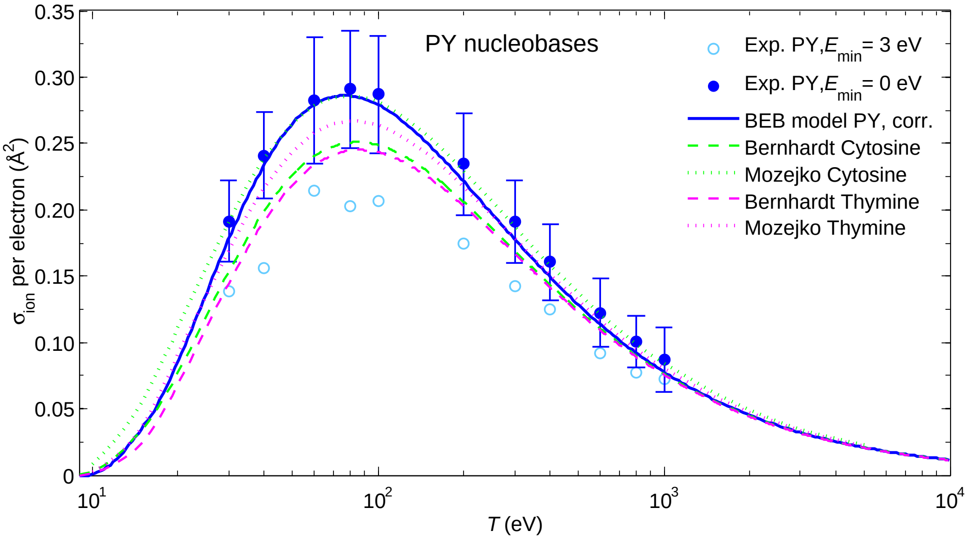

Figure 4.14: Total ionisation cross section of PY, cytosine and thymine, divided by the respective numbers of electrons in the molecule.

Sanche, while better agreement with the data of Bernhardt and Paretzke is observed at 1 keV. A third set of calculated cross sections for the nucleobases is provided by Tan et al. [176]. These authors calculated inelastic cross sections by applying the dielectric response theory and the first Born approximation. For energies above 80 eV, their inelastic cross sections (being the sum of ionisation and excitation cross sections) agree within 5% with the ionisation cross sections determined by Możejko and Sanche [139]. This indicates that either the data of Tan et al. are underestimating the inelastic cross section, or those of Możejko and Sanche and the model function for PY are too large. To draw final conclusions, more data on ionisation cross sections of PY are needed.

c) Purine.

Electron-impact ionisation cross sections of PU were determined by integrating the respective SDCS, using $E_{\text{min}} = 0$ eV. Those data, divided by the number of electrons in the PU molecule, are shown in figure 4.15. As model function, the BEB model was used with orbital energies from table 4.2 and factors n_{BEB} listed in table 4.5. Those factors were again obtained from the Mulliken population analysis for the PU molecule (table 4.3) when populations of atomic orbitals with principal quantum numbers larger than two were at least 0.48. This arbitrary value is similar to those found for THF and PY (0.40 and 0.47, respectively).

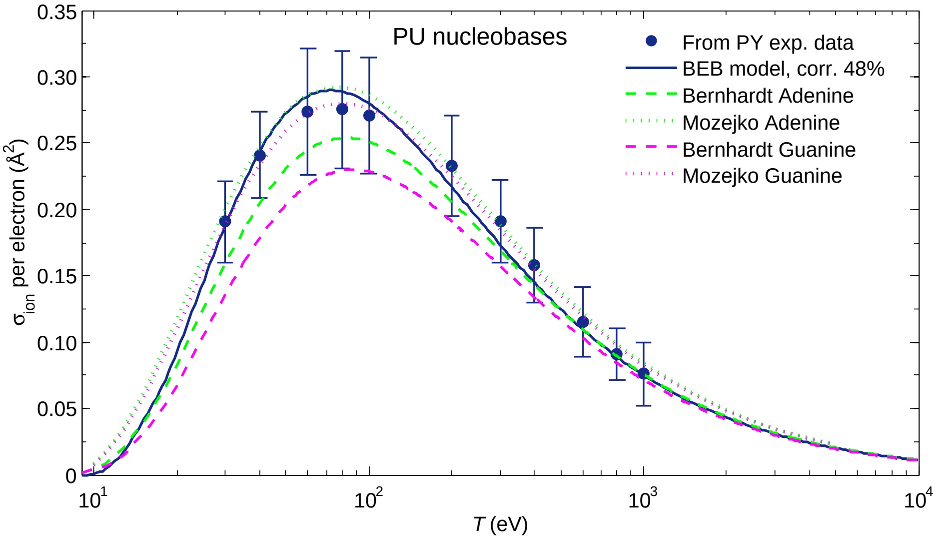

Figure 4.15: Total ionisation cross section of PU scaled from those of PY and calculated by the BEB model. The data are divided by the respective numbers of electrons in the molecule and compared to literature data for adenine and guanine.

The PU data compare reasonably well to literature data, calculated for the purine nucleobases adenine and guanine [9, 139, 176], as mentioned in the previous section when discussing the data for cytosine and thymine nucleobases. Generally, the absolute ionisation cross section of guanine is larger than for adenine and has the largest values of the four nucleobases. However, the situation reverses when ionisation cross sections are normalised to the number of electrons in the molecule (figure 4.15). The deviation between the data, normalised to the number of electrons in the respective molecule, is up to 27% in the region of the maximum and 15% at 1 keV. In fact, the ionisation cross section at energies above 1 keV scales with the number of electrons in the molecules. As for PY, the PU model function is best reproduced by the data of Możejko and Sanche [139] in the region of the maximum, while better agreement with the data of

Bernhardt and Paretzke [9] is observed at 1 keV. The inelastic cross sections of Tan et al. [176] are, again, up to 4% lower than the ionisation cross sections calculated by Możejko and Sanche. Also for PU nucleobases, more data are required to determine the ionisation cross sections more accurately.

d) Trimethylphosphate.

In figure 4.13 (page 140), ionisation cross sections of TMP are compared to data calculated by Domaracka et al. [43] for trimethylphosphine $P(CH_3)_3$ by means of the BEB model. In the graph, the latter data are multiplied by the ratio of the electron numbers of both molecules to enable comparison. In this case, the calculated data of both molecules agree within 10%. This agreement supports the previous suggestion that the absolute values of TMP data for energies 300–1000 eV were underestimated in the experiment. Hence, the BEB model data of TMP appear to be realistic.

4.4.4.4 Fano plot

A Fano plot is used in figure 4.16 to investigate the consistency of the total ionisation cross sections. The Fano plot was introduced in section 2.2.5. In the high energy range, a linear dependence of the normalised cross section data on $\ln(T/R)$ should occur. This is the case for the BEB model functions of THF and PY in this work, which have a slightly lower slope than the data of Możejko [140]. The data of Fuss [62] show the largest slope.

A comparison of the Bethe cross section of THF reveals that the slope of those data is in agreement with the slope in the data of Możejko but of lower magnitude on the y-axis (the data of Możejko are about 4% higher than the Bethe cross section). The BEB model data in our work were calculated with the nonrelativistic version and tend to have a decreasing slope towards higher energies. However, the relativistic version of the BEB model (not shown to keep readability) shows also good agreement with the slope of the Bethe model. In the case of TMP, the kink at 300 eV in the Fano plot supports the assumption made above, that the total ionisation cross sections derived from the experimental data are too low and the model function is a more realistic description. Nonetheless, a recalculation of the Bethe cross section, directly using oscillator strength data, would be necessary to further investigate the consistency of our data.

In summary, the BEB model functions for THF, PY and TMP are in agreement with literature data as well as with the Bethe cross section at high energies.

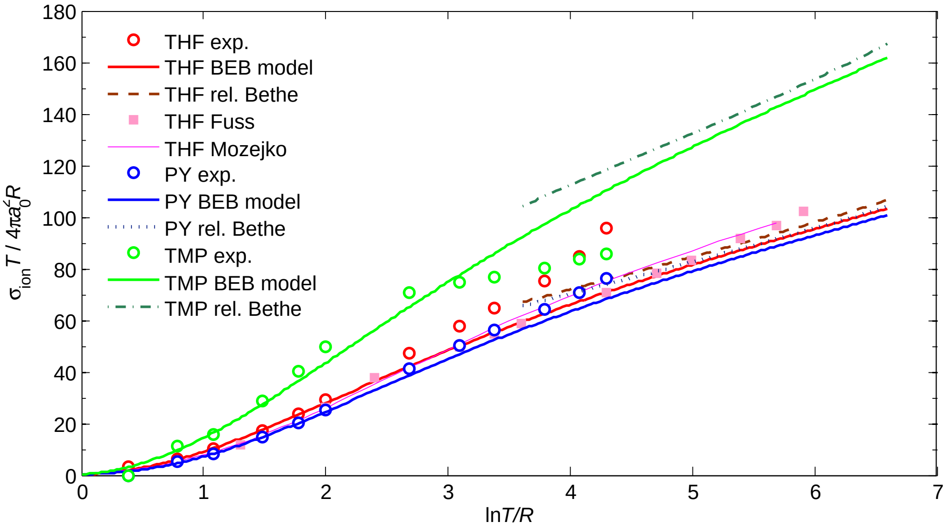

Figure 4.16: Fano plot of the total ionisation cross sections of THF, PY and TMP.

4.4.5 K-Shell ionisation cross section and Auger electron emission

K-edges and the respective Auger-electron emission peaks for carbon, nitrogen and oxygen are distinct features in the DDCS measurements as well as Auger-electron emission peaks arising from an L-shell ionisation of phosphorus in TMP (see figure 4.4). An ionisation of molecular inner (K-shell or L-shell) orbitals may lead to the production of Auger electrons. In this case, the K-shell vacancy is filled by an electron from another orbital and the excess energy, i.e. the difference between the binding energies of the vacant K-shell and the orbital of this electron, is transferred to an electron in an outermore orbital. Subsequently, this Auger electron is ejected and contributes to energy deposition in the medium. This process may continue within the molecule, whereby one vacancy after the other is filled, moving the vacancy towards the valence orbitals. In large molecules, cascades of Auger electrons can occur. In this section, cross sections for K-shell ionisation are provided and the Auger peaks in the experimental DDCS of THF, PY and TMP are evaluated to determine the probability and energy of an Auger electron emission.

Table 4.6: Overview of inner shell binding energies, K-edges and energy regions of Auger peaks identified in the DDCS measurements of 1 keV electrons. Units are in eV.

	carbon	nitrogen	oxygen	phosphorus
B, isolated neutral atoms [154]	291.00 (K)	404.85 (K)	537.28 (K)	187.15 (L1)
				139.14/138.18 (L2/L3)
B, molecules (table 4.2)	305.07–307.52	423.44	557.34–559.41	209.59
				152.4
K-edges in spectra (fig. 4.4)	705	590	455	—
B from spectra	295	410	545	
Auger peak regions in spectra	200–275	320–390	470–520	90–110

Important quantities for the evaluation of K-shell effects are the orbital binding energies. In the upper part of table 4.6 binding energies of inner shells for isolated neutral atoms [154] are compared with those calculated in this work for THF, PY and TMP by means of the system GAMESS, given in table 4.2[‡]. Also, the K-edges identified in the experimental spectra of 1 keV electrons are provided (see figure 4.4). The binding energies calculated from the observed K-edges are listed.

As seen in table 4.6, the calculated binding energies of the inner shells are 14–20 eV higher than the K-shell ionisation energies of isolated atoms. This is due to the rearrangement of the atomic orbitals within a molecule. The binding energies obtained from

---

[‡] Only inner shells with binding energies below 1 keV are considered.

the experimental DDCS support the increase of the K-shell binding energies relative to those for isolated atoms but are only 4–7 eV higher. Comparing these findings to the calculated orbital binding energies for THF by Champion [27], the statement in section 4.4.2 that the data presented in this thesis are more realistic is clearly supported by the measured electron spectra.

The energy regions of Auger peaks in the DDCS spectra are also given in table 4.6. Before discussing the Auger electron production in more detail, the K-shell ionisation cross sections are required to determine the probability for the emission of an Auger electron.

4.4.5.1 K-shell ionisation cross section

The K-shell ionisation cross sections for the collision of electrons of non-relativistic energies ($<$ 10 keV; 20% c) with atoms or molecules can be obtained from the BEB model [117] (see also section 2.2.6), the empirical formula of Casnati et al. [25] or the semi-empirical Deutsch-Märk formalism [38]. Casnati et al. fitted their formula to experimental data with assigned weighting factors. Reasonable agreement of both models with experimental data up to 20 keV was shown by Kim et al. [117]. On the other hand, using the Deutsch-Märk formalism results in significantly lower cross section values. It is known that the contribution of K-shell ionisation cross sections to the total ionisation cross section is rather low (about 0.1% at 1 keV and 1% at 10 keV).

The K-shell ionisation cross sections of THF and PY obtained by the BEB and the Casnati models deviate by less than 5% for energies above 3 keV, as seen in figure 4.17. For energies below, the Casnati model leads to as much as 35% higher values than the BEB model. A 20–30% higher maximum by the Casnati model was also observed by Kim et al. [117] for K-shell ionisation cross section of various atoms. In the graph, only the comparison for PY is shown, but the same discrepancies between both models are observed for THF and TMP. To maintain consistency with the calculation of partial ionisation cross sections of the subshells, the electron-impact K-shell ionisation cross sections are obtained from the BEB model in this work.
Ionisation cross sections, obtained by the BEB model for carbon, oxygen and nitrogen K-shells are also shown in figure 4.17. It is noticeable that the cross sections for the carbon K-shells of THF and PY are similar, which is due to their similar electronic properties.

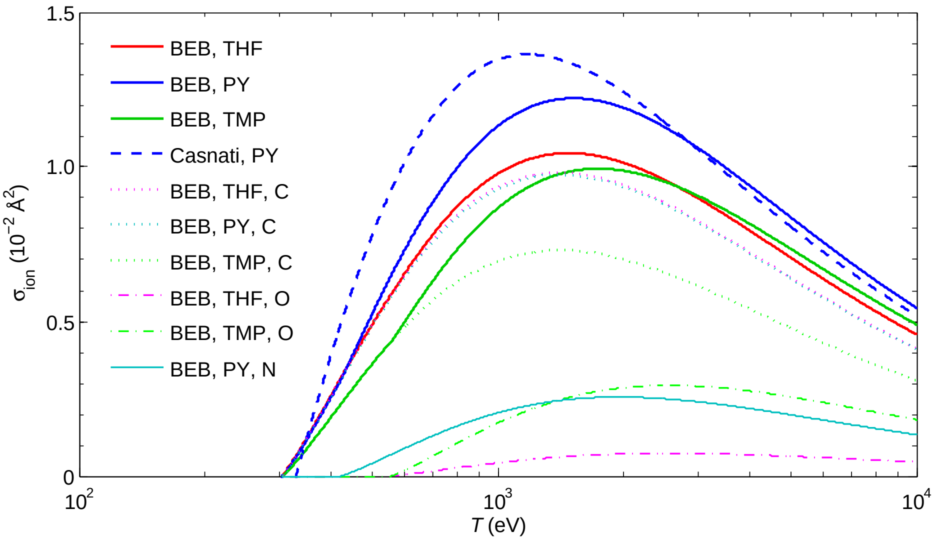

Figure 4.17: Electron-impact K-shell ionisation cross sections of THF, PY and TMP, obtained by the BEB model and the Casnati formula. Ionisation cross sections are also shown separately for the K-shells attributed to the carbon, oxygen and nitrogen atoms.

4.4.5.2 Auger electron emission

The emission probability and energy of Auger electrons following inner-shell ionisation was evaluated from the DDCS measurements. Unfortunately, an analysis of the Auger peaks is only feasible for the carbon, nitrogen and phosphorus Auger peaks of 1 keV electrons. The oxygen Auger peak of 1 keV electrons is superpositioned by the oxygen K-edge, while for 800 eV electrons, both the carbon and oxygen Auger peaks are superpositioned by the oxygen and carbon K-edge, respectively, in the case of THF. For 800 eV, the nitrogen K-edge occurs within the nitrogen Auger peak in the PY spectra. The spectra of 600 eV electrons were not analysed due to the high contribution of noise.

To investigate the carbon and nitrogen Auger peaks, the spline functions for 1 keV electrons were subtracted from the measured electron spectra (see figures 4.6 and fig.SplineFit2). The difference between both curves in the region of the Auger peaks is shown in figure 4.18 for selected emission angles. The Auger peaks were integrated over the secondary electron energy to investigate the dependence of the Auger electrons emission on the angle. The integrated values are shown in figure 4.19. The observed decrease of carbon or nitrogen Auger electron emission probability from THF and PY in forward emission angles may be due to an overestimation of the DDCS by the spline function in the energy range of the carbon Auger peak, which would lead to an underestimation of the Auger peak area.

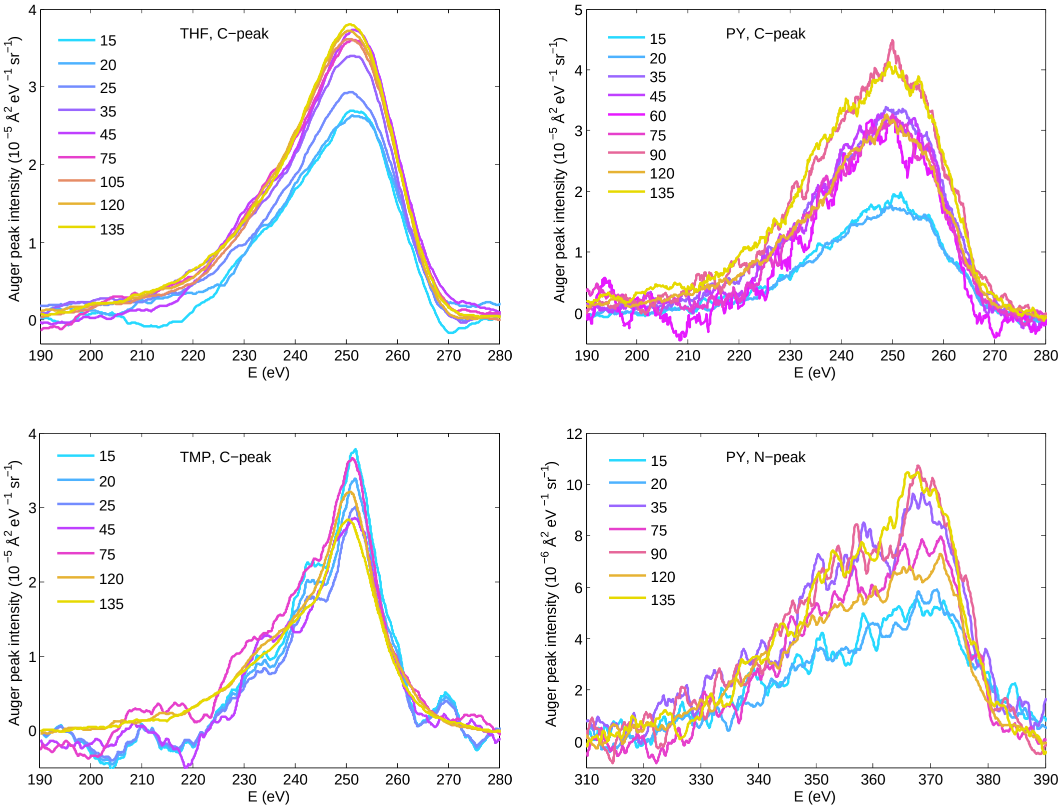

Figure 4.18: Auger peak intensities for carbon (THF, PY, TMP) and nitrogen (PY). The spline function for 1 keV electrons was subtracted from the measured electron spectra.

As, on the one hand, the resolutions of energy and emission angle in the measurements are too low to investigate the Auger electron emission in detail, and, on the other hand, the variations of the Auger peak intensity generally appear as not significant, an isotropic emission of Auger electrons is assumed. However, it is worth noting that in polyatomic molecules, the Auger electron emission might be anisotropic for an external directed beam [31]. The anisotropy arises from the nonequal population of molecular magnetic orbitals after the K-shell ionisation, which leads to an alignment of the ionised molecule relative to the beam axis. The angular distribution of Auger electron emission therefore depends on the total angular momentum of the ionised molecule and varies for different transitions [31, 87, 124]. For molecules with large dipole polarisability, this effect should be enhanced. This might explain the angular dependence of the emission of Auger electrons observed for THF and PY. Due to the lack of data for anisotropic emission, the assumption was made that the emission is isotropic. This assumption enables a reasonable description of Auger electron emission at 0° and 180°.

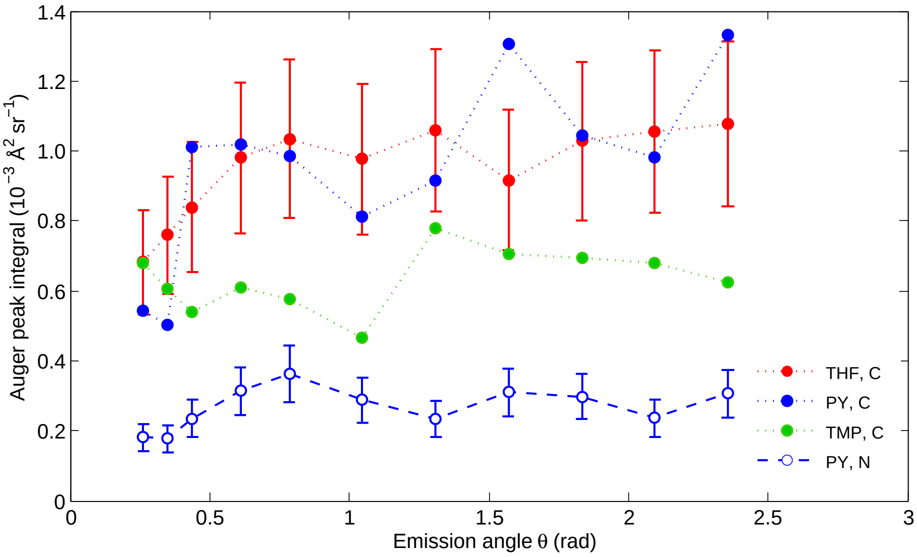

Figure 4.19: Integrated Auger peaks as function of emission angle after the impact-ionisation by 1 keV electrons of carbon and nitrogen K-shells. For some data, errorbars are omitted to improve readability.

The following probabilities for Auger electron emission were obtained by integrating the data shown in figure 4.19 over the emission angles assuming isotropic emission and dividing this value by the respective inner shell ionisation cross section:

- 1.3 ± 0.3 for carbon K-shell ionisation in THF and PY
- 1.1 ± 0.3 for carbon K-shell ionisation in TMP
- 1.6 ± 0.4 for nitrogen K-shell ionisation in PY
- 0.23 ± 0.05 for phosphorous L2-shell ionisation in TMP

In the simulations, it was assumed for simplicity that an ionisation of a K-shell of carbon leads to one Auger electron while two Auger electrons are emitted after ionisation of a nitrogen K-shell. Ionisation of the oxygen K-shell is followed by emission of one Auger electron. L-shell ionisations in TMP are omitted due to the low probability of Auger electron emission. In view of the fact that the K-shell ionisation cross section is only 0.1% of the total ionisation cross section for energies below 1 keV, a negligible modification of the particle track structure is made by those approximations.

4.4.5.3 Shape of Auger peak

Storchi et al. [169] measured and interpreted Auger spectra of PY for 1 keV electrons and found that Auger spectra of such large molecules are complex, particularly due to overlapping electronic transitions (over 5000 double ionised states were identified). For our purpose, it is sufficient to determine the shape of the Auger peaks from the measured spectra of 1 keV electrons. Again, isotropic emission of the Auger electron is assumed and the intensities for the carbon and nitrogen Auger peaks were determined by averaging over emission angles (figure 4.18). Also, the mean value of carbon Auger peaks from THF and PY were used. Two superpositioned Gaussian functions were fitted to the angle-averaged Auger peak as function of Auger electron energy E. A cumulative probability distribution $Y(E)$ was then obtained and fitted to directly calculate the Auger electron energy by

$$\log_{10} E_\mathrm{A} = f_1 \, |\log_{10} Y(E)|^{g_1} + f_2 \, |\log_{10} Y(E)|^{g_2} + f_3. \tag{4.46}$$

Table 4.7: Parameters for equations 4.38a–4.38d applying to both THF and PY.

	carbon THF/PY	carbon TMP	nitrogen PY
f_1	-7.330×10^{-2}	-5.700×10^{-2}	-7.52×10^{-2}
g_1	4.840×10^{-1}	5.200×10^{-1}	4.64×10^{-1}
f_2	3.310×10^{-5}	1.200×10^{-4}	1.18×10^{-4}
g_2	3.890×10^{0}	2.560×10^{0}	3.77×10^{0}
f_3	2.435×10^{0}	2.425×10^{0}	2.60×10^{0}

In the simulations, the respective Auger electron energy is determined for carbon and nitrogen K-shells from equation 4.46 with parameters provided in table 4.7 by random sampling, replacing $Y(E)$ with a uniformly distributed random variable. The average Auger peak intensities, calculated by the superpositioned Gaussian functions, are presented in figure 4.20. After ionisation of the oxygen K-shell, one Auger electron is emitted with a fixed energy of 495 eV, which is the energy of the oxygen Auger peak maximum in the measured spectra of THF and TMP.

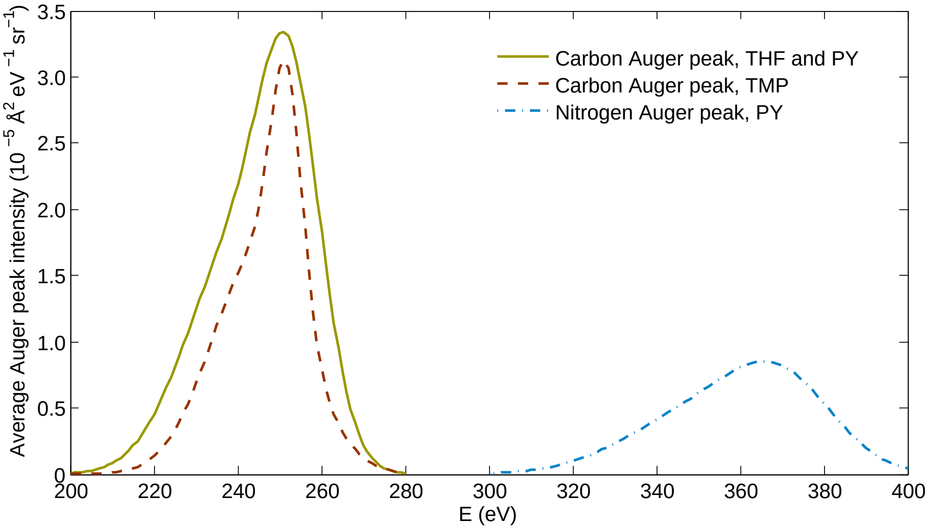

Figure 4.20: Angle-averaged values of carbon and nitrogen Auger peaks in THF, PY and TMP.

4.5 Elastic scattering cross sections

4.5.1 Differential elastic scattering cross sections

Differential elastic scattering cross sections (DelCS) $\mathrm{d}\sigma_{\mathrm{el}}/\mathrm{d}\Omega$ of THF, PY and TMP were measured at the PTB in a crossed-beam experiment for primary electrons with energies T ranging from 20 eV to 1 keV and scattering angles between 5° and 135° [Pub8]. The experiment was described in section 4.4.1.1 and in [Pub8]. In those measurements, the number of electrons ΔN scattered into an angular segment $\Delta\Omega$ is determined, where the energy of detected electrons E is equal to the energy of incident electrons T. The relation of $\Delta N/(\Delta\Omega\Delta E)$ to the absolute differential cross section $\mathrm{d}\sigma_{\mathrm{el}}/\mathrm{d}\Omega(T)$ is given in equation 4.30. While the DelCS of THF and PY were determined on the absolute scale, those of TMP had to be measured by the relative flow technique as described in [135]. This was necessary, because total scattering cross sections of TMP, required to put the measured DelCS on the absolute scale, were not measured due to the low vapour pressure of the gas. It should be pointed out that the contribution of rotational excitation processes is generally included when using the crossed-beam technique. This is due to the finite energy resolution ΔE of the hemispherical energy analyser.

a) Tetrahydrofuran.

The DelCS of THF measured at the PTB and published by Baek et al. [Pub8] cover the greatest range of energies and scattering angles of experimental data in the literature. The PTB data are mostly in reasonable agreement within experimental uncertainties with those of Allan [2] (0.1–20 eV, 10–180°), Colyer et al. [32] (6.5–50 eV, 10–130°), Dampc et al. [35] (6–20 eV, 20–180°), Gauf et al. [68] (0.75–30 eV, 10–130°), Homem et al. [89] (50–1000 eV, 5–130°) and Milosavljević et al. [135] (20–300 eV, 10–110°). The following deviations are observed in magnitude and angular dependence: The data measured at the PTB exhibit a shoulder at scattering angles of about 25°, which is supported by the data of Dampc et al., Gauf et al. and Colyer et al. but does not occur in the cross sections of Homem et al. and Milosavljević et al. Therefore, deviations exceeding the experimental uncertainties are observed when compared to the data of Homem et al. at scattering angles between 20° and 35°. For those of Milosavljević et al., deviations become larger with decreasing energy, where their data are up to three times larger at scattering angles below 60° than the PTB DelCS. At 30 eV and 40 eV, the data of Colyer et al. deviate from those of the PTB at scattering angles above 120°. At 20 eV, the data of Allan, Colyer et al. and Gauf et al. are about 20% lower at all angles, just exceeding the combined uncertainties. On the other hand, the DelCS of the PTB at this energy are in good agreement with those of Dampc et al.

The DelCS of the PTB [Pub8] at 20 eV and scattering angles below 20° are supported by the theoretical data of Trevisan et al. [182], obtained by the complex Kohn variational method. Winstead and McKoy [194] also calculated DelCS of THF for energies 3–50 eV, using the Schwinger multichannel method. At 20 eV, their data support those of the PTB for scattering angles above 20°, where those of Trevisan et al. are significantly higher. Theoretical data, calculated by Gauf et al. [68] using the same method, agree well with their measured data for energies between 6 eV and 20 eV and are in agreement with the data of the PTB at 20 eV and large scattering angles.

DelCS of THF in the higher energy range were calculated by Możejko and Sanche [140] (50 eV–2 keV) using the independent atom model (IAM). Applying the same approach, Baek et al. [Pub8] also provide theoretical values but improved the calculations by including also incoherent intramolecular multiple scattering effects. Another set of DelCS, calculated by the IAM-SCAR method, was published by Milosavljević et al. [134] (50–300 eV) and are in very good agreement with experimental data of the PTB [Pub8]. Also, the values of Możejko and Sanche and PTB are similar for energies of 50 eV, 100 eV and 200 eV between 20° and 180°. However, compared to the experimental data of the PTB, the calculated values are mostly larger, particularly in the energy range below 300 eV. Between 80 eV and 200 eV, the qualitative dependence on the scattering angle is only roughly represented. At 0°, the DelCS of Możejko and Sanche are nearly an order of magnitude higher than the calculated data of Baek et al. [Pub8] for all energies. Surprisingly, the greatest difference between both data sets is observed at 500 eV, where the applied theoretical model should provide more accurate results than in the low energy range. Compared to experimental results, the data of Baek et al. are in good agreement, slightly overestimating the DelCS at angles 110° and above. In contrast to these data, the cross section of Możejko and Sanche show a dip at about 90°, resulting in lower values between 50° and 140° by more than an order of magnitude. This could be due to a lower number of partial waves used in their calculation.

b) Pyrimidine.

DelCS of PY were measured by Maljković et al. [130] (50–300 eV, 20–110°) and Palihawadana et al. [150] (3–50 eV, 10–129°) using a crossed beam experiment and the relative flow method to determine the absolute values. The data are in good agreement with those of the PTB for all energies (figure 4.21). Deviations occur at 30 eV and scattering angles above 110°, where the data of Palihawadana et al. are nearly four times higher. For 200 eV and 300 eV, the data of Maljković et al. are about 40% lower than those of the PTB at scattering angles above 100°.

Calculations of the DelCS of PY were also published by both groups, using the screen corrected additivity rule procedure (SCARND) [130, 150] and the Schwinger variational technique [150]. The R-matrix method was applied by Mašín et al. [131] in the energy range up to 15 eV. The SCARND calculations of Maljković et al. for energies 100 eV and above support the PTB data as they are slightly larger than the measured data of Maljković et al. In agreement with their findings, Palihawadana et al. showed that results from the SCARND theory reproduce the experimental data only at higher energies and large scattering angles. Their calculations using the Schwinger variational technique better reproduce cross sections for low energies and small scattering angles. Superior agreement to the experimental data at 10 eV and 15 eV was obtained by Mašín et al. In summary, the DelCS of PY measured at the PTB are supported by the experimental and theoretical literature data.

c) Trimethylphosphate.

The measured DelCS of TMP are shown in figure 4.23 (page 166). Several data points were excluded from the graphs, as these data will be published in a peer-reviewed journal. Unfortunately, no experimental DelCS are available for comparison. Therefore, the DelCS of TMP were compared to those of THF, also shown in figure 4.23, where the THF data were multiplied by the ratio of the number of electrons in both molecules (74 in TMP and 40 in THF). At energies above 300 eV, good agreement between the experimental DelCS of TMP and THF is observed for scattering angles below 60°, while the probability for large angle scattering from TMP is up to a factor of two higher than for THF. At lower energies, the DelCS are up to a factor of two lower for TMP at scattering angles below 10°. On the other hand, excellent agreement of both data sets is observed at energies 20, 60 and 300 eV for scattering angles above 10°. At energies 30, 40, 80 and 100 eV the agreement is good at scattering angles between 10° and 30°, while the DelCS of THF are lower than those of TMP for large angle scattering by a factor of 2–3. This trend supports the qualitative angular dependence described at the higher energies. Hence in conclusion, the relative angular dependence of the DelCS of TMP is slightly less peaked in forward direction compared to the DelCS of THF. This dependence can be understood from the smaller dipole moment of TMP relative to the one of THF.

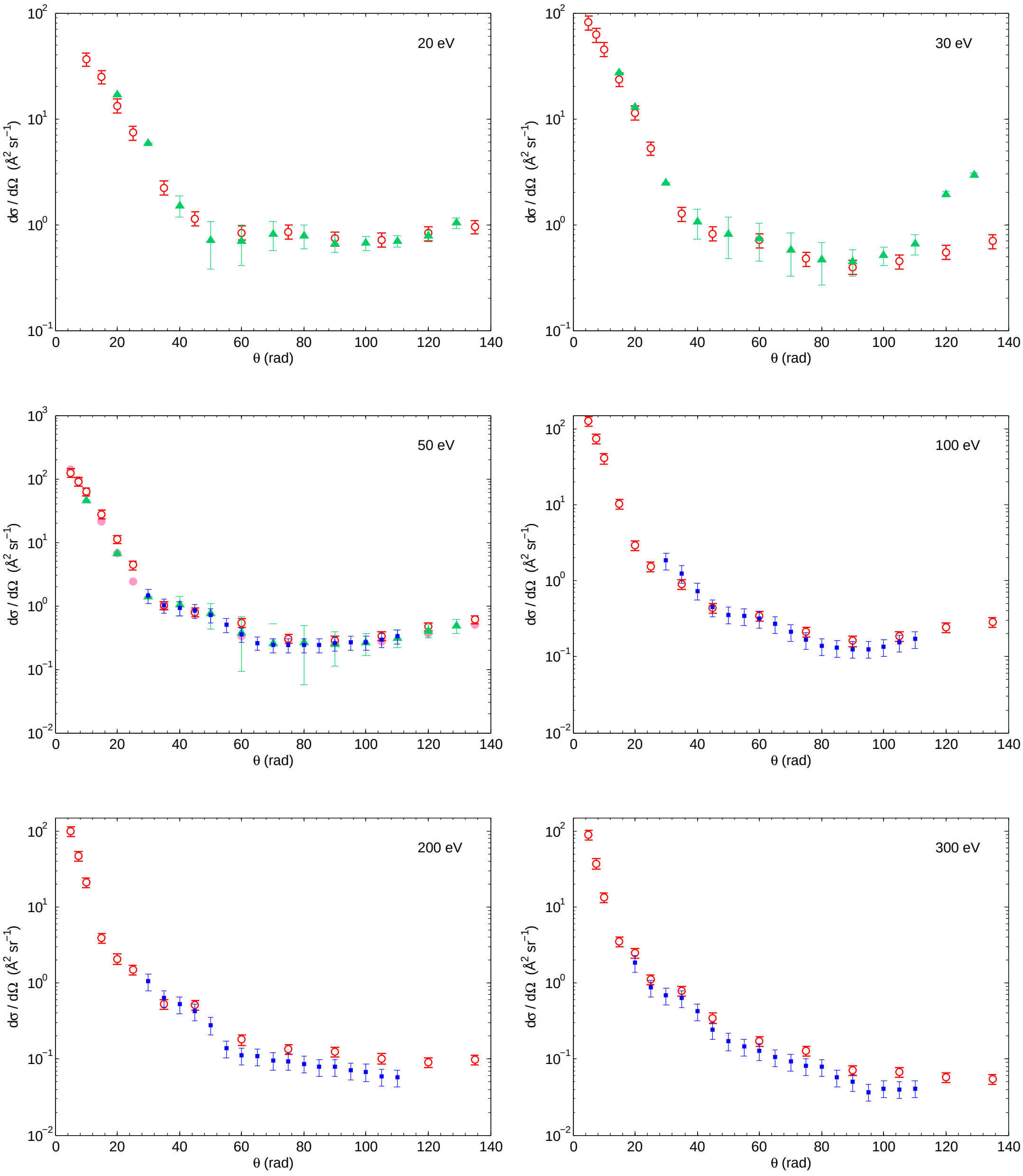

Figure 4.21: DelCS of PY as function of scattering angle for selected electron energies. The data of the PTB (red circles) are compared to those of Maljković et al. (blue squares) and Palihawadana et al. (green triangles). At 50 eV, PTB data for 40 eV (red open circles) and 60 eV (pink filled circles) are shown.

4.5.1.1 Interpolation and extrapolation procedure

In the following, the procedure for interpolation of the measured data of the PTB as a function of the scattering angle as well as the extrapolation to 0° and 180° are described. For electron energies below 20 eV, the experimental data of Baek [Pub8] were complemented by measurements of Colyer et al. [32] in the case of THF. For PY, the data of Palihawadana et al. [150] were taken between 3 eV and 15 eV.

In the lower energy range (up to 200 eV), the molecular phase-shift analysis technique was used [177]. This technique was suggested by Tanaka et al. [177] and is an approximation of the scattering amplitude by partial wave analysis. In fact, equation 4.47 was applied in this work (in units Å^2 sr^{-1}), as the differential cross section is equal to the square of the direct scattering amplitude [101]. This function was fitted via parameters δ_l and N to the measured values. In the description of the scattering amplitude, δ_l are the phase shifts which, however, have to be interpreted as fitting parameters in this procedure. Furthermore, the fit was performed to the DelCS on the log-scale, as the determination of suitable starting parameters was less time consuming due to the smaller range of the data. Partial waves with $l_{\max}$ between 5 and 7 were applied. A higher number of partial waves was unnecessary in this energy range and unfeasible for the higher energies (above 200 eV), where an appropriate number of parameters could lead to an overdetermined problem (only 13 or 14 data points are available from the measurements). Therefore, the angular dependence for higher energies was approximated by using a superposition of exponential functions as given in equation 4.48 (in units Å^2 sr^{-1}).

$$\log_{10}\left(\frac{\mathrm{d}\sigma_{\mathrm{el}}}{\mathrm{d}\Omega}\right)(T < 300\ \mathrm{eV}) = N\left|\sum_{l=0}^{l_{\max}}(2l+1)\left(\mathrm{e}^{2i\delta_l}-1\right)P_l(\cos\theta)\right|^2 - C \tag{4.47}$$

$$\log_{10}\left(\frac{\mathrm{d}\sigma_{\mathrm{el}}}{\mathrm{d}\Omega}\right)(T \geq 300\ \mathrm{eV}) = \sum_{j=1}^{3} a_j \mathrm{e}^{-b_j\times\theta} - C \tag{4.48}$$

Unfortunately, both models required the specification of the value at 180°, which was estimated using the available theoretical data. Below 200 eV, the phase-shift analysis technique provided a reasonable extrapolation to 0°. However, for higher energies the extrapolated values appeared too high due to the character of the exponential model function. For those energies, the extrapolated value at 0° was then estimated beforehand. Generally, the extrapolation to forward angles is a sensitive procedure, as the contribution to the integral of the DelCS is significant. Also, as discussed in the previous section, the contribution of rotational excitations is large at forward angles and can only be approximated from theoretical models. Under those circumstances, the condition that the total elastic scattering cross section is a continuously decreasing function of the electron energy for energies above 100 eV was used to determine the extrapolation (see section 4.5.2).

Uncertainties for the extrapolated data points at 0° and 180° were conservatively estimated to be twice as large as the uncertainties at 15° and 135°, respectively. The covariance matrix of the model function parameters were calculated using equation 4.24 and the covariance matrix in equation 4.21 assuming complete correlation of experimental data uncertainties. Uncertainties of the model function values were determined using equation 4.26.

4.5.1.2 Results for THF, PY and TMP

The results for the model functions of the DelCS of both THF and PY are shown in figure 4.22 and those of TMP in figure 4.23. Parameters for the model functions are given in table 4.8.

At energies up to 100 eV, the phase-shift analysis technique (equation 4.47) provides a good representation of measured data. This model well describes structures occurring in the intermediate angular range of the DelCS. The DelCS value at 0° is similar at all energies for both THF and PY and by about a factor of about two larger for TMP. For all molecules, it is followed by a steep drop of the DelCS up to roughly 25°.

At energies below 200 eV, the most pronounced structure at low energies is a minimum, present at 3 eV and 110° in the PY data. This minimum broadens and migrates to 90° at about 6 eV and to 60° at 15 eV. While only one minimum is present in the THF data, a second minimum occurs in the DelCS of PY at 140°, 10 eV, which shifts to 120° at 20 eV. At 20 eV, the DelCS of THF, PY and TMP is nearly isotropic at scattering angles above 25°. At 30 eV, the minima structures turn into a broad minimum with a dip at about 90°, which is then observed at the same position for energies up to 100 eV. The minimum region is symmetric about 90° as the value at 120° is similar to the one at 60°. The dip at about 90° is shallow for 30 eV but increases by an order of magnitude relative to the value at 20° at 100 eV.

At 200 eV, the DelCS still show the steep drop by two orders of magnitude between 0° and 20°. With increasing scattering angles, the DelCS is continuously decreasing, except for a shoulder structure occurring between 30° and 50° in the THF and PY data. As stated above, the number of partial waves applied in the model function was too few, so that artificial structures occur at scattering angles above 60° in the DelCS at 200 eV. However, the magnitude of those structures is within the experimental uncertainties.

For the DelCS of TMP, these structures are visible at 100 eV and 200 eV, where they lead to an unsatisfactory extrapolation between 135° and 180°. This can, however, be disregarded due to the much larger DelCS at forward scattering angles. For 300 eV and above, the interference of a large number of partial waves leads to an exponential decrease of the DelCS with increasing scattering angle. With increasing electron energy, the DelCS at large scattering angles decreases.

As seen in figure 4.22, the DelCS of THF are mostly similar to those of PY within combined uncertainties. This may be due to the similar dimensions, shape and electronic properties of both molecules. Significant deviations of THF and PY data occur only at 300 eV between 4° and 40° where the PY data are up to a factor of 2.5 higher than those of THF. At energies above 300 eV, the deviations between both data sets generally increase for large scattering angles but are well within the combined uncertainties of the fitted models (the largest uncertainties are 37% for the DelCS at 200 eV).

The finding that the DelCS of THF and PY are similar even at low electron energies contradicts the expected different behaviour at low scattering angles arising from the larger dipole moment and dipole polarisability of PY. Those properties lead to an increase of the DelCS in forward direction (see section 2.2). However, measurements cannot be performed for angles lower than 5° [Pub8] and the contribution of rotational excitations has to be estimated from theory. Hence, it may be underestimated for PY by the applied models. Additionally, a possible underestimation of the absolute DelCS values has been discussed in section 4.5.1 for molecules possessing a large dipole moment. A good agreement of angular dependences of molecules possessing similar shapes, electronic properties and dipole polarisabilities was demonstrated by Palihawadana et al. [151] for benzene, pyrimidine and pyrazine. In contrast to pyrimidine, benzene and pyrazine have no dipole moment, but Palihawadana et al. measured very similar DelCS for all three molecules in the energy region 10–50 eV and scattering angles 10–129°. This implies that dipole properties of the molecules have no significant impact on DelCS above 10° scattering angle.

In summary, the measured DelCS of THF and PY are of similar magnitude and dependence on the scattering angles for electrons with impact energies between 20 eV and 1 keV. Those data take into account rotational excitations only in part, as their contribution at angles below 5° cannot be determined in the experimental setup.

4.5.1.3 DelCS of purine

The differential elastic scattering cross sections of PU are determined from those of the other DNA constituents used in this work (THF, PY and TMP). Literature data of the DNA nucleobases adenine, cytosine, guanine and thymine were also taken into account. Such data were calculated by Możejko and Sanche [139] (50–4000 eV) by the independent atom model as well as by Blanco and García [13] (5 eV–10 keV) using the IAM-SCAR method. Both groups found similar angular dependence (within 3%) for the four nucleobases, while the absolute values of the elastic scattering cross sections were proportional to the molecular weights [13, 139]. They conclude that the elastic scattering cross section mainly depends on the molecular size and the number of atoms in the molecule while less influence arises from differences in the molecular geometries between pyrimidine and purine bases. In fact, the dipole polarisabilities of DNA nucleobases are generally large and differ by 30% (see section 2.1.2), so that an effect on the DelCS seems to be negligible. In the previous sections, the similarity of the angular dependence of elastic scattering cross sections was demonstrated for THF and PY and discussed for molecules of similar size, shape and electronic properties (benzene, pyrazine). Based on those findings, the angular dependence of elastic scattering cross sections for pyrimidine was also used for purine. The absolute values of the DelCS of PU were calculated by multiplying the DelCS of PY by the ratio of total scattering cross sections. As the total scattering cross sections are proportional to the molecular weights and the nucleobases consist of the same atoms, the uncertainty arising from this scaling procedure is negligible.

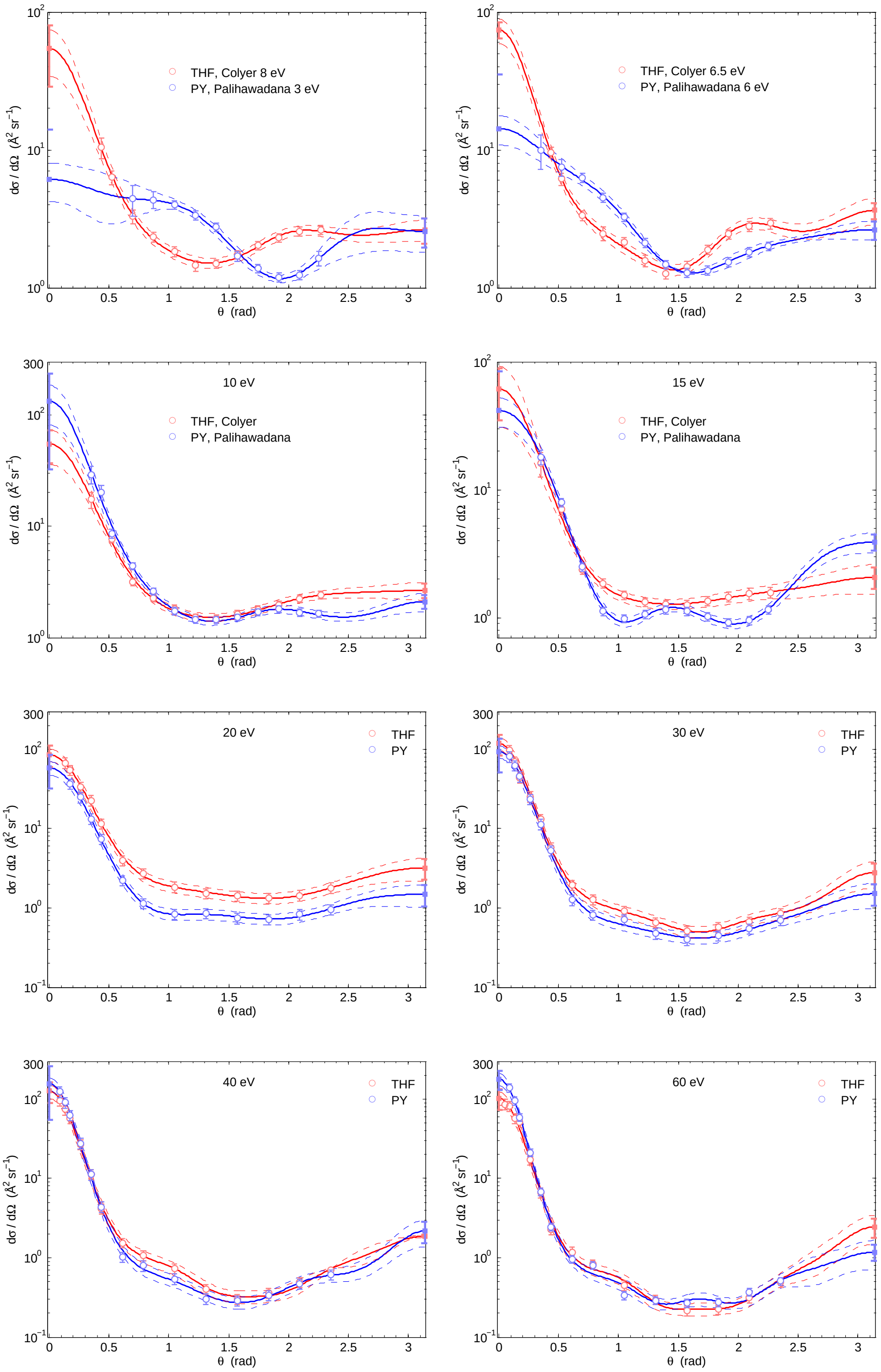

Figure 4.22: DelCS of THF and PY as function of scattering angle. Measured data are shown as well as the curves obtained from the best fit. Dashed lines indicate the uncertainties of the fit. Filled squares show the extrapolated values (see text).

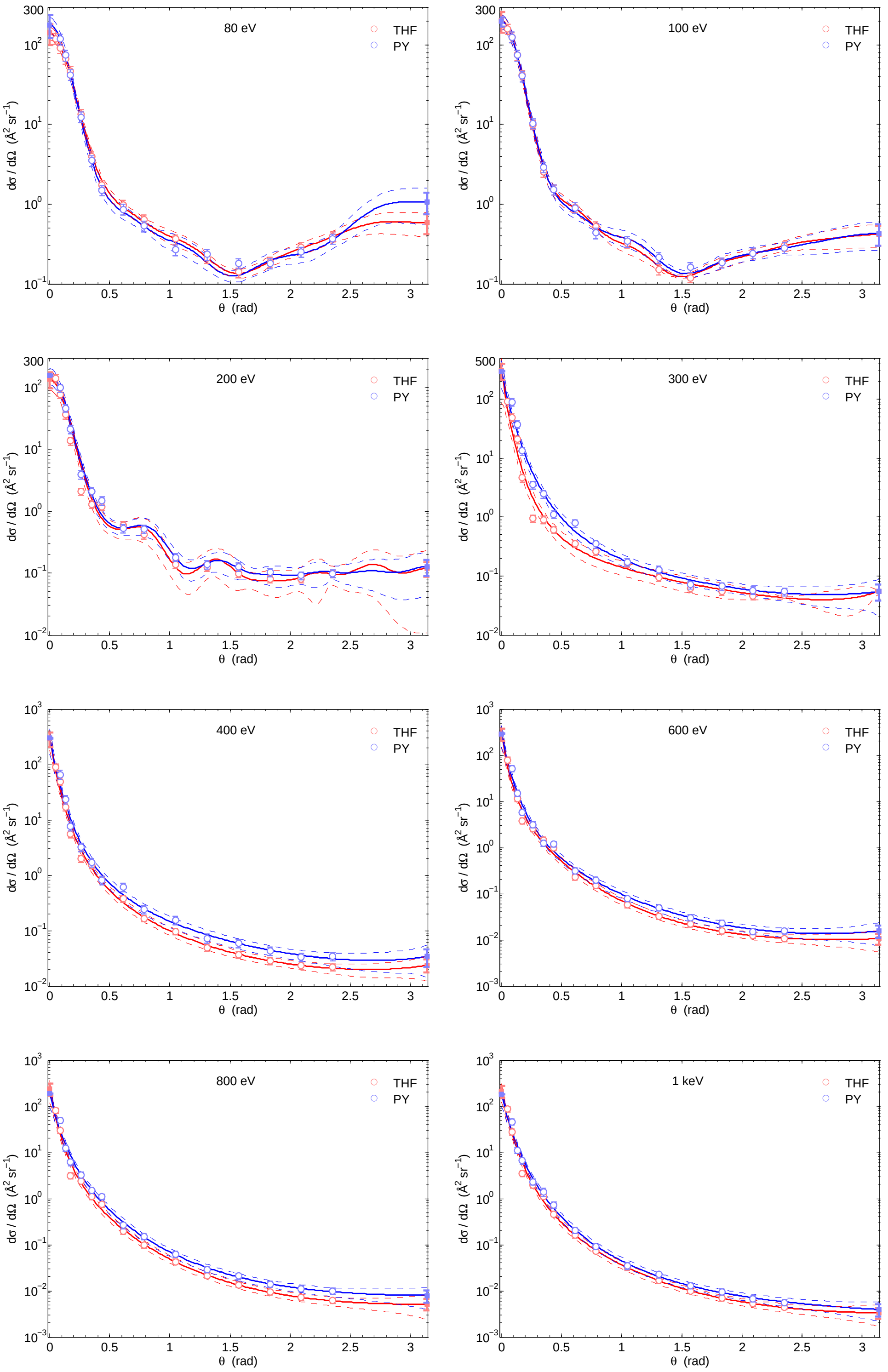

Figure 4.22: Continued.

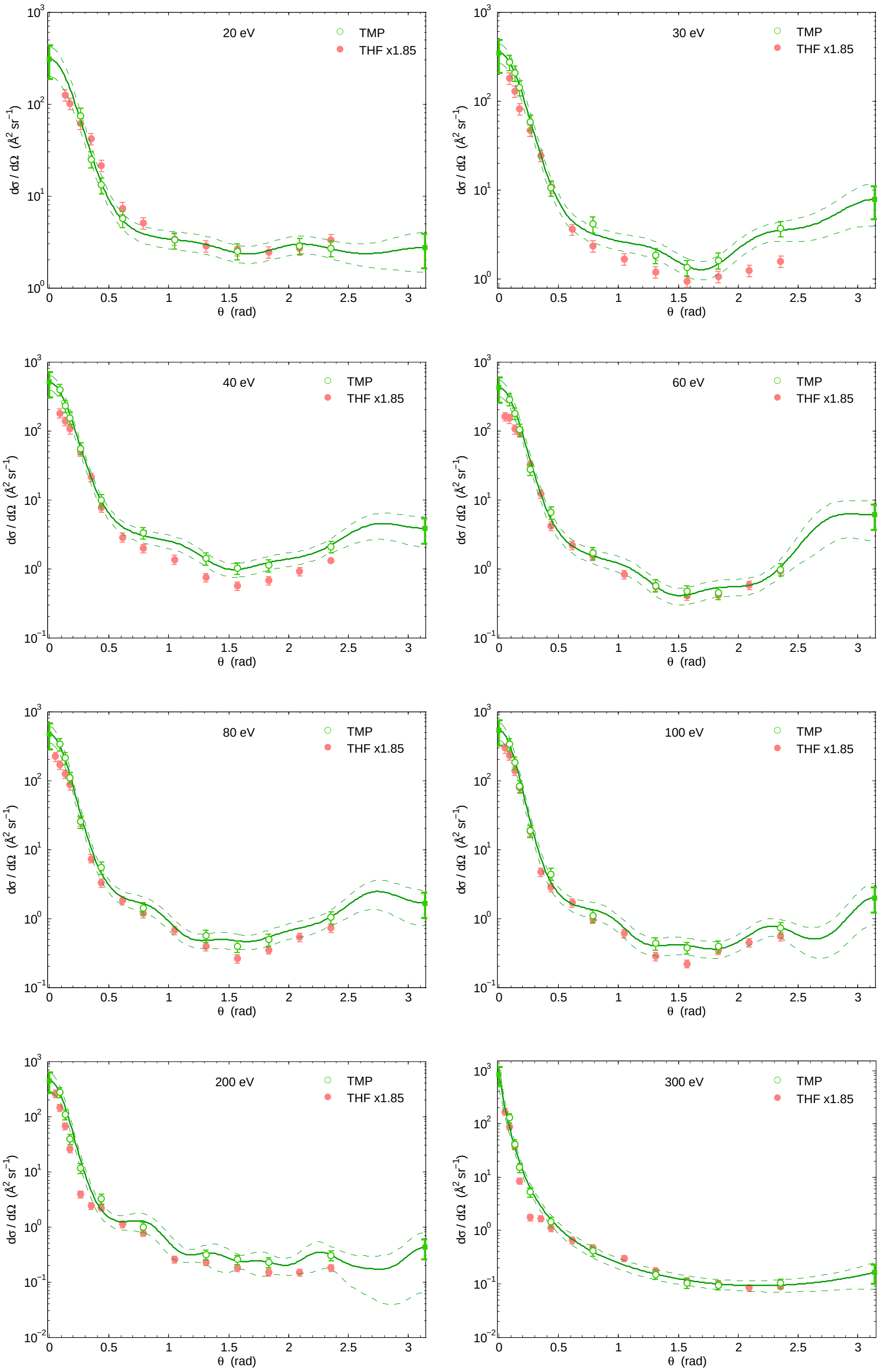

Figure 4.23: DelCS of TMP as function of scattering angle. Measured data and the curves obtained from the best fit are shown. Dashed lines indicate the uncertainties of the fit. Filled squares show the extrapolated values (see text). THF data are presented again for comparison.

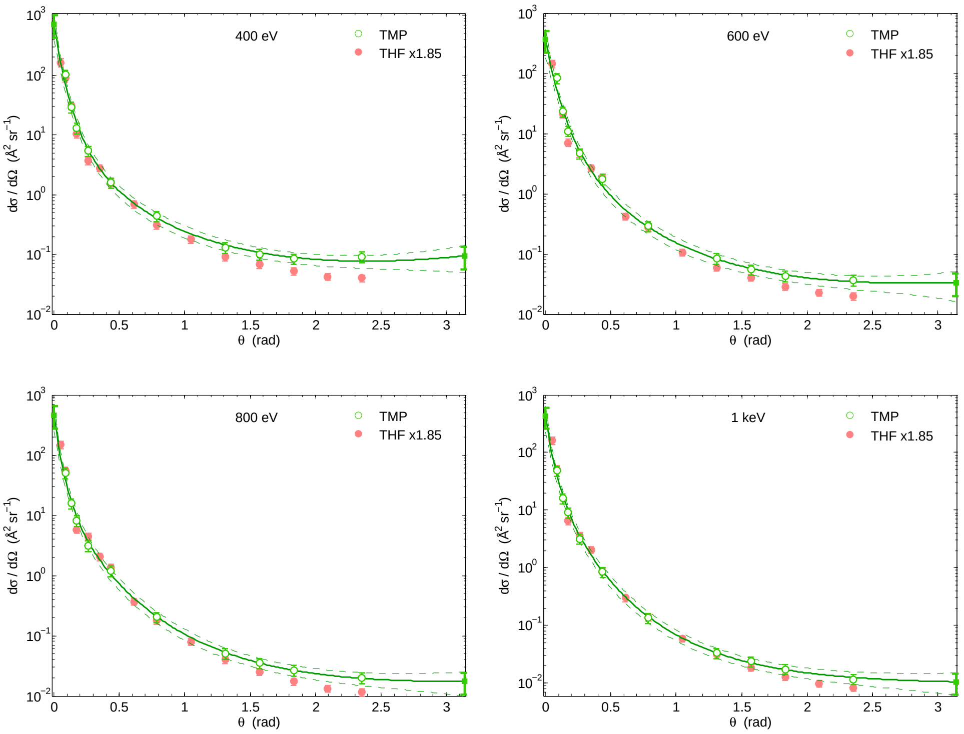

Figure 4.23: Continued.

Table 4.8: Parameters to calculate the DelCS of THF, PY and TMP via equations 4.47 and 4.48 for electrons of energy T. Numbers in parentheses indicate the order of magnitude.

Tetrahydrofuran

T (eV)	N	δ_0	δ_1	δ_2	δ_3	δ_4	δ_5	δ_6	δ_7	C
6.5	5.458(−2)	−8.497(−1)	6.803(−1)	1.054(−1)	−5.925(−3)	−3.101	−3.100			0
8	6.275(−2)	−8.533(−1)	5.721(−1)	1.459(−1)	1.975(−2)	−3.120	−3.124			0
10	5.742(−2)	−8.446(−1)	6.023(−1)	1.497(−1)	3.953(−2)	−3.119	−3.134			0
15	2.785(−1)	−1.319	2.428(−1)	6.475(−2)	2.640(−2)	−3.132	−3.138			1
20	2.908(−1)	−1.422	2.176(−1)	3.395(−2)	3.991(−2)	−3.126	−3.139			1
30	1.903(−1)	−1.363	3.339(−1)	1.085(−2)	2.794(−2)	−3.108	−3.119			1
40	2.559(−1)	1.037	−3.080	−3.022	3.142	−5.683(−3)	1.751(−2)	1.336(−2)		1
60	2.028(−1)	1.008	−3.080	−2.986	3.132	−1.188(−2)	2.151(−2)	1.987(−2)		1
80	5.357(−2)	9.535(−1)	−8.949(−1)	3.142	3.622(−2)	−7.055(−2)	−8.254(−2)	3.104	−1.069(−3)	1
100	3.560(−2)	7.860(−1)	−1.169	3.068	9.831(−2)	−8.300(−2)	−1.086(−1)	3.065	−1.534(−2)	1
200	2.464(−1)	1.633	−1.452(−1)	2.995	−2.831(−2)	1.422(−2)	3.215(−2)	3.142	−4.765(−2)	2
	a_1	b_1	a_2	b_2	a_3	b_3				
300	1.801	4.694(−1)	2.683	4.962	3.334(−5)	−2.927				2
400	2.672	9.992(−1)	1.795	5.772	9.684(−4)	−1.775				2
600	3.824	1.002	1.319	9.832	3.224(−1)	−3.127(−1)				3
800	3.842	9.615(−1)	1.394	7.619	1.454(−1)	−4.107(−1)				3
1000	3.656	9.518(−1)	1.575	5.875	1.003(−1)	−3.850(−1)				3

Pyrimidine

T (eV)	N	δ_0	δ_1	δ_2	δ_3	δ_4	δ_5	δ_6	δ_7	C
3	4.736(−2)	−1.833	5.419(−1)	−2.307(−1)	−7.889(−2)	−3.127	−3.149			0
6	3.281(−2)	−1.171	9.261(−1)	−5.013(−2)	−1.437(−1)	−3.174	−3.142			0
10	3.383(−2)	−8.830(−1)	8.237(−1)	2.545(−1)	4.911(−2)	−3.130	−3.109			0
15	2.577(−1)	−1.152	3.053(−1)	8.500(−2)	5.050(−2)	−3.148	−3.152			1
20	2.241(−1)	−1.272	2.621(−1)	7.646(−2)	5.297(−2)	−3.129	−3.143			1
30	1.707(−1)	−1.291	3.312(−1)	4.326(−2)	5.031(−2)	−3.109	−3.129			1
40	4.034(−1)	7.320(−1)	−3.110	−3.068	3.157	5.087(−3)	6.140(−3)	1.092(−2)		1
60	1.576(−1)	1.223	−3.060	−2.952	3.142	−2.166(−2)	3.241(−2)	2.542(−2)		1
80	4.977(−2)	7.982(−1)	−9.712(−1)	3.141	2.494(−2)	−5.332(−2)	−1.012(−1)	3.088	1.740(−3)	1
100	4.310(−2)	9.694(−1)	−9.621(−1)	3.115	6.731(−2)	−6.296(−2)	−1.045(−1)	3.084	−1.261(−2)	1
200	2.682(−1)	1.661	−1.563(−1)	3.029	−3.022(−2)	1.669(−2)	2.323(−2)	3.132	−3.700(−2)	2
	a_1	b_1	a_2	b_2	a_3	b_3				
300	2.037	5.396(−1)	2.431	3.531	7.004(−3)	−1.255				2
400	2.401	7.413(−1)	2.076	4.753	1.029(−3)	−1.807				2
600	3.608	7.009(−1)	1.756	6.057	1.006(−1)	−6.562(−1)				3
800	3.779	1.059	1.051	6.745	4.468(−1)	−1.708(−1)				3
1000	3.345	1.366	9.677(−1)	6.147	9.452(−1)	1.741(−1)				3

Trimethylphosphate

T (eV)	N	δ_0	δ_1	δ_2	δ_3	δ_4	δ_5	δ_6	δ_7	C
20	3.460(−1)	−1.514	1.802(−1)	2.572(−2)	5.956(−3)	−3.112	−3.121			1
30	3.018(−1)	−1.392	2.749(−1)	−1.966(−2)	3.935(−3)	−3.100	−3.115			1
40	2.608(−1)	−1.328	3.379(−1)	−8.721(−4)	−4.354(−3)	−3.123	−3.113	1.727(−2)		1
60	1.729(−1)	−1.192	4.677(−1)	−7.736(−3)	3.978(−3)	−3.130	−3.103	2.680(−2)		1
80	2.553(−1)	1.178	−3.114	−2.999	3.172	−1.802(−2)	−5.022(−3)	1.514(−2)	1.990(−2)	1
100	1.410(−1)	1.189	−4.679(−1)	3.070	−7.398(−4)	−1.725(−3)	−1.199(−2)	3.121	−2.938(−2)	1
200	3.524(−1)	−1.617	1.752(−1)	6.046(−2)	2.975(−2)	−3.132	−3.167	−2.318(−3)	3.785(−2)	2
	a_1	b_1	a_2	b_2	a_3	b_3				
300	2.554	7.971(−1)	2.258	5.097	1.123(−1)	−6.989(−1)				2
400	2.777	9.971(−1)	1.837	6.313	2.396(−1)	−4.054(−1)				2
600	3.176	1.053	1.437	5.655	9.429(−1)	−1.276(−1)				3
800	3.510	1.181	1.288	9.607	8.628(−1)	−9.270(−2)				3
1000	3.707	1.438	9.801(−1)	1.053(+1)	9.466(−1)	−1.151(−2)				3

4.5.2 Total elastic scattering cross sections

Total elastic scattering cross sections (TelCS) were obtained by numerical integration of the interpolated and extrapolated differential data in the previous section. The integration was carried out according to

$$\sigma_{\mathrm{el}} = 2\pi \int_0^\pi \sin\,\theta \frac{\mathrm{d}\sigma}{\mathrm{d}\Omega}\mathrm{d}\theta\ . \tag{4.49}$$

The integrated data of THF, PY and TMP are shown in figure 4.24. Uncertainty propagation was applied using the integrated values of the G-matrices, subject to

$$G_{\mathrm{TelCS}} = 2\pi \int_0^\pi \sin\,\theta\ G_{\mathrm{DelCS}}\ \mathrm{d}\theta\ . \tag{4.50}$$

to determine the squared uncertainties $u^2_{\mathrm{data}}(\vec{Y}_{\mathrm{el}})$ and $u^2_{\mathrm{model}}(\vec{Y}_{\mathrm{el}})$ of the TelCS $\vec{Y}_{\mathrm{el}}$ by equations 4.25a and b. The covariance matrix of the TelCS data uncertainties was obtained, taking into account the correlation of $u_{\mathrm{data}}(\vec{Y}_{\mathrm{el}})$ which arise from systematic contributions to the uncertainties of the experimental data. Hence, the following procedure was applied

$$C_{data}(\vec{Y}_{\mathrm{el}})_{i,j} = u_{\mathrm{data}}(Y_{\mathrm{el},i})\ u_{\mathrm{data}}(Y_{\mathrm{el},j})\ +\ \delta_{ij}u^2_{\mathrm{model}}(Y_{\mathrm{el},i}) \tag{4.51}$$

The sensitivity of the TelCS on the extrapolation was evaluated by integrating the DelCS in three steps. First, the integration was performed between the lowest scattering angles of the measurement and 180°. For the region 135–180°, it was assumed that the DelCS was constant. Second, the integration was repeated using the data from the model functions for angles up to 180°. Finally, the integration was performed over all scattering angles but the extrapolated DelCS values in the region from 5° to 0° were assumed to be constant. These data are also shown in figure 4.24.

Comparing the four different integration procedures, it was found that the extrapolation to 180° by the model functions influences the TelCS by up to 7%. On the other hand, the TelCS is sensitive to the extrapolation of the DelCS to 0°. In fact, the TelCS increases up to 30% when the DelCS is extrapolated by the model functions instead of assuming a plateau. A significant increase of the TelCS was observed for electrons of energy 300–1000 eV for THF, PY and TMP (up to 9%, 21% and 20%, respectively). Also, the TelCS of THF for energies below 15 eV were up to 29% higher when the model functions were used. It should be noted that this effect occurred even though the DelCS is 'weighted' by the sinus of scattering angles by which the contribution of forward scattering is of less importance than for intermediate scattering angles.

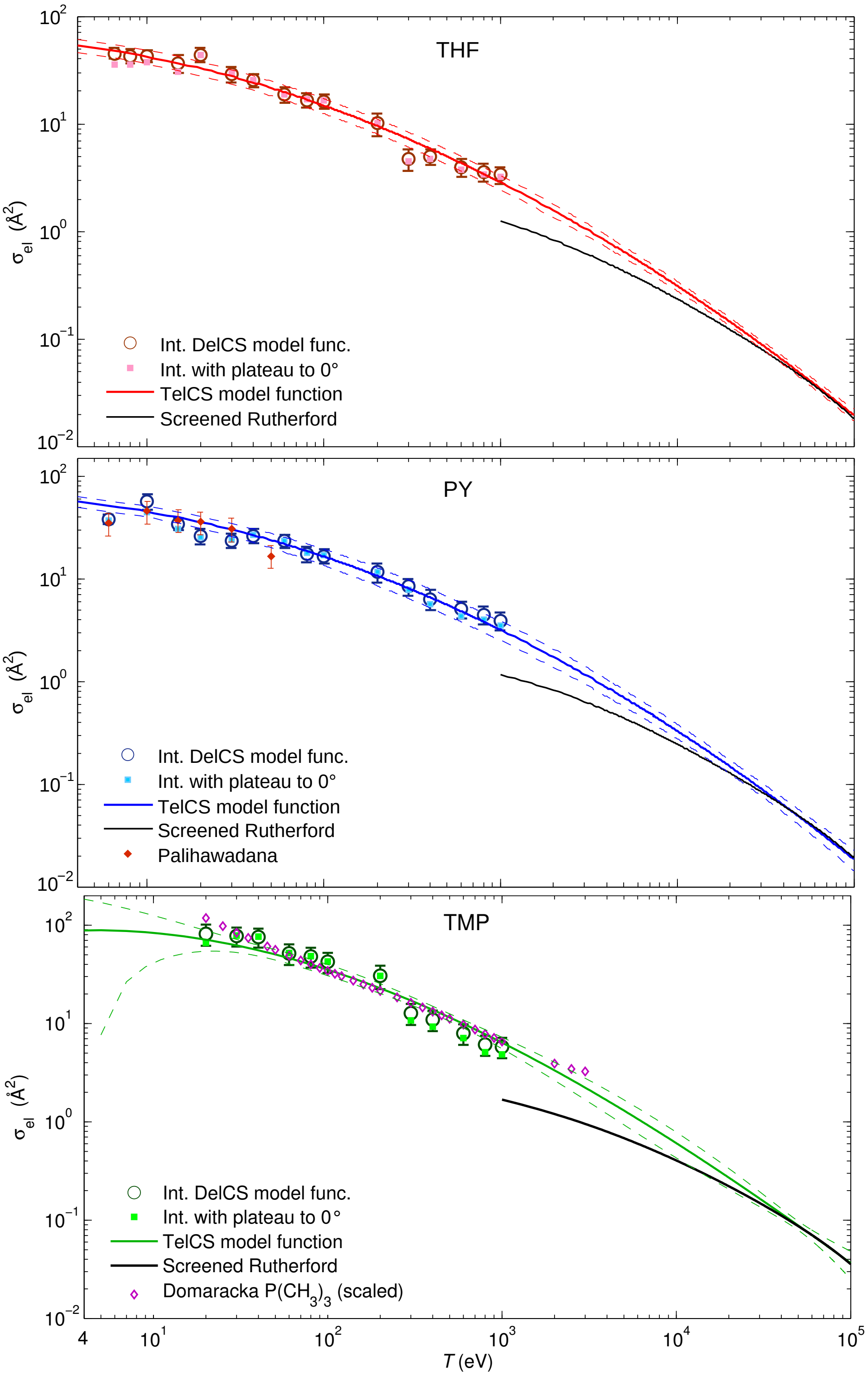

Figure 4.24: TelCS determined by integrating the DelCS model functions of THF, PY and TMP and respective model function for the TelCS. The integration was performed a second time, assuming that the DelCS at 0° is the same as at the lowest measured scattering angle. For PY and TMP, literature data of Palihawadana et al. and Domaracka et al. (trimethylphosphine) are also shown, respectively.

4.5.2.1 Model function

The integrated DelCS were fitted by the following model functions

$$\log_{10}(\sigma_{\text{el}}) = a\ \log_{10}(T)^b + c, \tag{4.52a}$$

$$\log_{10}(\sigma_{\text{el}}) = \sum_{i=0}^{3} d_i\ \log_{10}(T)^i \tag{4.52b}$$

where σ_{el} is in units Å^2 and T is in eV. The parameters are provided in table 4.9. Equation 4.52a is used for THF and PY but a polynomial function had to be used for TMP to satisfy the consistency requirements at low and high-energy limits. At low energies, the TelCS is restricted by the total scattering cross section. In the high-energy limit, the TelCS were calculated by the screened Rutherford formula (equation 2.12b), which appears to provide a physically meaningful extrapolation to energies above 50 keV (see figure 4.24).

Table 4.9: Parameters for the model function for the TelCS in equations 4.52a and 4.52b.

	a	b	c	
THF	–0.169	1.882	1.793	
PY	–0.153	1.952	1.806	
	d_0	d_1	d_2	d_3
TMP	1.921	0.188	–0.220	9.510×10^{-3}

The covariance matrix of the TelCS model function values were then calculated by

$$C(\vec{Y}_{\text{el,fit}}) = C_{\text{data}}(\vec{Y}_{\text{el,fit}}) + C_{\text{model}}(\vec{Y}_{\text{el,fit}}). \tag{4.53}$$

Using G_{TelCS} (equation 4.50), it is

$$C_{\text{data}}(\vec{Y}_{\text{el,fit}}) = G_{\text{TelCS}}\ C_{\text{data}}(\vec{a}_{\text{TelCS}})\ G^T_{\text{TelCS}}, \tag{4.54a}$$

$$C_{\text{model}}(\vec{Y}_{\text{el,fit}}) = G_{\text{TelCS}}\ C_{\text{model}}(\vec{a}_{\text{TelCS}})\ G^T_{\text{TelCS}}, \tag{4.54b}$$

Uncertainty propagation was taken into account in $C_{\text{data}}(\vec{a}_{\text{TelCS}})$, using the covariance matrix of the experimental TelCS $C_{\text{data}}(\vec{Y}_{\text{el}})$ (equation 4.51) in equation 4.20.

The covariance matrix $C_{\text{model}}(\vec{a}_{\text{TelCS}})$ accounts for the imperfect description of the experimental TelCS by the model function and is obtained by the reduced chi-square value in accordance with equation 4.23b.

A peculiarity of the fitting procedure was that the 'observables' were experimentally-based data at energies up to 1 keV, while the theoretical data were used to fit the model function above 50 keV. To prevent an overestimation of the quality of the fit, the reduced χ^2 value (equation 4.22) was evaluated from the experimental data up to 1 keV only. However, the G-matrices were determined for all observables by equation 4.5, to correctly assess the covariances of the data fit at high energies.

4.5.2.2 Comparison to literature data

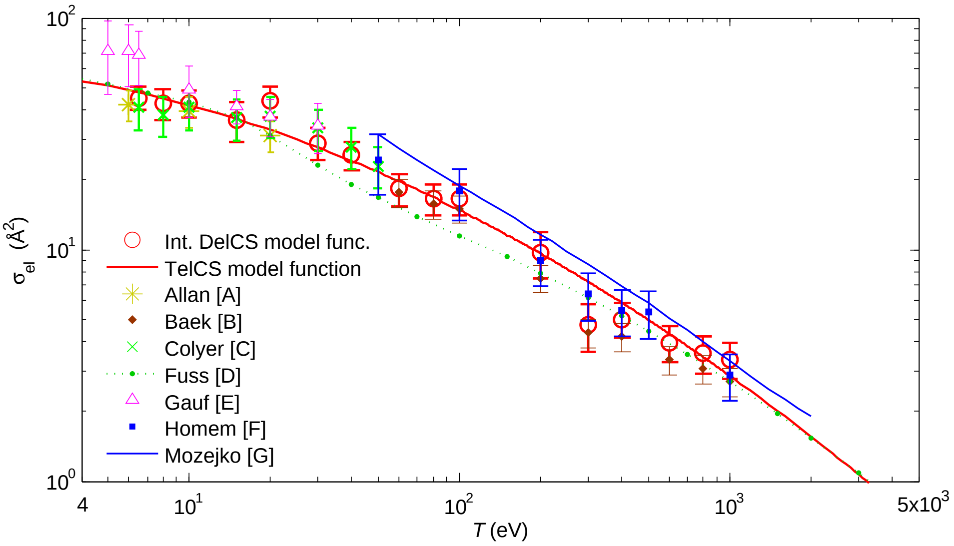

Figure 4.25: TelCS of THF from this work and other authors (A [2], B [Pub8], C [32], D [62], E [68], F [89], G [140]).

a) Tetrahydrofuran.

The TelCS of THF shown in figure 4.25 are between 5% and 33% higher than the values given previously by Baek et al. [Pub8] due to the different approaches for interpolation and extrapolation of the same data set. The TelCS of this work are in good agreement within experimental uncertainties with measured data of Allan [2] (0.1–20 eV), Colyer et al. [32] (6.5–50 eV), Gauf et al. [68] (0.75–30 eV) and Homem et al. [89] (50–1000 eV). At energies below 10 eV, the data of Gauf et al. are generally larger than those of the other authors. In the energy range up to 50 eV, those TelCS are supported by the Schwinger multichannel calculations of Winstead and McKoy [194] (not shown). The data calculated by Fuss et al. [62] (1 eV–10 keV) using the SCAR method agree generally well with our data for energies above 200 eV and below 20 eV. In the intermediate energy range, the data of Fuss et al. are up to 40% lower. The TelCS calculated by Możejko et al. [140] (50–2000 eV) by the IAM have a different energy dependence. Their values tend to have a steeper slope at energies below 1 keV than the data of the other authors, leading to higher values at 50 eV by 35% and nearly a factor of two when compared to the model function and the data of Fuss et al., respectively.

b) Pyrimidine.

In figure 4.24 above, the TelCS of PY determined by Palihawadana et al. [150] (3–50 eV) are shown. This group calculated the TelCS from measured DelCS after extrapolation by the molecular phase shift method. In this work, their DelCS data were used at energies below 20 eV with a similar extrapolation method and, hence, similar TelCS values were obtained. Elastic scattering cross sections of PY were also calculated by Mašín et al. [131] (up to 15 eV) by the R-matrix method (not shown). They point out that an integration of their DelCS over the scattering angles in the experiment of Palihawadana et al. lead to a good agreement with their data. However, the calculated data lead to a larger TelCS if integrated over all angles, due to the larger DelCS in forward direction.

The TelCS data of PY are mostly higher than those of THF, as seen in figure 4.26. This is due to the larger number of electrons in the molecule (42 for PY, 40 for THF). The values of the integrated DelCS model functions agree within combined uncertainties, except for the following data points: The TelCS at 300 eV for THF appears to be too low, which arises from the lower DelCS for scattering angles between 4° and 40° (see figure 4.22). The data point at 10 eV is 30% higher for PY than THF, which originates from the steeper rise of the DelCS at forward scattering angles. At 20 eV, the TelCS are a factor of 1.7 larger for THF (at this energy, the DelCS of THF are larger than those of PY across the entire angular range). The TelCS model functions, fitted to the integrated DelCS by equation 4.52a, are up to 12% larger for PY than those of THF with maximum deviations in the energy region between 100 eV and 1 keV.

c) Trimethylphosphate.

The TelCS of TMP is also shown in figure 4.24 (page 170). The model function describes the experimental data well within the uncertainties for all energies between 20 and 1000 eV. The TelCS of TMP is compared to the data of Domaracka [43], calculated by the independent atom model for trimethylphosphine [$P(CH_3)_3$]. Their data, multiplied by the ratio of the number of electrons in both molecules, are in excellent agreement with our TelCS values in the energy range 30–1000 eV. Towards 20 eV and 3 keV, the data of Domaracka become larger than those predicted by the model function. This behaviour

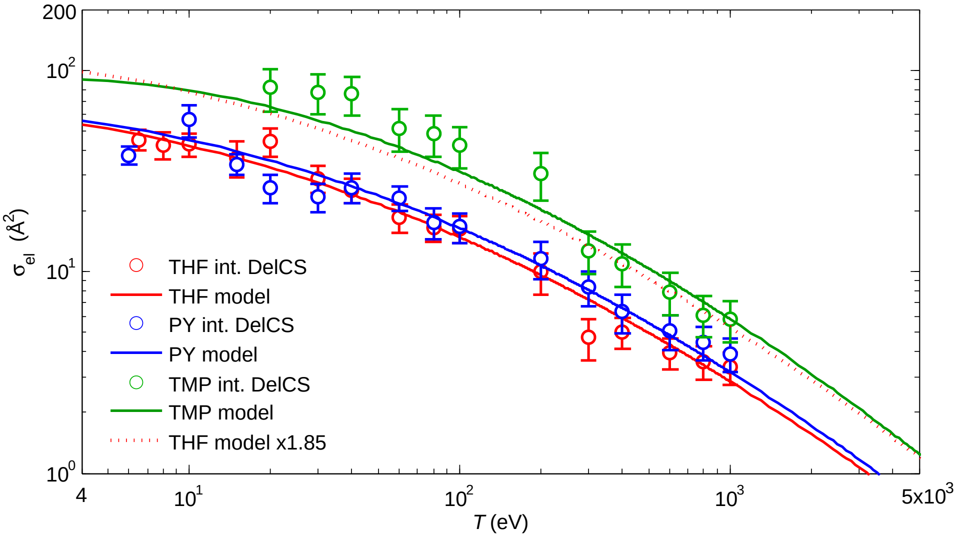

Figure 4.26: TelCS of THF, PY and TMP determined by integrating the DelCS model functions and from equations 4.52a and b. THF data were also scaled to yield TelCS of TMP according to the ratio of number of valence electrons.

has already been observed for the THF data, calculated by Możejko et al. [140] using the same theoretical approach. Furthermore, good agreement between the TelCS of TMP and THF is obtained, when the latter is scaled by the ratio of the number of electrons in the molecules.

4.5.2.3 TelCS of purine

The TelCS of PU were determined by multiplying those of PY with the ratio of total scattering cross sections. This had already been applied to the DelCS of PU in section 4.5.1.3, where the relation between TelCS of the nucleobases was discussed to mainly depend on the size, shape and electronic properties of the molecules [13, 139]. For completeness, the agreement of TelCS data for purine bases in the literature is briefly discussed. The TelCS of adenine were demonstrated by Blanco and García [13] to agree well with Schwinger multichannel calculations of Winstead and McKoy [193], calculated up to 20 eV. In the lower energy range (up to about 100 eV), good agreement of their data for all four nucleobases with those of Możejko and Sanche [139] is observed. However, the deviation between the two data sets increases up to a factor of two at 2 keV, with the data of Blanco and García [13] being larger than those of Możejko and Sanche [139]. Such a large deviation in the higher energy range is unexpected as the independent-atom approximation that was used as basis of the calculations by both groups should provide rather accurate values at these energies.

4.6 Excitation cross sections

Total excitation cross sections were calculated by subtracting the total cross sections for ionisation $\sigma_{\mathrm{ion}}(T)$ and elastic scattering $\sigma_{\mathrm{el}}(T)$ from the total scattering cross sections $\sigma_{\mathrm{t}}(T)$, such that

$$\sigma_{\mathrm{exc}}(T) = \sigma_{\mathrm{t}}(T) - \sigma_{\mathrm{ion}}(T) - \sigma_{\mathrm{el}}(T). \tag{4.55}$$

The complete set of total scattering cross sections of DNA constituents is shown in figure 4.27. Generally, the excitation cross section has the lowest probability of all processes, except in the energy region between the excitation threshold and 30 eV where the ionisation cross section experiences a steep rise and exceeds the excitation cross section above 30 eV. The elastic scattering cross section is always larger than the excitation cross section and dominant at energies below 100 eV for THF and 600 eV for PY and PU. Excitation cross sections, determined from equation 4.55, generally decrease with increasing electron energy after a maximum just below 10 eV. However, these data show a dip around 100 eV, the origin of which still has to be investigated. The depth of this dip increases with larger size of the molecule and was the reason for choosing higher TCS for PY and PU in this energy range (see section 4.3). In fact, the excitation cross section is nearly one order of magnitude lower than the TCS and therefore very sensitive to variations of a few percent in the TCS. An alternative to this procedure would be to decrease the ionisation cross section in the region of its maximum. However, the ionisation cross section has been carefully evaluated in this work and the variation of the model function to the TCS was generally within experimental uncertainties. Therefore, the modification of the TCS was chosen to achieve reasonable descriptions for the excitation cross section data, which have to be verified by experimental data.

Unfortunately, literature data on excitation cross sections of the DNA constituents of interest in this work is fragmentary. Therefore, the following section has the aim to investigate the accordance of the total excitation cross sections determined in equation 4.55 and to estimate the energy loss of an incident electron in an excitation process. The literature discussed in the following is not exhaustive.

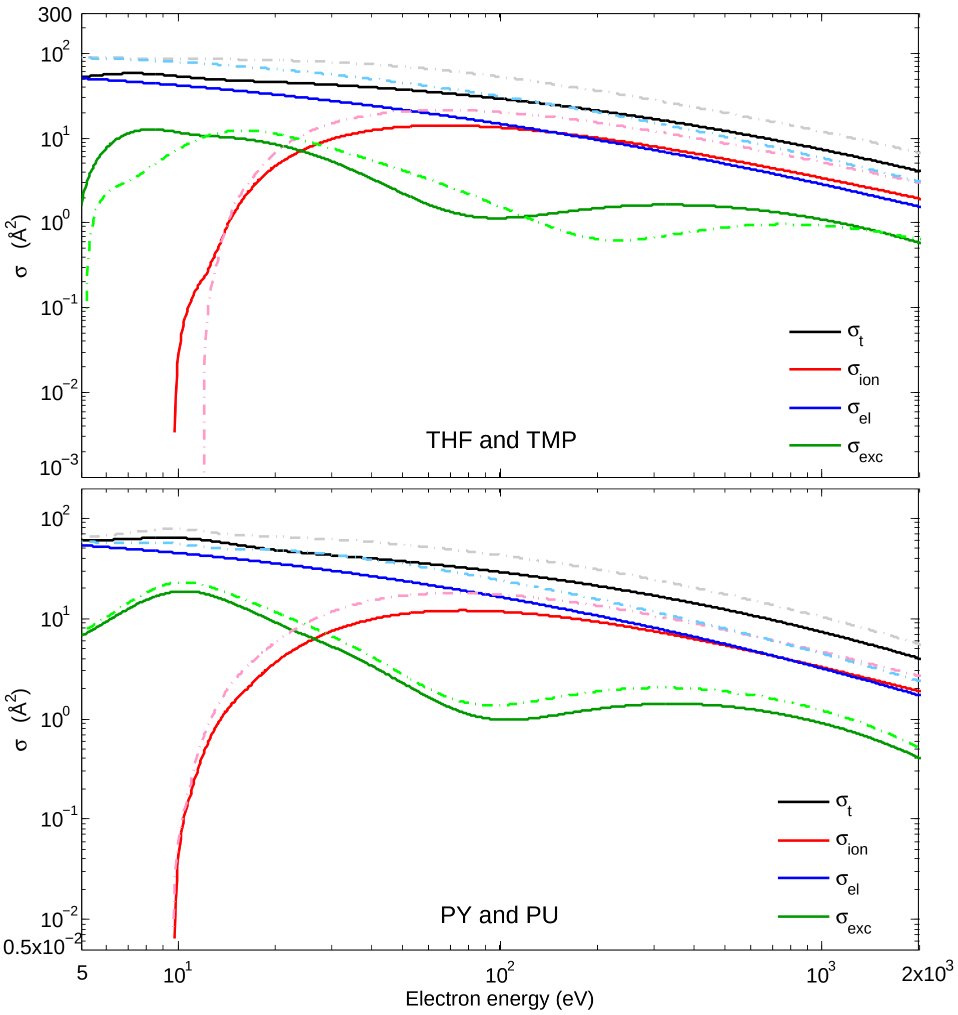

Figure 4.27: Total scattering cross sections σ_{t} and total cross sections for scattering of electrons on THF, PY (solid lines), TMP and PU (broken lines), leading to ionisation σ_{ion}, elastic scattering σ_{el} and excitation σ_{exc}.

a) Tetrahydrofuran.

Comprehensive summaries on the interactions of low-energy electrons with THF have been published by Bouchiha et al. [16], Bremner et al. [19], Do et al. [42] and Giuliani et al. [71]. Do et al. measured differential electron-impact cross sections (15–50 eV, 15–90°) of the three lowest lying Rydberg bands in THF, with vertical excitation energies of 6.6, 7.2 and 7.8 eV. Those data were then extrapolated to the entire range of scattering angles by molecular phase shift analysis [42]. The analysis of the experimental results of Do et al. was based on the detailed study of Giuliani et al. where absolute photoabsorption cross sections were determined from measurements between 5.8 eV and 10.6 eV and supported by *ab-initio* calculations. Their results are mostly in good agreement with the vacuum ultraviolet absorption spectra and electron energy loss spectra of Bremner et al. as well as with quantum-mechanical R-matrix calculations of Bouchiha et al. The sum of the integral excitation cross sections measured by Do et al. [42] for the three lowest Rydberg states is shown in figure 4.28. Three additional Rydberg states are present with vertical excitation energies of 8.1, 8.57 and 8.89 eV [16, 19] so that the data of Do et al. are lower than the total excitation cross sections. From this point of view, the total excitation cross section of THF obtained in this work is supported by their data.

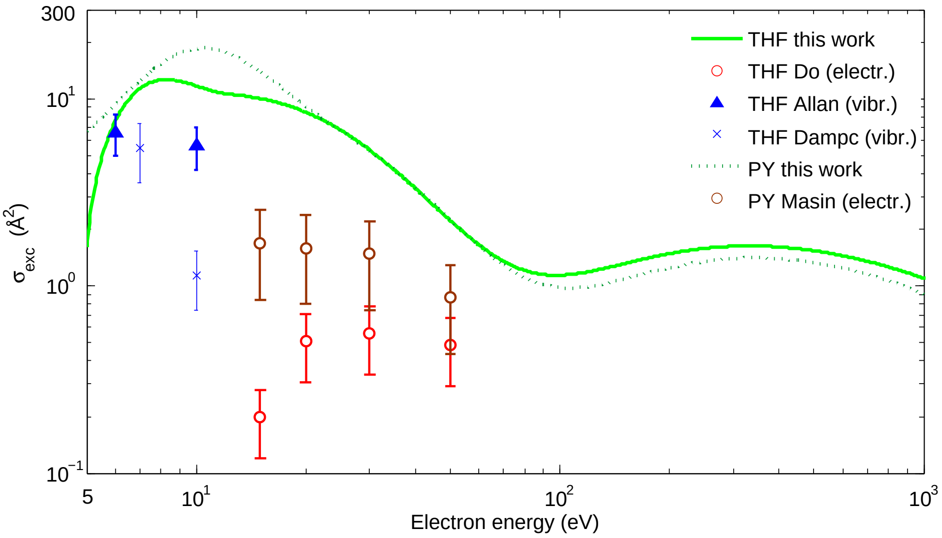

Figure 4.28: Total excitation cross sections of THF and PY.

Vibrational excitation cross sections of THF have been measured by Allan [2] (up to 16 eV, 45–180°) and Dampc et al. [34] (5–14 eV, 20–180°) with electron energy loss spectroscopy. These two integral cross section data sets agree at 7 eV but differ by a factor of five at 10 eV, while the differential data are qualitatively in excellent agreement according to Allan [2]. Values of both publications are shown in figure 4.28. A more complete set of excitation cross section data of THF would be necessary to evaluate the accuracy of our estimated values.

It is interesting to note that the THF molecule coexists in two conformations with C_2 and C_s symmetry and that the geometry has a significant impact on excitation energies and oscillator strengths [16, 71]. However, the mean value of the excitation energy is not significantly different for both conformers when calculated from the sum of excitation energies weighted by the oscillator strengths given by Giuliani et al. [71]. In this case, mean excitation energies for dipole-allowed transitions were 7.95 eV and 8.07 eV for the C_s and C_2 geometries, respectively. The average value of 8.01 eV was applied in the simulations.

b) Pyrimidine.

Electronic and vibrational excitation of PY has been investigated, for example, by Ferreira da Silva et al. [59], Mašin et al. [131] and Jones et al. [109]. Ferreira da Silva et al. [59] used vacuum ultraviolet absorption spectroscopy in the energy range 3.7–10.8 eV and electron energy loss spectroscopy between 2 eV and 15 eV and thoroughly compared their results to previous data. The vertical excitation energies of these authors agree well with those measured by Mašin et al. [131] by electron energy loss spectroscopy for the impact of electrons of energies 15–50 eV. The theoretical R-matrix calculations at 15 eV of the latter group are in reasonable agreement with the experimental data. Mašin et al. derived integral electron-impact cross sections for electronic excitations from their measurement of differential electron energy loss spectra [109] based on the known properties of the generalised oscillator strength for dipole allowed transitions [131]. In figure 4.28, the sum of their integral electronic excitation cross sections supports the total excitation cross section calculated in this thesis.

Mašin et al. [131] separately provided cross section values for 7 different electronic levels. Based on their data, the average energy loss was determined as function of incident electron energy. For electrons of 15, 20, 30 and 50 eV the average energy loss is 6.92, 7.34, 7.56 and 7.59 eV, respectively. Those values show asymptotic behaviour towards high electron energies. To verify the asymptotic value, the mean excitation energy was calculated similarly to the value for THF, i.e. using the oscillator strength distribution of Stener et al. [167]. Only electronic transitions with transition energies below the ionisation threshold of 9.7 eV were considered to compare the value to the data of Mašin et al. However, it should be kept in mind that intravalence transitions to excitation levels above the ionisation threshold have significant oscillator strengths. The mean excitation energy for dipole-allowed transitions with excitation energies below the ionisation threshold calculated in that way is 7.61 eV which is consistent with the data of Mašin et al.

As long as there exist no cross section data for the excitation to specific states for THF and by electrons of energies below 15 eV for PY, we believe that a negligible error is made in the simulations when the mean excitation energy of 7.61 eV in the dipole-limit is used. This statement will be investigated in section 5.4, where simulations are performed for PY medium using either the mean excitation energy, or interpolated values of cross sections for the discrete excitation levels of Mašin et al. [131].

c) Trimethylphosphate and purine.

As no literature data on excitation cross section data or oscillator strength distributions exist for TMP and PU, total excitation cross sections are calculated using equation 4.55. Due to the similarity in molecular structure of PY and PU, an excitation energy of 7.61 eV is also used for PU. In the case of TMP, the same excitation energy of THF of 8.01 eV was used as the bond structure of valence orbitals in both molecules is similar.

4.7 Conclusions

Model functions for calculating a cross section set for electron-impact on tetrahydrofuran, trimethylphosphate, pyrimidine and purine were developed. This cross section set is complete for electrons with energies between the ionisation threshold and 1 keV. Model functions for the individual cross sections are summarised in the following. Values for total cross sections are tabulated in appendix A.

Measured total scattering cross sections of THF and PY are interpolated by equation 4.27 and parameters given in table 4.1. These model functions neglect rotational excitations due to the finite energy and angular resolutions of the linear transmission device used in the experiment. The parameters for PU and TMP were obtained by fitting the sum of total scattering cross sections of molecular subgroups taking into account consistency requirements at low and high energies.

Model functions, which describe the angular dependence of measured double differential cross sections for ionisation (DDCS), enable an extrapolation of the measured data to forward and backward scattering angles. For incident electrons of energies above 200 eV the Rudd model in equation 4.32 is used, while superpositioned Legendre polynomials in equation 4.31 are applied for lower energies. The DDCS of PU can be scaled from those of PY by the ratio of their total scattering cross sections. Single differential ionisation cross sections (SDCS) for primary electron energies above 25 eV are described by equation 4.36 with parameters for THF, PY and TMP in table 4.4. Below 25 eV, a constant dependence of the SDCS on the secondary electron energy can be assumed. The SDCS of PU is again obtained by scaling the data of PY. Total ionisation cross sections are interpolated by the BEB model given in equation 2.19 with parameters in tables 4.2 and 4.5. The BEB model is also used to obtain partial ionisation cross sections for individual orbitals.

The evaluation of the Auger peak in the spectra of DDCS measurements reveals that, in the molecules studied, approximately one Auger electron is emitted after an ionisation of carbon or oxygen K-shells and two electrons in the case of a nitrogen K-shell. The energy of the Auger electrons is determined by random sampling using equation 4.46 with parameters in table 4.7 for carbon and nitrogen K-shells, while an energy of 495 eV is used after oxygen K-shell ionisation. The Auger electron emission is assumed to be isotropic.

Measured differential elastic scattering cross sections of THF, PY and TMP are well described and extrapolated to forward and backward scattering angles by the model functions in equations 4.47 and 4.48 for electrons of energies up to 200 eV and above 200 eV, respectively. Parameters are provided in table 4.8. Total elastic scattering cross sections of THF and PY are interpolated by the model functions provided in equation 4.52a, or b in the case of TMP. Parameters are given in table 4.9. DelCS and TelCS of PU can be scaled from those of PY by the ratio of total scattering cross sections.

Total excitation cross sections determined by equation 4.55 are consistent with the other cross sections used in this work as well as with the scarce literature on electronic and vibrational excitation cross sections of THF and PY. For each excitation process occurring in the simulation, we propose to use a mean excitation energy of 8.01 eV and 7.61 eV for THF and PY, respectively. Those values were determined based on oscillator strengths for discrete energy levels below the ionisation threshold. For PY, excitation cross section data for individual states exist for a restricted electron energy range, so that mean excitation energies could be substituted by the more detailed descriptions. Due to the lack of literature data for TMP and PU, mean excitation energies of 8.01 eV and 7.61 eV are applied, respectively, as an approximation.

Chapter 5

Track structure simulations in DNA medium and water

5.1 Introduction

In this chapter, electron cross section data of water and DNA constituents are compared and applied to simulate nanodosimetric parameters of the particle track structure.
In section 5.2, the electron-impact cross section data of DNA constituents, described in chapter 4, are directly compared to data for water vapour, which were investigated in chapter 3. Furthermore, simulated W-values for incident electrons are compared to experimental values in section 5.2a). The concept for the DNA target used in the simulations is introduced in section 5.3.1 and required modifications in the simulation procedure are described in section 5.3.2. The sensitivity of the simulated data on different parameterisations of the cross section data is described in section 5.4. Track structure parameters in form of cluster size distributions produced by incident monoenergetic electrons are provided in section 5.5. The influence of the water content in the DNA on simulation results is discussed in section 5.5.1. Finally, track structure parameters obtained in the vicinity of a proton trajectory are discussed in section 5.6.

5.2 Comparison of interaction cross section data

Total cross section data of DNA constituents THF, TMP and PY (see chapter 4) and water vapour (see chapter 3) are shown in figure 5.1. To compare the cross section data independent of the molecular size, they were divided by the number of valence electrons in the respective target molecule. Observing the total and elastic scattering cross sections (TCS and TelCS) per valence electron, it is evident that the energy dependence and magnitude for DNA constituents are similar. On the other hand, the TCS and TelCS of water are larger than those of the DNA constituents at low energies but continue towards higher energies with a larger slope. This leads to lower TCS and TelCS of water at energies above about 200 eV. For example, at 1 keV the normalised TelCS of DNA constituents scatter by 22% while they are 50–85% larger than the TelCS of water at the same energy. Similarly, at 30 eV, the normalised TelCS of the DNA constituents differ by up to 20% while the data for water are nearly a factor of two larger than the THF data.

Normalised ionisation cross sections of the DNA constituents show maxima at around 70 eV, where they scatter by 20%. The maximum of the total ionisation cross section of water is 25% lower than the PY data, with a maximum at 100 eV or 150 eV (depending on the cross section model). At 1 keV, the ionisation cross sections per number of valence electrons of water and the DNA constituents are in good agreement within 12%. A similar relation for the total ionisation cross sections of water relative to those of DNA constituents has been observed by Bernhardt and Paretzke [9].

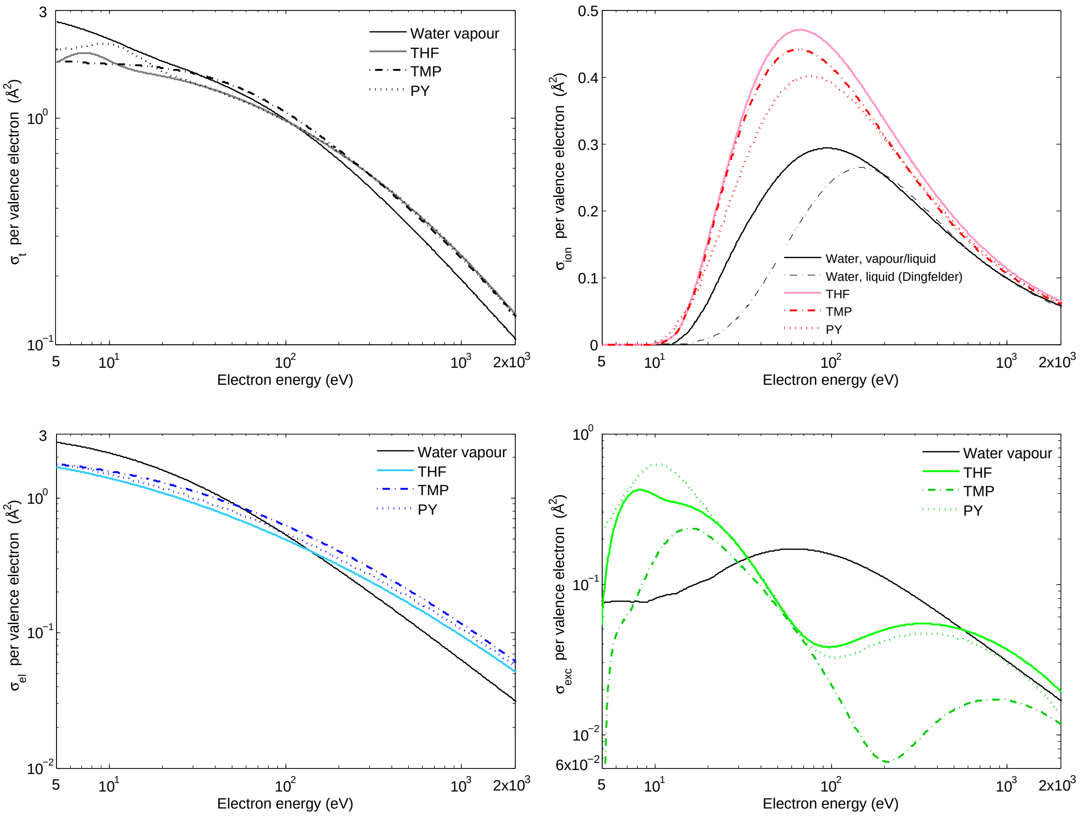

Figure 5.1: Total electron scattering cross sections σ_{t} and total electron cross sections for ionisation σ_{ion}, elastic scattering σ_{el} and excitation σ_{exc} of water vapour, THF, TMP and PY. The y-axis shows cross sections normalised to the number of target electrons.

Total cross sections for excitation, normalised to the number of valence electrons, are within the same order of magnitude for the DNA constituents and water but show a different energy dependence. While the excitation cross section data of the DNA constituents exhibit a maximum at around 10 eV and decrease towards higher energies with a dip at 100–200 eV, the excitation cross sections of water show a maximum at 100 eV. The dip in the data of the DNA constituents and the observed difference in energy dependence to water indicates an overestimation in the maximum region of the ionisation cross sections for DNA constituents (see section 4.7).

A possible overestimation of the ionisation cross sections of the DNA constituents is investigated by taking a closer look on the single differential ionisation cross sections (SDCS) of THF, TMP and PY relative to those of water in figure 5.2. Again, the cross sections were divided by the respective number of valence electrons to compare the data independent of the molecular size. Generally, the SDCS of THF and PY are higher than the calculated SDCS of water vapour at low secondary electron energies and decrease with a larger slope towards higher energies than the water data. On the other hand, the SDCS of TMP are similar to those of THF at energies up to 100 eV; at higher incident electron energies, however, they are similar to those of water vapour and rather fall below those at secondary electron energies above 10 eV due to a larger slope. The larger slope of the SDCS as function of the secondary electron energy arises from a stronger contribution of the exchange interaction between incident electron and target molecules which is due to the larger number of electrons in the target. The influence of the exchange interaction on the SDCS was illustrated in figure 4.11 (page 134). Furthermore, the production of low energy secondary electrons by dipole interactions has a higher probability for the DNA constituents than for water, presumably due to the larger dipole polarisability. The larger contribution of those electrons to the SDCS leads to higher values of the total ionisation cross section of the DNA constituents compared to water.

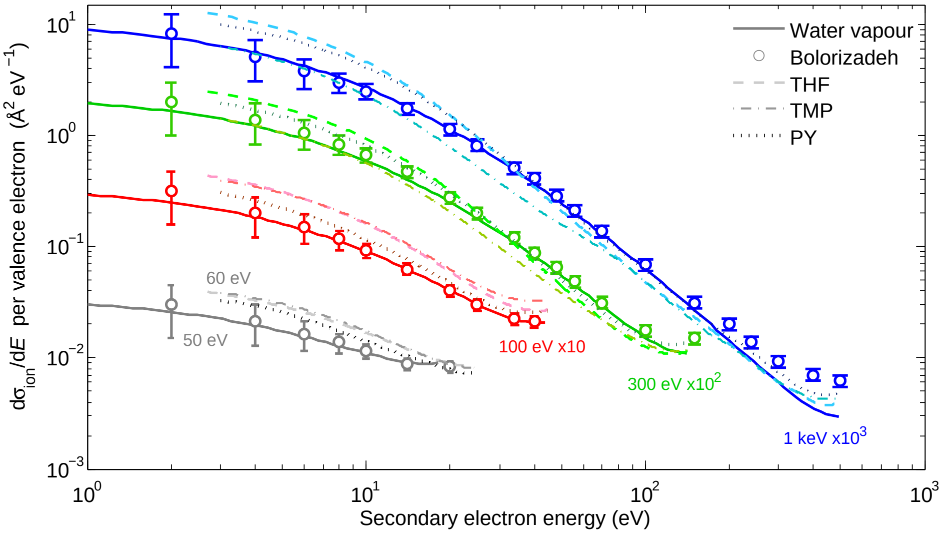

Figure 5.2: SDCS of water vapour, THF, TMP and PY for electrons of energies 50 eV (water data), 60 eV (THF and PY), 100 eV, 300 eV and 1 keV. The y-axis shows cross sections normalised to the number of target electrons. Experimental data from Bolorizadeh and Rudd [14] (symbols) and model functions (lines) are shown.

Different angular distributions after elastic scattering events are observed for the DNA molecules and water. Figure 5.3 compares differential elastic scattering cross sections for water vapour, THF, TMP and PY in the energy range between 300 eV and 1 keV, normalised to the respective total elastic scattering cross section. Generally, the angular distribution is stronger peaked in forward direction for the DNA constituents than for water vapour, due to the much larger dipole polarisability (53.78, 74.70, 57.97 a_0^3 for THF, TMP and PY, respectively, and 10.13 a_0^3 for water [141]). Hence, the greatest differences are found at forward scattering angles, where the normalised differential elastic scattering cross sections of the DNA constituents are about an order of magnitude larger compared to those of water.

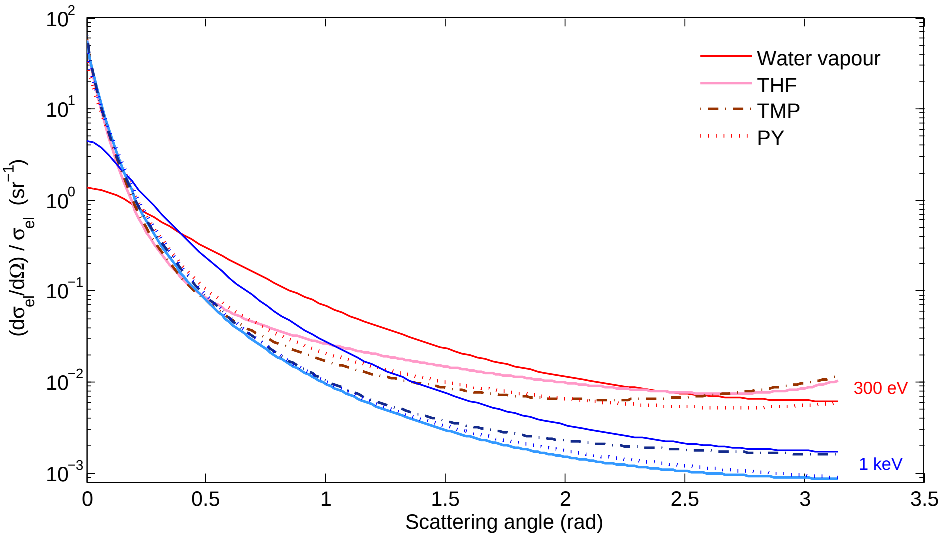

Figure 5.3: DelCS of water vapour and PY for electrons of energies 300 eV and 1 keV.

In summary, significant differences exist in the energy and angular dependence of cross section data for water and DNA constituents. The ionisation cross section is expected to have the greatest influence on electron transport in the respective medium. These cross sections (per valence electron) are significantly lower for water at energies below 500 eV. This is a consequence of the enhanced emission probability for low energy electrons in DNA constituents relative to water (figure 5.2). Elastic scattering cross sections show differences in energy and angular dependences, which would affect the simulated electron path. In the following sections, the effect of the different cross section data for water and DNA constituents on simulation results is investigated.

a) W-values.

W-values were calculated for the molecules investigated in this work for an electron energy of 1 keV, as this was the highest energy of the experimental cross section data for the DNA constituents. For this, simulations were performed in uniform media, using the respective interaction cross section data. The simulated volume was much larger than the ionisation range of the electrons so that the total number of ionisations produced by their complete slowing down could be obtained. The W-values of THF (26.0 eV), TMP (25.0 eV) and PY (25.7 eV) are similar among each other. Unfortunately, no experimental data are available for verification, but the W-values can be compared to those of water (see section 3.3.1), where the W-values at 1 keV are slightly higher than the asymptotic values, i.e. 29.4 eV in vapour and 23.8 eV in liquid water. Lower W-values for the DNA constituents (which are in the vapour phase) than those of water vapour were expected due to the lower ionisation threshold and the smaller mean free path lengths for ionisation in those molecules.

5.3 Simulation methods

5.3.1 Target concept

In the simulations performed in this work, a uniform and random distribution of DNA constituents within the medium was assumed. The size of the target volume was a DNA segment of 10 base pairs, modelled by a cylindrical volume of 3.4 nm in height and a diameter of 2.3 nm (see section 2.4). A uniform and random distribution of the molecules within the medium seems reasonable, particularly for an evaluation of parameters related to the track structure of secondary electrons. The random arrangement is restricted by the numbers of respective molecules present per volume element representing a DNA segment. In the case of 10 base pairs, there are 20 THF, TMP and nucleobase molecules, where the latter are assumed to consist of 10 PY and PU molecules. A critical point in modelling realistic DNA targets is the water content, as described in section 2.1.1. Therefore, simulations were performed with different number of water molecules per nucleotide. The influence of the water content on the simulation results will be discussed.

Highly structured DNA target models exist, for example the target model used in PARTRAC [61]. Such models provide a valuable tool to evaluate the track structure of heavy ions, which are densely ionising but do not significantly change their direction of momentum. For such particles, a highly structured target allows the assessment of DNA damage from direct and indirect interactions related to the spatial arrangement of the DNA chains. Those vary significantly with cell type and shape [73] as well as in different phases of the cell cycle [192]. The influence of a variation in the spatial arrangement of the DNA within a cell nucleus on predicted DNA damage could be investigated by applying detailed DNA target models [61].

However, the structure of the target may not provide additional information related to the track structure of secondary electrons for the following reason. The production of secondary electrons with energies up to several tens of electron volts has always the highest probability, as can be observed in the SDCS of incident electrons or protons (e.g. those shown in this work). Low-energy electrons with energies between the ionisation threshold and up to several hundreds of electron volts have short mean free path lengths (well below 1 nm) and directional changes due to elastic or inelastic scattering are significant. The latter have random distributions which are defined by differential inelastic or elastic scattering cross sections. Those cross sections are known to be nearly independent of scattering angle for electrons with energies below several tens of electron volts. For these reasons, the distribution of impact angles on the DNA target structure is nearly isotropic. On the nanometric scale, it may even be isotropic if the target of interest is reached after several scattering events. This rationale leads to the assumption in this thesis that a random orientation and distribution of DNA and water molecules within the medium is simulating a realistic nanometric target for electron impact.

5.3.2 Simulation procedure for DNA targets

The DNA medium is assumed to consist of uniformly distributed nucleotides (NT). The nucleotides are further assumed to be equal. This means that the fractions of nucleobases (NB) are assigned to each nucleotide. The total mean free path of electrons in a volume of nucleotides is calculated according to

$$\lambda = \frac{1}{n_{\mathrm{NT}}\ \sigma_{\mathrm{NT}}} \tag{5.1}$$

where the number density n_{NT} is given for nucleotides within a DNA segment of 10 base pairs length by

$$n_{\mathrm{NT}} = \frac{20}{\pi r_{\mathrm{target}}^2 h_{\mathrm{target}}} \tag{5.2}$$

with radius $r_{\mathrm{target}} = 1.15$ nm and height $h_{\mathrm{target}} = 3.4$ nm. The total scattering cross section σ_{NT} of a NT is given by

$$\sigma_{\mathrm{NT}} = \sigma_{\mathrm{THF}} + \sigma_{\mathrm{TMP}} + \sigma_{\mathrm{NB}} + N_{\mathrm{H_2O}}\ \sigma_{\mathrm{H_2O}}. \tag{5.3}$$

Equation 5.3 contains the sum of total scattering cross sections σ_{THF} and σ_{TMP} for the DNA backbone molecules, σ_{NB} of the nucleobases and $\sigma_{\mathrm{H_2O}}$ of water multiplied by the average number of water molecules $N_{\mathrm{H_2O}}$ present within a nucleotide. σ_{NB} contains the fractions of total scattering cross sections of pyrimidine and purine, such that

$$\sigma_{NB} = 0.5\ \sigma_{\mathrm{PY}} + 0.5\ \sigma_{\mathrm{PU}}. \tag{5.4}$$

This can easily be extended using cross section data for adenine, thymine, cytosine and guanine in varying relative content, mimicking different sequences of base pairs.

Different water content was used in the simulations as the number of water molecules within the DNA molecule varies with the environmental conditions in a living cell. If not further specified, $N_{\mathrm{H_2O}} = 6.28$ water molecules per nucleotide are used. In this case, the mass density of the DNA target is 1 g/cm^3 so that a comparison to results in water is independent of the mass density. This value for $N_{\mathrm{H_2O}}$ was obtained by the relation

$$\rho = \frac{M_{\mathrm{DNA}} + N_{\mathrm{H_2O}} M_{\mathrm{H_2O}}}{N_{\mathrm{Avo}}}\ n_{\mathrm{NT}}, \tag{5.5}$$

using the Avogadro constant N_{Avo}, the molar mass of water $M_{\mathrm{H_2O}}$ and the sum of molar masses of the DNA constituents $M_{\mathrm{DNA}} = 312.3$ g mol^{-1}. However, Franklin and Gosling [60] found that minimum eight water molecules per nucleotide have to be present in the DNA B-form (see section 2.1.1). Therefore, $N_{\mathrm{H_2O}} = 8$ water molecules per nucleotide are also used. To be able to evaluate the influence of the water content on nanodosimetric quantities, also $N_{\mathrm{H_2O}} = 12.5$ was applied, which might even be more realistic for native DNA as supported by experimental data [46].

The simulation procedure is adapted as follows: Using the mean free path calculated in equation 5.1, the distance to the next point of interaction is determined (see section 2.3). Subsequently, another simulation step is introduced, where the individual molecule participating in the interaction is selected. This is achieved by random sampling from the partial sums of total cross sections for a nucleotide in equation 5.3. The following simulation steps, continuing with the type of interaction, are then performed as described previously (section 2.3).

5.4 Influence of different parameterisations for cross section data

The influence of different approaches in the electron transport calculation on track structure parameters is investigated in this section. Those approaches concern the determination of the electron emission angle after an ionisation and the treatment of excitation processes. The investigation was for pyrimidine medium because excitation cross section data are available in the literature only for this molecule. Calculated track structure parameters in uniform PY medium were the probability distributions of cluster sizes for ionisation, excitation and inelastic collision as well as the respective first moments. The results are shown in figure 5.4 and 5.5 and are discussed in the following.

a) Emission angle of secondary electron.

Simulations were performed in which the emission angle of the secondary electron after an ionisation was determined by means of the model functions for the double differential ionisation cross sections (DDCS), given in section 4.4.1.3. This approach requires random sampling and is more time consuming than using equation 2.7 alternatively. Figure 5.5 shows that the deviation of track structure parameters is significant when either of those approaches is applied in the simulations. In fact, the use of the analytic model leads to a reduction of mean cluster sizes for inelastic collision by up to 6% in the energy range 100–1000 eV. The largest reduction of up to 16% is observed for the mean excitation cluster size. This reduction is due to lower probabilities for the production of large cluster sizes (figure 5.5).

The underestimation of the number of inelastic interactions when the analytical model is used is mainly due to the neglected backward scattering. The probability for backward scattering is higher for electrons of low energy. When backward scattering is omitted, these electrons are more likely to be scattered outside the target volume before interacting by excitation. For those electrons, the excitation cross section is relatively higher than the ionisation cross section and, consequently a higher effect on the excitation cluster size is observed.

It is obvious from these observations that the distribution of scattering angles, given by the DDCS, is essential for realistic track structure calculations and cannot be substituted by average values. The implementation of DDCS in such simulations is strongly recommended.

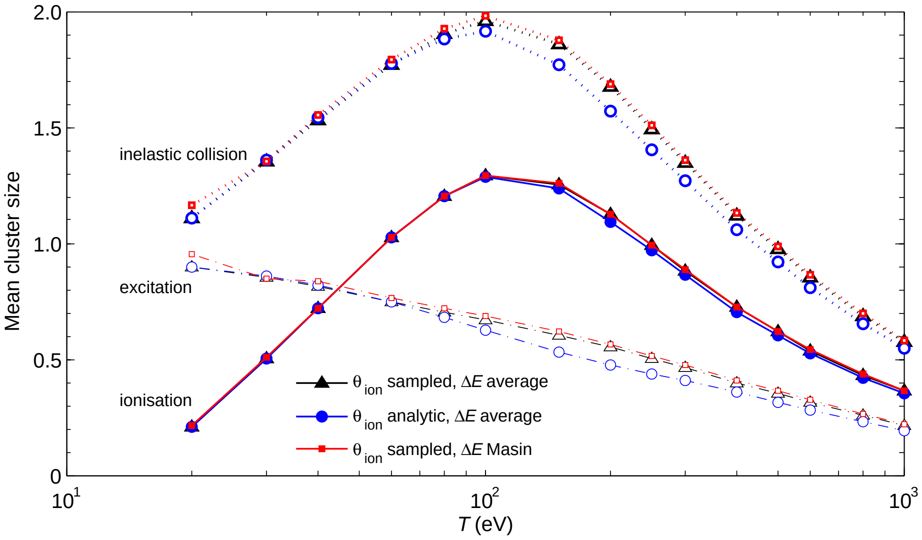

Figure 5.4: Mean cluster sizes for ionisation, excitation and all inelastic collisions by interactions of electrons with PY molecules. Different parameterisations are used for determining the scattering angle θ_{ion} after ionisation and the energy loss ΔE after excitation (see text).

b) Treatment of excitation processes.

Mean excitation energies of DNA constituents THF and PY were obtained from dipole oscillator strength distributions in section 4.6 due to a lack of cross section data for individual excitation states. Only for PY, such cross sections were published for impact electrons of energies between 15 and 50 eV by Mašin et al. [131]. The validity of the approximation of a mean excitation energy was investigated for PY by comparing track structure parameters obtained by using the mean excitation energy of 7.61 eV, on the one hand, and interpolated values of relative cross sections for the discrete excitation levels of Mašin et al. [131], on the other hand. For the latter, the relative cross sections for electron energies larger than 50 eV are assumed to be the same as at 50 eV. The same assumption is applied to energies below 15 eV where the data for electrons at 15 eV are used if the electron energy exceeds the lowest excitation energy. In both simulations, electron histories were terminated when the energy fell below 7 eV.

In figure 5.4, a minor influence on mean excitations cluster sizes of less than 3% is observed. In fact, the probability for large ionisation or excitation clusters (above 4) is slightly higher when the excitation cross section data set is used (figure 5.5). Based on this observation, the use of a mean excitation energy seems appropriate for a simulation of electrons down to an energy of 7.0 eV. Nonetheless, excitation cross section data of DNA constituents for electrons in the extended energy range are required to obtain more realistic simulation results for these low energy electrons.

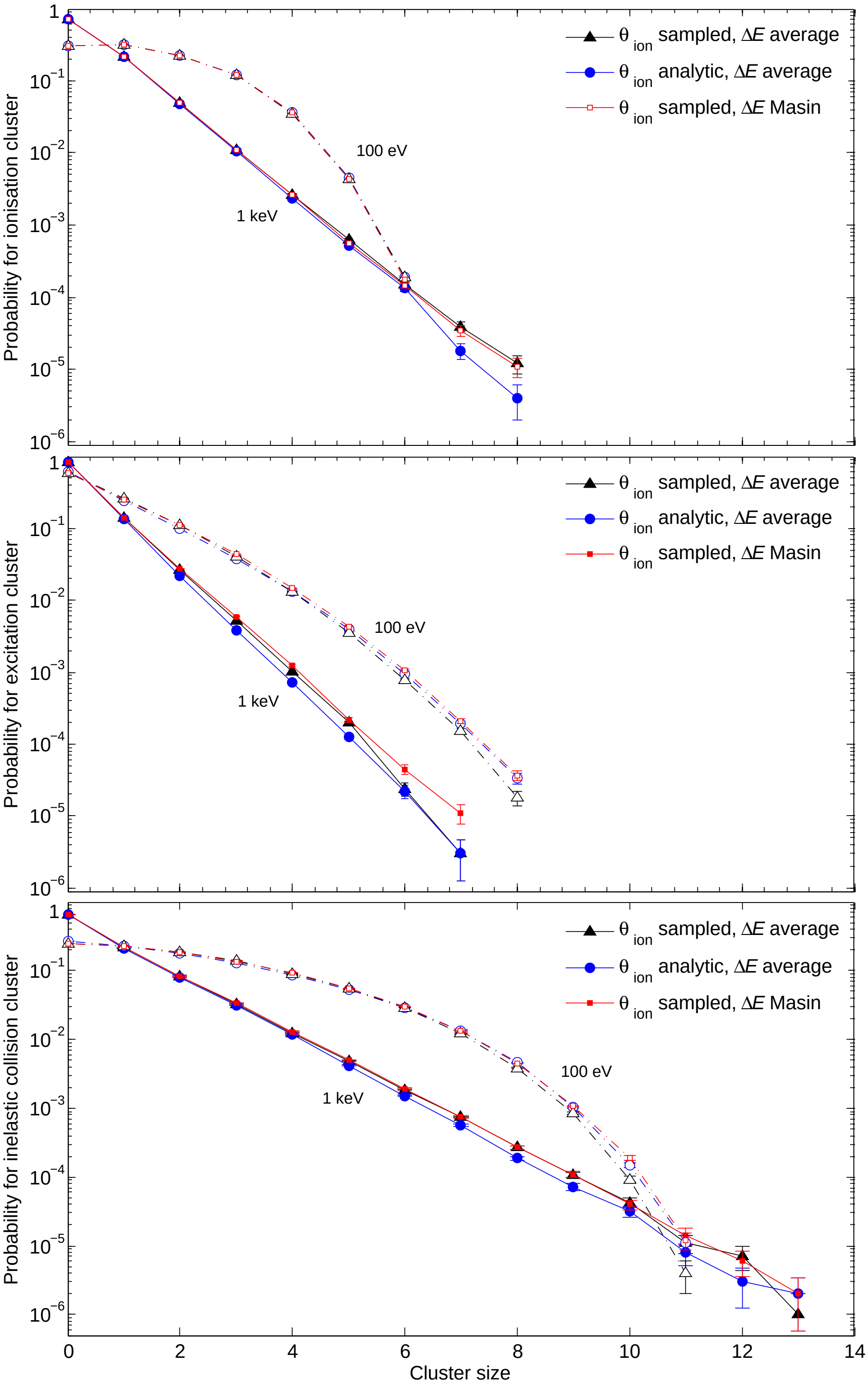

Figure 5.5: Probability distributions of cluster sizes for ionisation, excitation and all inelastic collisions by interactions of electrons with PY molecules. Different parameterisations are used for determining the emission angle θ_{ion} after ionisation and the energy loss ΔE after excitation (see text).

5.5 Nanodosimetric cluster size distributions in DNA targets compared to water

Nanodosimetric quantities produced by electrons in water vapour and liquid water have been discussed in section 3.3.3. In the following, those data are compared to simulation results obtained in targets consisting of DNA medium. The influence of the different parameterisations of cross section data for water on the electron track structure in DNA medium is discussed. In those simulations, the cross section data for water vapour as well as two different sets of data for liquid water (SigIon1 and SigIon2, defined on page 68) were used alternatively. As stated before, all these data are frequently applied in track structure simulations. The same mass density of 1 g cm^{-3} was assumed for all media. In this case, on average 6.28 water molecules per nucleotide are present in the DNA medium. Electrons were transported until their energy fell below 7 eV.

Figure 5.6 shows mean cluster sizes M_1 obtained by equation 2.25 (page 38) for ionisation, excitation and inelastic collisions. The mean ionisation cluster sizes obtained in DNA medium are nearly similar to the values calculated in only water when the cross section set SigIon1 is used. However, the energy dependence of the mean ionisation cluster size is different in both media as the values in DNA medium are up to 12% higher at energies below the maximum at 150 eV and up to 11% lower at higher energies. This leads to a shift of the maximum towards lower energies in DNA medium. The different cross section data for water applied for the simulation of the DNA medium affect the results by overall less than 11% and only 3% in the region of the maximum.

On the other hand, the application of the cross section set SigIon2 leads to 25% higher mean ionisation cluster sizes at 150 eV in DNA medium. Towards lower energies, the difference between the data is increasing to as much as a factor of two at 40 eV. Mean cluster sizes for excitation are shown in the middle part of figure 5.6. The results of the DNA medium are similar to the values for water vapour in the energy range above the maximum at 150 eV (less than 13% difference). At energies below 60 eV, the values for DNA medium exceed those for water up to a factor of two. This enhancement for DNA medium has to be further investigated when cross section data for individual excitation levels are available for an extended energy range for all DNA constituents.

Results obtained in liquid water are a factor of 2–2.5 lower than those of water vapour, which is mainly due to the contribution of neutral dissociative excitation states (see section 3.3.3). The difference in the cross section data for water leads to a scatter of only 5–10% in the mean excitation cluster sizes for DNA medium.

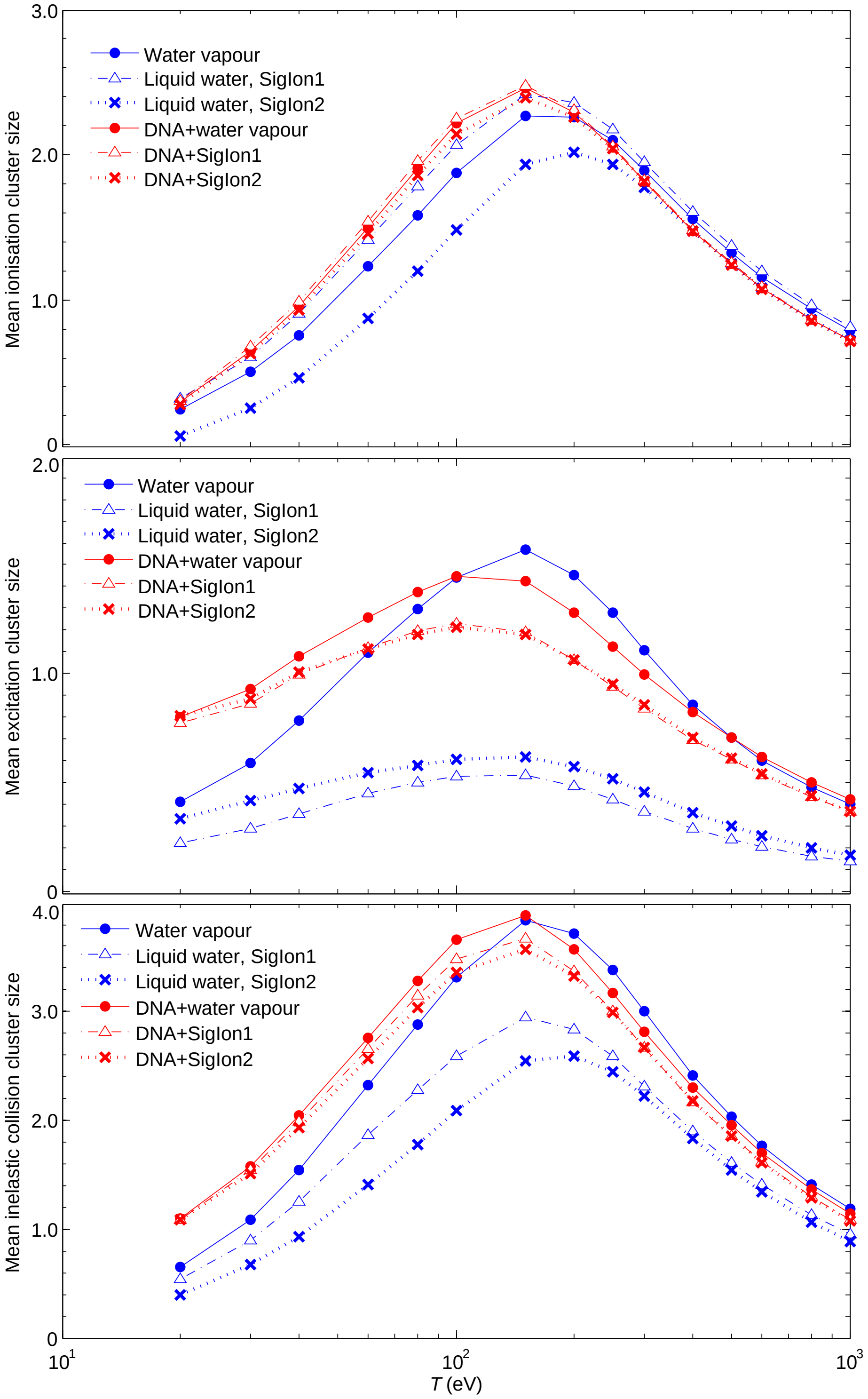

Figure 5.6: Mean cluster sizes for ionisation, excitation and all inelastic collisions by interactions of electrons with energy T in DNA medium or water. Statistical uncertainties are within the symbols.

The lower part of figure 5.6 shows mean cluster sizes for all inelastic collisions. As expected when observing the mean values for ionisation and excitation, the results for inelastic collisions are similar among the different media at energies above 150 eV when water vapour is used. In this energy range, the variation between the data sets is less than 7%, but increases towards lower electron energies to yield as much as 70% larger values in DNA medium. Again, simulations using SigIon2 lead to the largest differences between results in DNA medium and water. In this case, the data calculated in DNA medium are higher than those in water by 20% at energies above 300 eV, 40% higher in the region of the maximum at 150 eV and even a factor of three at 20 eV. The scatter of the mean inelastic collision cluster size in DNA medium due to the different cross section data for water is up to 9%.

In addition, the variances of the cluster size distributions for ionisation and all inelastic collision events are shown in figure 5.7. These data reveal that higher mean cluster sizes are generally accompanied by a higher variance of the distribution and, hence, by higher probabilities to produce intermediate clusters between 2 and 10. This has already been demonstrated by a comparison of probability distributions for cluster sizes arising from electrons of 200 eV and 1 keV in water (see figure 3.13, page 74). For electrons with an energy below 150 eV, the largest variances of the ionisation cluster size are obtained in DNA medium or water using SigIon1, while the variances lie within the scatter of the data for water at higher energies. The largest variances of the inelastic collision cluster size are present in DNA medium across the entire energy range. Similar variances are observed for the results in water vapour at energies above 200 eV. On the other hand, the variances in the cluster sizes obtained in water using SigIon2 are always less than in the other constellations.

To further investigate the differences in the particle track structure, figure 5.8 (top) shows the probability F_2 (equation 2.26, page 39) of a single electron to produce at least two interactions within the sensitive volume. The maximum probability of 0.66–0.68 is present for 100 eV electrons in DNA medium. The scatter of the values obtained in DNA medium due to the different cross section data for water is generally below 6% at energies above 80 eV and increasing with decreasing energy. In comparison, the F_2 values for water using SigIon1 reach a slightly lower maximum of 0.63, while the application of SigIon2 leads to a maximum of only 0.56 at 150 eV.

In the two lower parts of figure 5.8, F_2 is shown separately for the molecules comprising the DNA backbone, i.e. THF and TMP. F_2 calculated for the backbone is useful to estimate the probability for a DNA strand break by ionisation of the backbone molecules as will be discussed in the conclusions. Compared to the F_2 values obtained in water, the results for the backbone are generally lower, reaching a maximum of 0.39 at 150 eV. The different parameterisations of the water cross section data affect the results for the backbone within 14% in the energy range 60–1000 eV and is again increasing with decreasing energy.

In the following section, simulations were repeated for more realistic targets where, on average, 8 or 12.5 water molecules per nucleotide are present (see section 2.1.1).

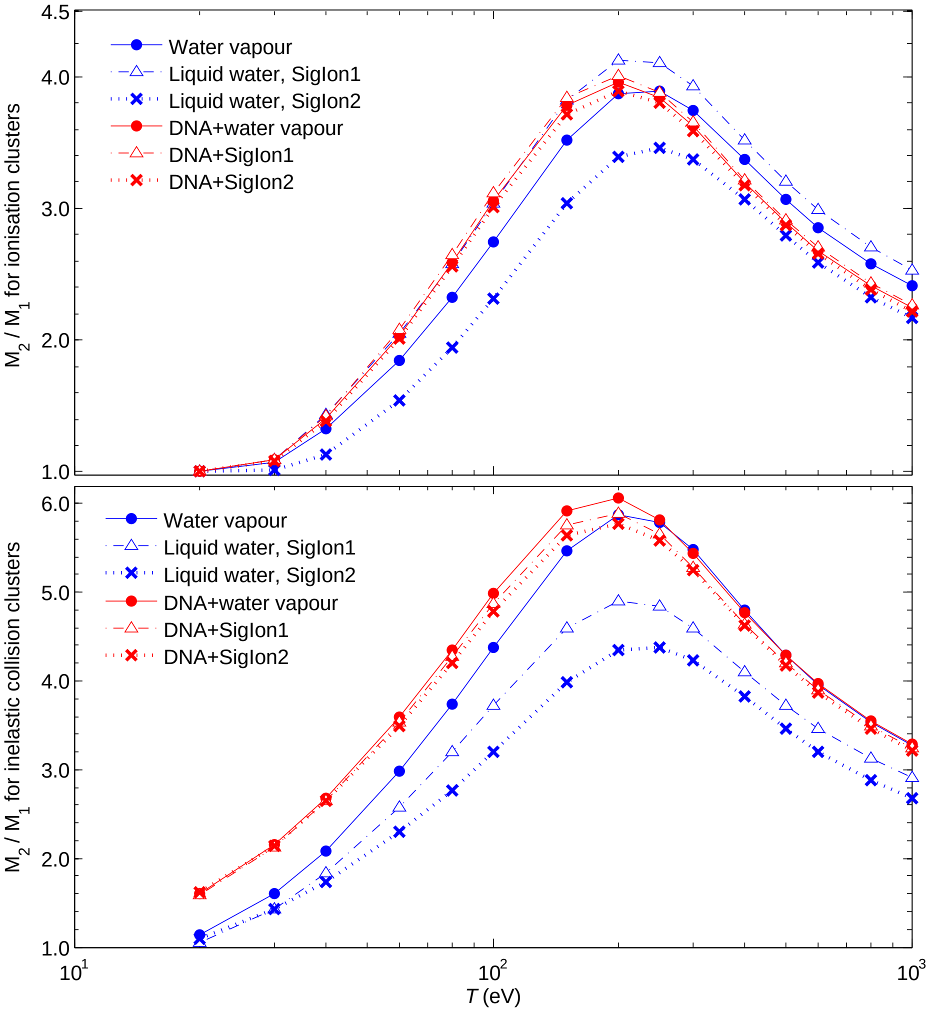

Figure 5.7: Variance of cluster size distributions, normalised to the mean values, for ionisation and all inelastic collisions by interactions of electrons with energy T in DNA medium or water. Statistical uncertainties are within the symbols.

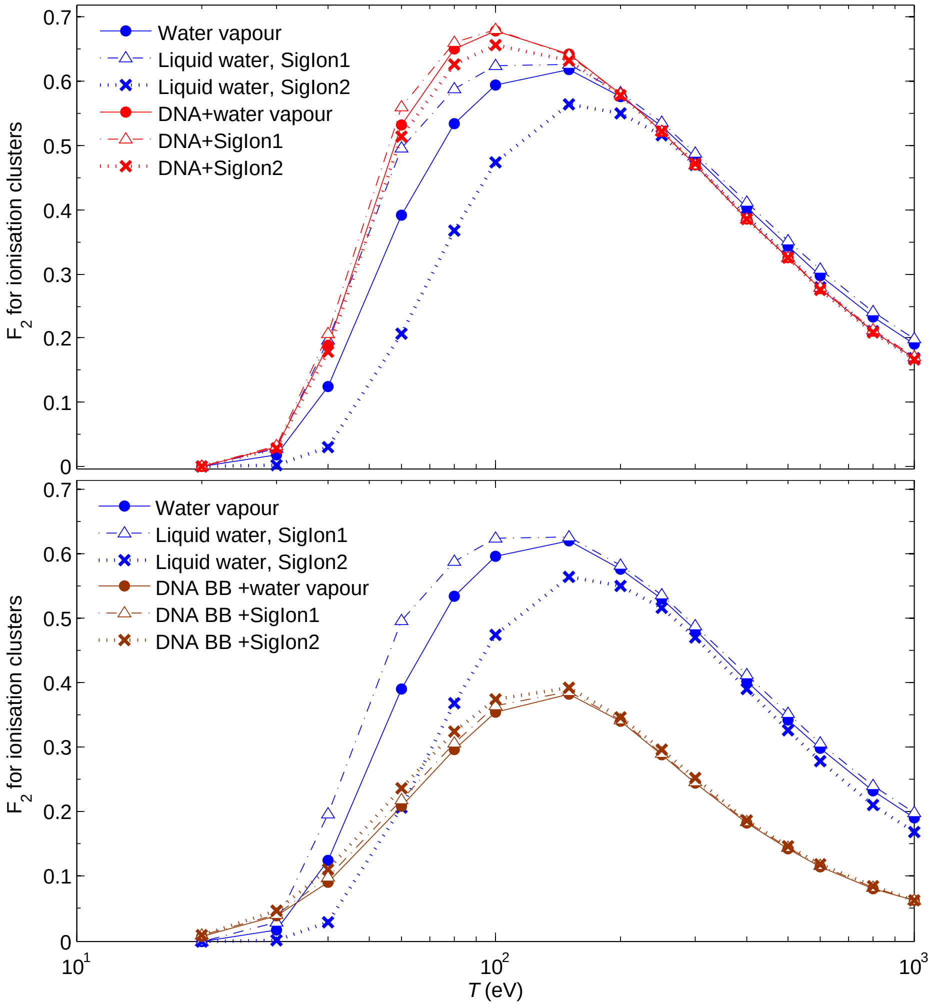

Figure 5.8: Probability F_2 for an electron of energy T to produce at least two ionisations water, DNA medium (top) and molecules of the DNA backbone (bottom).

5.5.1 Influence of the water content in the DNA

As described in section 5.3.2, simulations with 6.28, 8 and 12.5 water molecules per nucleotide (NT) were performed. The influence of the water content in the DNA target on nanodosimetric quantities is significant as seen for the mean ionisation cluster size and the variance of the respective probability distribution in figure 5.9.

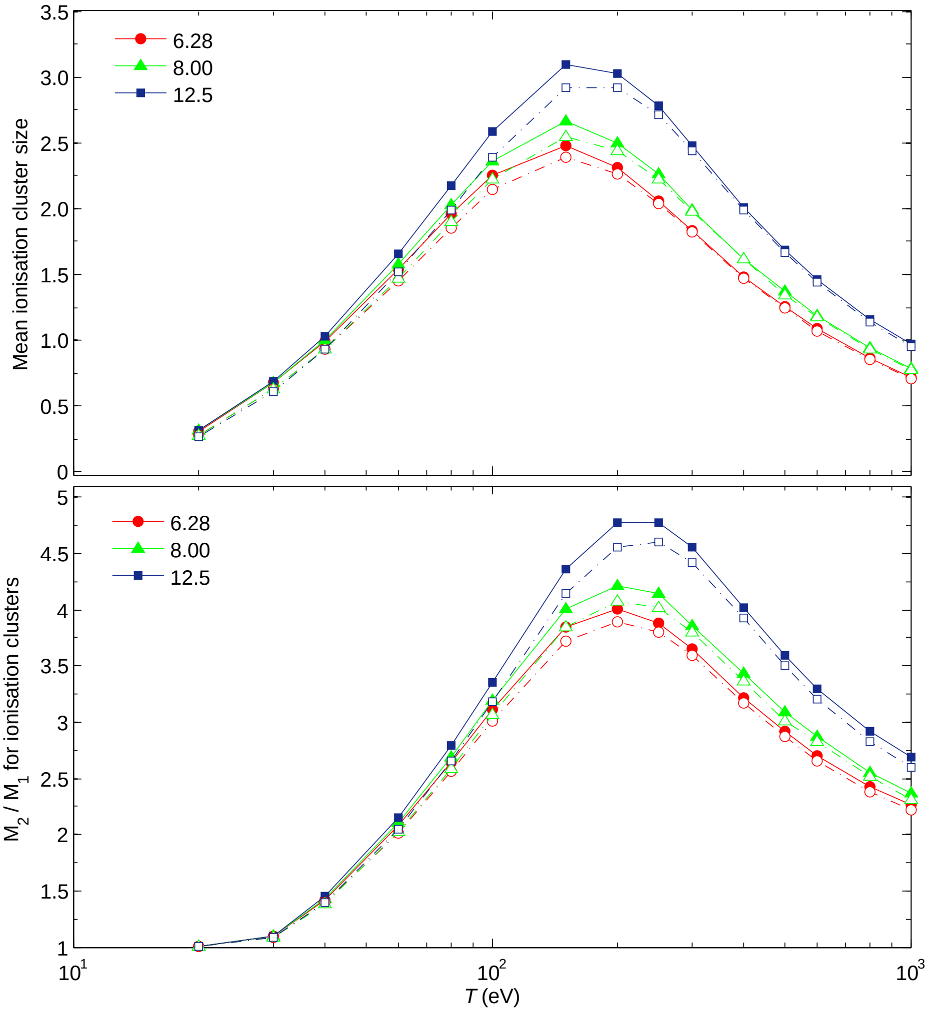

Figure 5.9: Mean cluster sizes for ionisation and variances of the distributions in DNA medium with indicated number of water molecules per nucleotide. Simulations were performed using the cross section sets SigIon1 (solid lines) and SigIon2 (broken lines) for liquid water.

The doubling of the water content to 12.5 per NT increases the mean ionisation cluster size by about 36% in the energy region above 200 eV and by 25% at the maximum of 150 eV. In addition, the maximum value for DNA medium with a higher water content is slightly shifted towards higher energies which is in accordance with the dependence of the mean ionisation cluster sizes obtained in water on electron energy. The different parameterisations of water cross sections lead to a scattering of the results by 10%. Similarly, the variance of the probability distribution, described by M_2/M_1, is larger if a higher water content is assumed. In this case, the maximum is shifted to a slightly higher electron energy of 200 eV.

The probabilities F_2 for an electron to produce at least two ionisations in DNA medium are shown in figure 5.10. As discussed above, the data set SigIon1 for electron-impact cross sections of water leads to the highest values, which increase in the maximum at an energy of 100 eV from 0.68 to 0.76 when the water content is doubled. Generally, the relative enhancement of the F_2 values for the higher water content of 12.5 per NT increases with increasing energy, leading to 42% higher F_2 values at 1 keV. When the cross section data set SigIon2 is used, the F_2 values are 5–30% lower than those obtained with SigIon1 in the energy region 30–100 eV, where the deviation increases with decreasing energy.

The bottom graph of figure 5.10 shows F_2 values obtained for the backbone molecules, THF and TMP, only. Data calculated using 6.28 and 12.5 water molecules per NT show maxima between 0.38 and 0.42 at 150 eV. As can be expected when observing the results for the DNA medium, the energy dependence of F_2 for the DNA backbone molecules is slightly shifted towards higher energies for the higher water content. At the same time, the scatter of F_2 values obtained with the different water cross sections is larger for the higher water content. In this case, the variation is up to 7% for energies above 150 eV, increasing to 30% at 60 eV. The largest results for the backbone molecules are obtained when using SigIon2, as the lower ionisation cross section of water (relative to SigIon1) leads to a relative increase of ionisations on the DNA molecules.

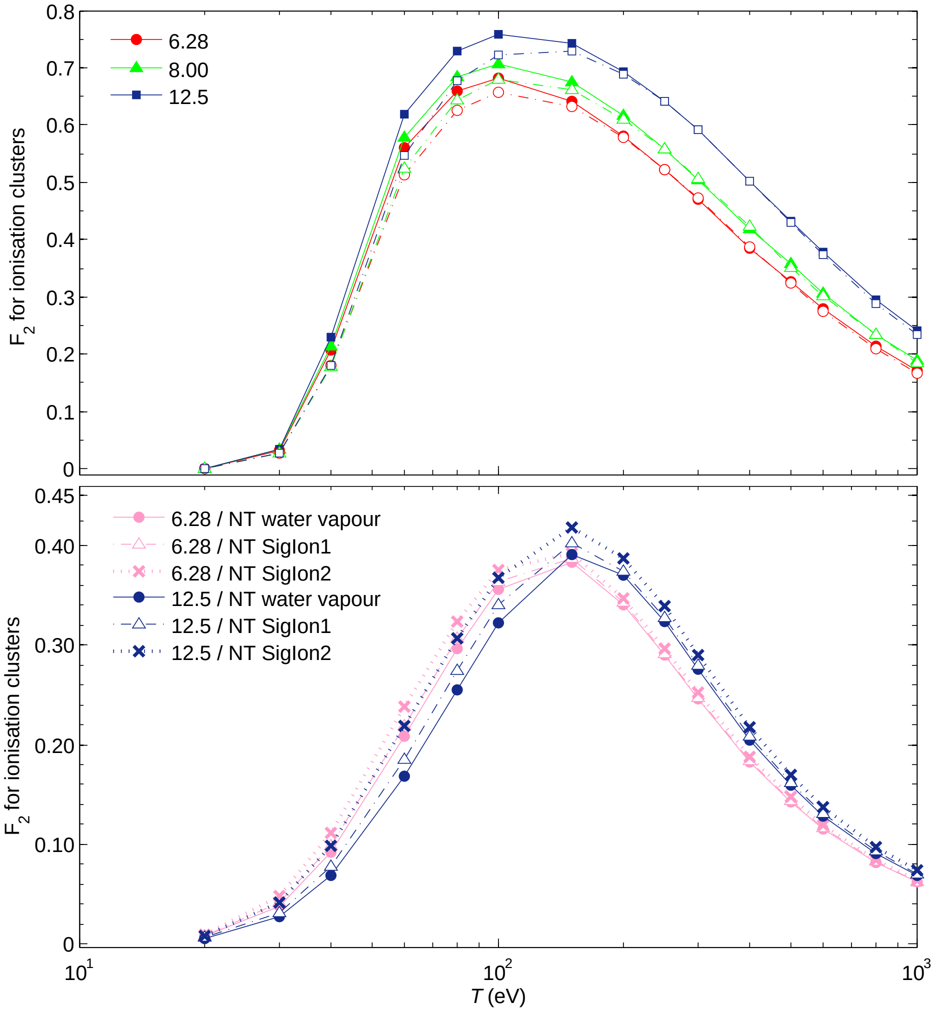

Figure 5.10: Probability F_2 for an electron of energy T to produce at least two ionisations in water, DNA medium (top) or molecules of the DNA backbone (bottom), obtained with different water content in the DNA medium (number of water molecules per nucleotide, NT). Simulations were performed using also the different cross section sets for water.

5.6 Track structure parameters in the vicinity of a proton trajectory

In the vicinity of an ion trajectory, energy depositions to the medium are solely due to secondary electrons. Most of those electrons have an energy below 1 keV as, for instance, shown in section 3.4.1, figure 1 and section 3.5, figure 2. In the following, track structure parameters are investigated for a model geometry, where the protons are assumed to interact with liquid water, while secondary electrons are transported in either water or DNA medium. This geometry serves as a simplified model protons traversing the cell nucleus under the assumption that the secondary electron production by protons in water and DNA medium are identical. Such an approach was necessary as an appropriate data set of interaction cross sections for protons with DNA constituents not yet exists.

In the simulations, protons were transported in liquid water, using the cross section data listed in table 3.2 (page 66). Secondary electrons were either transported in liquid water or DNA medium, including 6.28 water molecules per nucleotide to obtain the same mass density of both transport media. The lower energy cut-off in the simulations was at 5 eV. Due to insufficient knowledge of vibrational excitation cross sections of DNA constituents, these processes were omitted for water molecules. The geometrical setup is shown in figure 5.11. Target cylinders of 2.3 nm diameter and 3.4 nm height were placed in distances ρ between 1.15 nm and 10 nm to the proton trajectory.

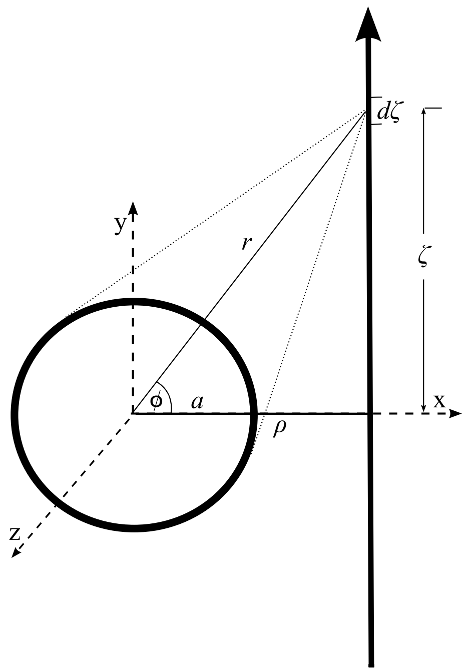

Figure 5.11: Geometrical setup for the simulation of track structure parameters in the vicinity of a proton trajectory. Secondary electrons produced within the trajectory segment $d\zeta$ may reach the target cylinder placed in distance ρ to the proton trajectory.

Figure 5.12 shows the frequency distribution of secondary electrons in different distance to the ion trajectory. It is obvious that the spectra for electron energies above 15 eV are similar when electron transport in DNA medium and water are compared. The dramatic differences in the spectra at energies below 10 eV obtained in both media are most likely due to the average energy loss assumed after an excitation of DNA constituents. This means that the observed difference is mainly artificial. However, due to the lower ionisation threshold of DNA constituents compared to water, a hardening of the electron spectra may be expected in a closer distance to the proton trajectory in the case of DNA medium.

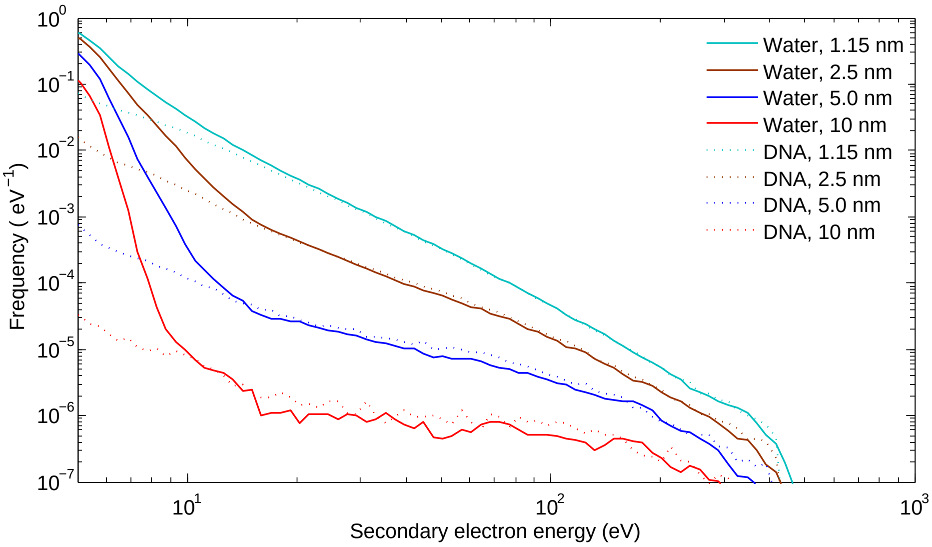

Figure 5.12: Absolute frequency distribution of secondary electrons per proton at the surface of target cylinders as function of the distance ρ to the 1 MeV proton trajectory in water and DNA medium.

The larger frequency of low-energy electrons in water relative to DNA medium leads to a larger fluence* of electrons passing through the surface of target cylinders placed as function of the distance to the proton trajectory is larger for water (figure 5.13). The fluence continuously decreases by a factor of ten for water and by three orders of magnitude for DNA medium at a distance of 10 nm. A decrease as function of the distance to the ion trajectory is expected due to the decrease in solid angle.

---

*The term ‘fluence’ in this work is different from the definition of the ICRU and is defined here as the effective number of electrons crossing the surface of the target cylinder facing the proton trajectory, taking the direction (in- or outgoing) into account. Units are normalised to the cylinder surface.

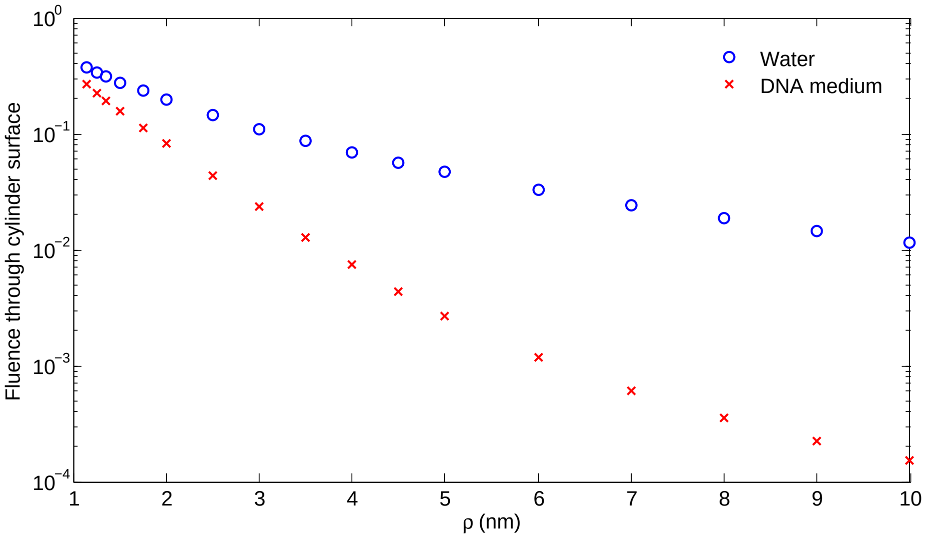

Figure 5.13: Electron fluence at the surface of target cylinders as function of the distance ρ to the 1 MeV proton trajectory in water and DNA medium.

The mean ionisation cluster size produced in the target volume by the passage of 1 MeV protons is decreasing by three orders of magnitude as the distance ρ increases from 1.15 nm to 10 nm (figure 5.14). The mean ionisation cluster size is by 6% higher for the DNA medium than for water in a distance below 2 nm. The deviation between the values obtained in both media increases with further distance to the proton trajectory, leading to 50% higher values at 10 nm.

The capability of secondary electrons to produce clustered damage to DNA segments in the vicinity of a proton trajectory is further investigated by comparing F_2 values (see equation 2.26 and figure 5.14). Similarly to the mean ionisation cluster size, the F_2 values are generally larger in DNA medium compared to water. The deviation increases from 16% at 1.15 nm to 50% at 10 nm.

The differences observed in mean cluster sizes and F_2 values for DNA medium and water are in accordance with the results obtained for monoenergetic incident electrons in section 5.5. In fact, the increasing deviation between the data obtained in both media as function of the distance ρ arises from the harder electron spectra. For example, in a distance of 10 nm, the spectra are nearly constant at energies 20–100 eV, while the frequency decreases by two orders of magnitude in this energy range at a distance of 1.15 nm (figure 5.12). For electrons in the energy range 60–150 eV, the mean ionisation cluster size as well as the F_2 values are higher in DNA medium relative to water. Therefore, higher results are obtained in the vicinity of a proton track using DNA medium.

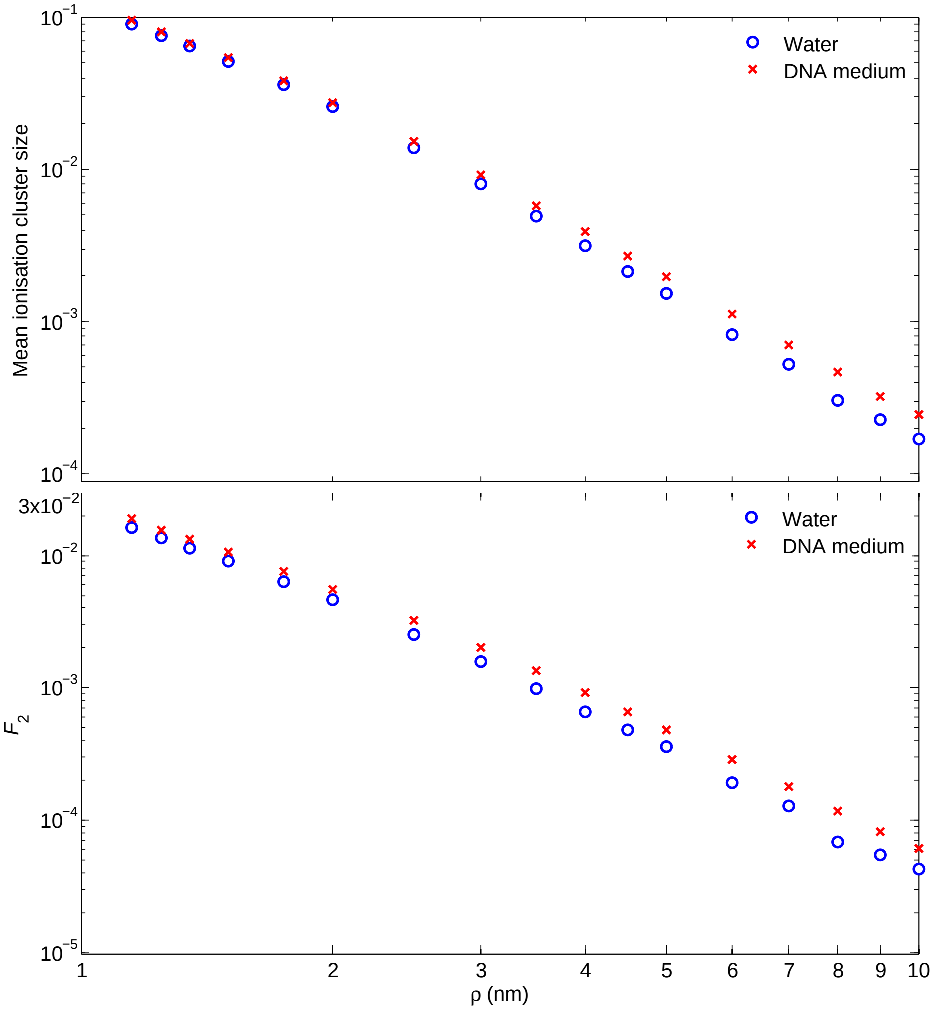

Figure 5.14: Mean ionisation cluster size and F_2 values as function of the distance ρ to the 1 MeV proton trajectory in water and DNA medium.

5.7 Conclusions

A direct comparison of electron-impact interaction cross sections of DNA constituents and water in section 5.2 shows significant differences, which would affect simulated electron tracks. The cross section data were normalised to the number of valence electrons in each molecule to enable their comparison independent of the molecular size.

In summary, total scattering cross sections and total elastic scattering cross sections of water possess a larger slope as function of electron energy. This leads to higher values for the DNA constituents at energies above 200 eV (50–85% at 1 keV). At lower energies, the situation reverses so that the data for water are a factor of two larger at an energy of 30 eV. Differential elastic scattering cross sections of the DNA constituents are generally stronger peaked in forward direction than those of water, due to the larger dipole polarisability. Total ionisation cross sections per valence electron are in good agreement at energies above 500 eV for all molecules. However, the maximum is shifted from 100-150 eV for water to 70 eV for the DNA constituents; additionally, 25–40% lower values are obtained for water in the region of the maximum, while the data for the DNA constituents vary among themselves by 20%. Single differential ionisation cross sections per valence electron are generally enhanced for an emission of low energy secondary electrons from DNA constituents relative to water. Total excitation cross sections of the DNA constituents and water are in the same order of magnitude but show different energy dependence. Particularly, the dip in the data of the DNA constituents at 100–200 eV is contradictory to the maximum at 100 eV observed for water and has to be further investigated when more complete excitation cross section data for DNA constituents are available. As a first step, W-values were simulated for electrons of 1 keV in media consisting of THF, TMP or PY. As expected, those are 3.4–4.4 eV lower than the W-value for water vapour, due to the lower ionisation threshold and the smaller mean free ionisation path length of the DNA constituents. Unfortunately, no experimental W-values exist for verification.

Results from track structure simulations using the set of interaction cross sections of DNA constituents developed as part of this work were compared to simulations in water medium in sections 5.4 and 5.5. The influence of the cross section model for the calculation of the secondary electron emission angle and different sets of excitation cross section data was investigated for nanodosimetric quantities obtained in PY medium. It was found that the implementation of detailed double-differential cross section data should be preferred to a calculation of an average emission angle by kinematic formulae. On the other hand, the implementation of excitation cross sections for the discrete excitation levels compared to the use of only the total excitation cross section and a mean excitation energy has no significant impact on the simulated quantities when electrons are transported down to an energy of 7 eV. Nonetheless, an extension of the excitation cross section data of DNA constituents is required to enable more realistic simulations for low energy electrons.

For electron transport simulations in DNA medium, the medium was assumed to consist of uniformly distributed nucleotides, which themselves are made up of fractions of THF, TMP, PY, PU and water molecules. The same mass density of 1 g cm^{-3} was used for DNA medium, water vapour and liquid water. For the latter, two different sets of ionisation cross sections, SigIon1 and SigIon2, were compared.

Calculated mean ionisation cluster sizes are similar for DNA medium and liquid water when the cross section set SigIon1 is used, but a different energy dependence leads to deviations up to 12%. The mean cluster sizes obtained for electrons of energy below 150 eV in water vapour are lower due to the higher contribution of energy loss by excitations. The largest difference to the results in DNA medium are present when SigIon2 is used. In this case, the mean ionisation cluster sizes are 25% higher in the region of the maximum at 150 eV and differ by a factor of two at 40 eV. This is due to the large difference in ionisation cross sections. Mean excitation cluster sizes obtained in DNA medium are similar to those in water vapour. Compared to liquid water, the results in DNA medium are a factor of 2.0–2.5 larger.

The probability F_2 to produce at least two ionisations in the sensitive volume also shows significant differences: The maximum F_2 value of 0.66–0.68 is obtained for 100 eV electrons in DNA medium, reaching only 0.56–0.63 for water. The ionisation of the backbone molecules THF and TMP has the largest contribution, as the F_2 values for the backbone reach a probability of 0.39 at 150 eV.

Native DNA contains about 12.5 water molecules per nucleotide. In this case, the mean ionisation cluster size is enhanced by up to 36% for energies above 100 eV, while the maximum F_2 value increases to 0.76 at an energy of 100 eV. The F_2 values for higher electron energies are up to 42% larger when the water content is doubled. In this case, the estimated DNA damage is significantly enhanced relative to pure water medium. F_2 values calculated for the backbone molecules are useful to estimate the probability for a DNA strand break by direct ionisation of the backbone molecules. However, one has to keep in mind that an ionisation is not always followed by a fragmentation of the DNA. On the other hand, its fragmentation may also occur through other processes, such as dissociative excitation states or ionisations of intrinsic water molecules. The latter process could lead to the formation of radicals, which easily reach the sensitive DNA molecules to enhance their damage. This means that the water content of the DNA has a large influence on the complexity of clusters and, hence, the DNA damage. Therefore, the F_2 values for ionisation may provide an estimation for the probability of DNA damage, if the number of ionisations which do not lead to a fragmentation is similar to the additional damage of DNA molecules through other fragmentation channels.

More realistic simulations were performed for 1 MeV proton tracks. The same mass density was again assumed for water and DNA media. Protons were always transported in water due to the lack of interaction cross section data for DNA constituents. The different media used for electron transport affect the track structure parameters in the vicinity of the proton trajectory. A larger frequency of secondary electrons with an energy below 15 eV is present in water, which is most likely due to the average energy loss assumed after an excitation of DNA constituents. This leads to a much larger fluence of electrons through target cylinders in water placed at different distances (1–10 nm) to the proton trajectory. Hence, a comparison of electron spectra and fluence is only realistic when an improved set of electron-impact excitation cross sections is used in the simulations.

Despite the larger frequency of electrons with energies between the ionisation threshold and about 15 eV in water, the mean ionisation cluster size is 5–50% higher in DNA medium at distances of 1–10 nm, respectively. Similarly, F_2 values are 16–50% higher at the different distances. These results are in accordance with the values obtained for monoenergetic electrons (figures 5.6 and 5.8).

It is expected that the differences of mean ionisation cluster size and F_2 values obtained in DNA medium and water become larger when electron-impact cross sections for individual excitation states are available for electrons of energy at least down to the lowest electronic excitation state. Particularly for electrons of energies between the thresholds for discrete excitation and ionisation, the energy loss is overestimated in the present simulations. Hence, the frequency of secondary electrons is reduced in this energy range.

Moreover, for a simulation of protons traversing a cell nucleus, an implementation of proton-impact cross sections of DNA constituents may alter the ionisation mean free path of the protons and, hence, the number of secondary electrons as well as the electron spectra. In addition, the use of highly-structured DNA target models for the proton transport may be advantageous, as, on the one hand, protons of energies above 100 keV do not significantly change their direction of motion and, on the other hand, the probability for an interaction as well as secondary electron spectra produced at different molecules of the DNA medium may vary substantially. The resulting electron spectra in the vicinity of the proton trajectory may be different from those obtained with a mean free path length, averaged over the different molecules comprising the DNA medium.

Chapter 6

Track structure simulations for protons and alpha particles

6.1 Introduction

This chapter forms the basis for an extension of the work on electron cross section data to ion-impact as those are important in heavy ion therapy. In particular, the benchmark of track structure simulations of protons and helium particles by experiments, performed in the ion-counting nanodosimeter at the PTB [67], is described. This involved a review of interaction cross sections of nitrogen and propane and simulations using nanodosimeter setup.

The presented work has been initiated and the literature review, the simulations and the major part of the preparation of the manuscript were performed by myself.
The article is reprinted with permission from Physical Review E as follows:
M. U. Bug, E. Gargioni, H. Nettelbeck, W. Y. Baek, G. Hilgers, A. B. Rosenfeld, H. Rabus. *Phys. Rev. E* **88**: 043308 1-21 (2013). [Pub10]. Copyright (2013) by the American Physical Society.

6.2 Ionisation cross section data of nitrogen, methane and propane for light ions and electrons and their suitability for use in track structure simulations

Abstract. Track structure Monte Carlo simulations are frequently applied in micro- and nanodosimetry to calculate the radiation transport in detail. The use of a well-validated set of cross section data in such simulation codes ensures accurate calculations of transport parameters, such as ionisation yields. These cross section data are, however, scarce and often discrepant when measured by different groups. This work surveys literature data on ionisation and charge-transfer cross sections of nitrogen, methane, and propane for electrons, protons, and helium particles, focusing on the energy range between 100 keV and 20 MeV. Based on the evaluated data, different models for the parametrisation of the cross section data are implemented in the code PTra, developed for simulating proton and alpha particle transport in an ion-counting nanodosimeter. The suitability of the cross section data is investigated by comparing the calculated mean ionisation cluster size and energy loss with experimental results in either nitrogen or propane. For protons, generally good agreement between measured and simulated data is found when the Rudd model is used in PTra. For alpha particles, however, a considerable influence of different parametrisations of cross sections for ionisation and charge transfer is observed. The PTra code using the charge-transfer data is, nevertheless, successfully benchmarked by the experimental data for the calculation of nanodosimetric quantities, but remaining discrepancies still have to be further investigated (up to 13% lower energy loss and 19% lower mean ionisation cluster size than in the experiment). A continuation of this work should investigate data for the energy loss per interaction as well as differential cross section data of nitrogen and propane. Interpolation models for ionisation and charge-transfer data are proposed. The Barkas model, frequently used for a determination of the effective charge in the ionisation cross section, significantly underestimates both the energy loss (by up to 19%) and the mean ionisation cluster size (up to 65%) for alpha particles. It is, therefore, not recommended for particle-track simulations.

PHYSICAL REVIEW E **88**, 043308 (2013)

Ionization cross section data of nitrogen, methane, and propane for light ions and electrons and their suitability for use in track structure simulations

Marion U. Bug,[1,2] Elisabetta Gargioni,[3] Heidi Nettelbeck,[1] Woon Yong Baek,[1]
Gerhard Hilgers,[1] Anatoly B. Rosenfeld,[2] and Hans Rabus[1]
[1]*Physikalisch-Technische Bundesanstalt (PTB), Bundesallee 100, 38116 Braunschweig, Germany*
[2]*Centre for Medical Radiation Physics (CMRP), University of Wollongong, Wollongong, New South Wales 2522, Australia*
[3]*University Medical Center Hamburg-Eppendorf, Martinistrasse 52, 20246 Hamburg, Germany*

(Received 8 August 2013; published 29 October 2013)

Track structure Monte Carlo simulations are frequently applied in micro- and nanodosimetry to calculate the radiation transport in detail. The use of a well-validated set of cross section data in such simulation codes ensures accurate calculations of transport parameters, such as ionization yields. These cross section data are, however, scarce and often discrepant when measured by different groups. This work surveys literature data on ionization and charge-transfer cross sections of nitrogen, methane, and propane for electrons, protons, and helium particles, focusing on the energy range between 100 keV and 20 MeV. Based on the evaluated data, different models for the parametrization of the cross section data are implemented in the code PTRA, developed for simulating proton and alpha particle transport in an ion-counting nanodosimeter. The suitability of the cross section data is investigated by comparing the calculated mean ionization cluster size and energy loss with experimental results in either nitrogen or propane. For protons, generally good agreement between measured and simulated data is found when the Rudd model is used in PTRA. For alpha particles, however, a considerable influence of different parametrizations of cross sections for ionization and charge transfer is observed. The PTRA code using the charge-transfer data is, nevertheless, successfully benchmarked by the experimental data for the calculation of nanodosimetric quantities, but remaining discrepancies still have to be further investigated (up to 13% lower energy loss and 19% lower mean ionization cluster size than in the experiment). A continuation of this work should investigate data for the energy loss per interaction as well as differential cross section data of nitrogen and propane. Interpolation models for ionization and charge-transfer data are proposed. The Barkas model, frequently used for a determination of the effective charge in the ionization cross section, significantly underestimates both the energy loss (by up to 19%) and the mean ionization cluster size (up to 65%) for alpha particles. It is, therefore, not recommended for particle-track simulations.

DOI: 10.1103/PhysRevE.88.043308 PACS number(s): 07.05.Tp, 87.53.Bn

I. INTRODUCTION

Micro- and nanodosimetric approaches have been under development for several years [1–6] as a means to characterize the track structure of ionizing radiation. This characterization is particularly important for an estimation of initial radiation-induced biological effects on the microscopic scale. At such small dimensions, the stochastic nature of radiation interactions with the medium, manifesting in the track structure, has to be considered in detail. The particle track consists of a sequence of single interactions of the primary particle with the traversed medium and the interactions of secondary particles, which are produced during ionization processes and subsequently propagate in the medium. A description of the track structure is particularly important for densely ionizing radiation, such as ions (with an energy of their stopping power maximum) or low-energy secondary electrons (below about 1 keV). These particles deposit a large amount of their energy within volumes of a few micrometers or even nanometers and therefore lead to significant damage of the microscopic structure of matter. In the case of the DNA, this may lead to carcinogenesis or cell death. Therefore, track structure quantities describing the density of interactions, which potentially produce lesions to the DNA on the microscopic scale, need to be accurately determined.

Track structure quantities are experimentally investigated in micro- and nanodosimetry using detectors filled with a low density gas [1,7,8]. Such experiments have, in fact, proven to effectively model parameters related to the track structure in microscopic compartments of human cells for particles of different type and energy (defining the radiation quality) [8]. While microdosimeters often use tissue-equivalent gases, consisting of a mixture of propane, nitrogen, and carbon dioxide, nanodosimeters are usually operated with either nitrogen or propane gas [1,2,7].

In addition to experiments, Monte Carlo track structure simulations are important for characterizing particle tracks in condensed media, such as human cells. In such media, track structure quantities cannot be experimentally determined, owing to the limitations of current detector technology. Particle-track simulation codes can, however, be benchmarked with measured data by modeling a micro- or nanodosimetric experiment, which is performed in millimeter-sized volumes of low-pressure gas [7,8]. To simulate the particle track, the history of an incident projectile is followed interaction by interaction through the medium [3,8,9]. For such detailed simulations, the cross sections for the physical interactions of the incident particles with the molecules comprising the medium are essential input data.

The most important cross sections for nano- and microdosimetric applications are those for impact ionization since these dosimeters measure the number of ionized target molecules or the energy deposited by ionizations. Despite the frequent use of propane in dosimetry, a survey of the literature indicates that ionization or charge-transfer cross sections for light ions in this medium have rarely been measured. For example, measured data on proton or alpha particle impact-ionization cross sections of propane are still missing. However, propane data can be scaled from those of methane as explained in Sec. IV D. For nitrogen, on the other hand, a large amount of interaction cross section data for protons and electrons are available as well as a few data for helium particles. However, some of these data appear inconsistent in overlapping energy ranges.

The aim of this work is to recommend cross section data sets of nitrogen and propane for light ions (i.e., protons and helium particles) and electrons, which can be implemented in track structure codes that simulate nano- and microdosimetry experiments. For this purpose, data on impact-ionization cross sections of nitrogen, propane, and methane available in the literature are surveyed for electrons, as well as for protons and helium particles of different charge states. Charge-transfer cross sections for helium particles are reviewed as well. Methods to provide a complete data set for an implementation in track structure simulations are investigated, using model functions for interpolation. Simulated nanodosimetric quantities are compared with experimental results to benchmark the simulations. Also, the influence of different models used for parameterizing the interaction cross sections on calculated quantities is assessed.

Section II briefly introduces the nanodosimetric approach applied in this work. Details on the track structure simulation by means of the PTRA code are presented in Sec. III. Review, analysis, and modeling of the cross section data are discussed in Sec. IV. In Sec. V, simulation results are compared to experimental data.

II. BASIC NANODOSIMETRIC QUANTITIES

The nanodosimetric approach applied in this work is based on the evaluation of the ionization cluster size, which is defined as the number of ionizations produced by a passage of a single incident particle within a specified target volume. Ionizations of the primary ions and secondary electrons occur at random positions along the track and subsequent ionizations are spatially separated, on average, by the ionization mean free path. Therefore, the ionization cluster size is a stochastic quantity and can be characterized by a probability distribution. The ionization mean free path is a function of the radiation quality Q so that the probability distribution $P(\nu|Q)$ of ionization cluster size ν is a quantity characterizing the track structure of a specific radiation quality. $P(\nu|Q)$ is subject to the normalization condition

$$\sum_{\nu=0}^{\infty} P(\nu|Q) = 1. \tag{1}$$

Further characteristic quantities describing the track structure for a given radiation quality can be derived from momenta of $P(\nu|Q)$. For example, the mean ionization cluster size M_1 is defined by its first moment,

$$M_1 = \sum_{\nu=0}^{\infty} \nu P(\nu|Q). \tag{2}$$

III. PTRA TRACK STRUCTURE SIMULATIONS

The Physikalisch-Technische Bundesanstalt (PTB) track structure code “PTRA” is dedicated for applications in nanodosimetry [4,8]. This code also models the experimental setup of the ion-counting nanodosimeter which has been developed by the PTB and Weizmann Institute of Science (WIS) and has been comprehensively described in [7]. In brief, the nanodosimeter operates with either nitrogen or propane at a pressure on the order of 120 Pa. It was used at the PTB ion accelerator facilities to measure track structure parameters of protons and alpha particles of energies between 100 keV and 20 MeV. Incident ions enter a gas-filled chamber through a Mylar window. They subsequently traverse 230 mm of gas before reaching the so-called sensitive volume of the nanodosimeter, which is defined by an electrical field. It is approximately cylindrical in shape with a height of 50 mm and a diameter of about 1 mm. Gas ions created inside the sensitive volume by the passage of an incident particle drift along an appropriate electric field and are then extracted through an aperture and counted. The spatial variation of the extraction efficiency of the gas ions is taken into account in the simulations. After traversing the sensitive volume, the residual energy of the primary ion is recorded by a silicon detector, positioned 75 mm downstream of the sensitive volume.

In the past years, PTRA was used to simulate the transport of protons and alpha particles with energies above 1 MeV/u, for which charge-transfer processes can be neglected. Simulations with the PTRA code have shown to reproduce well the probability distribution of ionization cluster sizes produced by 4.6-MeV alpha particles in volumes of nitrogen, measured with another nanodosimeter known as the Jet Counter [4]. Furthermore, experimental cluster size distributions in propane obtained with an ion-counting nanodosimeter, similar to that of PTB/WIS, for 4.3-MeV alpha particles and protons of energies above 7 MeV also showed good agreement with calculated data [7]. Even simulated cluster size distributions for protons of energies between 0.4 and 3.5 MeV in propane are in overall good agreement with the data measured in the PTB/WIS ion-counting nanodosimeter [10].

In the simulations, the ions are started behind the Mylar window and the history of each primary ion, traversing the interaction chamber, is calculated until it reaches the detector plane.[1] Secondary electrons are transported until their energy falls below the ionization threshold of the gas molecules (only the yield of ionization events is of interest in this work). Particle tracks are calculated in PTRA by taking into account the processes described in the following. Elastic scattering of electrons is included, where the direction of an electron is changed according to the differential elastic scattering cross section and without any deposition of energy. Impact ionization by an ion or electron leads to the emission of a secondary electron, which is subsequently transported. In the case of an electronic excitation, the projectile transfers some energy to the target molecule, resulting in the excitation of an electron to a higher energy level. In the simulations, a

---

[1] Versions PTra-n2-1302 and PTra-c3h8-1302 were used for simulations in nitrogen and propane, respectively.

potential change in direction of the projectile by excitation processes was neglected. Moreover, only a minor fraction of the energy loss by an incident particle originates from excitation processes, since the excitation cross section is significantly lower than that for ionization and, on average, less energy is transferred in an excitation event [11,12]. Therefore, the influence of electronic excitations of gas molecules by ions on the ionization cluster size is negligible and these processes are not further discussed in this work. The total and differential cross section data for the processes described above, previously implemented in PTRA, are summarized in Refs. [4,8,13].

For an accurate transport simulation of low-energy protons (below 1 MeV) and alpha particles (below 4 MeV) through a medium, it is necessary to consider charge-transfer processes of the projectile, which become increasingly important as the particle energy decreases [14]. Charge-transfer processes for protons in the energy range down to 100 keV may not have a considerable effect on the proton's track structure, as is discussed in Sec. IV C; therefore, charge-transfer processes are only described for alpha particles in the following. In a charge-transfer process, alpha particles can ionize the target molecule by capturing one or two of the target's electrons and then continue their passage as singly charged helium ions, He^+, or neutral helium atoms, He^0. A He^+ ion can, in turn, capture another electron to become a neutral He^0 atom. Since the probability for a He^0 atom to capture an electron is almost negligible [15], this process is not further considered here. The cross sections for ionization of gas molecules by helium particles of lower charge states are significantly lower than for alpha particles. Both He^+ and He^0 projectiles can also experience electron loss, where one or two electrons are stripped off the projectile. Such electrons will travel through the medium with a well-defined probability of ionization, depending on their energy. In summary, the charge-transfer processes considered for simulating the transport of low-energy alpha particles are: the single and double electron-capture cross sections for He^{2+} (σ_{21} and σ_{20}); the single electron-capture and electron-loss processes for He^+ (σ_{10} and σ_{12}); and the single and double electron-loss cross sections for He^0 (σ_{01} and σ_{02}).

An incident (monoenergetic) helium beam reaches a state of charge equilibrium after a few interactions. In this case, the probability for a specific charge state is determined by the equilibrium condition that the rate of projectiles gaining a specific charge state is equal to the rate of those losing this charge state. More specifically, for an ensemble of helium particles, a particular electron-capture process σ_{ij} is always balanced by the corresponding electron-loss process σ_{ji}, such that

$$f_i\sigma_{ij} = f_j\sigma_{ji}, \tag{3}$$

where f_i and f_j are the equilibrium fractions of projectiles present in a specific charge state i and j, respectively, subject to

$$\sum_{i=0}^{i_{\max}} f_i = 1, \tag{4}$$

where $i_{\max} = 2$ for helium projectiles. Therefore, the equilibrium charge distribution is independent of the initial charge distribution in the beam and is only a function of the projectile energy.

Charge-transfer processes were included in the track structure simulation using two different approaches. In the first approach, the cross section data of these processes were directly incorporated in the random sampling procedure, where each interaction type was determined by taking into account the charge state of the helium projectile (in particular, the cross section data for ionization and charge transfer as well as total scattering cross sections). In the case of charge transfer, the charge of the helium particle was modified accordingly, before sampling the path length to the next point of interaction. In this, several assumptions were made. For example, in an electron-capture process, the energy change of the projectile is neglected. This energy change would arise from the difference in the binding energy of the electron initially bound in the target molecule and the binding energy in the final bound state in the projectile on the one hand and the energy required to accelerate the captured electron to the velocity of the projectile on the other hand. Furthermore, the energy required to remove the electron from the projectile in an electron-loss process was also neglected. This is reasonable as the binding energies are small compared to the projectile energies and the electron mass is much smaller than the mass of the projectile ion. In this case, the alteration in projectile energy due to the above mentioned effects would not lead to a significant change in the projectile's interaction cross sections. Finally, free electrons produced by electron-loss processes of the projectile were further transported through the medium, with their initial velocity assumed to be equal to that of the projectile with a momentum in the forward direction. The second approach used the equilibrium fractions of the charge states [according to Eq. (3)] to calculate an effective ionization cross section, which *per se* takes the above listed assumptions into account (see Sec. IV G).

IV. IONIZATION AND CHARGE-TRANSFER CROSS SECTIONS

This section provides a literature survey of the total ionization and charge-transfer cross sections of nitrogen, methane, and propane for interactions with electrons, protons, and helium particles. A review of semiempirical models is also included and recommendations on cross section data, suitable for an application in track structure simulations, are given. The literature review is not exhaustive for all particle types and energies, but rather focuses on data covering the energy range of interest for track structure simulations of protons and alpha particles in nanodosimetry (i.e., 100 keV to 20 MeV).

A. Electrons in nitrogen

A large number of cross section data exist for the interaction of electrons with nitrogen. Itikawa [16] comprehensively surveyed the literature and recommended a cross section data set. The recommended data agree within experimental uncertainties with probably the most referenced cross section data of Rapp and Englander-Golden [17] (Fig. 1). The binary-encounter-Bethe (BEB) model [19] (see Appendix A) predicts the measured data down to the maximum of the cross section at

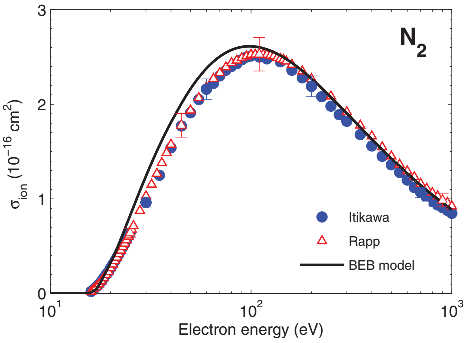

FIG. 1. (Color online) Electron-impact-ionization cross sections σ_{ion} of nitrogen recommended by Itikawa [16], measured by Rapp and Englander-Golden [17], and determined using the BEB model [18].

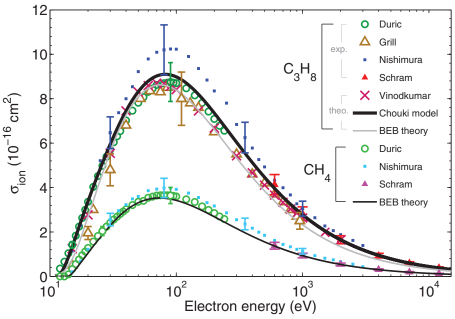

FIG. 2. (Color online) Electron-impact-ionization cross sections σ_{ion} of methane and propane (references are listed in Table I). Error bars are only shown for selected data points to improve readability.

an energy of 100 eV within a stated experimental uncertainty of 5%. For lower energies, the deviation is as much as 30% and occurs at an energy of about 30 eV. This deviation might be due to the approximation of differential oscillator strengths in the model. Nevertheless, the PTRA code uses the BEB model with the molecular orbital data from Hwang *et al.* [18] for describing the electron ionization processes in nitrogen, because this model provides also partial ionization cross sections for the subshells (needed to determine the projectile's enery loss).

B. Electrons in propane and methane

Electron interaction cross sections have been experimentally and theoretically determined for both propane and methane by several groups (e.g., those referenced in Table I). Figure 2 shows a selection of ionization cross sections for both molecules. In the case of methane, the BEB model in combination with the molecular orbital data of the NIST database [18,20] reproduces the measured data of Durić *et al.* [21] and Schram *et al.* [22] within the experimental uncertainties. The cross sections measured by Nishimura *et al.* [23], on the other hand, are systematically larger (up to 20% in the energy range between 100 eV and 2 keV) than those predicted by the BEB model, although an acceptable agreement is reached at lower energies when considering experimental uncertainties. All three groups determined the total ionization cross section by measuring the current originating from the collection of positive charges, produced by the passage of an electron beam.

TABLE I. Electron-impact-ionization cross section data of methane and propane and model functions for an interpolation of cross sections. Data are in eV.

	Experimental	
Durić *et al.* [21]	CH_4, C_3H_8	12–240
Grill *et al.* [24]	CH_4	15–950
Nishimura *et al.* [23]	CH_4, C_3H_8	15–3000
Schram *et al.* [22]	CH_4, C_3H_8	600–12 000
	Theoretical	
De Souza *et al.* [25]	CH_4	2–500
Vinodkumar *et al.* [26]	CH_4	15–2000
	Models	
BEB model [19] (see Appendix A)		
Chouki model [27] (see Appendix B)		

For propane, larger deviations between the available cross section data sets for electrons are observed (Fig. 2). Again, the data of Nishimura are systematically higher (up to 25%) than those determined by Durić *et al.* [21], especially in the intermediate energy range between 50 eV and 1 keV. This deviation exceeds the reported experimental uncertainties, which were between 10% and 15% for all experimental data. On the contrary, the cross section data of Grill *et al.* [24] are systematically lower than those of Durić *et al.* (up to 65% below 30 eV), although the discrepancy above 30 eV (approximately 10%) can be considered negligible within the overall uncertainty. Grill *et al.* determined partial ionization cross sections by measuring the number of positively charged molecular fragments, produced by the passage of an electron beam, by means of a mass spectrometer. For higher electron energies (above 600 eV), the cross section data measured by Schram *et al.* [22] agree with the data of Grill *et al.* and Nishimura *et al.* within about 10%.

The data of Durić *et al.* are supported by the inelastic cross sections of de Souza *et al.* [25], calculated by an *ab initio* approach, which are not shown in Fig. 2 in the interest of readability. However, for energies above 400 eV de Souza's predictions fall even below the predictions of the BEB model. Unfortunately, their data are only provided for energies up to 500 eV, thus not allowing the assessment of the high-energy behavior. Also the theoretical cross section data of Vinodkumar *et al.* [26], determined by the spherical complex optical potential approach, support the data of Durić *et al.* for energies below 80 eV, but better reproduce those of Grill *et al.* for energies between the maximum of the electron cross section at about 80 eV and 1 keV. In this energy range, the two data sets agree within 10% to 15%, which is within the stated experimental uncertainties. Above 1 keV, the cross sections of Vinodkumar *et al.* are in good agreement with those measured by Schram *et al.* (well within the 11% experimental uncertainty).

The BEB model using the molecular orbital data for propane [20], agrees well with the experimental data and those calculated by Vinodkumar *et al.* up to an electron energy of about 400 eV. Above this energy, however, the data obtained from the BEB model are lower than those of Schram *et al.* and Vinodkumar *et al.* (about 20% at 1 keV) and this deviation even increases with increasing energy (25% at 12 keV). This observation seems to be in contrast to the good agreement of the BEB model with Schram's measured data for methane over the same energy range, but this tendency has also been observed by Hwang *et al.* [18]. Their comparison of the BEB model with experimental ionization cross section data for different hydrocarbon molecules indicated larger deviations at higher energies for alkanes of higher order. It is not clear whether this deviation arises from systematical uncertainties of the measurements or from deficiencies of the model. For this reason, the parametrization of electron ionization cross sections of propane for the use in PTRA was obtained by calculating the mean value of the measured cross section data of Grill *et al.*, Schram *et al.*, Durić *et al.*, and Nishimura *et al.* The Chouki model [27] was then used to fit this data set. This model, together with the parameters for propane, is summarized in Appendix B. In the high-energy range, the Chouki model gives about 20% larger cross section values than the BEB model (Fig. 2).

C. Protons in nitrogen

Total ionization cross sections of nitrogen for protons in the energy range of interest in this work (between 100 keV and 20 MeV) were measured by several groups (see Table II) and a comprehensive survey and evaluation of literature data has been published by Rudd *et al.* in 1985 [28].

Figure 3 illustrates that the data of energies above 80 keV are generally in good agreement within the experimental uncertainties (which were between 10% and 25%). The measurements of Knudsen *et al.* [31] differ by less than 10% from those of the other groups (no uncertainty was provided), with the exception of the two lowest energy data points. Knudsen *et al.* determined the single-ionization cross sections by measuring the yield of positively charged fragments produced after the passage of a proton through a low-density gas. This yield was then corrected for the fraction of hydrogen atoms produced by electron-capture processes. The authors normalized their data to those of electron-impact cross sections. Rudd *et al.* [32] measured the number of electrons produced by a proton traversing a gas volume, thereby not taking into account *per se* electron-capture processes. The same method was used by De Heer *et al.* [30], while Crooks *et al.* [29] measured the double differential ionization cross sections and obtained the total ionization cross section by integrating over electron energy and scattering angle.

TABLE II. Impact-ionization cross section data and equilibrium fractions for hydrogen projectiles in nitrogen and model functions for an interpolation of cross sections. Data in keV.

Ionization cross section, H^+	
Crooks *et al.* [29]	50–300
De Heer *et al.* [30]	10–140
Knudsen *et al.* [31]	50–6000
Rudd *et al.* [32]	5–5000
Ionization cross section, H^0	
Puckett *et al.* [15]	150–400
Equilibrium fractions of hydrogen charge states	
Allison [33]	
Models	
Rudd model [28] (see Appendix C)	
Green model [34] (see Appendix D)	

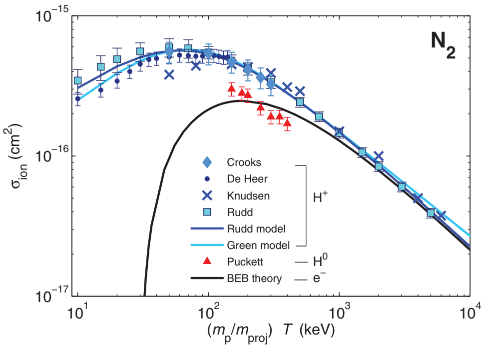

FIG. 3. (Color online) Ionization cross sections σ_{ion} of nitrogen for protons and electrons. Shown are measured ionization cross section data for protons and neutral hydrogen atoms (symbols) as well as results of semiempirical models (lines) (see Table II for references). Electron ionization cross sections were calculated by the BEB model [19] for comparison (the x axis of these data was multiplied by the ratio of proton mass m_p to the electron-projectile mass m_{proj} such that data for particles of the same velocity are compared).

In the higher energy range (above about 1 MeV), the proton cross sections measured by Rudd *et al.* and Knudsen *et al.* also agree well with those of electrons of equal velocity. This is consistent with the theoretical expectation based on the first Born approximation, where plane waves are used to describe the initial and final states of a bare projectile. According to Bethe [11], this approximation is applicable if the projectile potential constitutes a small perturbation, as is the case for projectiles of low charge and high velocity (much higher than the velocity of the target electrons). Using the first Born approximation, Bethe showed that the ionization cross section of a bare nucleus moving with velocity v is proportional to the number of electrons Z_{targ} of the target molecule and to the square of the projectile charge Z_{proj}, such that

$$\sigma_{\text{ion}} \propto \frac{Z_{\text{targ}} Z_{\text{proj}}^2}{\beta^2} \ln(\beta^2), \tag{5}$$

where $\beta = v/c$. This relation is independent of the particle type and was previously shown to hold for electrons with energies above 300 eV and for protons with energies greater than 550 keV [35] (see also Fig. 3).

For proton energies below about 1 MeV, the ionization cross section is higher than that for electrons of the same velocity. This is due to exchange interactions between incoming and bound electrons and the smaller energy range of secondary electrons in the case of electron impact [28]. For decreasing

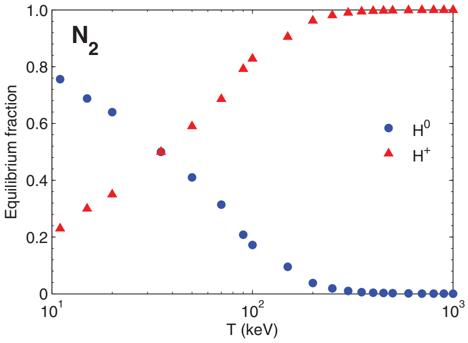

FIG. 4. (Color online) Equilibrium fractions of hydrogen particles H^0 and H^+ traveling in nitrogen (reference in Table II).

proton energy, charge-transfer processes become increasingly important [33] (Fig. 4). In the energy range of interest in this work, however, the probability of an electron-capture process to produce a hydrogen atom is less than 20%. Furthermore, the ionization cross section for neutral hydrogen atoms H^0, measured by Puckett *et al.* [15], is about a factor of two lower than the proton cross section (see Fig. 3). For these reasons, charge-transfer processes for protons were not modeled in PTRA and protons were assumed to keep their charge state.

Figure 3 also shows cross section values obtained using two semiempirical models, which were developed and parametrized by Rudd *et al.* [28] and by Green and McNeal [34] (see Appendices C and D, respectively). In the following, these models are referred to as the Rudd model and the Green model. For proton energies below 2 MeV, both models reproduce the experimental data of all groups within the experimental uncertainties. At higher energies, the predictions by the Rudd model are in good agreement with the electron data, where the measured electron cross sections are well described by the BEB model within 10% (see Sec. IV A). However, the discrepancy between the Green model and the BEB model increases with increasing energy, leading to about 30% higher values at 10 MeV for the Green model. This deviation might be due to the limited energy range of the experimental data used by Green and McNeal to fit their model. From their publication it seems that measured data had only been available up to proton energies of about 1.5 MeV.

The Rudd model [28] was implemented in PTRA to parametrize ionization cross sections for protons in nitrogen, owing to the better agreement with the electron data at higher energies, which is in accordance with theoretical expectations based on the Bethe theory.

D. Protons in propane and methane

While ionization cross sections of propane for electron interactions have been determined by many groups (as discussed in Sec. IV B), no experimental data for light ions were found in the literature during this review. These cross section data for both protons and alpha particles, which are required for particle-track simulations, were obtained from those of methane (largely available) by using a scaling procedure.

TABLE III. Proton-impact ionization cross section data of methane and a semiempirical model for interpolation of the data. Data in MeV.

Experimental	
Ben-Itzhak *et al.* [36]	1–12.0
Knudsen *et al.* [31]	0.5–6.0
Luna *et al.* [37]	0.5–3.5
Lynch *et al.* [38]	0.25, 1, and 2
Rudd *et al.* [32]	0.005–5.0
Model	
Rudd model [28] (see Appendix C)	

Ionization cross sections of methane for protons were measured in the past by several groups [a selection is referenced in Table III and shown in Fig. 5(a)]. A comprehensive survey and evaluation of literature data has been published previously

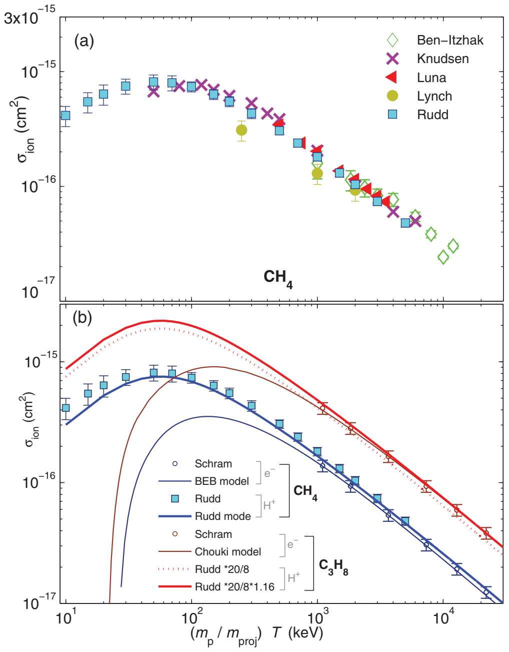

FIG. 5. (Color online) (a) Proton-impact-ionization cross sections σ_{ion} of methane measured by the authors given in Table III. For the data of Luna *et al.*, error bars are within the symbols. (b) Scaling of proton ionization cross sections of methane to propane. Symbols, experimental data; lines, results from model functions. For methane, a measured data set is shown as an example along with results from the Rudd model (references given in Table III). The scaled Rudd model for propane is also given. For comparison, electron-impact-ionization cross sections of Schram *et al.* and obtained by the BEB model and Chouki model are given for methane and propane, respectively (see Table I). Electron data were multiplied by the ratio of proton mass m_p to electron-projectile mass m_{proj} to achieve that both particle types are of the same velocity.

[28]. Rudd *et al.* [32] measured the yield of secondary electrons produced by ionization of methane molecules by single traversing protons. Luna *et al.* [37] determined absolute cross sections for the production of charged methane fragments $\mathrm{CH}_n{}^+$ ($n = 0$–4) after an impact of protons by time-of-flight spectrometry. The sum of these cross section data is the total ionization cross section shown in Fig. 5(a). These data are in agreement with those of Rudd *et al.*, within the experimental uncertainty of about 10%. Ben-Itzhak *et al.* [36] used a similar method as Luna *et al.* to determine the relative yield of multiply charged methane fragments. The total ionization cross section data were also obtained by summing the cross sections for the production of methane fragments. Below about 3 MeV, the cross sections determined by Ben-Itzhak *et al.* [36] agree closely with the data of Luna *et al.* [37] and Rudd *et al.* [32], but when compared to the data of Rudd *et al.* at higher energies, they are nearly 20% larger.

The same kind of measurement was applied by Knudsen *et al.* [31] to determine the single-ionization cross section. The authors normalized their data to those of electron-impact cross sections in order to obtain absolute cross section values. Their results generally agree with those of Rudd *et al.* and Luna *et al.* within the experimental uncertainties across the entire energy range. As for nitrogen (see Fig. 3), the lowest two data points cause a shift of the maximum cross section to higher energies (110 keV) when compared to the data of Rudd *et al.*, who observed a maximum at about 70 keV. In the measurements of Knudsen *et al.*, only single ionizations were taken into account, whereas the other authors included also multiple ionizations. Nevertheless, these data can be compared because the double-ionization cross section for methane was found to be two orders of magnitude smaller than the single-ionization cross section and therefore has a negligible contribution to the total ionization cross section [36]. Lynch *et al.* [38] determined the absolute ionization cross section for protons by an integration of the measured double differential ionization cross section as a function of secondary electron energy and scattering angle. Their data are lower than those of the other authors, deviating from those of Rudd *et al.* by as much as 40% at 250 keV.

Ionization cross section data of propane, missing in the literature, were implemented in the simulation code by multiplying the methane data by the ratio of the number of valence electrons in both molecules (i.e., 8 for methane and 20 for propane). Both methane and propane belong to the group of alkanes and thus have a similar bond structure. It can therefore be assumed that the relative energy dependence of the cross sections is similar. Scaling by the number of valence electrons of the target molecules is a reasonable approximation for particles of high velocities (above 1 MeV/u), where the Born approximation is valid [38,39]. In fact, the probability of ionization of the inner shells by ion impact is much lower than that of the valence shells, and it can thus be assumed that only the valence electrons participate in the interaction. This can be seen in Fig. 5(b), where the ratio of the electron cross sections for propane to methane is about 2.7 at an energy of 550 keV, increasing to about a factor of 3 in the MeV range.

In order to obtain a suitable model for proton cross sections of propane for use in the simulations, the Rudd model for methane [28] was first scaled using the factor 2.5 (i.e., the ratio of the number of valence-shell electrons $Z_{\mathrm{propane}}/Z_{\mathrm{methane}}$) and then multiplied by an additional factor of 1.16 to match the electron data for propane at energies greater than about 550 keV [Fig. 5(b)]. Thus, the ionization cross section data of propane used in the simulations for protons were determined by means of the Rudd model, which was parameterized for methane and multiplied by a total factor of 2.9.

E. Helium particles in nitrogen

1. Ionization cross sections

The available data for ionization cross sections of nitrogen for helium particles in the energy range of interest in this work are shown in Fig. 6(a) and references with respective energy ranges are listed in Table IV. In those experiments, a transverse electric field was used to collect electrons as well as positively charged ions produced by the projectile as it traversed the gas target, providing absolute cross sections for the production of electrons (σ_-) and slow positive ions (σ_+), respectively. For He^+ and He^0, electron-loss processes would contribute to the measured number of electrons, thereby yielding a cross section σ_-, which is larger than the ionization cross section. Similarly,

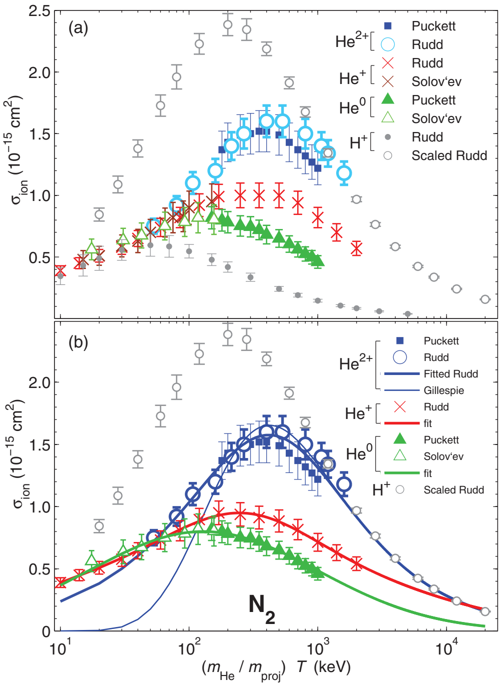

FIG. 6. (Color online) (a) Measured ionization cross sections σ_{ion} of nitrogen for helium particles of different charge states (references given in Table IV). Proton data of Rudd *et al.* [32] are shown for comparison. To compare particles of the same velocity, the abscissa was also multiplied by the ratio of the masses of helium particles (m_{He}) and protons (m_{p}) and the ordinate was scaled by Z^2. (b) Models for an interpolation of the experimental data of nitrogen shown in (a) (see Table IV for references).

TABLE IV. Impact-ionization and charge-transfer cross section data as well as equilibrium fractions for helium projectiles in nitrogen. Also listed are model functions and correction terms, investigated for an interpolation of cross sections. Data in keV.

Ionization cross sections	
He^{2+}	
Puckett *et al.* [15]	180–1000
Rudd *et al.* [43] ($^3He^{2+}$)	30–900
He^{+}	
Langley *et al.* [41]	133–1000
Pivovar *et al.* [42]	200–1800
Rudd *et al.* [40]	10–2000
Solov'ev *et al.* [44]	15–150
He^{0}	
Puckett *et al.* [15]	150–1000
Solov'ev *et al.* [44]	17–160
Models and correction terms	
Fitted Rudd model for He^{2+} [28] (Appendix C)	
Rudd model including Gillespie correction [46] [Eq. (6)]	
Model functions for He^{+} and He^{0} (Appendix E)	
Charge-transfer cross sections	
σ_{21}	
Itoh *et al.* [47]	700–2000
Rudd *et al.* [43] ($^3He^{2+}$)	15–450
σ_{20}	
Itoh *et al.* [47]	700–2000
Rudd *et al.* [43] ($^3He^{2+}$)	15–450
σ_{10}	
Barnett and Stier [48]	4–200
Gilbody *et al.* [49]	10–200
Itoh *et al.* [47]	700–2000
Rudd *et al.* [40]	5–350
σ_{01}	
Barnett and Stier [48]	4–200
Gilbody *et al.* [50]	60–350
Hvelplund and Horsdal Pedersen [51]	100–4000
Itoh *et al.* [52]	700–2000
σ_{02}	
Hvelplund and Horsdal Pedersen [51]	100–4000
Itoh *et al.* [52]	700–2000
σ_{12}	
Itoh *et al.* [52]	700–2000
Rudd *et al.* [40]	5–350
Equilibrium f_0, f_1, f_2 of helium charge states	
Barnett and Stier [48]	4–200
Pivovar *et al.* [53]	300–1000
Model functions	
Phenomenological functions (Appendix E)	

the ionization cross sections for He^{2+} and He^{+} ions are lower than the respective cross sections for the production of positive charges. This is because positively charged target ions may be left behind, due to ionization of the target molecules by electron capture of the projectile. For He^{2+}, the ionization cross section is equal to the cross section σ_-, as the electron-loss probability is zero. Similarly, the ionization cross section for He^0 equals σ_+, since the electron-capture cross section is negligible [15].

Since He^+ ions are able to capture or lose an electron, the cross section for single electron loss has to be subtracted from σ_- in order to obtain the desired ionization cross section. Therefore, the electron-loss cross section σ_{12}, determined by Rudd *et al.* [40], was subtracted from the σ_- cross sections, determined by the same authors [15,40–42]. The resulting ionization cross sections for He^+ ions were thereby reduced by a few percent at the lower energies and as much as 15% at about 1 MeV, where the electron-loss cross section has its maximum [Fig. 6(a)]. This reduction was still within the uncertainties associated with the experimental data of σ_-. It should be mentioned that ionization cross sections for He^+ ions were determined by Langley *et al.* [41] and by Pivovar *et al.* [42] by assuming that the probability for electron-loss ionization (electron loss in combination with an ionization of the target molecule) is much higher than for electron loss only. Their ionization cross sections are, therefore, up to 30% smaller than σ_- (not shown).

The ionization cross sections for He^{2+} ions[2] and $^3He^{2+}$, shown in Fig. 6(a), were measured by Puckett *et al.* [15] and by Rudd *et al.* [43], respectively. The cross sections by Rudd *et al.* were set to be equal to those of He^{2+} for the same velocity of both projectiles. For energies below about 800 keV, these data agree well with those of Puckett *et al.* (within the experimental uncertainties of 8% and 11% for the data of Rudd *et al.* and Puckett *et al.*, respectively). At higher energies, the deviation reaches 17% at 1 MeV, which is still within the combined uncertainty values. The cross sections for He^+ measured by Rudd *et al.* [40], Solov'ev *et al.* [44], and Pivovar *et al.* [42] (not shown to keep readability) agree well in the overlapping energy range. Those of Langley *et al.* [41] (not shown) are by as much as 25% larger with increasing deviation for decreasing energy. Only two sets of measured ionization cross section data for He^0 were found in the literature, those by Puckett *et al.* [15] and by Solov'ev *et al.* [44]. Within the overlapping energy regions, the He^+ and He^0 cross sections of the different groups are in excellent agreement and well within the experimental uncertainties, which are between 10% (Rudd *et al.*) and 15% (Solov'ev *et al.*).

Figure 6(a) also shows cross section data for He^{2+} ions obtained from those of protons H^+ with the same velocity, which were scaled by the square of alpha particle charge Z^2 according to Eq. (5). The figure shows that the ionization cross section for alpha particles is approaching the scaled cross section for protons at energies above 1 MeV, where the first Born approximation is valid. Below 1 MeV, the He^{2+} cross sections are lower than the scaled proton cross sections by as much as 45% at 100 keV. Furthermore, the maximum of the ionization cross section for the measured He^{2+} data occurs between 350 and 450 keV (for the data of Puckett *et al.* and Rudd *et al.*, respectively), while it is at about 70 keV for protons, which corresponds to an energy of about 280 keV for alpha particles of equal velocity.

The reduction of the cross section for low-energy alpha particles with respect to the scaled proton data is due to two-center phenomena. The target-centered charge distribution of

---

[2] Note that the mass number of helium projectiles mentioned in this work is always 4 unless indicated otherwise.

initially bound electrons adjusts adiabatically to the long-range Coulomb potential of the (slow) traversing projectile [45]. Due to the subsequent screening of the projectile potential by the attracted electron distribution, the emission probability of an electron decreases with decreasing projectile energy. Also, if the encounter of the projectile to the target is close, the projectile's potential reaches inside the orbit of the target electrons. This leads to an increased binding energy of the electrons and, subsequently, to a decrease in the ionization cross section. Two-center effects are not included in the first Born approximation and the ionization cross section is no longer proportional to the square of the nuclear charge Z [as described by Eq. (5)]. Gillespie [46] proposed a simple model for an effective projectile charge Z_{eff}, which enables more realistic scaling between the proton and alpha particle cross sections,

$$Z_{\mathrm{eff}}^2 = Z^2 \exp(-\lambda Z \alpha^2/\beta^2), \tag{6}$$

where α is the fine structure constant and $\beta = v_{\mathrm{proj}}/c$.

In his work, Eq. (6) was fitted for an impact of different ions ($Z = 1$–13) on H_2 and He, where the value of λ was 1 for H_2 and 2 for He. Figure 6(b) shows that, down to 150 keV, a good agreement of the scaled proton cross section with the measured ionization cross section for alpha particles is obtained when the parameter λ is adjusted to $7/R$, where R is 13.61 eV. Below this energy, the predicted values of the Gillespie model underestimate the experimental data, for example, at 100 keV it is 35% lower.

As an alternative to this model for effective-charge correction, the Rudd model [28] was fitted to the He^{2+} ionization cross section, adjusting only the parameter C_{Rudd} (see Table VII and Appendix C). As can be seen in Fig. 6(b), the resulting fit curve (referred to as fitted Rudd model in the following) is in good agreement with the measured data. Above 1 MeV, the fitted Rudd model agrees well with the original Rudd model (scaled by the square of alpha-particle charge). Ionization cross sections, calculated using the effective charge obtained according to the Gillespie model, are only as much as 5% larger than the predictions of the fitted Rudd model in the region of the maximum (i.e., between about 400 keV and 2 MeV) and 35% lower at 100 keV. In summary, the fitted Rudd model was implemented in PTRA due to its good agreement with experimental cross sections for alpha particle across a wide energy range.

The ionization cross sections for He^0 and He^+ are not well described by the combination of the original Rudd model [28] and the effective charge obtained from the Gillespie model. Therefore, to facilitate the implementation of the ionization cross sections for He^0 and He^+ in the code, Gaussian functions were found to provide the best fit to the experimental data [see Eq. (E1), as well as Fig. 6(b)]. The large deviation between the He^+ or He^0 and the He^{2+} cross sections [refer to Fig. 6(a)] is due to the electron(s) in the bound projectile state screening the nuclear charge [14]. This screening effect results in an effective projectile charge, which decreases with increasing adiabatic radius (a measure for the distance between the projectile and the target electron) [54]. The adiabatic radius is a function of projectile velocity as well as of kinetic energy and binding energy of the electron that is ejected in the ionization process. In the case of He^+, the effective projectile charge varies between 1 for small momentum transfers (producing secondary electrons of low energies in glancing collisions) and 2 for large momentum transfers (producing secondary electrons of high energies in close collisions), which preferably occur for low and high energetic projectiles, respectively. This can be seen in Fig. 6(a) for energies below about 60 keV, where the ionization cross sections for singly charged helium ions and protons are similar. Above this energy, the He^+ cross section data increase more rapidly, forming a broad maximum at about 200 keV, where the He^+ and the He^{2+} cross sections appear to converge at an energy of about 10 MeV, as suggested in [14]. This high-energy behavior was taken into account in the fitting procedure.

2. *Charge-transfer cross sections*

Charge-transfer cross sections of nitrogen have been frequently measured in the past, as referenced in Table IV. The cross sections for electron capture σ_{ji} (transferring the helium projectile from a charge state j to a lower state i) and those for electron loss σ_{ij} are shown in Figs. 7(a) and 7(b), respectively. Gilbody *et al.* [49,50] determined the charge-transfer cross sections σ_{10}, as well as σ_{01}, by means of a beam attenuation technique, where the double electron loss was assumed to be negligible. Hvelplund and Horsdal Pedersen [51] measured the electron-loss cross sections σ_{01} and σ_{02} by means of the initial growth method, in which the fractions of charge states (produced by an incident helium particle of specific charge)

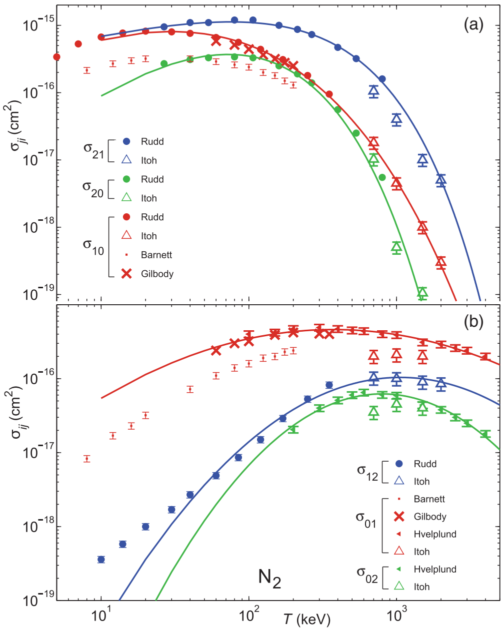

FIG. 7. (Color online) Cross section data of nitrogen for (a) electron-capture σ_{ji} and (b) electron-loss σ_{ij} processes of helium projectiles, measured by the authors referenced in Table IV (symbols). For some data sets error bars are within the symbols. The lines show the data obtained by the model functions given in Appendix E.

were measured for different densities of the target gas. Using the same method, Rudd *et al.* [40,43] determined the single and double electron-capture cross sections σ_{21} and σ_{20} for $^3He^{2+}$, as well as the cross sections for single electron capture and loss for He^+, σ_{10} and σ_{01}, respectively. The electron-capture cross sections for He^{2+} were obtained from those for $^3He^{2+}$ of the same velocity. The cross section data determined by these authors are in good agreement within the stated experimental uncertainties, which were about 10%.

In an early publication, Barnett and Stier [48] measured the cross sections σ_{10} and σ_{01}, using the initial growth method. Their results are approximately two times lower than those reported by other authors. It is, however, interesting that these data also appear in a publication by Allison [33] but in comparative studies published by Gilbody *et al.* [49,50] and Hvelplund and Horsdal Pedersen [51] they are a factor of two larger. Considering that the data obtained by Barnett and Stier for other molecules (H_2, He, Ne, Ar) agree well with (and in some cases are even larger than) those determined by the other two groups, it seems possible that a correction factor of two may have been applied to their data for nitrogen. In this case, their data are up to 15% and 30% lower than the data of Rudd *et al.* [40] for σ_{01} and σ_{10}, respectively. Itoh *et al.* [47,52] also used the initial growth method to measure single and double electron-capture as well as electron-loss cross sections. Some of their data (i.e., σ_{21}, σ_{01}, and σ_{02}) are generally a factor of two lower than those of other authors and exhibit a different qualitative behavior, particularly for σ_{01} and σ_{02}. For σ_{12}, σ_{10}, and σ_{20} no data were available for comparison during the compilation of this work, at least in the energy range of interest.

Experimental data were fitted by exponential and polynomial functions [given in Eqs. (E2) and (E3)], excluding the data from Barnett and Stier and the two electron-loss cross section data of Itoh *et al.* mentioned above. The electron-capture cross sections σ_{21} of Itoh *et al.* were given a lower weight of 0.5, as these were a factor of two lower than other data. The fitted curves are the solid lines shown in Fig. 7.

In order to test the consistency of these fitted cross sections, the equilibrium fractions f_0, f_1, and f_2 (which correspond to the three helium charge states He^0, He^+, and He^{2+}, respectively), as measured by Barnett and Stier [48] and Pivovar *et al.* [53], were compared to the charge-transfer cross section data calculated using Eq. (3). This comparison, shown in Fig. 8, included three different approaches.

(v1) The measured equilibrium fractions were fitted by the functions summarized in Eqs. (E4a)–(E4c). These were used, together with the functions fitted to the electron-capture cross sections σ_{10}, σ_{20}, and σ_{12}, to determine the electron-loss cross sections σ_{01}, σ_{02}, and σ_{21} by means of Eq. (3).

(v2) The functions fitted to the cross sections σ_{01}, σ_{10}, σ_{12}, and σ_{21} were used to calculate the equilibrium fractions of the helium charge states by means of Eq. (3).

(v3) The same approach as (v2), except that the cross sections σ_{01}, σ_{10}, σ_{02}, and σ_{20} were used.
In approaches (v2) and (v3) the charge-transfer cross section data for He^+ were used, since the agreement of the fitted models with the experimental data appear to be most reliable. In all three approaches, the fraction f_1 was chosen to be determined by subtracting f_0 and f_2 from unity [see Eq. (4)].

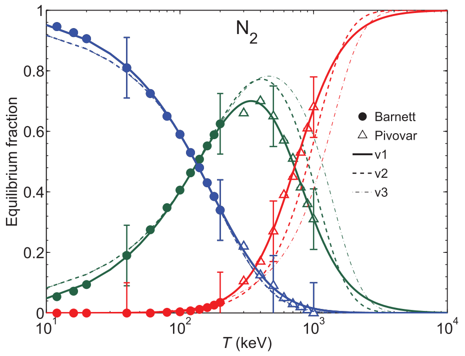

FIG. 8. (Color online) Equilibrium fractions f_0 (blue), f_1 (green), and f_2 (red) of helium particles traveling in nitrogen. Measured fractions (symbols) and fractions obtained by the model functions (solid lines) are shown (for references, see Table IV). Equilibrium fractions were also calculated from charge-transfer cross section data [(v2) and (v3)], as described in Sec. IV E2.

Up to an energy of 200 keV, the equilibrium fractions determined from the fitted models [approach (v1)] agree well with the data measured by Barnett and Stier, deviating by less than 5% (Fig. 7). Above this energy, the equilibrium fractions of He^+ and He^{2+} measured by Pivovar *et al.* differ by up to 15% from those determined by approach (v2). An even larger deviation of up to 25% occurs for energies between 200 keV and 3 MeV using approach (v3), revealing some inconsistency of the data in the literature. For helium particles of energies above 2 MeV, the probability for electron capture can be neglected in all three approaches as the fraction of He^{2+} ions with these energies is greater than 95%. Due to their large deviations, (v1) and (v3) are used in Secs. IV G and V to investigate the sensitivity of simulation data on the different equilibrium fractions. Recommendations for the implementation of the cross sections are then given in Sec. VI.

F. Helium particles in propane and methane

1. *Ionization cross sections*

There are no published experimental ionization cross section data of propane for helium projectiles. Rudd *et al.* [40,43], however, measured σ_- of methane for He^{2+} and He^+ ions (see Table V). The ionization cross sections of methane can be scaled to obtain those of propane according to Bethe's theory (refer to Sec. IV C).

The Rudd model [28] was used to fit the He^{2+} ionization cross section of methane by varying the parameter C_{Rudd} (see Appendix C and compare to Sec. IV E1). As can be seen in Fig. 9, the data calculated using the fitted Rudd model are in good agreement with the measured data as they are within the experimental uncertainty of about 8%. Also plotted are the cross section data obtained by the original Rudd model with a correction term for the effective charge, Z_{eff}, according to the Gillespie model using the parameter $\lambda = 10$ [see Eq. (6)]. The predicted values of this model are within the experimental uncertainty for energies above 110 keV but steeply decrease with decreasing energy, such that it already deviates by 15%

TABLE V. Impact-ionization and charge-transfer cross section data as well as equilibrium fractions for helium projectiles in methane and propane. Also listed are models and correction terms, investigated for an interpolation of cross sections. Data in keV.

Ionization cross sections		
	He^{2+}	
Rudd *et al.* [43]	30–900	$^3He^{2+}$,CH_4
	He^+	
Rudd *et al.* [40]	10–2000	CH_4
	Models and correction terms	
Fitted Rudd model [28] (Appendix C)		
Rudd model incl. Gillespie correction [46] [Eq. (6)]		
	Charge-transfer cross sections	
	σ_{21}	
Itoh *et al.* [47]	700–2000	CH_4,C_3H_8
Rudd *et al.* [43]	15–450	$^3He^{2+}$,CH_4
	σ_{20}	
Itoh *et al.* [47]	700–2000	CH_4,C_3H_8
Rudd *et al.* [43]	15–450	$^3He^{2+}$,CH_4
	σ_{10}	
Itoh *et al.* [47]	700–2000	CH_4,C_3H_8
Rudd *et al.* [40]	5–350	CH_4
Sataka *et al.* [55]	300–1800	CH_4
	σ_{01}	
Itoh *et al.* [52]	700–2000	CH_4,C_3H_8
Sataka *et al.* [55]	300–1800	CH_4
	σ_{02}	
Itoh *et al.* [52]	700–2000	CH_4,C_3H_8
Sataka *et al.* [55]	300–1800	CH_4
	σ_{12}	
Itoh *et al.* [52]	700–2000	CH_4,C_3H_8
Rudd *et al.* [40]	5–350	CH_4
Sataka *et al.* [55]	300–1800	CH_4
	Model function	
Phenomenological functions (Appendix E)		

at 100 keV from the measured data. The maximum of the He^{2+} cross sections predicted by these models occurs at about 350 keV, which is similar to the energy of the maximum in the nitrogen cross section data.

The He^+ ionization cross sections of methane were determined from the σ_- data by subtracting σ_{12}, which was also measured by Rudd *et al.* [40] (see also Sec. IV E1). The He^+ ionization cross section data were then fitted using a superposition of two Gaussian functions, given by Eq. (E1). Ionization cross sections of propane for alpha particles and He^+ ions were then obtained by scaling the corresponding cross sections of methane by a factor of 2.9 (see Sec. IV D, where this factor was previously used when scaling the proton ionization cross section data of methane to those of propane).

For He^0 atoms, ionization cross section data of both methane and propane could not be found in the literature. Figure 9, however, reveals that the He^+ ionization cross sections of nitrogen and methane have a similar energy dependence and deviate as much as 28% in the energy region between 170 keV and 1.4 MeV (mostly within the experimental uncertainties of 10%). Due to this similarity and the lack of data, the ionization cross sections of methane for He^0 were assumed to be equal to those of nitrogen. The ionization cross sections of propane for He^0 were then obtained by multiplying the cross sections of nitrogen by the factor of 2.9.

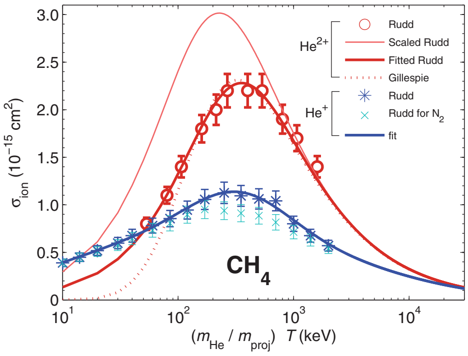

FIG. 9. (Color online) Ionization cross sections of methane for helium projectiles (symbols, experimental data; lines, model functions). Shown are the data referenced in Table V as well as the Rudd model [28] for protons with the same velocity as the helium particles (their abscissa was multiplied by the ratio of the masses of helium particles m_{He} to protons m_{proj} and the ordinate was scaled by Z^2). The measured ionization cross sections of nitrogen for He^+ [40] is shown for comparison.

2. Charge-transfer cross sections

Measured electron-capture and electron-loss cross sections for methane and propane are also listed in Table V and shown in Fig. 10, together with the different models used previously to fit the nitrogen cross sections (see Sec. IV E and Appendix E). The single electron-capture and electron-loss cross sections of methane for He^+ ions, σ_{10} and σ_{12}, were measured for He^+ ions by Rudd *et al.* in the energy range between 5 and 350 keV [40]. These data are about 20% lower than those measured by Sataka *et al.* [55], judging by the small overlap of the energy ranges. Electron-capture cross sections of methane for $^3He^{2+}$, σ_{21} and σ_{20}, were also measured by Rudd *et al.* [43]. The $^3He^{2+}$ cross sections were used to determine the electron-capture cross sections for $^4He^{2+}$ of the same velocity. In the energy range between 700 keV and 2 MeV, the electron-capture cross sections are complemented by the data of Itoh *et al.* [47]. The electron-loss cross sections σ_{01} and σ_{02} of methane were measured by Sataka *et al.* [55], but are up to a factor of two larger than those determined by Itoh *et al.* [52]. In fact, only Itoh *et al.* measured all six charge-transfer cross sections for methane.

It is worth noting that the fits of the charge-transfer cross section data of nitrogen for helium particles (Fig. 10) generally also reproduce the measured data for methane with satisfactory agreement. Exception are the electron-loss cross sections σ_{02} of methane measured by Sataka *et al.* and all of the methane data of Itoh *et al.*, which are a factor of two lower than those calculated with the nitrogen models. The agreement of charge-transfer cross sections of nitrogen with those of methane is, however, plausible because they strongly depend on the velocity distribution of valence electrons in

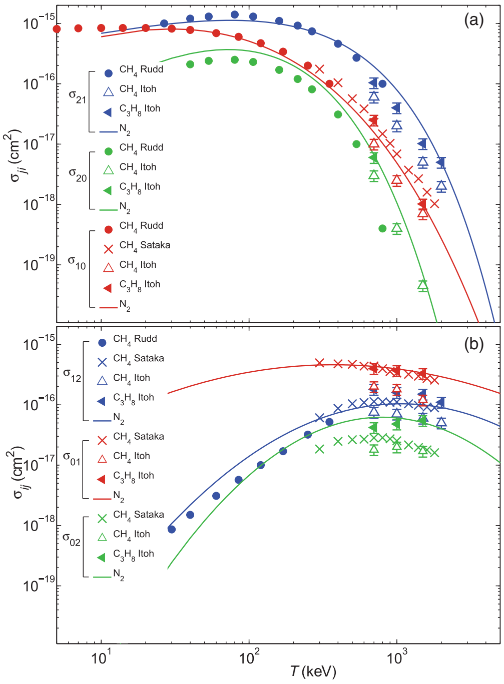

FIG. 10. (Color online) Cross section data for (a) electron capture σ_{ji} and (b) electron loss σ_{ij} of methane CH$_4$ and propane C$_3$H$_8$ for helium projectiles, measured by the authors referenced in Table V (symbols). For some data sets error bars are within the symbols. The lines show the model functions fitted to the nitrogen data given in Appendix E.

the target with respect to the projectile velocity. For example, electron-capture processes for helium particles are maximum when the velocity of the projectile corresponds to the velocity of an outer valence electron in the medium. The energy-loss processes, on the other hand, can be interpreted as a projectile ionization by the target potential, which is largely determined by the binding energies of the valence electrons. In fact, the binding energies of the ten or eight valence electrons in nitrogen and methane, respectively, are quite similar [20], so that the same charge-transfer cross sections can be expected. On the other hand, propane has 20 valence electrons with binding energies of the six outermost well below those of nitrogen or methane [20].

For propane, the only available data set for charge-transfer cross sections for helium particles was published by Itoh *et al.*, who measured all six charge-transfer cross sections (see again Table V and Fig. 10). Their cross sections for propane are generally about a factor of two larger than their methane data. However, their propane data are in agreement with measured methane cross sections of other authors, while their methane cross section data are generally a factor of two lower than those determined by other groups (see discussion in the previous subsections). The same tendency was observed for most of their nitrogen data in Sec. IV E2. These findings indicate that their data for propane may be about a factor of two too low. Itoh *et al.*, however, determined their data in a narrow energy region between 0.7 and 2 MeV with only one to four data points, so that, in our point of view, these can only be interpreted as being supportive to the relative energy dependence of the methane cross section data of the other authors. Therefore, the nitrogen model functions were also used to model the charge-transfer cross sections of propane. However, the influence of a factor of two larger charge-transfer cross sections for propane was quantified for the nanodosimetric parameters studied in the PTRA simulations (see Sec. V A).

G. Effective ionization cross sections for helium particles

Target molecules are generally ionized by the three helium charge states (He^0, He$^+$, and He^{2+}) in either direct impact-ionization processes or electron capture to a bound state of the projectile. The resulting effective ionization cross section σ_{eff} for a given helium particle energy is then the sum of the cross sections for those processes, weighted by the equilibrium fractions of the helium charge states (see Sec. III), such that

$$\sigma_{\mathrm{eff}} = f_0\,\sigma_{\mathrm{He}^0} + f_1(\sigma_{\mathrm{He}^+} + \sigma_{10}) + f_2(\sigma_{\mathrm{He}^{2+}} + \sigma_{21} + \sigma_{20}). \tag{7}$$

The equilibrium fractions f_0, f_1, f_2 were taken from the functions fitted to the experimental data [see Eqs. (E4a)–(E4c) and Fig. 8]. For the calculation of σ_{eff}, the ionization cross sections of nitrogen and methane for alpha particles $\sigma_{\mathrm{He}^{2+}}$ were determined from the fitted Rudd model. For He$^+$ and He^0, the ionization cross sections were obtained using Eq. (E1). The He^0 ionization cross sections of nitrogen were also used for methane, owing to the similarity of the He$^+$ ionization cross section data of methane and nitrogen (Fig. 9) and the lack of respective literature data. The charge-transfer cross sections for nitrogen and methane were obtained from Eqs. (E2) and (E3). Effective ionization cross sections were then determined for both nitrogen and methane using Eq. (7). The reader should be reminded that the ionization cross sections of propane for He^{2+}, He$^+$, and He^0 were calculated using those of methane, multiplied by a factor of 2.9 (see Sec. IV F).

Figure 11 shows a comparison of different effective ionization cross sections (σ_{eff}) of nitrogen to the corresponding measured ionization cross sections for He^{2+} ions, $\sigma_{\mathrm{He}^{2+}}$ [43]. For energies of 2 MeV and higher, the measured proton cross sections of Rudd *et al.* [32] are also plotted (scaled to the same velocity as an alpha particle and multiplied by the square of the alpha particle's charge). The effective ionization cross section of nitrogen has a maximum at about 700 keV where it is about 30% lower than the ionization cross section of alpha particles. Beyond the maximum, the effective ionization cross sections approach the scaled ionization cross section for protons and coincide at 2 MeV. This is due to the low equilibrium fractions of He$^+$ and He^0 particles at high energies. Below the energy of the maximum, the effective cross section decreases slightly with decreasing energy, coinciding again with the alpha particle ionization cross section at 100 keV.

As an alternative to Eq. (7), an empirical model was developed by Barkas [56,57] to estimate the effective charge of the projectile arising from higher-order interactions as well as charge-transfer processes. Similar to the model of Gillespie

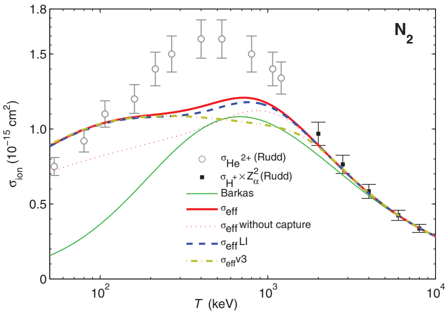

FIG. 11. (Color online) Effective ionization cross sections of nitrogen for helium particles (σ_{eff}), determined using both the Barkas correction and Eq. (7). Shown are also effective cross sections, which would be obtained by omitting electron-capture processes, by considering loss ionization (LI) processes in the He$^+$ ionization cross section, and by using approach (v3) (see Sec. IV E). Further, ionization cross sections for alpha particles ($\sigma_{\mathrm{He}^{2+}}$) and protons (abcissa scaled to give particles of same velocities and the ordinate was scaled by the square of the alpha particle charge, $\sigma_{\mathrm{H}^+} Z^2$) are compared.

[see Eq. (6)], it contains only a single fitting parameter. Barkas fitted the energy loss as a function of projectile velocity for different ions in silver halide emulsions,

$$Z_{\mathrm{eff}}^2 = Z^2[1 - \exp(-a\beta Z^{-2/3})]^2, \tag{8}$$

where $\beta = v_{\mathrm{proj}}/c$, v_{proj}, and c are the velocity of the projectile and light, respectively. The adjustable parameter $a = 125$ was found by Barkas and co-workers to be applicable for a wide range of projectiles, target gases, and solids [56].

The Barkas model is widely used in the literature to determine ionization cross sections for slow ions [58]. In this work, however, it was observed that the application of the Barkas correction is rather unsatisfactory. Multiplying the square of the effective charge with the energy-scaled proton cross section leads to a much lower effective ionization cross section than previously obtained: At about 2 MeV it is already by about 10% lower, showing also a maximum at 700 keV, and decreases for lower energies to about 1/3 of the alpha particle cross sections which coincide with the previously obtained effective cross section at 100 keV.

The divergence between ionization cross sections obtained using the Barkas model or σ_{eff} is, in part, due to the contribution of electron-capture processes to the latter cross section. When the contribution of electron-capture processes was omitted from Eq. (7) (Fig. 11), a reduction of up to 27% (at 100 keV) in the effective ionization cross sections of nitrogen and up to 10% for propane (not shown) are observed. The influence of electron-capture processes on the effective ionization cross section of propane is less than that for nitrogen. This is because only the ionization cross sections of propane were scaled (using the methane cross sections), while for both methane and propane the same models for the electron-capture cross sections fitted to the nitrogen data were used. The applicability of the Barkas model to obtain nanodosimetric quantities from track structure simulations is discussed in Sec. V.

Furthermore, several authors suggested that electron-loss ionization (LI) contributes to the measured data for the impact of He$^+$ ions (see Sec. IV E1). To investigate a possible influence on the effective ionization cross sections, it was assumed in this work that 50% of the collected charges are due to single electron-loss processes and 50% include an additional ionization of the target molecules. Based on this assumption, the ionization cross sections of He$^+$ were recalculated. Subsequently, the effective ionization cross sections obtained by assuming single electron loss only results in being reduced by up to 3.5% and 8% for nitrogen and propane, respectively, in the energy range between 100 keV and 2 MeV.

Another important question is how the different equilibrium fractions shown in Sec. IV E2 influence the effective ionization cross section. For this purpose, the equilibrium fractions in nitrogen as well as the electron-capture cross section σ_{21} used in Eq. (7) were calculated as described in Sec. IV E2 (v3) [i.e., the fits of the cross sections σ_{01}, σ_{10}, σ_{02}, and σ_{20} were used to calculate the equilibrium fractions of the helium charge states by means of Eq. (3)]. Note that single electron loss only was assumed. This procedure led to a quite different energy dependence of the equilibrium fraction than obtained from measurements (v1), revealing some inconsistency of the charge-transfer data in the literature (see Fig. 8). As expected, the influence on the effective ionization cross section is significant with a reduction in the energy range between 200 keV and 2 MeV (by as much as 16% at 800 keV). The effect on simulation results of the deviation between the effective ionization cross sections obtained by approaches (v1) and (v3) is shown in the following section.

For propane, only one data set for charge-transfer cross sections was found in the literature, which may be a factor of two higher than those of methane (see Sec. IV F2). Including this assumption in Eq. (7), an increase of electron-capture cross sections by a factor of two would increase the effective ionization cross section for energies below 1 MeV. At energies below 100 keV, this amounts to 8% (Fig. 11). The effect of this factor on simulation results is shown in Sec. V.

V. SUITABILITY OF CROSS SECTION DATA INTERPOLATIONS FOR PARTICLE-TRACK SIMULATIONS

The suitability of the reviewed cross section data for calculating realistic particle-track parameters with the code PTRA was investigated by benchmarking simulated nanodosimetric quantities with experimental results obtained with the PTB/WIS nanodosimeter (see Sec. III). In particular, the mean ionization cluster size, M_1, and the total energy loss were calculated for protons and alpha particles of different energies, with the nanodosimeter being operated with either nitrogen or propane. Also, the influence of different ionization cross section models for alpha particles on those quantities was investigated in this work, with the purpose of assessing the data robustness and to give a rough estimate on associated model uncertainties.

The following models for describing different ionization cross sections for helium particles were implemented in the PTRA code and tested for suitability.

(i) The Rudd model [28] was fitted to the average of measured ionization cross sections of alpha particles (see Sec. IV E and Appendix C). These data are referred to as fitted Rudd model in the following.

(ii) The proton ionization cross section was multiplied by the square of an effective charge, Z_{eff}^2, according to the Barkas model [56], using $a = 125$ for both nitrogen and propane (see Sec. IV G).

(iii) Ionization cross sections for alpha particles were obtained by the fitted Rudd model and, additionally, all the charge-transfer processes and ionization cross sections of He^0 and He^+ (see Appendix E) were taken into account during the interaction sampling.

(iv) Effective ionization cross sections σ_{eff} were used as described in Sec. IV G.

In all simulations, it was assumed that both ionization and electron-capture processes (when applied) contribute to the ionization cluster size distributions, since the target molecule is ionized in both cases.

A. Mean ionization cluster size M_1

1. M_1 for nitrogen

Figure 12 shows the measured and calculated mean ionization cluster size, obtained for protons and alpha particles in nitrogen as a function of the projectile energy (see also Refs. [59,60]). For protons, measured and simulated results agree within the experimental uncertainties (up to 14%) for energies above 300 keV. Below this energy, the simulated cluster sizes are up to 17% lower than the measured data. Even though the model function applied in PTRA for the ionization cross section data in this energy region agrees well with the respective experimental data (refer to Sec. IV C), the uncertainties of those data were between 10% and 25%. Keeping this in mind, the benchmark test based on the M_1 values for protons in nitrogen was successful. The recently published comparison of simulated and measured distributions of ionization cluster sizes for protons demonstrated also a good agreement [60].

A similar behavior can be observed for alpha particles. The values of M_1, calculated with PTRA using the fitted Rudd model reproduce the measured data well within the experimental uncertainties (which are between 7% and 22%) for energies above 1 MeV. Below this energy, the calculations yield values up to 23% larger than the measured data. The ratio of measured to simulated data in Fig. 12(b) reveals that the relative discrepancy rises with decreasing projectile energy. The maximum calculated value of M_1 appears at about 400 keV, which is slightly lower than 500 keV observed in the experiments. The deviations found in such an artificial simulation (transporting, in fact, only alpha particles) illustrate the importance of considering charge-transfer interactions in the simulations.

Another set of simulation results obtained for incident alpha particles using the Barkas model compares well with the measured data down to an energy of about 2 MeV. With decreasing energy, however, M_1 determined using the Barkas model deviates dramatically from the experimental data. In fact, at the lowest helium particle energy (about 130 keV), the results from the Barkas model are a factor of 1.65 lower than the measured data. This finding supports the indication of an unsatisfactory correction of the effective charge of helium projectiles in the ionization cross sections of nitrogen (see Sec. IV G). On the other hand, a substantial deviation of results obtained including the Barkas model is due to the neglegted electron-capture processes when counting the number of ionizations. Considering those would increase the total M_1 value for helium particles of low energies. It is concluded that the Barkas model is not suitable for an application in track structure simulations for nanodosimetry.

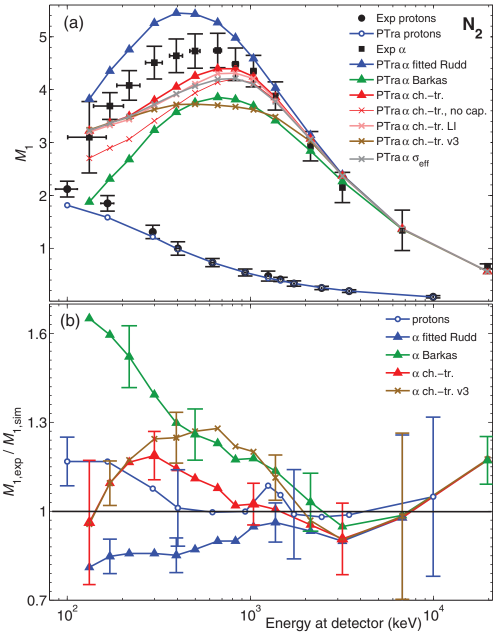

FIG. 12. (Color online) (a) Mean ionization cluster size M_1 of protons and alpha particles in nitrogen. The following cross section models for alpha particles were used: (i) fitted Rudd model (PTra α fitted Rudd); (ii) Barkas model for effective charge correction (PTra α Barkas); (iii) simulations including charge-transfer processes (PTra α ch.-tr.); (iv) as in (iii), but including only impact ionizations in M_1 (PTra α ch.-tr., no cap); (v) as in (iii), but taking LI into account in the He^+ ionization cross section (PTra α ch.-tr. LI); (vi) as in (iii), but using version (v3) to determine the equilibrium fractions of helium charge states (PTra α ch.-tr. v3); and (vii) using the effective ionization cross section σ_{eff} (PTra α σ_{eff}). (b) Ratio of the measured $M_{1,\mathrm{exp}}$ to simulated values $M_{1,\mathrm{sim}}$ using (i) (α fitted Rudd), (ii) (α Barkas), (iii) (α ch.-tr.), and (vi) (α ch.-tr. v3). The statistical uncertainties of the simulations are contained within the symbols of the graphs.

Figure 12 also shows simulated M_1 values for alpha particles obtained with the inclusion of charge-transfer cross sections ("PTra α ch.-tr." in the figure). The experimental mean ionization cluster size is reproduced well for energies above 800 keV but underestimated by up to 19% for energies between 150 and 800 keV. This deviation is, however, still within the overall experimental uncertainties of the cross section data (between 8% and 15%) and equilibrium fractions (about 10%). The maximum calculated M_1 is found at about 700 keV, which coincides with the maximum predicted by the Barkas model and is higher than the experimental maximum (at approximately 550 keV).

Substituting the charge-transfer and ionization cross sections for the different helium charge states by the effective ionization cross section σ_{eff} (see Sec. IV G) gives similar results for M_1 in nitrogen. The largest deviation to M_1, obtained by accounting for charge-transfer processes, is 5% in the region of the maximum (labeled "PTra α σ_{eff}" in Fig. 12). The observed reduction of M_1 is due to the neglected transport of electrons produced in electron-loss processes of the helium projectiles in σ_{eff}. Electron-loss processes have broad maxima above 300 keV, which leads to the production of electrons with corresponding energies between 40 and 200 eV as these electrons were assumed to have the same velocity as the projectile in the code. Electrons at such low energies have a small ionization mean free path (about 0.66 mm at 100 eV for a pressure of 120 Pa in nitrogen). Therefore, they are likely to produce a significant number of ionizations within the sensitive volume (about 1 mm in diameter). As stated above, the contribution of electrons produced by electron-loss processes is, however, small due to the low charge-transfer cross section when compared with the ionization cross section. For example, if an He^{2+} ion experiences electron capture followed by electron loss, the respective cross sections σ_{21} and σ_{12} are both about an order of magnitude smaller than the corresponding ionization cross sections. Hence, the accuracy of the simulations is not significantly compromised when the cross section data set for ionization and charge-transfer processes are replaced by the effective ionization cross section (see Sec. IV G).

The contribution of electron-capture processes to the ionization of the target molecules was investigated to further evaluate the reason for the low M_1 values obtained using the Barkas model. For this purpose, the same cross section data set for ionization and charge transfer as above was used (i.e., "PTra α ch.-tr.") and only the number of impact ionizations per ion track was counted while ionizations arising from electron-capture interactions were not scored. The results of these simulations, also shown in Fig. 12, have a similar behavior as the cross section data shown previously in Sec. IV G: Compared to the results obtained by scoring electron-capture interactions (i.e., "PTra α ch.-tr."), the M_1 values are underestimated with decreasing alpha particle energies below 1 MeV by up to 16%. This deviation clearly shows that the contribution of ionizations produced in electron-capture interactions is significant for helium particles in this energy range. This contribution alone, however, does not entirely amount to the reduced M_1 values observed when using the Barkas model.

Furthermore, it has already been discussed in Sec. IV G that the impact-ionization cross sections of He^+ ions may be reduced by electron-loss ionization (LI) events. Hence, it was assumed that 50% of the literature cross sections for the production of positive ions or electrons are due to LI and 50% arise from single electron-loss processes. Nevertheless, as for the effective ionization cross section, the calculated reduction of M_1 values due to this assumption is not more than 3.5% and therefore not significant (labeled "PTra α ch.-tr. LI" in Fig. 12).

A significant reduction of the mean ionization cluster size in the energy region between 200 keV and 2 MeV by as much as 16% is observed when the equilibrium charge-state fractions are calculated as described in Sec. IV E2 (v3) ("PTra α ch.-tr. v3"). This is again consistent with the differences observed in the effective ionization cross section data (see Sec. IV G).

2. M_1 *for propane*

Measured and simulated mean ionization cluster sizes for protons and alpha particles in propane are shown in Fig. 13. For protons, calculated M_1 values favorably compare (within the experimental uncertainties of about 7%) with the measured data across the entire energy range. Hilgers *et al.* [10,60] demonstrated also a good agreement of simulated and measured distributions of ionization cluster sizes for protons.

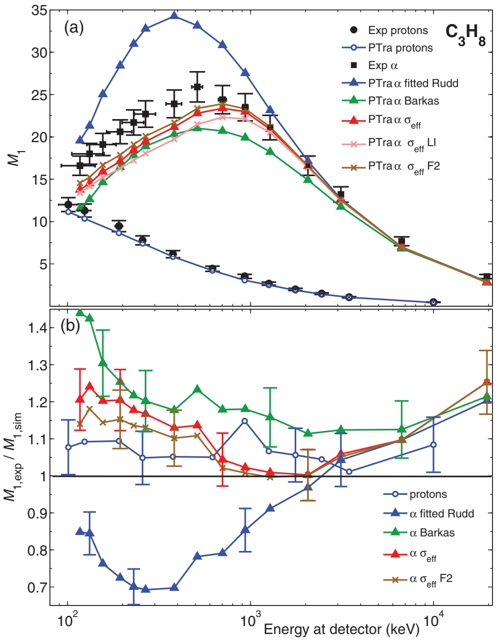

FIG. 13. (Color online) (a) Mean ionization cluster size M_1 of protons and alpha particles in propane. The following cross section models were used for alpha particles: (i) fitted Rudd model (PTra α fitted Rudd); (ii) Barkas model for effective charge correction (PTra α Barkas); (iii) effective ionization cross section σ_{eff} (PTra α σ_{eff}); (iv) σ_{eff}, taking LI into account in the He^+ ionization cross section (PTra α σ_{eff} LI); and (v) σ_{eff}, multiplying the electron-capture cross sections by a factor of two (PTra α σ_{eff} F2). (b) Ratio of the measured $M_{1,\text{exp}}$ to simulated values $M_{1,\text{sim}}$ using (i) (α fitted Rudd), (ii) (α Barkas), (iii) (α σ_{eff}), and (v) (PTra α σ_{eff} F2). The statistical uncertainties of the simulations are contained within the symbols of the graphs.

For alpha particles, M_1 values calculated using the fitted Rudd model also agree with the measured data (within experimental uncertainties) for energies above 2 MeV (labeled "PTra α fitted Rudd" in the figure). For lower energies, the simulations yield cluster sizes up to about 42% larger. The maximum value (at an energy of about 400 keV) is found at a lower energy than the experimental maximum (at 500 keV).

The Barkas model [56] leads to an underestimation of the M_1 values across the entire energy range by 10% to 20% and as much as 45% at the lowest investigated energy of about 130 keV ("PTra α Barkas"). As for nitrogen, the Barkas model (using $a = 125$) appears, therefore, unsuitable as a model for the effective charge of the ionization cross section of propane in track structure simulations.

A much better agreement with the measured data is achieved when using the effective ionization cross section ("PTra α σ_{eff}"). In this case, the maximum value of M_1 is calculated at about 700 keV. For energies above 700 keV, the simulated data agree well with the measured data (within the experimental uncertainties), while below this energy, the calculated M_1 values are up to 24% smaller. This deviation is large compared to the contribution of electron-loss processes, resulting in a relatively minor reduction of M_1 values (see Sec. V A1). This justifies the implementation of σ_{eff} of propane instead of the detailed inclusion of charge-transfer interactions in the simulation, thereby neglecting the further transport of electrons produced in electron-loss processes.

Considering the contribution of electron-loss ionization processes in the He^+ ionization cross section (see Sec. IV G) reduces the mean ionization cluster size by as much as 7% in the energy region between 200 keV and 1 MeV (labeled "PTra α σ_{eff} LI" in Fig. 13). The influence on the propane data is significant and larger than for nitrogen. This is because the He^+ ionization cross section used for propane is larger than the charge-transfer cross sections.

Another unknown bias of propane cross sections may arise from the sparse and inconsistent literature data on charge-transfer cross sections of propane (see Secs. IV F2 and IV G). The review conducted in this work indicated that propane cross sections may be a factor of two larger than those of methane. This factor is considered in the calculation of the mean ionization cluster size ("PTra α σ_{eff} F2"). For energies below 1 MeV, the M_1 values are then as much as 6% larger than those calculated previously (i.e., "PTra α σ_{eff}"). M_1 values calculated by this approach are then up to 18% lower than the experimental data, yielding the best agreement of all simulation results.

B. Ion energy loss

Another quantity used for the benchmark test of PTRA is the energy loss of incident protons and alpha particles during the passage of more than 30 cm of gas in the nanodosimeter setup. For this purpose, the average energy of projectile ions arriving at the trigger detector were measured and calculated. Results from the simulations are also compared to the energy loss calculated for the same geometry but using the stopping power from the PSTAR and ASTAR libraries [61].

For protons in nitrogen, the energy losses determined using the three approaches deviate by less than 3%, which is well within the experimental uncertainty of as much as 11% [Fig. 14(a)]. The assessment of the uncertainty in energy loss was based on the uncertainty of the experimental energy determination at the trigger detector. Experimental values of the energy loss of alpha particles agree well (within 2%) with data calculated from the stopping power for the entire energy range investigated. Also, simulations of alpha particles in nitrogen using the fitted Rudd model led to less than 5% deviation in energy loss. Deviations of up to 12% and 16% between measured and simulated energies are found at energies below 1 MeV when effective ionization cross sections or the Barkas model were used, respectively. For all investigated cross section models, this disagreement is, for most data points, within the experimental uncertainties evaluated for the energy loss (which increased with decreasing energy to as much as 17%).

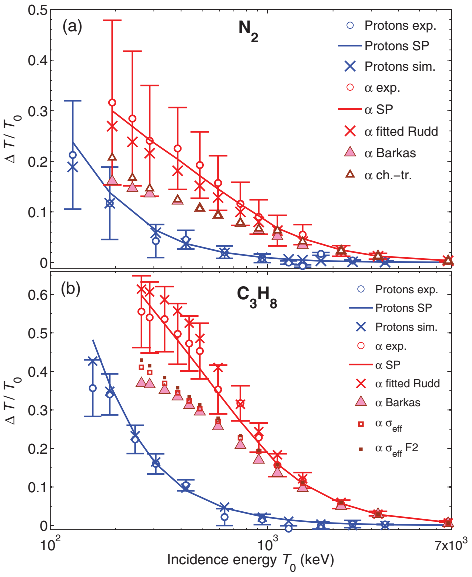

FIG. 14. (Color online) Relative energy loss of incident protons and alpha particles, obtained from measurements (exp), the stopping power (SP), and simulations (sim) in (a) nitrogen and (b) propane after passing through the nanodosimeter volume. Different cross section models for alpha particles were used [(i), (ii), and (iii) in captions of Figs. 12 and 13, as well as (v) in the latter caption].

For propane, good agreement between the energy loss of protons determined from experiment, simulations, and stopping power can be seen in Fig. 14(b). Here, the deviation in energy losses is less than 3%, with the exception of the lowest initial energy of 157 keV, which was reduced to 100 keV in the experiment but to only 87 keV in the simulations. Using the stopping power to calculate the energy at the detector position gives 81 keV, which is closer to the simulated value.

The simulated energy loss of alpha particles with energies above 1 MeV in propane (obtained by the different cross section models) compares within 5% with the measured values. Below 1 MeV, the calculated energy loss of the alpha particles shows significant deviations from the measured values for some of the investigated cross section models. The experimental values, on the other hand, are supported by the stopping power calculations from which they deviate by no more than 5% (this is within experimental uncertainties determined for the energy loss, which increased with decreasing energy to as much as 8%). Similar to the simulation results for nitrogen, the use of the fitted Rudd model in the simulations leads to as much as 7% higher energy loss than in the experiment, while the application of the Barkas model or the effective ionization cross section resulted in up to 19% or 15% lower energy loss when compared to the measured data. Multiplying the charge-transfer cross sections of propane by a factor of two leads to calculated energy losses of as much as 13% lower than the measured data [labeled "PTra α σ_{eff} F2" in Fig. 14(b)]. The energy losses for alpha particles of incident energy below 1 MeV are, nonetheless, significantly lower (experimental uncertainty is up to 10%) when charge-transfer processes were considered in the simulations.

C. Contribution of secondary electrons to M_1

Secondary electrons are produced within the sensitive volume as well as in the surrounding medium by ionization and electron-loss processes of the projectiles. The contribution of secondary electrons to M_1 was investigated to gain insight into the importance of the ionization cross sections of electrons for the central passage of a primary ion beam through a sensitive volume.

Figure 15 shows the fraction of M_1 that is produced by secondary electrons only (instancing results in nitrogen). It can be seen that the contribution of secondary electrons to M_1 is generally smaller than that of ions, but still significant (between about 15% and 30% for the range of ion energies investigated in this work). This is due to the fact that ions of such energies traverse the sensitive volume without being scattered, whereas electrons experience a change in direction due to elastic and inelastic scattering. Electrons therefore have a probability of being scattered out of the sensitive volume before undergoing ionization. This is particularly the case for electrons with energies above 400 eV, since their ionization mean free path is larger than the diameter of the sensitive volume.

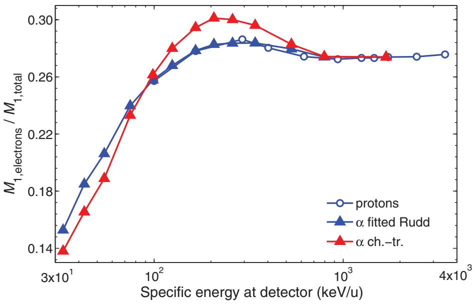

FIG. 15. (Color online) Ratio of the secondary electron contribution to the simulated mean ionization cluster size ($M_{1,\text{electrons}}$) to the total mean ionization cluster size ($M_{1,\text{total}}$) for the passage of protons and helium particles through the center of the sensitive volume of the nanodosimeter operated with nitrogen. For helium particles, either the fitted Rudd model or charge-transfer cross sections were used in the code.

In the overlapping energy range, the contribution from secondary electrons to M_1 is similar for protons and alpha particles (fitted Rudd model), since the electron spectra produced by protons and alpha particles of equal velocity are the same. In both cases, the electron contribution increases with increasing energy to about 28% at 200 keV, then plateaus at higher energies. The electron contribution was also assessed when accounting for charge transfer, where the electron contribution to the M_1 produced by helium particles of energies below about 100 keV/u drops by about 2% due to the inclusion of electron capture in M_1. This is in agreement with the differences observed in M_1, determined from the same kind of simulations with and without including electron-capture events to M_1. For energies between 100 keV/u and 1 MeV/u, the electron contribution is by as much as 2% larger than the one obtained by the fitted Rudd model due to secondary electrons produced in electron-loss processes.

VI. CONCLUSIONS

Cross section data for ion and electron scattering in gases are required for modeling the track structure of radiation. The validity of these data is essential for the accurate calculation of transport parameters and ionization yields with applications in detector development, space research, and radiation dosimetry. Unfortunately, those data are scarce and often discrepant in the literature; ionization cross section data for the interaction of light ions in propane were, for example, not found. Propane cross section data were therefore derived from those of methane. The literature review in this work contributes to the collection and dissemination of ionization and charge-transfer cross section data for electron, proton, and helium particle interactions with nitrogen, methane, and propane. Those data were obtained from measurements or theoretical calculations or described by semiempirical models. In this work, data for ion projectiles of energies between 100 keV and 20 MeV were of interest. The simulation of proton and helium particle transport in the PTB/WIS nanodosimeter, using the PTRA Monte Carlo track structure code, successfully benchmarked a set of cross section data of nitrogen and propane by comparing the calculated energy loss and mean ionization cluster size M_1 to measured results. This benchmark test offered the possibility to investigate the influence of different models and subsequent parametrizations of ionization cross sections on the calculated quantities. This influence was significant and the observed deviations may be used as an estimate of the expected overall uncertainty of calculated results, arising from uncertainties of the cross section data.

Ionization cross sections of nitrogen and methane for protons in the energy range of interest in this work, are mostly in good agreement within the experimental uncertainties. Those data are well described by the semiempirical Rudd and Green models but the Green model significantly overestimates the cross section data for protons and those based on electron-impact data at high energies (30% at 10 keV). The use of the Rudd model [28] in simulations with both nitrogen and propane led to a good agreement (within the experimental uncertainties) with the measured energy losses as well as with the M_1, except for proton energies below 300 keV in nitrogen, where measured and simulated M_1 values deviated by up to 17%. A comparison of this deviation to the uncertainties associated with the experimental cross section data (between 10% and 25%) leads to the conclusion that the benchmark test for protons was successful. Therefore, the Rudd model is recommended as an interpolation function for proton-impact-ionization cross section data.

Impact-ionization cross sections of nitrogen for He^{2+} and He^0 have been measured by few authors, but are in agreement within the experimental uncertainties (up to 17% deviation). For He^+, larger discrepancies (up to 25%) occur between the reported data, which were in all cases obtained by subtracting the measured electron-loss cross section σ_{12} from the cross section for the production of electrons σ_-. For methane, only one author reported ionization cross sections for He^{2+} and He^+ ions. The best fit curves for alpha particles was obtained by refitting the Rudd model [28] (originally for protons) to the experimental cross section data, while Gaussian functions were used to fit the data for He^+ and He^0 projectiles. Charge-transfer cross sections were measured by several groups but often in different energy ranges. The data in overlapping energy ranges agree mostly within 20%. Two data sets, however, show deviations of more than a factor of two which seem to be of systematic origin. Model functions were fitted to the charge-transfer data of nitrogen and also used for those of methane due to the similarity of the charge-transfer cross sections of both molecules. Equilibrium fractions of the charge states in a helium particle beam, calculated using the model functions of the charge-transfer cross sections deviate by up to 20% from those measured by two groups in complementing energy ranges. The measured equilibrium fractions were also fitted by model functions for use in the Monte Carlo code. Based on the data for equilibrium fractions and charge-transfer cross sections, effective ionization cross sections, accounting also for ionization by electron-capture processes, were calculated.

The different interpolation model functions were used in the code PTRA to parametrize ionization and charge-transfer cross sections of incident alpha particles. Results for the M_1 values and the energy loss of incident alpha particles are consistent within the simulated data since a larger energy loss corresponds to the larger M_1 values, obtained when using only the fitted Rudd model and compared to simulations including charge-transfer processes. This is due to the role played by charge-transfer processes: When the He^{2+} ion undergoes electron capture, the helium particles does not experience (significant) energy loss, but it has a lower charge state (He^+ or He^0) and, consequently, a lower ionization cross section. Therefore, the average ionization cross section of the helium particle is reduced when charge transfer is considered in the simulations. For this reason, helium particles simulated under these conditions lose less energy when traversing the gas than those simulated using the fitted Rudd model. On the other hand, the discrepancy of the calculated energy loss to the experimental values is larger when accounting for charge transfer (up to 13% lower energy loss) instead of using the fitted Rudd model for alpha particle ionization cross sections (up to 7% higher). This is in contradiction with the larger deviation of the calculated M_1 values from the experimental data when the fitted Rudd model is used (up to 42% larger and 24% lower M_1 when the fitted Rudd model or the charge-transfer data are used, respectively). A possible reason for this contradiction is that the calculated energy loss of an ion per single interaction is not large enough (the HKS model was used in PTRA [62]). If this would be the case, the calculated total energy loss would increase (particularly for particles of lower energies), while the M_1 values would not significantly change. Further investigation of the cross section data used to determine the energy loss per interaction in PTRA is therefore necessary and will be conducted.

Furthermore, the results of this work lead to the conclusion that the Barkas model [56] is inadequate for use in track structure simulations as the largest deviations (up to 65%) of all calculated data to the experimental values are observed. It can, however, not be disclaimed that the low energy loss could be due to an underestimated energy loss per single interaction (as described above), while lower M_1 values definitely also arise from the neglected contribution of ionizations by electron capture (the contribution of those ionizations to M_1 at energies below 1 MeV is up to 16%). The latter reason alone, in fact, leads to the unsuitability of the Barkas model for a simulation of nanodosimetric quantities. However, also the discrepancy observed in Sec. IV G has to be further investigated. Here it was shown that the effective ionization cross section based on the Barkas model was only $1/3$ of the same cross section, calculated from charge-transfer data and equilibrium charge states of helium particles.

The overall contribution of ionizations by secondary electrons to M_1 was found to be as much as 30% for a central passage of an ion beam through the sensitive volume. This underlines the importance of accurate electron-impact cross section data, which deviated by up to 65% and 30% for propane and nitrogen, respectively. Particulary in the view that electrons are exclusively responsible for energy depositions in the vicinity of an ion trajectory, more accurate cross section data and benchmark experiments for such a scenario are needed [63].

Based on the literature review and the results in this work, the BEB model and Chouki model are recommended as interpolation functions for electron-impact-ionization cross sections of nitrogen and propane, respectively. For proton-impact, the Rudd model [28] is recommended. Due to the best agreement of calculated and measured M_1 and energy losses, the implementation of the charge-transfer processes as used in (v1) (Sec. IV E) is recommended when alpha particles are incident. For this purpose, the fitted Rudd model and Gaussian functions are proposed as interpolation models for ionization cross sections for He^{2+}, He^+, and He^0, where He^0 cross section of nitrogen may also be used for methane. For propane, the methane data should be multiplied by a factor of 2.9. Model functions for the charge-transfer cross sections in nitrogen are also proposed and may be multiplied by a factor of two to obtain a reasonable estimate for the data of propane. Alternatively to the calculation of the specific charge state of each helium projectile in every simulation step, an effective ionization cross section is proposed in Eq. (7). In this case, the production of electrons in electron-loss processes and their subsequent potential to produce additional ionizations is neglected in favor of computation time. Ionizations by those neglected electrons have, however, only a minor effect (as much as 7%) on the simulation results.

The uncertainty of calculated results for M_1 and energy loss arising from different parametrizations of effective ionization cross sections may be estimated from the difference between the values determined in "PTra α ch.-tr." and those from "PTra α v3" for nitrogen. Both data sets, as well as the one used to calculate "PTra α ch.-tr. LI," seem equally justified to model a realistic effective ionization cross section. In this case, the calculated M_1 values would have an assigned uncertainty of up to 20% for helium projectile energies between 300 keV and 1.5 MeV and an uncertainty below 2% for energies outside this range. The energy loss, on the other hand, is less sensitive to the different parametrizations of the effective ionization cross section, showing deviations below 2%.

The PTRA code using the recommended cross section data of nitrogen and propane can be considered as being successfully benchmarked by the experiments with protons and alpha particles of energies between 100 keV and 20 MeV in the nanodosimeter. Further improvement is necessary, and requires the measurement of cross section data, particularly for light ions in propane but also electron and ion cross section data of nitrogen and methane are needed. This work will be continued for differential cross section data as well as for excitation and elastic scattering cross sections to further improve particle transport simulations with the code PTRA.

ACKNOWLEDGMENTS

We thank Daniel Bennett for carefully reading the manuscript. The research leading to these results was, in part, carried out within the EMRP joint research Project No. SIB06 BioQuaRT. The EMRP is jointly funded by the EMRP participating countries within EURAMET and the European Union.

APPENDIX A: BEB MODEL

The BEB model [19] describes the electron-impact-ionization cross section for the electron energy range up to about 10 keV, without requiring empirical parameters. It combines the binary-encounter theory with the Bethe-Born approximation, which are expected to be realistic models for low and high incidence electron energies, respectively. The Bethe-Born approximation is applicable if the energy of the incident electron is much greater than that of the bound target electrons. In this case, the projectile potential can be treated as a small perturbation to the target electrons because energy transfers, produced in soft collisions, are likely to be small. In the binary-encounter theory, a velocity distribution is assigned to the bound target electrons, enabling a better description of hard collisions. The total ionization cross section is described by the (nonrelativistic) BEB model as

$$\sigma_{\text{ion}}(T) = \sum_{i=1}^{i_{\max}} \left(\frac{4\pi a_0^2 R^2}{t+u+1} \frac{N_i}{B_i^2} \left\{ 0.5\left(1 - \frac{1}{t^2}\right)\ln(t) + \left[\left(1 - \frac{1}{t^2}\right) - \frac{\ln(t)}{t+1} \right] \right\} \right), \tag{A1}$$

where R is the Rydberg constant, a_0 is the Bohr radius, i is an index for the subshells, and N_i is the number of electrons occupying the ith shell [18]. The primary electron energy T and the kinetic energy U_i of an orbital electron in shell i are normalized to the binding energy of the orbital electron B_i to give $t = T/B_i$ and $u = U_i/B_i$. The molecular orbital data for nitrogen are shown in Table VI.

TABLE VI. Parameters of the BEB model for nitrogen [18].

i	N_i	B_i (eV)	U_i (eV)
1	2	15.58	54.91
2	4	17.07	44.30
3	2	21.00	63.18
4	2	41.72	71.13

APPENDIX B: CHOUKI MODEL

Chouki *et al.* [27] developed a semiempirical model for electron-impact-ionization cross sections of hydrocarbons. Their model is based on the Bethe-Born approximation and includes corrections for the low-energy region, obtained by fitting experimental data. The Chouki model is defined by

$$\sigma_{\text{ion}}(T) = 4\pi a_0^2 R \frac{C}{T} \ln\left(1 + \frac{T-I}{R}\right)\Phi(T), \tag{B1}$$

with

$$\Phi(T) = a_1\, e^{-b_1/T} + a_2\, e^{-b_2/T^2} + a_3\, e^{-b_3(T-I)/T^2}, \tag{B2}$$

where R is the Rydberg constant, a_0 is the Bohr radius, and I is the ionization threshold of 11.08 eV for propane. The parameters for propane were obtained by fitting the model to the average value of experimental ionization cross sections in literature (see Sec. IV B), giving $C = 16.0$, $a_1 = 1.0$, $a_2 = -59.96$, $a_3 = 59.84$, $b_1 = 45.84$ eV, $b_2 = 0.16$ (eV)^2, and $b_3 = -0.13$ eV.

APPENDIX C: RUDD MODEL

Rudd *et al.* [28] fitted a semiempirical function to experimental proton ionization cross sections of various gases which they comprehensively collected from the literature and critically evaluated by assigning a weight to each data set. This function consists of two components, appropriate for the high- and low-energy regions (σ_{high} and σ_{low}, respectively). The Rudd model function for protons of energy T is given by

$$\sigma_{-}(T) = \left(\sigma_{\text{low}}^{-1} + \sigma_{\text{high}}^{-1}\right)^{-1}, \tag{C1a}$$

$$\sigma_{\text{low}} = 4\pi a_0^2\, C_{\text{Rudd}}\, x^{D_{\text{Rudd}}}, \tag{C1b}$$

$$\sigma_{\text{high}} = 4\pi a_0^2 [A_{\text{Rudd}} \ln(1+x) + B_{\text{Rudd}}]/x, \tag{C1c}$$

TABLE VII. Parameters of the Rudd model for protons [28] and alpha particles in nitrogen and methane.

	N_2, H^+	N_2, He^{2+}	CH_4, H^+	CH_4, He^{2+}
A_{Rudd}	3.82	3.82	4.55	4.55
B_{Rudd}	2.78	2.78	2.07	2.07
C_{Rudd}	1.80	0.85	2.54	1.15
D_{Rudd}	0.70	0.70	1.08	1.08

TABLE VIII. Parameters of the model function for the ionization cross sections [Eq. (E1)].

	N_2, σ_{He^+}	N_2, σ_{He^0}	CH_4, σ_{He^+}
a_1	6.90	8.00	7.60
b_1	2.30	2.11	2.30
c_1	1.70	1.26	1.60
a_2	2.62		3.90
b_2	2.43		2.53
c_2	0.70		0.60

where R is the Rydberg constant, a_0 the Bohr radius, and $x = T/R$. The fit parameters determined by Rudd *et al.* for the impact of protons on nitrogen and methane are provided in Table VII, together with those for the impact of alpha particles (obtained by fitting the Rudd model to measured cross sections of N_2 and CH_4).

APPENDIX D: GREEN MODEL

The model proposed by Green and McNeal [34] for the ionization cross section of protons is a semiempirical analytic function, which has been fitted to experimental proton ionization cross sections of various rare gases and diatomic molecules. In the case of N_2, they used the data of de Heer *et al.* [30] in the low-energy range and for high energies the model data of Hooper *et al.* [35], which is based on the Bethe-Born approximation and has been fitted to experimental data itself.

The Green model for protons of energy T (in keV) is given by

$$\sigma_{\text{ion}}(T) = \sigma_0 \frac{(Za)^{\Omega}(T-I)^{\nu}}{J^{\Omega+\nu} + T^{\Omega+\nu}}, \tag{D1}$$

with the parameters $\sigma_0 = 2.93 \times 10^{-16}$ cm^2, the total number of electrons in the target $Z = 7$, $a = 120.36$, $\Omega = 0.75$, $\nu = 0.77$, $J = 67.15$, and the ionization threshold $I = 15.58$ eV.

APPENDIX E: PHENOMENOLOGICAL MODELS FOR IONIZATION AND CHARGE-TRANSFER CROSS SECTIONS

The experimental data for ionization and charge-transfer cross sections as well as for equilibrium charge states of helium projectiles were fitted as function of $x = \log_{10}(T/\text{keV})$, where T is the projectile energy. The best fit curves, valid in the energy range between 100 keV and 20 MeV, are shown in Secs. IV E and IV F). Parameter values are provided in Table VIII.

TABLE IX. Parameters of the model functions for charge-transfer cross sections [Eqs. (E2) and (E3)].

	σ_{21}	σ_{20}	σ_{10}	σ_{12}	σ_{02}	σ_{01}
p_1	15.62	17.51	15.55			
q_1	−0.03	−0.11	−0.11			
p_2	0.012	0.10	0.584			
q_2	1.71	1.33	0.78			
r_1				−0.83	−1.19	−0.38
r_2				5.00	6.88	1.93
r_3				−23.55	−26.19	−17.82

The model functions for He$^+$ and He^0 were obtained by the Gaussian expressions

$$\sigma_{He^z}(T) = \left[a_1\, e^{-\left(\frac{x-b_1}{c_1}\right)^2} + a_2\, e^{-\left(\frac{x-b_2}{c_2}\right)^2}\right] 10^{-16}\ \text{cm}^2 \tag{E1}$$

for helium particles of charge Z.

The electron-capture cross sections of nitrogen are described by

$$\log_{10}(\sigma_{21}/\text{cm}^2) = -p_1\, e^{q_1 x} - p_2\, e^{q_2 x} \tag{E2}$$

and the model functions for nitrogen electron-loss cross sections are

$$\log_{10}(\sigma_{12}/\text{cm}^2) = r_1\, x^2 + r_2\, x + r_3. \tag{E3}$$

Parameters for both Eqs. (E2) and (E3) are given in Table IX.

The best-fit model functions obtained for the equilibrium fractions of helium charge states measured by Barnett and Stier as well as Pivovar *et al.* [48,53] are obtained by

$$f_{0,\text{exp}} = 1308/\left(35.22 + e^{0.62x^2}\right)^2, \tag{E4a}$$

$$f_{2,\text{exp}} = 1.045 \times 10^{-7}/(1.044 \times 10^{-7} + e^{-5.6x}), \tag{E4b}$$

$$f_{1,\text{exp}} = 1 - f_{2,\text{exp}} - f_{0,\text{exp}}. \tag{E4c}$$

---

[1] H. H. Rossi and M. Zaider, *Microdosimetry and Its Applications* (Springer-Verlag, Heidelberg, 1996).

[2] A. M. Kellerer, Radiat. Prot. Dosim. **99**, 17 (2002).

[3] W. Friedland, P. Jacob, H. G. Paretzke, and T. Stork, Radiat. Res. **150**, 170 (1998).

[4] B. Grosswendt and S. Pszona, Radiat. Environ. Biophys. **41**, 91 (2002).

[5] H. Nikjoo, P. O'Neill, M. Terrissol, and D. T. Goodhead, Radiat. Environ. Biophys. **38**, 31 (1999).

[6] R. W. Schulte, A. J. Wroe, V. A. Bashkirov, G. Y. Garty, A. Breskin, R. Chechik, S. Shchemelinin, E. Gargioni, B. Grosswendt, and A. B. Rosenfeld, Z. Med. Phys. **18**, 286 (2008).

[7] G. Garty, S. Shchemelinin, A. Breskin, R. Chechik, G. Assaf, I. Orion, V. Bashkirov, R. Schulte, and B. Grosswendt, Nucl. Instr. Meth. Phys. Res. A **492**, 212 (2002).

[8] B. Grosswendt, Radiat. Environ. Biophys. **41**, 103 (2002).

[9] H. Nikjoo, S. Uehara, D. Emfietzoglou, and F. A. Cucinotta, Radiat. Meas. **41**, 1052 (2006).

[10] G. Hilgers, E. Gargioni, B. Grosswendt, and S. Shchemelinin, Radiat. Prot. Dosim. **126**, 467 (2007).

[11] H. Bethe, Ann. Phys. **397**, 325 (1930).

[12] M. Inokuti, Rev. Mod. Phys. **43**, 297 (1971).

[13] B. Grosswendt and W. Y. Baek, in *Basic Physical Data in Organic Gases* (INFN-Laboratori Nazionali di Legnaro, Padova, Italy, 2000), pp. 5–26.

[14] N. Stolterfoht, R. D. DuBois, and R. D. Rivarola, *Electron Emission in Heavy Ion-atom Collisions* (Springer, Berlin, 1997).

[15] L. J. Puckett, G. O. Taylor, and D. W. Martin, Phys. Rev. **178**, 271 (1969).

[16] Y. Itikawa, J. Phys. Chem. Ref. Data **35**, 31 (2006).

[17] D. Rapp and P. Englander-Golden, J. Chem. Phys. **43**, 1464 (1965).

[18] W. Hwang, Y.-K. Kim, and M. E. Rudd, J. Chem. Phys. **104**, 2956 (1996).

[19] Y.-K. Kim and M. E. Rudd, Phys. Rev. A **50**, 3954 (1994).

[20] National Institute of Standards and Technology, *Electron-impact Cross Sections for Ionization and Excitation* (2012), http://physics.nist.gov/PhysRefData/Ionization/molTable.html.

[21] N. Durić, I. Čadež, and M. Kurepa, Int. J. Mass. Spectrom. **108**, R1 (1991).

[22] B. L. Schram, M. J. van der Wiel, F. J. de Heer, and H. R. Moustafa, J. Chem. Phys. **44**, 49 (1966).

[23] H. Nishimura and H. Tawara, J. Phys. B **27**, 2063 (1994).

[24] V. Grill, G. Walder, D. Margreiter, T. Rauth, H. U. Poll, P. Scheier, and T. D. Märk, Z. Phys. D **25**, 217 (1993).

[25] G. L. C. de Souza, M.-T. Lee, I. P. Sanches, P. Rawat, I. Iga, A. S. dos Santos, L. E. Machado, R. T. Sugohara, L. M. Brescansin, M. G. P. Homem *et al.*, Phys. Rev. A **82**, 012709 (2010).

[26] M. Vinodkumar, K. N. Joshipura, C. G. Limbachiya, and B. K. Antony, Eur. Phys. J. D **37**, 67 (2006).

[27] A. Chouki, Ph.D. thesis, University Paul Sabatier, Toulouse, 1994.

[28] M. E. Rudd, Y.-K. Kim, D. H. Madison, and J. W. Gallagher, Rev. Mod. Phys. **57**, 965 (1985).

[29] J. B. Crooks and M. E. Rudd, Phys. Rev. A **3**, 1628 (1971).

[30] F. J. de Heer, J. Schutten, and H. Moustafa, Physica **32**, 1766 (1966).

[31] H. Knudsen, U. Mikkelsen, K. Paludan, K. Kirsebom, S. P. Møller, E. Uggerhøj, J. Slevin, M. Charlton, and E. Morenzoni, J. Phys. B **28**, 3569 (1995).

[32] M. E. Rudd, R. D. DuBois, L. H. Toburen, C. A. Ratcliffe, and T. V. Goffe, Phys. Rev. A **28**, 3244 (1983).

[33] S. K. Allison, Rev. Mod. Phys. **30**, 1137 (1958).

[34] A. E. S. Green and R. J. McNeal, J. Geophys. Res. **76**, 133 (1971).

[35] J. W. Hooper, D. S. Harmer, D. W. Martin, and E. W. McDaniel, Phys. Rev. **125**, 2000 (1962).

[36] I. Ben-Itzhak, K. D. Carnes, D. T. Johnson, P. J. Norris, and O. L. Weaver, Phys. Rev. A **49**, 881 (1994).

[37] H. Luna, E. G. Cavalcanti, J. Nickles, G. M. Sigaud, and E. C. Montenegro, J. Phys. B **36**, 4717 (2003).

[38] D. J. Lynch, L. H. Toburen, and W. E. Wilson, J. Chem. Phys. **64**, 2616 (1976).

[39] W. E. Wilson and L. H. Toburen, Phys. Rev. A **11**, 1303 (1975).

[40] M. E. Rudd, T. V. Goffe, A. Itoh, and R. D. DuBois, Phys. Rev. A **32**, 829 (1985).

[41] R. A. Langley, D. W. Martin, D. S. Harmer, J. W. Hooper, and E. W. McDaniel, Phys. Rev. **136**, A379 (1964).

[42] L. I. Pivovar, Y. Z. Levchenko, and A. N. Grigor'ev, Sov. Phys. JETP **27**, 699 (1968).

[43] M. E. Rudd, T. V. Goffe, and A. Itoh, Phys. Rev. A **32**, 2128 (1985).

[44] E. S. Solov'ev, R. N. Il'in, V. A. Oparin, and N. V. Fedorenko, Sov. Phys. JETP **18**, 342 (1964).

[45] P. D. Fainstein, V. H. Ponce, and R. D. Rivarola, J. Phys. B **24**, 3091 (1991).

[46] G. H. Gillespie, Phys. Lett. A **93**, 327 (1983).

[47] A. Itoh, M. Asari, and F. Fukuzawa, J. Phys. Soc. Jpn. **48**, 943 (1980).

[48] C. F. Barnett and P. M. Stier, Phys. Rev. **109**, 385 (1958).

[49] H. B. Gilbody, K. F. Dunn, R. Browning, and C. J. Latimer, J. Phys. B **4**, 800 (1971).

[50] H. B. Gilbody, K. F. Dunn, R. Browning, and C. J. Latimer, J. Phys. B **3**, 1105 (1970).

[51] P. Hvelplund and E. Horsdal Pedersen, Phys. Rev. A **9**, 2434 (1974).

[52] A. Itoh, K. Ohnishi, and F. Fukuzawa, J. Phys. Soc. Jpn. **49**, 1513 (1980).

[53] L. I. Pivovar, V. M. Tubaev, and M. T. Novikov, Sov. Phys. JETP **14**, 20 (1962).

[54] S. T. Manson and L. H. Toburen, Phys. Rev. Lett. **46**, 529 (1981).

[55] M. Sataka, A. Yagishita, and Y. Nakai, J. Phys. B **23**, 1225 (1990).

[56] W. H. Barkas, *Nuclear Research Emulsions. I. Techniques and Theory* (Academic Press, New York and London, 1963).

[57] H. H. Heckman, B. L. Perkins, W. G. Simon, F. M. Smith, and W. H. Barkas, Phys. Rev. **117**, 544 (1960).

[58] G. Kraft, M. Krämer, and M. Scholz, Radiat. Environ. Biophys. **31**, 161 (1992).

[59] G. Hilgers, Radiat. Meas. **45**, 1228 (2010).

[60] G. Hilgers, M. U. Bug, E. Gargioni, and H. Rabus [Radiat. Prot. Dosim. (to be published)].

[61] National Institute of Standards and Technology, *Pstar and Astar Databases*, http://www.nist.gov/pml/data/star/index.cfm.

[62] E. Gargioni and B. Grosswendt, Nucl. Instrum. Meth. A **580**, 81 (2007).

[63] V. Conte, P. Colautti, L. D. Nardo, A. Ferretti, M. Poggi, D. Moro, M. Lombardi, G. Tornielli, and B. Grosswendt, Radiat. Prot. Dosim. **143**, 455 (2011).

Chapter 7

Conclusions and Outlook

This thesis investigated the accuracy by which cross sections of water can be used to represent DNA media when applied in track structure simulations for nanodosimetry. This problem is of particular importance as parameters of the particle track structure are used in nanodosimetry to estimate direct DNA damage. These parameters are obtained by simulations, which require cross section data for the interaction of particles with molecules comprising the medium. Conventionally, cross section data for water are used to represent DNA medium, as previously no complete set of interaction cross section data for DNA constituents existed. This work presents, for the first time, electron-impact cross section data for DNA constituents based on experimental data. The evaluated data set allowed the investigation of the following questions:

1. How accurate are cross sections of water?
2. How different are the electron-impact cross section data for water and DNA constituents?
3. How sensitive are simulated nanodosimetric parameters to differences in cross section data?

The first question is addressed in chapter 3 where a literature review of cross section data for interactions of electrons and protons with gaseous or liquid water revealed significant deviations in the data obtained by different authors. In summary, total electron-impact ionisation cross section data of liquid water agree well among each other at energies above 200 eV but deviate by a factor of two for energies below. The data obtained by the model yielding the larger ionisation cross section values for liquid water are similar to those of the vapour phase. Excitation cross sections are as much as a factor of five larger for the vapour phase than for the liquid. Different model data agree within 50%. Unfortunately, the calculated cross sections of liquid water were not yet experimentally verified but the observed deviations in the cross section data may be used as estimates for the data uncertainties.

The track structure code PTra was extended for simulations of electron and proton transport in water vapour and liquid water with different options for ionisation cross section data of liquid water to investigate a possible influence on simulation results. The simulations in water media in the gaseous and liquid phases were validated by calculating W-values and G-values. The code was then used to investigate the sensitivity of nanodosimetric quantities on the different cross section data for water. Significant differences were again observed, for example, the mean ionisation cluster size varies by 20% in the region of its maximum at 150 eV; however at 40 eV, the variation is a factor of two.

Electron cross sections of liquid water were indirectly verified by benchmarking the secondary electron transport in the codes PTra and Geant4-DNA. For this purpose, simulations of a specifically designed experiment [180] were performed. In this experiment, a beam of 6 MeV protons was used to produce secondary electrons in a 40 nm thick layer of water and electron emission spectra were measured as function of the emission angle. The benchmark was published for the previous version of PTra [Pub6] and the simulation of this experiment was repeated with the version developed in this work. Excellent agreement with the experimental electron spectra was again achieved. An important finding of these investigations is that the combination of cross section data for protons and electrons is crucial and, hence, cross section data should be selected carefully.

The second part of this work contains the evaluation of the experimental electron-impact cross sections of DNA constituents (chapter 4). These data were evaluated to provide model functions for a convenient implementation in simulation codes. The provided cross section data set is complete for electrons with energies between about 7 eV and 1 keV. The molecules of interest were tetrahydrofuran (THF), trimethylphosphate (TMP), pyrimidine (PY) and purine (PU).

The experimental data consisted of total scattering cross sections for energies 5 eV–1 keV, differential elastic scattering cross sections for energies 20 eV–1 keV and scattering angles 5–135° as well as double differential ionisation cross sections for energies 20 eV–1 keV, secondary electron energies down to 2.7 eV or 3 eV and emission angles 15–135°. The data for PU had not been measured but were scaled from those of pyrimidine by the ratio of total scattering cross sections. Extrapolations of the experimental data to forward and backward scattering angles as well as to zero secondary electron energy were carefully performed. The influence of different extrapolation approaches on the integrated cross section data was investigated. Uncertainty propagation was applied throughout the data analysis, taking into account two contributions: the uncertainties of the experimental data points and the imperfect description of the experimental data by the fitted model functions. Probabilities for Auger electron emission after a K-shell ionisation could be derived from the experimental double-differential spectra. The Auger peak region was fitted to obtain an estimation of the electron energy in the simulation. Total cross sections for ionisation and elastic scattering generally compared well with literature data within the combined uncertainties. While there existed literature data for THF by several authors, only one reference was found for either of those cross sections of PY and the values for TMP could only be compared to data for trimethylphosphine. Hence, more total cross section data for both PY and TMP would be useful to verify our integrated values. Furthermore, no literature data were available for the differential ionisation cross sections of all molecules investigated in this work. However, when observing the angular and energy dependence as well as the absolute values (normalised to the number of valence electrons in the respective molecule), good agreement was found among THF, PY and TMP. Total excitation cross sections were calculated by subtracting the ionisation and elastic scattering cross section from the total scattering cross section. The resulting cross section data for PY and THF were on the same order of magnitude as experimental literature data. These excitation cross sections were, however, only available in limited energy ranges and selected excitation states. Therefore, a mean excitation energy was calculated from optical oscillator strength distributions in the literature. Those values can only be used when the electron energy is significantly above the highest excitation level. Due to these limitations, a more complete cross section data set for separate excitation states for an extended energy range would be essential for more realistic simulations of electrons with energies below the ionisation threshold.

Chapter 5 aimed to answer questions two and three. The set of interaction cross section data of DNA constituents, developed as part of this thesis, and water were compared in section 5.2. While the cross section data, normalised to the number of valence electrons in each molecule, were in the same order of magnitude, the energy and angular dependences were significantly different so that the simulated electron track was affected as discussed in sections a) and later. Simulations were tested by calculating W-values for electrons of 1 keV in media consisting of THF, TMP or PY. Those were 3.4 - 4.4 eV lower than the W-value for water, due to the lower ionisation threshold and the smaller mean free ionisation path length in the DNA constituents.

Electron transport in DNA medium was simulated, assuming that the medium consisted of uniformly distributed nucleotides, which themselves were equal and made up of fixed fractions of THF, TMP, PY, PU and water molecules. The first set of simulations was performed using the same mass density of 1 gcm^{-3} for the DNA medium, water vapour and two different sets of ionisation cross sections of liquid water. Calculated mean cluster sizes for ionisation were similar within 12% for DNA medium and water when the cross section set SigIon1 was used. However, the values in DNA medium compared to water using SigIon2 were 25% higher in the region of the maximum at 150 eV and by a factor of two at 40 eV. Mean excitation cluster sizes obtained in DNA medium were similar to those in water vapour, while the results in DNA medium were a factor of 2.0–2.5 larger compared to liquid water. The maximum F_2 value of 0.66–0.68 was obtained for 100 eV electrons in DNA medium, reaching only 0.56–0.63 for water. Clustered ionisations of the backbone molecules THF and TMP were significant, as the F_2 values reach a probability of 0.39 at 150 eV.

Native DNA contains about 12.5 water molecules per nucleotide. In this case, the mean ionisation cluster size was enhanced by up to 36% for energies above 100 eV, while the maximum F_2 value increased to 0.76 at an energy of 100 eV. The F_2 values for higher energies were up to 42% larger when the water content was doubled. Consequently, the estimated DNA damage would be significantly enhanced relative to pure water medium. F_2 values calculated for the backbone molecules are useful to estimate the probability for a DNA strand break by direct ionisation of the backbone molecules. However, one has to keep in mind that an ionisation is not always followed by a fragmentation of the DNA. On the other hand, its fragmentation may also occur through other processes, such as dissociative excitation states or ionisations of intrinsic water molecules. The latter process could lead to the formation of radicals, which easily reach the sensitive DNA molecules to enhance their damage. This means that the water content of the DNA has a large influence on the complexity of clusters and, hence, the DNA damage. Hence, the F_2 values for ionisation may provide an estimation for the probability of DNA damage, if the number of ionisations which do not lead to a fragmentation is similar to the additional damage of DNA molecules through other fragmentation channels.

More realistic simulations were performed for a 1 MeV proton track, calculating track structure parameters in the vicinity of the proton trajectory. Protons were transported in water, while either water or DNA medium was used for the secondary electrons. A larger frequency of secondary electrons with an energy below 15 eV was present in water, leading to a much larger fluence of electrons through target cylinders placed at different distances (1–10 nm) to the proton trajectory. These differences were most likely due to the average energy loss assumed in an excitation of DNA constituents so that an improved set of electron-impact excitation cross sections is required for more realistic simulations. Despite the larger frequency of electrons with energies between the ionisation threshold and about 15 eV in water, the mean ionisation cluster size was 5–50% higher in DNA medium at distances of 1–10 nm, respectively. Similarly, F_2 values were 16–50% higher with increasing distance to the proton trajectory. These results were in accordance with the values obtained for monoenergetic electrons. It is expected that the differences in the results become larger when electron-impact cross sections for individual excitation states are available for electrons of energy at least down to the lowest electronic excitation state. Due to the implementation of a mean excitation energy obtained from optical oscillator strength distributions, the energy loss in excitation processes was overestimated in the present simulations, particularly for electrons of energies between the thresholds for discrete excitation and ionisation. Hence, the frequency of electrons was reduced in this energy range.

For a simulation of protons traversing a cell nucleus, an interaction cross section data set for proton-impact on DNA constituents is required. An implementation of such a cross section set may alter the mean free ionisation path of the protons and, hence, the number of secondary electrons, as well as on the electron spectra. In addition, the use of highly-structured DNA target models in the proton transport may affect secondary electron distributions in the vicinity of the proton trajectory. Protons of energies above 100 keV do not significantly change their direction of motion and, on the other hand, the probability for an interaction as well as secondary electron spectra produced at different molecules of the DNA medium may vary substantially. Therefore, electron spectra in the vicinity of the proton trajectory may be different from those obtained with a mean free path length, averaged over the molecules comprising the DNA medium.

In chapter 6, a cornerstone is placed for future work on ion transport through DNA media. The simulations of protons and alpha particles in nitrogen and propane were benchmarked by comparing simulated and measured nanodosimetric quantities. Ion projectiles of energies between 100 keV and 20 MeV were used in those experiments.

The work in this chapter and published in [Pub10] involved another literature review of ionisation and charge-transfer cross section data for electron, proton and helium particle interactions with nitrogen, methane and propane. In the literature, those data were obtained from measurements, theoretical calculations or described by semiempirical models. Ionisation cross section data for the interaction of light ions in propane were not found. Hence, propane cross section data were derived from those of methane, which was shown to be appropriate at least for projectile energies above 1 MeV/u. Another issue in this investigation was that the charge-transfer cross sections and measured charge-equilibrium fractions for helium projectiles were often determined only in limited energy ranges. This leads to a scatter of the data by up to 20%.

Based on the literature review, cross section models for ionisation and charge-transfer were recommended and implemented in PTra. Measured nanodosimetric quantities obtained in nitrogen or propane were in excellent agreement for protons (100 keV–10 MeV) as well as for helium projectiles with energies above 1 MeV. At energies below, deviations up to 19% and 24% were present for mean ionisation cluster sizes in nitrogen and propane, respectively.

For an improvement of those track structure simulations, cross section data are required for interactions of protons and alpha particles with propane. Also, more experimental data on electron-impact ionisation cross sections and charge-transfer data for helium particles in nitrogen would be useful to verify the recommended data.

Outlook.

In addition to the urgently requested cross section data set for the interaction of light ions with DNA constituents and electron-impact excitation, the following future improvements in the particle transport simulation are required to improve the accuracy of particle track modelling.

Focussing only on physical aspects, it is obvious that the DNA constituents used in this work are different to real DNA chains as they contain somewhat different atomic configurations, on the one hand, and are assumed to be evaporated, on the other hand. The first point may be solved by using calculated data for the DNA nucleobases and backbone molecules, where several data sets are readily available in the literature (for example in [9, 27, 176, 193, 194]). However, some of these data show significant deviations related to the different theoretical approaches applied. Moreover, fragmentation patterns of the molecules have to be taken into account to estimate the severity of an ionisation with respect to potential rupture of chemical bonds. Cross sections for fragmentation exist only for THF and PY molecules in the literature [35, 62, 128].

The second issue is more difficult to solve, even though a lot of publications already discuss different aspects of condensed phase effects on DNA. Additionally to the changes in electronic potential by the arrangement of DNA molecules in the solid state [58, 176, 193, 194], the solvation environment will also affect the electronic charge distribution [163] and, hence, interaction cross sections and fragmentation patterns. Phase effects are particularly important for low-energy electrons of energies up to several electron volts. Such electrons are able to cause significant DNA damage by dissociative electron attachment [17, 163]. There exist, for example, molecular dynamic effects such as adiabatic through-bond electron transfer where it has been shown that 1 eV electrons can attach at a π^* orbital of a pyrimidine nucleobase and move through the deoxyribose to the phosphate unit where they cause a cleavage of the sugar-phosphate σ-bond. This effect depends strongly on the electron energy and the solvation environment and, hence, supports the importance to consider condensed phase effects to improve the accuracy of estimated DNA damage from simulation results in the future.

References

[1] K. Aflatooni, A. M. Scheer, and P. D. Burrow. Total dissociative electron attachment cross sections for molecular constituents of DNA. *J. Chem. Phys.*, 125:054301, 2006.

[2] M. Allan. Absolute angle-differential elastic and vibrational excitation cross sections for electron collisions with tetrahydrofuran. *J. Phys. B*, 40:3531–3544, 2007.

[3] S. K. Allison. Experimental results on charge-changing collisions of hydrogen and helium atoms and ions at kinetic energies above 0.2 keV. *Rev. Mod. Phys.*, 30:1137–1168, 1958.

[4] W. M. Ariyasinghe, T. Wijerathna, and D. Powers. Total electron scattering cross sections of PH_3 and SiH_4 molecules in the energy range 90-3500 eV. *Phys. Rev. A*, 68:032708, 2003.

[5] W. Y. Baek and B. Grosswendt. W values of protons in liquid water. *Radiat. Prot. Dosim.*, 126:93–96, 2007.

[6] Woon Yong Baek, Physikalisch-Technische Bundesanstalt, Braunschweig, Germany. private communication.

[7] M. A. Bernal. Evaluation of the mean energy deposit during the impact of charged particles on liquid water. *Phys. Med. Biol.*, 57:1745–1757, 2012.

[8] M. A. Bernal and J. A. Liendo. The HKS model for electron production in liquid water by light ions. *Nucl. Instr. Meth. Phys. Res. B*, 251:171–176, 2006.

[9] P. Bernhardt and H. G. Paretzke. Calculation of electron impact ionization cross sections of DNA using the Deutsch-Märk and Binary-Encounter-Bethe formalisms. *Int. J. Mass Spectrom.*, 223–224:599–611, 2003.

[10] H. Bethe. Zur Theorie des Durchgangs schneller Korpuskularstrahlen durch Materie. *Ann. Phys.*, 5:325–400, 1930.

[11] E. A. Bigildeev and V. Michalik. Charged particle tracks in water of different phases. Monte Carlo simulation of electron tracks. *Radiat. Phys. Chem.*, 47:197–207, 1992.

[12] G. L. Blackman, R. D. Brown, and F. R. Burden. The microwave spectrum, dipole moment, and nuclear quadrupole coupling constants of pyrimidine. *J. Molec. Spectr.*, 35:444–454, 1970.

[13] F. Blanco and G. García. A screening-corrected additivity rule for the calculation of electron scattering from macro-molecules. *J. Phys. B*, 42:145203, 2009.

[14] M. A. Bolorizadeh and M. E. Rudd. Angular and energy dependence of cross sections for ejection of electrons from water vapor. i. 50-2000-eV electron impact. *Phys. Rev. A*, 33:882–887, 1986.

[15] R. Bosque and J. Sales. Polarizabilities of solvents from the chemical composition. *J. Chem. Inf. Comput. Sci.*, 42:1154–1163, 2002.

[16] D. Bouchiha, J. D. Gorfinkiel, L. G. Caron, and L. Sanche. Low-energy electron collisions with tetrahydrofuran. *J. Phys. B*, 39:975–986, 2006.

[17] B. Boudaïffa, P. Cloutier, D. Hunting, M. A. Huels, and L. Sanche. Resonant formation of DNA strand breaks by low-energy (3 to 20 eV) electrons. *Science*, 287:1658–1660, 2000.

[18] B. H. Bransden and C. J. Joachain. *Physics of atoms and molecules.* Longman London and New York, 1983.

[19] L. J. Bremner, M. G. Curtis, and I. C. Walker. Electronic states of some simple ethers studied by vaccum ultraviolet absorption and near-threshold electron energy-loss spectroscopy. *J. Chem. Soc. Faraday Trans.*, 87:1049–1055, 1991.

[20] D. J. Brenner and J. F. Ward. Constraints on energy deposition and target size of multiply damaged sites associated with DNA double-strand breaks. *Int. J. Radiat. Biol.*, 61:737–748, 1992.

[21] D. J. Brenner and M. Zaider. A computationally convenient parameterisation of experimental angular distributions of low energy electrons elastically scattered off water vapour. *Phys. Med. Biol.*, 29:443–447, 1983.

[22] S. J. Buckman, M. J. Brunger, and M. T. Elford. Photon and electron interactions with atoms, molecules and ions. In Y. Itikawa, editor, *Landolt-Börnstein Vol I/17, subvolume C*. Springer Verlag, 2003.

[23] Bundesministerium für Umwelt, Naturschutz und Reaktorsicherheit (BMU); Bundesamt für Strahlenschutz (BfS). Umweltradioaktivität und Strahlenbelastung im Jahr 2011. `http://nbn-resolving.de/urn:nbn:de:0221-2013060410695`, 2013.

[24] Bureau International des Poids et Mesures (BIPM). JCGM 100:2008, Evaluation of measurement data - Guide to the Expression of Uncertainty in Measurement (GUM), 2008. ISBN 92-67-10188-9.

[25] E. Casnati, A. Tartari, and C. Baraldi. An empirical approach to K-shell ionisation cross section by electrons. *J. Phys. B*, 15:155–167, 1982.

[26] C. Champion. Theoretical cross sections for electron collisions in water: structure of electron tracks. *Phys. Med. Biol.*, 48:2147–2168, 2003.

[27] C. Champion. Quantum-mechanical predictions of electron-induced ionization cross sections of DNA components. *J. Chem. Phys.*, 138:184306, 2013.

[28] C. Champion, S. Incerti, H. Aouchiche, and D. Oubaziz. A free-parameter theoretical model for describing the electron elastic scattering in water in the Geant4 toolkit. *Radiat. Phys. Chem.*, 78:745–750, 2009.

[29] M. Chaplin. Do we underestimate the importance of water in cell biology? *Nature Rev. Molec. Cell Biol.*, 7:861–866, 2006.

[30] H. Cho, Y. S. Park, H. Tanaka, and S. J. Buckman. Measurements of elastic electron scattering by water vapour extended to backward angles. *J. Phys. B*, 37:625, 2004.

[31] B. Cleff and W. Mehlhorn. On the angular distribution of Auger electrons following impact ionization. *J. Phys. B*, 7:593–604, 1974.

[32] C. J. Colyer, V. Vizcaino, J. P. Sullivan, M. J. Brunger, and S. J. Buckman. Absolute elastic cross-sections for low-energy electron scattering from tetrahydrofuran. *New. J. Phys.*, 9:41, 2007.

[33] D. Combecher. Measurement of W values of low-energy electrons in several gases. *Radiat. Res.*, 84:189–218, 1980.

[34] M. Dampc, I. Linert, A. R. Milosavljević, and M. Zubek. Vibrational excitation of tetrahydrofuran by electron impact in the low energy range. *Chem. Phys. Lett.*, 443:17–21, 2007.

[35] M. Dampc, A. R. Milosavljević, I. Linert, B. P. Marinković, and M. Zubek. Differential cross sections for low-energy elastic electron scattering from tetrahydrofuran in the angular range 20°–180°. *Phys. Rev. A*, 75:042710, 2007.

[36] M. Dampc, E. Szymańska, B. Mielewska, and M. Zubek. Ionization and ionic fragmentation of tetrahydrofuran molecules by electron collisions. *J. Phys. B*, 44:055206, 2011.

[37] L. DeNardo, V. Conte, M. Poggi, S. Canella, P. Colautti, D. Moro, and G. Tornielli. The STARTRACK experiment. *Radiat. Prot. Dosim.*, 126:453–456, 2007.

[38] H. Deutsch, K. Becker, and T. D. Märk. Theoretical determination of absolute electron-impact ionization cross sections of molecules. *Int. J. Mass Spectrom.*, 177:47, 1998.

[39] M. Dingfelder, D. Hantke, M. Inokuti, and H. G. Paretzke. Electron inelastic-scattering cross sections in liquid water. *Radiat. Phys. Chem.*, 53:1–18, 1998.

[40] M. Dingfelder, M. Inokuti, and H. G. Paretzke. Inelastic-collision cross sections of liquid water for interactions of energetic protons. *Rad. Phys. Chem.*, 59:255–275, 2000.

[41] M. Dingfelder, A. Travia, R. A. McLawhorn, J. L. Shinpaugh, and L. Toburen. Electron emission from foils and biological materials after proton impact. *Rad. Phys. Chem.*, 77:1213–1217, 2008.

[42] T. P. T. Do, M. Leung, M. Fuss, G. García, F. Blanco, K. Ratnavelu, and M. J. Brunger. Excitation of electronic states in tetrahydrofuran by electron impact. *J. Chem. Phys.*, 134:144302, 2011.

[43] A. Domaracka, P. Możejko, E. Ptasińska-Denga, and C. Szmytkowski. Collisions of electrons with trimethylphosphine [$P(CH_3)_3$] molecules. *Phys. Rev. A*, 76:042701, 2007.

[44] A. Domaracka, P. Możejko, E. Ptasińska-Denga, and C. Szmytkowski. Electron-scattering total cross sections for complex molecules: group additivity rule. *Publ. Astron. Obs. Belgrade*, 84:35–38, 2008.

[45] S. Edel, M. Terrissol, A. Peudon, E. Kümmerle, and E. Pomplun. Computer simulation of strand break yields in plasmid pBR322: DNA damage following ^{125}I decay. *Radiat. Prot. Dosim.*, 122:136–140, 2006.

[46] M. Egli, V. Tereshko, M. Teplova, G. Minasov, A. Joachmiak, R. Sanshvili, C. M. Weeks, R. Miller, M. A. Maier, H. An, P. D. Cook, and M. Manoharan. X-ray crystallographic analysis of the hydration of A- and B-form DNA at atomic resolution. *Biopolymers*, 48:234–252, 2000.

[47] C. G. Elles, A. E. Jailaubekov, R. A. Crowell, and S. E. Bradforth. Excitation-energy dependence of the mechanism for two-photon ionization of liquid H_2O and D_2O from 8.3 to 12.4 eV. *J. Chem. Phys.*, 125:044515, 2006.

[48] D. Emfietzoglou, F. A. Cucinotta, and H. Nikjoo. A complete dielectric response model for liquid water: a solution of the Bethe ridge problem. *Radat. Res.*, 164:202–211, 2005.

[49] D. Emfietzoglou, K. Karava, G. Papamichael, and M. Moscovitch. Monte Carlo simulation of the energy loss of low-energy electrons in liquid water. *Phys. Med. Biol.*, 48:2355–2371, 2003.

[50] D. Emfietzoglou, I. Kyriakou, I. Abril, R. Garcia-Molina, and H. Nikjoo. Inelastic scattering of low-energy electrons in liquid water computed from optical-data models of the Bethe surface. *Int. J. Radiat. Biol.*, 88:22–28, 2012.

[51] D. Emfietzoglou and M. Moscovitch. Inelastic collision characteristics of electrons in liquid water. *Nucl. Instrum. Meth. Phys. Res. B*, 193:71–78, 2002.

[52] D. Emfietzoglou and H. Nikjoo. The effect of model approximations on single-collision distributions of low-energy electrons in liquid water. *Radat. Res.*, 163:98–111, 2005.

[53] D. Emfietzoglou, G. Papamichael, K. Kostarelos, and M. Moscovitch. A Monte Carlo track structure code for electrons (10 eV - 10 keV) and protons (0.3-10 MeV in water: partitioning of energy and collision events. *Phys. Med. Biol.*, 45:3171–3194, 2000.

[54] P. D. Fainstein, V. H. Ponce, and R. D. Rivarola. Two-centre effects in ionization by ion impact. *J. Phys. B*, 24:3091–3119, 1991.

[55] U. Fano. Ionizing collisions of very fast particles and the dipole strength of optical transitions. *Phys. Rev.*, 95:1198–1200, 1954.

[56] M. Faubel, B. Steiner, and J. P. Toennies. Photoelectron spectroscopy of liquid water, some alcohols, and pure nonane in free micro jets. *J. Chem. Phys.*, 106:9013–9031, 1997.

[57] J. M. Fernández-Varea, X. Llovet, and F. Salvat. Cross sections for electron interactions in condensed matter. *Surf. Interface Anal.*, 37:824–832, 2005.

[58] J. M. Fernández-Varea, F. Salvat, M. Dingfelder, and D. Liljequist. A relativistic optical-data model for inelastic scattering of electrons and positrons in condensed matter. *Nucl. Instrum. Meth. B*, 229:187–218, 2005.

[59] F. Ferreira da Silva, D. Almeida, G. Martins, A. R. Milosavljević, B. P. Marinković, S. V. Hoffmann, N. J. Mason, Y. Nunes, G. García, and P. Limão-Vieira. The electronic states of pyrimidine studied by VUV photoabsorption and electron energy-loss spectroscopy. *Phys. Chem. Chem. Phys.*, 12:6717–6731, 2010.

[60] R. E. Franklin and R. G. Gosling. The structure of sodium thymonucleate fibres. I. The influence of water content. *Acta Cryst.*, 6:673–677, 1953.

[61] W. Friedland, P. Jacob, H. G. Paretzke, M. Merzagora, and A. Ottolenghi. Simulation of DNA fragment distributions after irradiation with photons. *Radiat. Environ. Biophys.*, 38:39–47, 1999.

[62] M. Fuss, A. Muñoz, J. C. Oller, F. Blanco, D. Almeida, P. Limão-Vieira, T. P. D. Do, M. J. Brunger, and G. García. Electron-scattering cross sections for collisions with tetrahydrofuran from 50 to 5000 eV. *Phys. Rev. A*, 80:052709, 2006.

[63] E. Gargioni and B. Grosswendt. Influence of ionization cross-section data on the Monte Carlo calculation of nanodosimetric quantities. *Nuc. Instrum. Meth. A*, 580:81–84, 2007.

[64] E. Gargioni and B. Grosswendt. Electron scattering from argon: data evaluation and consistency. *Rev. Mod. Phys.*, 80:451–480, 2008.

[65] G. Garty, R. Schulte, S. Shchemelinin, B. Grosswendt, C. Leloup, G. Assaf, A Breskin, R Chechik, and V. Bashkirov. First attempts at prediction of DNA strand-break yields using nanodosimetric data. *Radiat. Prot. Dosim.*, 122:451–454, 2006.

[66] G. Garty, R. Schulte, S. Shchemelinin, C. Leloup, G. Assaf, A. Breskin, R. Chechik, V. Bashkirov, J. Milligan, and B. Grosswendt. A nanodosimetric model of radiation-induced clustered DNA damage yields. *Phys. Med. Biol.*, 55:761–781, 2010.

[67] G. Garty, S. Shchemelinin, A. Breskin, R. Chechik, G. Assaf, I. Orion, V. Bashkirov, R. Schulte, and B. Grosswendt. The performance of a novel ion-counting nanodosimeter. *Nucl. Instr. Meth. Phys. Res. A*, 492:212–235, 2002.

[68] A. Gauf, L. R. Hargreaves, A. Jo, J. Tanner, and M. A. Khakoo. Low-energy electron scattering by tetrahydrofuran. *Phys. Rev. A*, 85:052717, 2012.

[69] L. George, K. S. Viswanathan, and S. Singh. Ab initio study of trimethyl phosphate: Conformal analysis, dipole moments, vibrational frequencies, and barriers for conformer interconvention. *J. Phys. Chem. A*, 101:2459–2464, 1997.

[70] F. A. Gianturco and A. Jain. The theory of electron scattering from polyatomic molecules. *Phys. Reports*, 143:347–425, 1986.

[71] A. Giuliani, P. Limão-Vieira, D. Duflot, A. R. Milosavljević, B. P. Marincović, S. V. Hoffmann, N. Mason, J. Delwiche, and M.-J. Hubin-Franskin. Electronic states of neutral and ionized tetrahydrofuran studied by VUV spectroscopy and ab initio calculations. *Eur. Phys. J. D*, 51:97–108, 2008.

[72] D. T. Goodhead. Initial events in the cellular effects of ionizing radiations: clustered damage in DNA. *Int. J. Radiat. Biol.*, 65:7–17, 1994.

[73] D. T. Goodhead. Mechanisms for the biological effectiveness of high-LET radiations. *J. Radiat. Res.*, 40:S1–S13, 1999.

[74] D. T. Goodhead. Energy deposition stochastics and track structure: What about the target? *Radiat. Prot. Dosim.*, 122:3–15, 2006.

[75] Gordon research group. The General Atomic and Molecular Electronic Structure System (GAMESS). `http://www.msg.ameslab.gov/gamess/`. Online, accessed 10/2013.

[76] J. D. Gorfinkiel, L. A. Morgan, and J. Tennyson. Electron impact dissociative excitation of water within the adiabatic nuclei approximation. *J. Phys. B*, 35:543, 2002.

[77] A. E. S. Green and T. Sawada. Ionization cross sections and secondary electron distributions. *J. Atm. Terr. Phys.*, 34:1719–1728, 1972.

[78] A. E. S. Green and R. S. Stolarski. Analytic models of electron impact excitation cross sections. *J. Atmosph. Terr. Phys.*, 34:1703–1717, 1972.

[79] B. Grosswendt. Formation of ionization clusters in nanometric structures of propane-based tissue-equivalent gas or liquid water by electrons and alpha-particles. *Radiat. Environ. Biophys.*, 41:103–112, 2002.

[80] B. Grosswendt. Nanodosimetry, from radiation physics to radiation biology. *Radiat. Protec. Dosim.*, 115:1–9, 2005.

[81] B. Grosswendt and E. Waibel. Transport of low energy electrons in nitrogen and air. *Nucl. Instrum. Meth.*, 155:145–156, 1978.

[82] Bernd Grosswendt, Braunschweig. private communication.

[83] H. Hayashi, N. Watanabe, and Y. Udagawa. Optical spectra of liquid water in vacuum uv region by means of inelastic x-ray scattering spectroscopy. *J. Chem. Phys.*, 108:823–825, 1998.

[84] H. Hayashi, N. Watanabe, Y. Udagawa, and C.-C. Kao. The complete optical spectrum of liquid water measured by inelastic x-ray scattering. *PNAS*, 97:6264–6266, 2000.

[85] J. M. Heller, R. N. Hamm, R. D. Birkhoff, and L. R. Painter. Collective oscillation in liquid water. *J. Chem. Phys.*, 60:3483–3486, 1974.

[86] G. Hilgers, E. Gargioni, B. Grosswendt, and S. Shchemelinin. Proton-incuded frequency distributions of ionization cluster size in propane. *Radiat. Prot. Dosim.*, 126:467–470, 2007.

[87] A. Hiltunen, S. Aksela, G. Víkor, S. Ricz, Á. Kövér, and B. Sulik. High resolution carbon and oxygen K-LL Auger spectra of carbon dioxide. *Nucl. Instrum. Meth. B*, 154:267–271, 1999.

[88] M. G. P. Homem, A. López-Castillo, M. Barbatti, L. F. S. Rosa, P. Iza, R. L. Cavasso-Filho, L. S. Faranzena, M. T. Lee, and I. Iga. Experimental and theoretical investigations on photoabsorption and photoionization of trimethylphosphate in the vacuum-ultraviolet energy range. *J. Chem. Phys.*, 137:184305, 2012.

[89] M. G. P. Homem, R. T. Sugohara, I. P. Sanches, M. T. Lee, and I. Iga. Cross sections for elastic electron collisions with tetrahydrofuran. *Phys. Rev. A*, 80:032705, 2009.

[90] J. W. Hooper, D. S. Harmer, D. W. Martin, and E. W. McDaniel. Comparison of electron and proton ionization data with the Born approximation predictions. *Phys. Rev.*, 125:2000–2004, 1962.

[91] W. G. Horner. A new method of solving numerical equations of all orders, by continuous approximation. *Transactions of the Royal Society of London*, pages 308–335, 1819.

[92] N. S. Hush and A. S. Cheung. Ionization potentials and donor properties of nucleic acid bases and related compounds. *Chem. Phys. Lett.*, 34:11–13, 1975.

[93] W. Hwang, Y.-K. Kim, and M. E. Rudd. New model for electron-impact ionization cross sections of molecules. *J. Chem. Phys.*, 104:2956–2966, 1996.

[94] S. Incerti, A. Ivanchenko, M. Karamitros, A. Mantero, P. Moretto, H. N. Tran, B. Mascialino, C. Champion, V. N. Ivanchenko, M. A. Bernal, Z. Francis, C. Villagrasa, G. Baldacchino, P. Gueye, R. Capra, P. Nieminen, and C. Zacharatou. Comparison of GEANT4 very low energy cross section models with experimental data in water. *Med. Phys.*, 37:4692–4708, 2010.

[95] M. Inokuti. Inelastic collisions of fast charged particles with atoms and molecules – the Bethe theory revisited. *Rev. Mod. Phys.*, 43:297–347, 1971.

[96] M. Inokuti. How is radiation energy absorption different between the condensed phase and the gas phase? *Radiat. Effects Defects Solids*, 117:143–162, 1991.

[97] International Atomic Energy Agency (IAEA). Dosimetry in diagnostic radiology: an international code of practice. Technical reports series no. 457, 2007.

[98] The International Commission on Radiation Units and Measurements (ICRU). Average energy required to produce an ion pair (ICRU report no. 31), 1979.

[99] The International Commission on Radiation Units and Measurements (ICRU). Stopping powers and ranges for protons and alpha particles (ICRU report no. 49), 1993.

[100] The International Commission on Radiation Units and Measurements (ICRU). Secondary electron spectra from charged particle interactions (ICRU report no. 55), 1996.

[101] The International Commission on Radiation Units and Measurements (ICRU). Elastic scattering of electrons and positrons (ICRU report no.77), 2007.

[102] The International Commission on Radiation Units and Measurements (ICRU). Fundamental quantities and units for ionizing radiation (ICRU report no.85a-revised), 2011.

[103] K. K. Irikura, M. A. Ali, and Y.-K. Kim. Electron-impact total ionization cross-sections of the chlorofluoromethanes. *Int. J. Mass Spectrom.*, 222:189–200, 2003.

[104] Y. Itikawa. Cross sections for electron collisions with nitrogen molecules. *J. Phys. Chem. Ref. Data*, 35:31–53, 2006.

[105] Y. Itikawa. Cross sections for electron collisions with oxygen molecules. *J. Phys. Chem. Ref. Data*, 38:1–20, 2009.

[106] Y. Itikawa and N. Mason. Cross sections for electron collisions with water molecules. *J. Phys. Chem. Ref. Data*, 34:1–22, 2005.

[107] P. G. Jasien and G. Fitzgerald. Molecular dipole moments and polarizabilities from local density functional calculations: application to DNA base pairs. *J. Chem. Phys.*, 93:2554–2560, 1990.

[108] C. D. Jonah, M. S. Matheson, J. R. Miller, and E. J. Hart. Yield and decay of the hydrated electron from 100 ps to 3 ns. *J. Phys. Chem.*, 80:1267–1270, 1976.

[109] D. B. Jones, S. M. Bellm, F. Blanco, M. Fuss, G. García, P. Limão-Vieira, and M. J. Brunger. Differential cross sections for the electron impact excitation of pyrimidine. *J. Chem. Phys.*, 137:074304, 2012.

[110] I. G. Kaplan and V. Y. Sukhonosov. Simulation of the passage of fast electrons and the early stage water radiolysis by the Monte Carlo method. *Radiat. Res.*, 127:1–10, 1991.

[111] A. Katase, K. Ishibashi, Y. Matsumoto, T. Sakae, S. Maezono, E. Murakami, K. Watanabe, and H. Maki. Elastic scattering of electrons by water molecules over the range 100-1000 eV. *J. Phys. B*, 19:2715–2734, 1986.

[112] A. M. Kellerer and D. Chmelevsky. Concepts of microdosimetry, I. Quantities. *Rad. Environm. Biophys.*, 12:61–69, 1975.

[113] A. M. Kellerer and D. Chmelevsky. Concepts of microdosimetry, II. Probability distributions of the microdosimetric variables. *Rad. Environm. Biophys.*, 12:205–216, 1975.

[114] A. M. Kellerer and D. Chmelevsky. Concepts of microdosimetry, III. Mean values of the microdosimetric distributions. *Rad. Environm. Biophys.*, 12:321–335, 1975.

[115] H. Khesbak, O. Savchuk, S. Tsushima, and K. Fahmy. The role of water H-bond imbalances in B-DNA substate transitions and peptide recognition revealed by time-resolved FTIR spectroscopy. *J. Am. Chem. Soc.*, 133:5834–5842, 2011.

[116] Y.-K. Kim and M. E. Rudd. Binary-encounter-dipole model for electron-impact ionization. *Phys. Rev. A*, 50:3954–3967, 1994.

[117] Y.-K. Kim, J. P. Santos, and F. Parente. Extension of the binary-encounter-dipole model to relativistic incident electrons. *Phys. Rev. A*, 62:052710, 2000.

[118] M. Kimura, O. Sueoka, A. Hamada, and Y. Itikawa. A comparative study of electron- and positron-polyatomic molecule scattering. *Adv. Chem. Phys.*, 111:537, 2000.

[119] T. Koopmans. Über die Zuordnung von Wellenfunctionen und Eigenwerten zu den einzelnen Elektronen eines Atoms. *Physica*, 1:104–113, 1933.

[120] G. Kraft, M. Krämer, and M. Scholz. LET, track structure and models. *Radiat. Environ. Biophys.*, 31:161–180, 1992.

[121] G. J. Kutcher and A. E. S. Green. A model for energy deposition in liquid water. *Radat. Res.*, 67:408–425, 1976.

[122] J. A. LaVerne and A. Mozumder. Differential and integral W-values for ionization in gaseous water under electron and proton irradiation: consistency of inelastic collision cross sections. *Radiat. Res.*, 131:1–9, 1992.

[123] J. A. LaVerne and A. Mozumder. Concerning plasmon excitation in liquid water. *Radiat. Res.*, 133:282–288, 1993.

[124] J. Lehmann and K. Blum. Angular distribution of Auger electrons emitted by polyatomic molecules. *J. Phys. B*, 30:633–646, 1997.

[125] T. Liamsuwan and H. Nikjoo. A Monte Carlo track structure simulation code for the full-slowing-down carbon projectiles of energies 1 keV u^{-1} - 10 MeV u^{-1} in water. *Phys. Med. Biol.*, 58:673–701, 2013.

[126] T. Liamsuwan, S. Uehara, D. Emfietzoglou, and H. Nikjoo. Physical and biophysical properties of proton tracks of energies 1 keV to 300 MeV in water. *Int. J. Radiat. Biol.*, 87:141–160, 2011.

[127] D. Liljequist, T. Liamsuwan, and H. Nikjoo. Elastic scattering cross section models used for Monte Carlo simulation of electron tracks in media of biological and medical interest. *Int. J. Radiat. Biol.*, 88:29–37, 2012.

[128] I. Linert, M. Dampc, B. Mielewska, and M. Zubek. Cross sections for ionization and ionic fragmentation of pyrimidine molecules by electron collisions. *Eur. Phys. J. D*, 66:20, 2012.

[129] X. Llovet, C. J. Powell, F. Salvat, and A. Jablonski. Cross sections for inner-shell ionization by electron impact. *J. Phys. Chem. Ref. Data*, 43:013102, 2014.

[130] J. B. Maljković, A. R. Milosavljević, F. Blanco, D. Šević, G. García, and B. P. Marinković. Absolute differential cross sections for elastic scattering of electrons from pyrimidine. *Phys. Rev. A*, 79:052706, 2009.

[131] Z. Mašín, J. D. Gorfinkiel, D. B. Jones, S. M. Bellm, and M. J. Brunger. Elastic and inelastic cross sections for low-energy electron collisions with pyrimidine. *J. Chem. Phys.*, 136:144310, 2012.

[132] M. Michaud, A. Wen, and L. Sanche. Cross sections for low-energy (1-100 eV) electron elastic and inelastic scattering in amorphous ice. *Radiat. Res.*, 159:3–22, 2003.

[133] J. H. Miller and A. E. S. Green. Proton energy degradation in water vapor. *Radiat. Res.*, 54:343–363, 1973.

[134] A. R. Milosavljević, F. Blanco, G. García, and B. P. Marinković. Elastic scattering of electrons from tetrahydrofurfuryl alcohol. *Eur. Phys. J. D*, 40:107–114, 2006.

[135] A. R. Milosavljević, A. Giuliani, D. Šević, M.-J. Hubin-Franskin, and B. P. Marinković. Elastic scattering of electrons from tetrahydrofuran molecule. *Eur. Phys. J. D*, 35:411–416, 2005.

[136] A. R. Milosavljević, J. Kočišek, P. Papp, D. Kubala, B. P. Marinković, P. Mach, J. Urban, and Š. Matejčík. Electron impact ionization of furanose alcohols. *J. Chem. Phys.*, 132:104308, 2010.

[137] P. Możejko, A. Domaracka, E. Ptasińska-Denga, and C. Szmytkowski. Total cross-section measurements for electron collisions with α-tetrahydrofurfuryl alcohol ($C_5H_{10}O_2$). *Chem. Phys. Lett.*, 429:378–381, 2006.

[138] P. Możejko, E. Ptasińska-Denga, A. Domaracka, and C. Szmytkowski. Absolute total cross-section measurements for electron collisions with tetrahydrofuran. *Phys. Rev. A*, 74:012708, 2006.

[139] P. Możejko and L. Sanche. Cross section calculations for electron scattering from DNA and RNA bases. *Radiat. Environ. Biophys.*, 42:201–211, 2003.

[140] P. Możejko and L. Sanche. Cross sections for electron scattering from selected components of DNA and RNA. *Radiat. Phys. Chem.*, 73:77–84, 2005.

[141] National Institute of Standards and Technology (NIST). Computational chemistry comparison and benchmark database. `http://cccbdb.nist.gov/`. Online, accessed 10/2013.

[142] National Institute of Standards and Technology (NIST). Electron-impact cross sections for ionization and excitation. `http://physics.nist.gov/PhysRefData/Ionization/molTable.html`. Online, accessed 10/2013.

[143] H. Nettelbeck and H. Rabus. Nanodosimetry: the missing link between radiobiology and radiation physics? *Radiat. Meas.*, 46:893–897, 2011.

[144] H. Nikjoo and P. Girard. A model for the cell nucleus for DNA damage calculations. *Int. J. Radiat. Biol.*, 88:87–97, 2012.

[145] H. Nikjoo and D. T. Goodhead. Track structure analysis illustrating the prominent role of low-energy electrons in radiobiological effects of low-LET radiations. *Phys. Med. Biol.*, 36:229–238, 1991.

[146] H. Nikjoo, P. O'Neill, D. T. Goodhead, and M. Terrissol. Computational modelling of low energy electron-induced DNA damage by early physical and chemical events. *Int. J. Radiat. Biol.*, 71:467–483, 1997.

[147] H. Nikjoo, S. Uehara, D. Emfietzoglou, and F. A. Cucinotta. Track-structure codes in radiation research. *Radiat. Meas.*, 41:1052–1074, 2006.

[148] J. J. Olivero, R. W. Stagat, and A. E. S. Green. Electron deposition in water vapor, with atmospheric applications. *J. Geophys. Res.*, 77:4797–4811, 1972.

[149] C. B. Opal, E. C. Beaty, and W. K. Peterson. Tables of secondary-electron-production cross sections. *Atomic Data*, 4:209–253, 1972.

[150] P. Palihawadana, J. Sullivan, M. Brunger, C. Winstead, V. McKoy, G. García, F. Blanco, and S. Buckman. Low-energy elastic electron interactions with pyrimidine. *Phys. Rev. A*, 84:062702, 2011.

[151] P. Palihawadana, J. P. Sullivan, S. J. Buckman, and M. J. Brunger. Electron scattering from pyrazine: elastic differential and integral cross sections. *J. Chem. Phys.*, 137:204307, 2012.

[152] H. G. Paretzke, J. E. Turner, R. N. Hamm, R. H. Ritchie, and H. A. Wright. Spatial distribution of inelastic events produced by electrons in gaseous and liquid water. *Radiat. Res.*, 127:121–129, 1991.

[153] H. G. Paretzke, J. E. Turner, R. N. Hamm, H. A. Wright, and R. H. Ritchie. Calculated yields and fluctuations for electron degradation in liquid water and water vapor. *J. Chem. Phys.*, 84:3182–3188, 1986.

[154] S. T. Perkins, D. E. Cullen, and S. M. Seltzer. Tables and graphs of electron-interaction cross sections from 10 eV to 100 GeV derived from the LLNL Evaluated Electron Data Library (EEDL), Z=1-100. Technical report, Lawrence Livermore National Laboratory, University of California, 1991.

[155] S. M. Pimblott and A. Mozumder. Structure of electron tracks in water, 2. distribution of primary ionizations and excitations in water radiolysis. *J. Phys. Chem.*, 95:7291–7300, 1991.

[156] Australian Radiation Protection and Nuclear Safety Agency. `http://www.arpansa.gov.au/radiationprotection/factsheets/is_rad.cfm`. Online, accessed 10/2013.

[157] S. Pszona, J. Kula, and S. Marjanska. A new method for measuring ion clusters produced by charged particle in nanometre track sections of DNA size. *Nuc. Instrum. Meth. A*, 447:601–607, 2000.

[158] L. J. Puckett, G. O. Taylor, and D. W. Martin. Cross sections for ion and electron production in gases by 0.15-1.00-MeV hydrogen and helium ions and atoms. *Phys. Rev.*, 178:271–287, 1969.

[159] H. H. Rossi and M. Zaider. *Microdosimetry and its applications.* Springer-Verlag Heidelberg, 1996.

[160] M. E. Rudd. Differential and total cross sections for ionization of helium and hyrogen by electrons. *Phys. Rev. A*, 44:1644–1652, 1991.

[161] M. E. Rudd, Y.-K. Kim, D. H. Madison, and J. W. Gallagher. Electron production in proton collisions: total cross sections. *Rev. Mod. Phys.*, 57:965–994, 1985.

[162] M. E. Rudd, Y. K. Kim, D. H. Madison, and T. J. Gay. Electron production in proton collisions with atoms and molecules: energy distributions. *Rev. Mod. Phys.*, 64:441–490, 1992.

[163] L. Sanche. Low energy electron-driven damage in biomolecules. *Eur. Phys. J. D*, 35:367–390, 2005.

[164] R. W. Schulte, A. J. Wroe, V. A. Bashkirov, G. Y. Garty, A. Breskin, R. Chechik, S. Shchemelinin, E. Gargioni, B. Grosswendt, and A. B. Rosenfeld. Nanodosimetry-based quality factors for radiation protection in space. *Z. Med. Phys.*, 18:286–296, 2008.

[165] I. I. Shafranyosh, M. I. Sukjoviya, and M. I. Shafranyosh. Absolute cross sections of positive- and negative-ion production in electron collision with cytosine molecules. *J. Phys. B*, 39:4155–4162, 2006.

[166] A. V. Solov'yov, E. Surdutovich, E. Scifoni, I. Mishustin, and W. Greiner. Physics of ions beam cancer therapy: a multiscale approach. *Phys. Rev. E*, 79:011909, 2009.

[167] M. Stener, P. Decleva, D. M. P. Holland, and D. A. Shaw. A study of the valence shell electronic states of pyrimidine and pyrazine by photoabsorption spectroscopy and time-dependent density functional theory calculations. *J. Phys. B*, 44:075203, 2011.

[168] N. Stolterfoht, R. D. DuBois, and R. D. Rivarola. *Electron emission in heavy ion-atom collisions.* Springer, 1997.

[169] L. Storchi, F. Tarantelli, S. Veronesi, P. Bolognesi, E. Fainelli, and L. Avaldi. The Auger spectroscopy of pyrimidine and hologen-substituted pyrimidines. *J. Chem. Phys.*, 129:154309, 2008.

[170] H. C. Straub, B. G. Lindsay, K. A. Smith, and R. F. Stebbings. Absolute partial cross sections for electron-impact ionization of H_2O and D_2O from threshold to 1000 eV. *J. Chem. Phys.*, 108:109, 1998.

[171] O. Sueoka and S. Mori. Total cross sections for low and intermediate energy positrons and electrons colliding with CH_4, C_2H_4 and C_2H_6 molecules. *J. Phys. B*, 19:4035–4050, 1986.

[172] T. Sumiyoshi, K. Tsugaru, T. Yamada, and M. Katayama. Yields of solvated electrons at 30 picoseconds in water and alcohols. *Bull. Chem. Soc. Jpn.*, 58:3073–3075, 1985.

[173] C. Szmytkowski. On trends in total cross sections for electron (positron) scattering on atoms and molecules at intermediate energies. *Z. Phys. D*, 13:69–73, 1989.

[174] C. Szmytkowski and S. Kwitnewski. Electron scattering on C_3H_6 isomers. *J. Phys. B*, 35:2613–2623, 2002.

[175] C. Szmytkowski, Ł. Kłosowski, A. Domaracka, M. Piotrowicz, and E. Ptasińska-Denga. Scattering of electrons from hydride molecules: PH_3. *J. Phys. B*, 37:1833–1840, 2004.

[176] Z. Tan, Y. Xia, X. Liu, M. Zhao, Y. Ji, and B. Huang. Cross sections of electron inelastic interactions in DNA. *Radiat. Environ. Biophys.*, 43:173–182, 2004.

[177] H. Tanaka, T. Okada, L. Boesten, T. Suzuki, T. Yamamoto, and M. Kubo. Differential cross sections for elastic scattering of electrons by CH_4 in the energy range of 3 to 20 eV. *J. Phys. B*, 15:3305–3319, 1982.

[178] K. Tasaki, X. Yang, S. Urano, S. Fetzer, and P. R. LeBreton. UV photoelectron and ab initio quantum mechanical characterization of nucleotides: the valence electronic structures of 2'-deoxycytide-5'-phosphate. *J. Am. Chem. Soc.*, 112:538–548, 1990.

[179] R. M. Thomson and I. Kawrakow. On the Monte Carlo simulation of electron transport in the sub-1 keV energy range. *Med. Phys.*, 38:4531–4534, 2011.

[180] L. H. Toburen, S. L. McLawhorn, R. A. McLawhorn, K. D. Carnes, M. Dingfelder, and J. L. Shinpaugh. Electron emission from amorphous solid water induced by passage of energetic protons and fluorine ions. *Radiat. Res.*, 174:107–118, 2010.

[181] L. H. Toburen and W. E. Wilson. Energy and angular distributions of electrons ejected from water vapor by 0.3-1.5 MeV protons. *J. Chem. Phys.*, 66:5202–5213, 1977.

[182] C. S. Trevisan, A. E. Orel, and T. N. Rescigno. Elastic scattering of low-energy electrons by tetrahydrofuran. *J. Phys. B*, 39:L255–L260, 2006.

[183] J. E. Turner, H. G. Paretzke, R. N. Hamm, H. A. Wright, and R. H. Ritchie. Comparative study of electron energy deposition and yields in water in the liquid and vapor phases. *Radiat. Res.*, 92:47–60, 1982.

[184] S. Uehara and H. Nikjoo. Monte Carlo simulation of water radiolysis for low-energy charged particles. *J. Radiat. Res.*, 47:69–81, 2006.

[185] S. Uehara, H. Nikjoo, and D. T. Goodhead. Cross-sections for water vapour for the Monte Carlo electron track structure code from 10 eV to the MeV region. *Phys. Med. Biol.*, 37:1841–1858, 1992.

[186] S. Uehara, H. Nikjoo, and D. T. Goodhead. Comparison and assessment of electron cross sections for Monte Carlo track structure codes. *Radiat. Res.*, 152:202–213, 1999.

[187] Marcus Unverricht-Yeboah, Forschungszentrum Jülich GmbH, Geschäftsbereich Sicherheit und Strahlenschutz (S-US), Arbeitsgruppe Strahlenbiologie, 52425 Jülich, Deutschland.

[188] C. von Sonntag and M. Dizdaroglo. The reactions of OH radicals with D-ribose in deoxygenated and oxygenated aqueous solution. *Carbohyd. Res.*, 58:21–30, 1977.

[189] N. Watanabe, H. Hayashi, and Y. Udagawa. Inelastic X-ray scattering study on molecular liquids. *J. Phys. Chem. Solids*, 61:407–409, 2000.

[190] J. D. Watson and F. H. C. Crick. Molecular structure of nucleic acids: a structure for deoxyribose nucleic acid. *Nature*, 171:737–738, 1953.

[191] R. C. Weast, S. M. Selby, and C. D. Hodgman. *Handbook of Chemistry and Physics (65th edition)*. CRC Press, 1984.

[192] R. E. Wilkinson, D. T. Goodhead, and J. Thacker. Induction of chromosome aberations by very short tracks at different stages of the cell cycle. *Radiat. Prot. Dosim.*, 13:161–165, 1985.

[193] C. Winstead and V. McKoy. Interaction of low-energy electrons with the purine bases, nucleosides, and nucleotides of DNA. *J. Chem. Phys.*, 125:244302, 2006.

[194] C. Winstead and V. McKoy. Low-energy electron scattering by deoxyribose and related molecules. *J. Chem. Phys.*, 125:074302, 2006.

[195] B. Winter, R. Weber, W. Widdra, M. Dittmar, M. Faubel, and I. V. Hertel. Full valence band photoemission from liquid water using EUV synchrotron radiation. *J. Phys. Chem.*, 108:2625–2632, 2004.

[196] J.-S. Yoon, M.-Y. Song, J.-M. Han, S. H. Hwang, W.-S. Chang, B. J. Lee, and Y. Itikawa. Cross sections for electron collisions with hydrogen molecules. *J. Phys. Chem. Ref. Data*, 37:913–931, 2008.

[197] S. M. Younger and T. D. Märk. Semi-empirical and semi-classical approximations for electron ionization. In T. D. Märk and G. H. Dunn, editors, *Electron ionization*, pages 24–41. Innsbruck University Press, 2010.

[198] M. Zaider, D. J. Brenner, and W. E. Wilson. The applications of track calculations to radiobiology i. Monte Carlo simulation of proton tracks. *Radiat. Res.*, 95:231–247, 1983.

[199] A. Zecca, L. Chiari, G. García, F. Blanco, E. Trainotti, and M. J. Brunger. Total cross sections for positron and electron scattering from pyrimidine. *J. Phys. B*, 43:215204, 2010.

[200] A. Zecca, G. Karwasz, S. Oss, R. Grisenti, and R. S. Brusa. Total absolute cross sections for electron scattering on H_2O at intermediate energies. *J. Phys. B*, 20:L133, 1987.

[201] A. Zecca, C. Perazzolli, and M. J. Brunger. Positron and electron scattering from tetrahydrofuran. *J. Phys. B*, 38:2079, 2005.

[202] L. Zhang and Z. Tan. A new calculation on spectrum of direct DNA damage induced by low-energy electrons. *Radiat. Environ. Biophys.*, 49:15–26, 2010.

Appendix A

Total electron-impact cross sections of THF, TMP, PY and PU

Total electron-impact cross sections of THF, TMP, PY and PU, obtained from the evaluated model functions, are given in tables A.1 and A.2 together with the evaluated uncertainties. Uncertainties of ionization cross sections were not determined for energies lower than 20–30 eV as no experimental data were available, on the one hand, and the BEB model may not be accurate at energies close to the ionization threshold, on the other hand. Subsequently, the uncertainties of excitation cross sections were also omitted in the respective energy region.

Table A.1: Total electron-impact cross sections of THF and TMP. Units are in Å^2.

	THF				TMP			
T (eV)	σ_{t}	σ_{ion}	σ_{el}	σ_{exc}	σ_{t}	σ_{ion}	σ_{el}	σ_{exc}
9	55.91 ± 0.54	0.00 ± —	43.48 ± 2.49	12.44 ± —	86.83	0.00 ± —	80.97 ± 51.79	5.86 ± —
10	53.85 ± 0.48	0.02 ± —	42.07 ± 2.31	11.75 ± —	86.63	0.00 ± —	79.16 ± 45.75	7.47 ± —
15	48.00 ± 0.62	1.34 ± —	36.62 ± 1.74	10.04 ± —	85.22	2.22 ± —	71.33 ± 26.92	11.67 ± —
20	45.92 ± 0.63	4.64 ± 3.51	32.79 ± 1.48	8.49 ± 6.42	83.29	7.35 ± —	65.18 ± 17.62	10.75 ± —
25	44.23 ± 0.59	7.55 ± 2.06	29.89 ± 1.33	6.79 ± 1.88	81.12	12.26 ± —	60.24 ± 12.57	8.63 ± —
30	42.66 ± 0.51	9.72 ± 2.29	27.60 ± 1.24	5.34 ± 1.28	78.85	15.69 ± 13.30	56.15 ± 9.74	7.01 ± 6.07
35	41.20 ± 0.48	11.29 ± 2.06	25.72 ± 1.17	4.19 ± 0.79	76.55	18.01 ± 10.53	52.70 ± 8.13	5.84 ± 3.53
40	39.84 ± 0.46	12.37 ± 2.29	24.14 ± 1.12	3.33 ± 0.64	74.27	19.58 ± 7.76	49.73 ± 7.22	4.95 ± 2.09
45	38.59 ± 0.46	13.11 ± 2.30	22.79 ± 1.07	2.70 ± 0.49	72.04	20.67 ± 7.47	47.15 ± 6.68	4.23 ± 1.64
50	37.44 ± 0.46	13.59 ± 2.30	21.62 ± 1.03	2.24 ± 0.39	69.89	21.36 ± 7.18	44.88 ± 6.34	3.66 ± 1.33
60	35.36 ± 0.45	14.04 ± 2.30	19.67 ± 0.96	1.66 ± 0.28	65.84	21.98 ± 6.59	41.04 ± 5.91	2.82 ± 0.94
70	33.56 ± 0.46	14.09 ± 2.29	18.10 ± 0.90	1.36 ± 0.23	62.15	22.01 ± 6.61	37.90 ± 5.59	2.24 ± 0.75
80	31.97 ± 0.46	13.94 ± 2.28	16.81 ± 0.84	1.21 ± 0.21	58.82	21.73 ± 6.64	35.28 ± 5.30	1.81 ± 0.62
90	30.55 ± 0.48	13.67 ± 2.51	15.73 ± 0.80	1.15 ± 0.22	55.82	21.28 ± 6.35	33.05 ± 5.02	1.49 ± 0.50
100	29.28 ± 0.49	13.35 ± 2.73	14.79 ± 0.76	1.14 ± 0.24	53.11	20.75 ± 6.06	31.12 ± 4.75	1.24 ± 0.41
150	24.46 ± 0.53	11.58 ± 2.45	11.56 ± 0.61	1.32 ± 0.29	42.91	17.96 ± 4.68	24.34 ± 3.57	0.61 ± 0.18
200	21.17 ± 0.56	10.09 ± 2.16	9.59 ± 0.51	1.49 ± 0.33	36.26	15.63 ± 3.30	20.17 ± 2.72	0.47 ± 0.12
250	18.76 ± 0.58	8.92 ± 2.03	8.25 ± 0.45	1.59 ± 0.37	31.59	13.81 ± 2.55	17.29 ± 2.13	0.48 ± 0.11
300	16.88 ± 0.59	7.99 ± 1.90	7.27 ± 0.40	1.63 ± 0.40	28.12	12.38 ± 1.80	15.18 ± 1.72	0.56 ± 0.10
400	14.15 ± 0.60	6.63 ± 1.61	5.90 ± 0.34	1.62 ± 0.41	23.25	10.28 ± 2.13	12.25 ± 1.25	0.71 ± 0.16
500	12.22 ± 0.59	5.69 ± 1.55	4.99 ± 0.31	1.54 ± 0.44	19.95	8.82 ± 1.99	10.30 ± 1.04	0.82 ± 0.20
600	10.78 ± 0.58	4.99 ± 1.49	4.33 ± 0.29	1.45 ± 0.45	17.53	7.75 ± 1.85	8.90 ± 0.96	0.89 ± 0.23
700	9.65 ± 0.56	4.45 ± 1.46	3.84 ± 0.27	1.36 ± 0.46	15.68	6.92 ± 1.71	7.84 ± 0.93	0.92 ± 0.25
800	8.74 ± 0.55	4.03 ± 1.42	3.44 ± 0.26	1.27 ± 0.46	14.20	6.26 ± 1.56	7.00 ± 0.92	0.93 ± 0.26
900	7.99 ± 0.54	3.68 ± 1.45	3.13 ± 0.25	1.18 ± 0.48	12.98	5.73 ± 1.50	6.33 ± 0.91	0.92 ± 0.28
1000	7.36 ± 0.52	3.39 ± 1.47	2.86 ± 0.24	1.10 ± 0.49	11.97	5.28 ± 1.45	5.78 ± 0.91	0.91 ± 0.29

Table A.2: Total electron-impact cross sections of PY and PU. Units are in Å^2.

	PY				PU			
T (eV)	σ_{t}	σ_{ion}	σ_{el}	σ_{exc}	σ_{t}	σ_{ion}	σ_{el}	σ_{exc}
9	63.94 ± 1.92	0.00 ± —	46.42 ± 3.40	17.56 ± —	78.23	0.00	56.75	21.48
10	63.64 ± 1.99	0.04 ± —	45.02 ± 3.13	18.62 ± —	78.51	0.06	55.49	22.97
15	54.97 ± 2.04	1.51 ± —	39.50 ± 2.39	14.02 ± —	68.61	2.44	49.23	16.94
20	48.34 ± 2.00	3.60 ± —	35.56 ± 2.12	9.24 ± —	65.76	5.73	48.30	11.73
25	45.03 ± 2.02	5.71 ± —	32.55 ± 2.01	6.83 ± —	63.72	9.00	45.97	8.74
30	42.88 ± 2.01	7.46 ± 1.42	30.15 ± 1.95	5.34 ± 1.10	61.69	11.65	43.28	6.76
35	41.17 ± 2.00	8.80 ± 1.42	28.16 ± 1.90	4.27 ± 0.77	59.76	13.61	40.79	5.35
40	39.69 ± 1.99	9.83 ± 1.42	26.49 ± 1.86	3.43 ± 0.58	57.93	15.09	38.57	4.26
45	38.37 ± 2.00	10.58 ± 1.56	25.05 ± 1.82	2.80 ± 0.48	56.21	16.15	36.61	3.44
50	37.18 ± 2.00	11.11 ± 1.71	23.80 ± 1.77	2.32 ± 0.42	54.60	16.89	34.86	2.84
60	35.09 ± 2.02	11.74 ± 1.99	21.71 ± 1.69	1.70 ± 0.33	51.67	17.70	31.88	2.09
70	33.30 ± 2.03	11.99 ± 1.94	20.02 ± 1.61	1.36 ± 0.26	49.09	17.96	29.43	1.71
80	31.75 ± 2.03	12.01 ± 1.88	18.63 ± 1.54	1.17 ± 0.22	46.80	17.91	27.37	1.52
90	30.37 ± 2.03	11.91 ± 1.88	17.44 ± 1.47	1.08 ± 0.21	44.75	17.68	25.62	1.46
100	29.14 ± 2.03	11.73 ± 1.88	16.43 ± 1.41	1.04 ± 0.20	42.90	17.35	24.10	1.45
150	24.45 ± 2.01	10.48 ± 1.77	12.88 ± 1.16	1.14 ± 0.24	35.79	15.31	18.77	1.71
200	21.24 ± 1.99	9.28 ± 1.66	10.71 ± 0.99	1.30 ± 0.29	30.91	13.46	15.51	1.94
250	18.86 ± 1.99	8.29 ± 1.54	9.22 ± 0.88	1.40 ± 0.33	27.30	11.96	13.28	2.06
300	17.00 ± 1.99	7.48 ± 1.42	8.12 ± 0.80	1.45 ± 0.35	24.51	10.76	11.64	2.10
400	14.26 ± 2.01	6.27 ± 1.27	6.59 ± 0.70	1.44 ± 0.39	20.42	8.98	9.39	2.05
500	12.31 ± 2.02	5.41 ± 1.20	5.57 ± 0.64	1.37 ± 0.41	17.54	7.73	7.89	1.93
600	10.85 ± 2.03	4.76 ± 1.13	4.84 ± 0.60	1.28 ± 0.42	15.39	6.80	6.82	1.78
700	9.70 ± 2.03	4.26 ± 1.00	4.28 ± 0.57	1.19 ± 0.41	13.72	6.08	6.01	1.63
800	8.77 ± 2.02	3.87 ± 0.88	3.84 ± 0.55	1.09 ± 0.39	12.37	5.50	5.37	1.49
900	8.00 ± 2.01	3.54 ± 0.98	3.48 ± 0.54	1.01 ± 0.41	11.26	5.04	4.86	1.37
1000	7.36 ± 2.00	3.27 ± 1.07	3.19 ± 0.52	0.93 ± 0.42	10.33	4.65	4.44	1.25